Controlling Vesicle Systems by Amphiphilic Copolymers

Steuerung und Kontrolle von Vesikelsystemen durch amphiphile Copolymere

vorgelegt von
Dipl.-Chem.
Katharina Bressel
aus Berlin, Deutschland

Von der Fakultät II - Mathematik und Naturwissenschaften
der Technischen Universität Berlin
zur Erlangung des akademischen Grades

Doktor der Naturwissenschaften
Dr. rer. nat.

genehmigte Dissertation

Promotionsausschuss:

Vorsitzende: Prof. Dr. rer. nat. Karola Rück-Braun
Gutachter: Prof. Dr. rer. nat. Michael Gradzielski
Gutachter: Dr. rer. nat. Theyencheri Narayanan

Tag der wissenschaftlichen Aussprache: 5.August 2013

Berlin 2014
D83

Für Mattis Emil

∗ *27 Juli 2012*

Acknowledgements

The presented thesis was elaborated under the supervision of Prof. Dr. Michael Gradzielski at the Technische Universität Berlin in the time of April 2008 to August 2013.

First I would like to thank my supervisor Prof. Dr. Michael Gradzielski for giving me the opportunity to work in his laboratory and in his group. He helped me finding this interesting topic and initiated this project, where I had the pleasure of being part of it. His advice and motivation led to important breakthroughs in this thesis.

I am grateful to Dr. Theyencheri Narayanan for reviewing my thesis.

I am indebted to the Deutsche Forschungsgemeinschaft for their financial support in the Schwerpunktprojekt 1273 and the women's representative for financial support under the framework of the "Berliner Programms zur Förderung der Chancengleichheit von Frauen in Forschung und Lehre, 2012-2015" and the European Synchrotron Radiation Facility (ESRF), the Institut Laue-Langevin (ILL) and the Jülich Centre for Neutron Science (JCNS) for the allocation of beam time.

I would like to thank Dr. Theyencheri Narayanan and Dr. Jérémie Gummel for their help with the SAXS measurements and for providing me with such a good instrument, which was crucial for my work.

I would like to express my gratitude to Dr. Isabelle Grillo and Dr. Marie-Sousai Appavou for their cooperation in SANS measurements that provided essential information for my studies.

I am grateful to Prof. Dr. Heinz Rehage for giving me the opportunity to work in his laboratory on rheological measurements and to Dr. Evelin Schmitte for introducing me to this method and for her help with the measurements.
I am thankfull to Prof. Dr. Joachim Koetz and Brigitte Tiersch, who provided me with pictures from the electron microscope.

Special thanks go to Dr. Sylvain Prévost and Michael Muthig for their patience in lengthy but fruitful discussions with me about my work. Without the tool SASET designed by Michael my work would have been impossible. Sylvain took part in all my SANS and SAXS beam times and nearly everything I know about scattering measurements I learned from him.

Additionally I would like to thank Dr. Paula Malo de Molina, Dr. Peggy Heunemann and Dr. Martin Medebach for their help during beam times and Dr. Anina Barth who introduced me to the stopped-flow method.

I owe my gratitude to Dr. René Strassnick, Rolf Kunert, Detlef Klabunde, Erik Sallwey and Michael Knuth for the assembly of the stopped-flow apparatus and all the minor and major services concerning engineering and to Gabriele Hedicke, Michaela Dzionara and Jana Lutzki, who provided support and help in the laboratory whenever it was necessary and kept the laboratory running. Christiane Abu-Hani, Maria Blobel and Petra Erdmann were always friendly and helpful in everything concerning organisation.

I would like to thank all my colleagues for the last nice years and their help and support. I always felt comfortable and at home in the group. Ingo Hoffmann, Mahmoud Elgammal and Carolin Ganas were the best room mates I could imagine and I enjoyed our conversations.

I am very thankful to my family for their support and especially to my husband Holger for his love, support and patience.

Publications

[1] Katharina Bressel, Michael Muthig, Sylvain Prévost, Isabelle Grillo, and Michael Gradzielski
"Mesodynamics: watching vesicle formation in situ by small-angle neutron scattering"
Colloid and Polymer Science, 2010, **288**(8), 827–840, doi:10.1007/s00396-010-2212-z.
Contains parts of chapter 4

[2] Katharina Bressel, Sylvain Prévost, Marie-Sousai Appavou, Brigitte Tiersch, Joachim Koetz, and Michael Gradzielski
"Phase behaviour and structure of zwitanionic mixtures of perfluorocarboxylates and tetradecyldimethylamine oxide - dependence on chain length of the perfluoro surfactant"
Soft Matter, 2011, **7**(23), 11232–11242, doi:10.1039/C1SM05618B.
Contains chapter 2

[3] Katharina Bressel, Michael Muthig, Sylvain Prévost, Jérémie Gummel, Theyencheri Narayanan, and Michael Gradzielski
"Shaping Vesicles - Controlling Size and Stability by Admixture of Amphiphilic Copolymer"
ACS Nano, 2012, **6**(7), 5858–5865, doi:10.1021/nn300359q.
Contains parts of chapter 6

Zusammenfassung

Die vorliegende Arbeit beschäftigt sich mit der spontanen Vesikelbildung in wässrigen Tensidmischungen und der Kontrolle der Vesikelstruktur. Dazu wurden Tensidsysteme aus anionischen Perfluortensiden und dem nichtionischen Tetradecyldimethylaminoxid (TDMAO) mit Hilfe des pH-Werts, der Leitfähigkeit, Dynamischer Lichtstreuung (DLS), Viskosität und Neutronenkleinwinkelstreuung (SANS) charakterisiert, um Vesikelbereiche zu identifizieren. Anhand von Neutronenbeugungsexperimenten an gemischten Tensidkristallen aus nichtionischen oder kationischen Kohlenwasserstofftensiden und anionischen Perfluortensiden, die Kristalle aus gestapelten Tensiddoppelschichten bilden, konnten Informationen über die Struktur der entsprechenden Tensiddoppelschichten in Vesikeln gefunden werden.
Die Bildungskinetik und der Vesikelbildungsmechanismus wurden an ausgewählten Vesikelsystemen aus Lithiumperfluoroktylsulfonat (LiPFOS) und TDMAO untersucht, um über den Mechanismus und intermediäre Strukturen, die während der Vesikelbildung auftreten, den Bildungsprozess zu lenken und die Endstrukturen zu beeinflussen. Zur Untersuchung wurde die Stopped-flow Methode in Kombination mit SANS, Röntgenkleinwinkelstreuung (SAXS) und DLS als Detektionsmethode verwendet. Die Analyse zeigte, daß sich beim Mischen einer mizellaren TDMAO-Lösung mit einer mizellaren LiPFOS-Lösung erst gemischte Scheibchenmizellen bilden, die bis zu einer maximalen Größe wachsen und sich dann in Vesikel mit einer Polydispersität von nur 5% kurz nach der Bildung umwandeln. Dabei bestimmt die Balance zwischen der Linienspannung des Scheibchenrandes und der Biegesteifigkeit der Membran die Größe der gebildeten Vesikel. Temperaturabhängige Messungen dienten dazu, die Biegesteifigkeit zu bestimmen.
Mit Hilfe amphiphiler Copolymere vom Pluronic-Typus ($PO_nEO_mPO_n$ oder $EO_nPO_mEO_n$), die sich in den Rand der Tensidscheibchenmizellen einlagern können, konnte die Linienspannung verändert werden und damit die Größe der gebildeten Vesikel kontrolliert werden. Außerdem zeigte sich, daß sich die Polymere nach der Vesikelbildung in die Tensiddoppelschicht einlagern und die Vesikel gegenüber Alterungsprozessen stabilisieren. Systematische Änderungen der Polymerstruktur gaben Auskunft über den Einfluß der Polymerarchitektur auf den Vesikelbildungsprozess und die Vesikelgröße und auf die Stabilität der gebildeten Vesikel. Dabei zeigte sich, daß die Vesikelgröße mit der Polymerkonzentration und der Anzahl der Propylenoxidgruppen (PO) zunahm während die Vesikel umso stabiler waren je größer die Anzahl der Ethylenoxidgruppen (EO) war. Ob der Polymerkern aus Polyethylenoxid oder aus Polypropylenoxid bestand hatte keinen signifikanten Einfluß auf die Vesikelstruktur und die Stabilität.

Abstract

In this work a study about the spontaneous vesicle formation in aqueous surfactant mixtures and the control over the vesicle structure is presented. For that purpose surfactant systems consisting of anionic perfluoro surfactants and the nonionic tetradecyldimethylamine oxide (TDMAO) were characterised by means of the pH value, conductivity, Dynamic Light Scattering (DLS), viscosity and Small Angle Neutron Scattering (SANS) in order to identify vesicle phase regions.

By means of Neutron Diffraction experiments on mixed surfactant crystals consisting of nonionic or cationic hydrocarbon surfactants and anionic perfluoro surfactants, that form crystals of stacked surfactant bilayers, information about the structure of correspondent surfactant bilayers in vesicles could be found.

The kinetics and the mechanism of vesicle formation were investigated in selected vesicle systems consisting of lithium perfluorooctylsulfonate (LiPFOS) and TDMAO in order to control the formation process and in order to influence the final aggregate structures via the mechanism of formation and intermediate structures. Investigations were carried out with the stopped-flow mixing in combination with SANS, Small Angle X-ray Scattering (SAXS) and DLS as methods of detection. The analysis shows, that upon mixing a micellar TDMAO solution with a micellar LiPFOS solution, first mixed disc-like micelles are formed that grow up to a maximum size and then transform into vesicles with a polydispersity of only 5% shortly after formation. The balance between the line tension of the disc rim and the bending elasticity of the membrane determines the size of the formed vesicles. Temperature dependent measurements were performed in order to determine the bending elasticity.

Amphiphilic copolymers of the pluronic type ($PO_nEO_mPO_n$ or $EO_nPO_mEO_n$) can be incorporated into the rim of the disc-like surfactant micelles and thereby can alter the line tension and as a result controls the size of the formed vesicles. Furthermore measurements revealed that the polymers are incorporated into the surfactant membrane during the vesicle formation and stabilise the vesicles against ageing processes. Systematic variations of the polymer structure allowed to obtain information about the influence of the polymer architecture on the vesicle formation process and the vesicle size and on the stability of the formed vesicles. As a result it could be shown that the vesicle size increases with the polymer concentration and the number of propylene oxide groups (PO), while the stability increases with the number of ethylene oxide groups (EO). Whether the polymer backbone consisted of polyethylene oxide or of polypropylene oxide had no significant influence on the vesicle structure and stability.

Contents

Introduction

Amphiphilic molecules show self aggregation in aqueous solution. Depending on the conditions like concentration, temperature, salt content and the type of amphiphilic molecules a wide range of different aggregate types can be observed. The principles of self aggregation due to the hydrophobic interactions of the molecules in water and the reduction in entropy during self aggregation were first introduced by Tanford, who developed a model for the relation between the shape of the amphiphile and the shape of the aggregate[137,138], which was later refined by Israelachvili et al. and led to the packing parameter p as it is defined in eqn (1.0.1) with the volume of the amphiphile v, the area of the head group in aggregates a_{H} and the length of the hydrophobic chain of the amphiphile l_{C}.[76,87]

$$p = \frac{v}{a_{\mathrm{H}} \cdot l_{\mathrm{C}}} \tag{1.0.1}$$

The packing parameter is directly related to the shape of the aggregates in equilibrium. Amphiphiles with bulky heads or a relatively short tail have a smaller packing parameter, which leads to spherical or rodlike micelles, while amphiphiles with bulky hydrophobic chains and small heads have a larger packing parameter and tend to form curved or flat bilayers as it is depicted in Table 1.0.1.

The packing parameter can either be influenced by the architecture of the amphiphile itself, by mixtures of different amphiphiles and their interactions or by admixing oils or cosurfactants. A cosurfactant is a surface active component, that does not itself form micelles, but can be incorporated into surfactant aggregates. Due to their small head group they usually increase the packing parameter and induce a phase transition.[48,49,83]

Studies about morphological changes due to changes in the packing parameter open a wide field and this topic has been studied extensively in the past.[81,104,119,146]

In this work the focus lies on the formation of vesicles. A suitable model system has to be found to study the vesicle formation process and based on such a fundamental understanding to be able to modify this process. For that purpose the kinetics have to be studied in detail. The conditions for vesicle formation[14,26,47,48,50,60,75,76,78,79,126–128] as well as their formation process[9,36,45,46,49,52,89,91,92,109,118,130,132,141,142] have been studied before, but still there are open questions as how to optimise the formation process and how to control it in order to obtain vesicles especially tailored in size, polydispersity and stability for different applications. Knowledge over the vesicle formation process offers the possibility to interfere with intermediate structures in order to control the final structure. The idea here is to introduce additives that interact with those intermediates and lead to different end products.

Table 1.0.1: Structures predicted by the packing parameter

structure of the amphiphile or amphiphilic pair	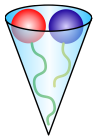	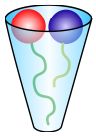	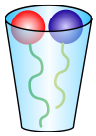	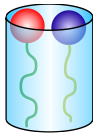
packing parameter	$p \leq \frac{1}{3}$	$\frac{1}{3} < p < \frac{1}{2}$	$\frac{1}{2} \leq p \leq 1$	$1 < p < 2$
structure of aggregate	spherical micelles	ellipsoidal micelles or rod-like micelles	vesicles	planar lamellae or discs
	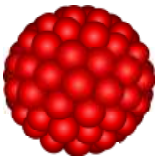	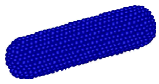	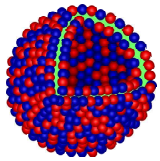	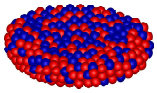

In surfactant mixtures often catanionic mixtures are regarded. These mixtures show strong attractive interactions between their head groups, which leads to a reduction in the head group area and results in an increase of the packing parameter. In these kind of mixtures vesicle formation can be observed.[18,28,33,55,63,71,81,86,98–100,148] The tendency for vesicles can even be facilitated, if one of the surfactants is a perfluoro surfactant due to the large volume of the hydrophobic chain. Several mixtures of hydrocarbon and perfluoro surfactants have been investigated before[42,53,56,73,78,93,122,125,143] and often show wide areas, where vesicles form spontaneously. Due to these findings we try to find a suitable model system among hydrocarbon/perfluoro surfactant mixtures.

Vesicles Vesicles are spherical shells, which consist of surfactant bilayers and where the interior is filled with the solvent. They are classified by their size and structure. Unilamellar vesicles only consist of one shell while multilamellar vesicles (MLV see Fig. 1.0.1c) are formed by several concentrical bilayers and multivesicular vesicles (MVV see Fig. 1.0.1d) are larger vesicle shells, that encapsulate several smaller vesicles. Unilamellar vesicles can be divided into two different classes by their size. Vesicles with a radius between 4 and 50nm are classified as small unilamellar vesicles (SUV see Fig. 1.0.1a). Vesicles with radii between 50nm and 10μm are called large unilamellar vesicles (LUV see Fig. 1.0.1b). The important

point to distinguish between SUV and LUV is the ratio between the thickness of the bilayer or the length of the amphiphile in the bilayer l_C and the radius of the vesicle $R_{ves.}$. If $l_C/R_{ves.} \ll 1$, then the bilayer can be regarded as a flat bilayer on the length scale of the surfactant length and the vesicles are LUV.[32]

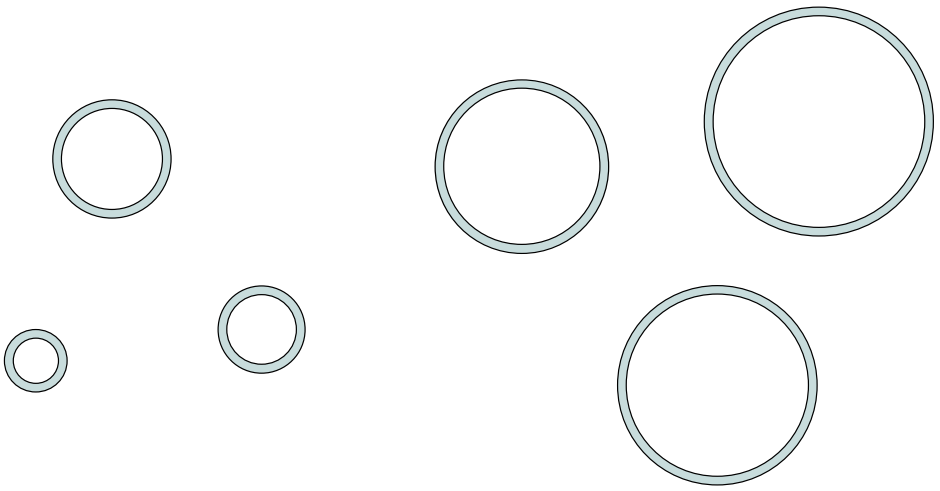

(a) Small unilamellar vesicles

(b) Large unilamellar vesicles

(c) Multilamellar vesicles

(d) Multivesicular vesicles

Figure 1.0.1: Different types of vesicles

The preposition for vesicle formation is a sufficiently high packing parameter. This can be achieved with amphiphiles with a relatively bulky chain or with double chain surfactants like phospholipids[10,76,115,136] or esterquats[22,23], in catanionic mixtures with strong head group interactions and small head group areas,[18,28,33,55,63,71,81,86,98–100,148] by admixing cosurfactants with a small head group area, that increase the volume of the chain,[13,48,49,64–67,110] or by using gemini surfactants, where the head group area is reduced by a covalent bond between two conventional surfactants.[15,30,111,112,121]

Vesicles can be prepared by various methods, where the method of preparation depends on

the vesicle system.

Often vesicles are prepared from lamellar phases. Especially when the bilayers are very stiff or if the water solubility of the surfactant is low this phase transition can only be achieved by introducing large amounts of energy into the system. In this case the surfactant system is often below its Krafft point and the hydrophobic chains are in a frozen state in the bilayer. A classical way to introduce energy to the system is by dispersing lamellar phases in water and breaking these lamellas by sonification[70] or by extrusion,[69,97,102,114] that means by pressing the dispersion through a diaphragm of defined pore size. Above the chain melting temperature this method is as well often used to produce vesicles of a defined size from larger vesicles.

A method were no external energy is introduced is the thin film hydration technique. Here the surfactant usually has a low solubility in water. For this preparation method it is dissolved in an organic volatile solvent like chloroform, the solvent is evaporated in order to form a thin surfactant film in the reagent vessel, and then these films are swollen and finally dissolved in water. As a result mostly multilamellar vesicles are formed in water.[16,41,133]

In the methods described above it can be expected, that the formed vesicles are not in equilibrium state. The vesicle state is metastable either due to the low membrane flexibility, that prevents fusion processes, or due to the low solubility of the surfactant in water that prevents ageing processes due to Ostwald ripening or both. In these systems the properties of the vesicles are strongly influenced by the vesicle formation technique and the energetic input. In solutions of water soluble double chain surfactants, in catanionic mixtures or if cosurfactants are added, vesicle formation can appear spontaneously. Here the conditions, when vesicle formation is thermodynamically favoured, have to be considered. The first precondition for vesicle formation is, that the packing parameter lies between 0.5 and 1. In addition the rigidity of the bilayer has to allow for the formation of a spherical shell instead of a flat bilayer. This depends on the free energy F_b of the bilayer.[57] Helfrich derived the free energy of a bilayer, that forms an ellipsoidal shape with the half axis R_1, R_2 and R_3, in analogy to a harmonic oscillator in dependence on the curvatures $c = 1/R$ with an energetic minimum at the spontaneous curvature c_0 (eqn (1.0.2), see section A.1).

$$F_\mathrm{b} = \int \left(\frac{\kappa}{2} \left(c_1 + c_2 - 2c_0 \right)^2 + \overline{\kappa} c_1 c_2 \right) dA \tag{1.0.2}$$

That means the free bending energy κ can not be too high. In addition the Gaussian modulus or saddle-splay modulus $\overline{\kappa}$ has to be negative. In that case the second summand in eqn (1.0.2) becomes negative and the free energy of the membrane decreases, if c_1 and c_2 have the same sign. c_1 and c_2 are the mean curvatures of the bilayer, c_0 is the spontaneous

curvature and A is the bilayer area.
Vesicles in general are interesting systems since they can be used as model systems for biological membranes in the case of phospholipid vesicles[12,31,94] and there are attempts to use them as drug carrier systems either by encapsulating water soluble drugs in the vesicle interior or by introducing hydrophobic drugs into the vesicle membrane.[38,88,144] Stable vesicles can be used as templates to synthesise hollow capsules[29,59,96,103,113] or mesoporous materials.[72,117,145] In detergency and cosmetic applications systems are used, that show spontaneous vesicle formation in order to influence the rheologic properties of the formulations.

Mixtures of hydrocarbon and perfluoro surfactants In the present study mixtures of hydrocarbon and perfluoro surfactants are investigated. When dealing with those mixtures the first question that arises is whether these two surfactants form mixed aggregates since their hydrophobic chains are immiscible. This can only be achieved, if the attractive interactions between the head groups are high enough. This question was addressed by several works before. In mixtures of a cationic hydrocarbon surfactant with a cationic perfluoro surfactant or an anionic hydrocarbon surfactant with an anionic perfluoro surfactant a demixing tendency and two micellar populations one rich in hydrocarbon surfactant and one rich in perfluoro surfactant or a local demixing within the micelles could be observed by fluorescence quenching,[4,80] NMR experiments,[3,5,11,80] or by scattering methods by contrast matching one of the two surfactants with a suitable solvent mixture.[1,2]
The demixing of hydrocarbon and perfluorocarbon surfactants of the same charge is due to their solubility in water and the repulsive interactions between their head groups and the demixing of the chains, that does not compensate for the gain in entropy, that could be expected in mixed micelles. In contrast perfluorinated cosurfactants like long perfluorinated alcohols have a low water solubility and are therefore incorporated into micelles of hydrocarbon surfactants. This is not due to thermodynamic reasons but due to the gain in entropy and the hydrophobic effect of the cosurfactant. The large volume of the cosurfactant chain and the small cosurfactant head group lead to an increased packing parameter, so in mixtures of hydrocarbon surfactants and perfluoro cosurfactants either the formation of long rod-like micelles or vesicle formation can be expected. When incorporating hydrocarbon cosurfactants into micelles of perfluoro surfactants a similar behaviour can be observed.[13,67,149]
In surfactant mixtures with attractive interactions between the head groups the situation is different to surfactant mixtures with similar head group charge. Here mixed micelles could be observed[122] due to synergistic interactions of the head groups and like in pure hydrocarbon catanionic mixtures the formation of long rod-like micelles and vesicle formation can be

observed.[122,125] The difference to pure hydrocarbon systems is that vesicle formation even takes place for shorter surfactants than in the hydrocarbon systems due to the higher chain volume of perfluoro surfactants.[56,73,122,125]

Aim and motivation of this work The general aim of this work was to gain a thorough insight into the mechanism of spontaneous vesicle formation for the case of mixing anionic with cationic or zwitterionic surfactants, and using such knowledge for a systematic control of this process. Typically that process has been seen to proceed via intermediate disc-like micelles. In that context we varied the relevant structural parameters of the surfactant, like alkyl chain length and type of the hydrophilic head group, in order to see how this parameters influence the ability for vesicle formation and its kinetics. Based on the knowledge of this detailed structural information we proceeded then to manipulate the vesicle formation in a systematic way by addition of amphiphilic copolymers. The idea here being to have a simple way for controlling size and stability of unilamellar vesicles, which are key properties for their application but in general properties that are not easily controlled.

Structure of this work In the sections 2 and 4 the influence of the packing parameter on the vesicle formation in model systems consisting of a synergistic surfactant mixture is studied. The packing parameter is influenced by changing the head group interactions between both surfactants and by changing the chain length. In addition the formation process is studied and the mechanism of vesicle formation and intermediate aggregates were investigated. This section serves as the basis for the following sections. Here a suitable model system is identified and this system is used in the following sections.
Section 3 describes the structure of crystals formed in systems similar to them described in the sections 2 and 4. This offers some insight into the structure of surfactant lamellas as they are found in vesicles as well.
In section 5 temperature dependent measurements are analysed in order to calculate the bending energy and to identify the energetic conditions of the vesicle formation process. The bending energy plays the crucial part in the vesicle formation process and determines the rate of the process and the size of final aggregates.
In section 6 the findings obtained in the preceding sections are used in order to produce well defined vesicles by admixing amphiphilic polymers that interact with intermediate structures and thereby define the structure of final aggregates.
In section 7 the structure of the polymer was varied systematically in order to identify the influences of structural features of the polymer on the vesicle formation process.

Zwitanionic Mixtures of Tetradecyldimethylamine Oxide (TDMAO) and Lithium Perfluoroalkanoates

Mixtures of cationic or zwitterionic and anionic surfactants (catanionics or zwitanionics) have been studied intensively before, with a particular emphasis on catanionic surfactants.[6,33,40,47,61,82] Such catanionic mixtures are well known to form vesicles spontaneously, as shown for a variety of systems of single alkyl chain[78,81,98,139] or double alkyl chain surfactants[99] and for these systems energetically stabilized vesicles are predicted on a theoretical basis.[126] In addition, it is also possible to have entropic stabilisation of vesicles which can occur for bilayers with low bending rigidity.[78] However, catanionics have a tendency for precipitation around equimolar mixing ratios. In contrast, mixtures of anionic and zwitterionic surfactants possess less synergistic interaction between the surfactant pairs, therefore are less prone to precipitation, but may also form vesicular systems.[53,56,101,125,140,141] Especially for the case of mixing a zwitterionic hydrocarbon surfactant with an anionic perfluoro surfactant one may observe the formation of vesicles.

This is not surprising due to the fact that perfluoro surfactants are known to have a propensity for the formation of bilayers, due to their much more voluminous and stiffer alkyl chains compared to hydrocarbon chains.[17,74] Accordingly in recent investigations the phase behaviour of mixtures of the zwitterionic tetradecyldimethylamine oxide (TDMAO) and the anionic lithium perfluorooctanoate ($C_7F_{15}CO_2Li$) has been studied by us before. They show an extended range of formation of unilamellar vesicles.[143] Studies on the kinetics of their formation process show, that it proceeds via disc-like intermediates.[141,142] Similar results have been observed for mixtures of TDMAO and lithium perfluorooctanesulfonate (LiPFOS) by SANS (see section 4). The formation process via disc-like micelles has been well established for mixtures of surfactants above the cmc (critical micelles concentration), while new investigations indicate that the mechanism may proceed via a torus-like state, if the anionic surfactant is below the cmc.[52] Generally, in these surfactant mixtures long-time stable unilamellar vesicles are formed spontaneously which do not precipitate. In comparison the corresponding catanionic mixtures with tetradecyltrimethylammonium bromide (TTABr) show a tendency for precipitation. Accordingly zwitanionic surfactant mixtures are interesting as they allow for the formation of long-time stable unilamellar vesicles.

As a logical extension of these previous studies we were now interested in the precise effect of the molecular composition of the surfactant mixture in such systems on the stability for spontaneous formation of vesicles. The stability of formed vesicles should depend on the interaction between the surfactants, which is controlled by the length of their alkyl chains,

and on the extent of attractive interaction between the head groups. To obtain a more general understanding on a molecular level here the length of the perfluoro chain of the anionic surfactant was varied in a systematic fashion. For that purpose perfluorohexanoate and -heptanoate were employed and compared to the formerly studied perfluorooctanoate. In addition the transfer from a zwitanionic system to a partially cationic system was studied by charging the TDMAO head group to a certain extent with HCl thereby altering the head group interactions in the mixture. The advantage of the TDMAO is that it allows for a continuous transition from a zwitanionic to a catanionic surfactant mixture in a moderate pH-range of pH=5-9. A measure for the interactions between the surfactant head groups is the interaction parameter β. The interaction parameter between TDMAO and the various perfluoro surfactants was obtained from the determination of the cmc of the mixed micelles, a classical way to obtain this parameter[124].

2.1 cmc-Measurements: Determination of the Interaction Parameter β

The tendency for the formation of mixed aggregates for lithium perfluorocarboxylates and TDMAO is directly related to the interaction parameter β as it can be determined from the cmc values of the pure surfactants c_1 and c_2 and of surfactant mixtures $c^\star$ using the model from Holland and Rubingh.[68] Therefore the cmc values were determined by conductivity measurements (Figs. A.2.1 to A.2.7) and eqn (2.1.1) was solved with an iterative method to calculate the molar fraction x_1 of surfactant 1 in the micelles.

$$\frac{x_1^2 \ln\left[\frac{c^\star \alpha_1}{c_1 x_1}\right]}{(1-x_1)^2 \ln\left[\frac{c^\star(1-\alpha_1)}{c_2(1-x_1)}\right]} = 1 \tag{2.1.1}$$

With the molar fraction x_1 of the surfactant 1 in the mixed aggregates the interaction parameter β was calculated for all molar ratios α_1 according to:

$$\beta = \frac{\ln\left(\frac{c^\star \alpha_1}{c_1 x_1}\right)}{(1-x_1)^2} \tag{2.1.2}$$

The mean value for β was determined and the results for the corresponding values for the theoretical cmc values according to the regular solution theory are plotted in Fig. 2.1.1.
The $c^\star$ values are in the same order of magnitude for all three different mixed systems despite the fact that the cmc values for the three pure lithium perfluorocarboxylates strongly depend

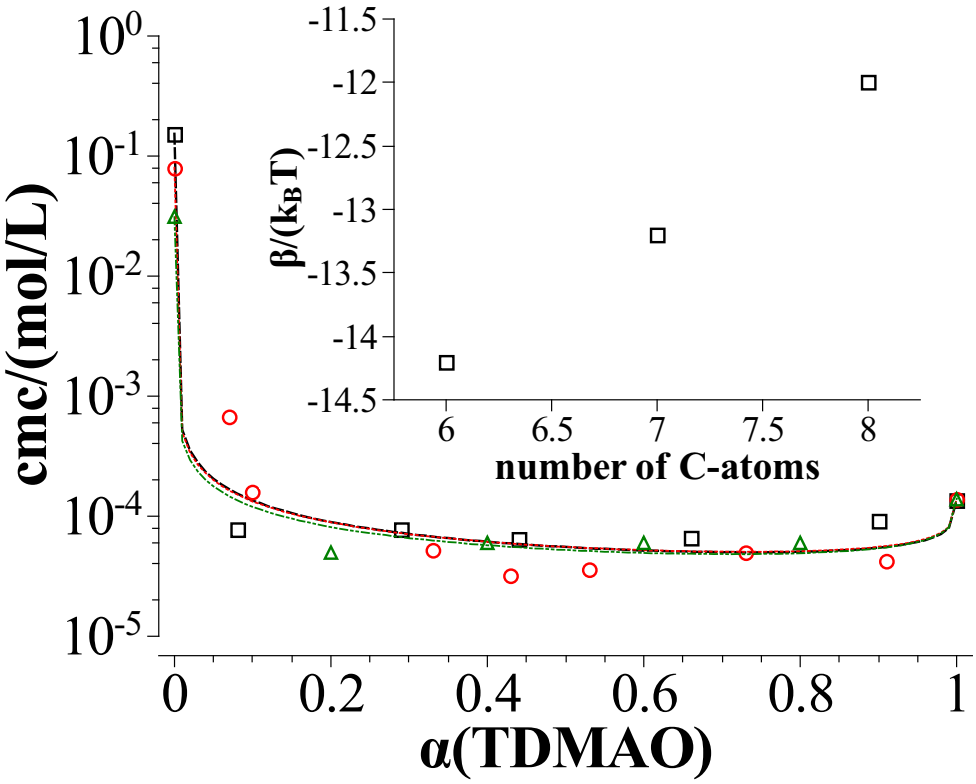

Figure 2.1.1: Critical micelle concentration (*cmc*) determined by conductivity measurements; TDMAO- $C_5F_{11}CO_2Li$ measurement - □, theory with $\beta = -14.2k_BT$ - dashed line; TDMAO- $C_6F_{13}CO_2Li$ measurement - ◯, theory with $\beta = -13.2k_BT$ - dotted line; TDMAO- $C_7F_{15}CO_2Li$[143] measurement - △, theory with $\beta = -12k_BT$ - dashed-dotted line; inset: average interaction parameter (β) for the synergistic interaction between TDMAO and perfluoro carboxylates as a function of the length of the anionic perfluoro surfactant

on the chain length and decrease with increasing number of C-atoms in the chain by about a factor of 2.5-3 per CF_2 group. That corresponds to a reduction of the Gibbs free energy of micellisation of $1.1k_BT$ per CF_2 group. The cmc value for $C_5F_{11}CO_2Li$ and as a result the value of the change of the Gibbs free energy is lower than the value given by Moroi et al.,[105] but close to the value for $C_5F_{11}CO_2Na$ ($cmc = 0.172$mM) given by Iampietro and Kaler.[73] This might be due to the methods for cmc determination.

Apparently the synergistic interaction between the perfluoro surfactants and TDMAO is the stronger the shorter the perfluoro surfactant chain (Fig. 2.1.1). This is reasonable as the interaction of the perfluorinated chains with the hydrocarbon chains is unfavourable, while the head group interaction should basically be identically attractive. The interaction parameter β is reduced by $1.1k_BT$ per CF_2 group, describing the repulsion between hydrocarbon and fluorocarbon chains. That means the loss of energy is quite similar while

transferring a fluorocarbon chain into an aqueous environment or into a hydrocarbon environment. The pronounced reduction of the Gibbs free energy in the mixed systems proves the pronounced synergistic interactions between the head groups of TDMAO and the anionic perfluoro caboxylates. In that context it might be noted that for the perfluorooctantoate in the catanionic mixture a value of $-21k_BT$ has been reported.[143] This means that by switching from a cationic-anionic (ion-ion interaction) to a zwitterionic-anionic (dipole-ion interaction) surfactant pair one reduces the attractive interaction of the head groups by about $9k_BT$. According to these values of the interaction parameter, mixed aggregates will be formed. Apparently the increase of the repulsive interaction with growing chain length of the perfluoro surfactant just compensates the parallely lower cmc's of the pure compounds as the $c^\star$'s of the mixtures are quite similar.

Table 2.1.1: Density ρ, scattering length density SLD, critical micelle concentration cmc, molecular weight M_W of the used surfactants, and Gibbs free energy ΔG_{mic} of micellisation

molecular formular	ρ /(g/mL)	$SLD/(nm^{-2})$	$M_W/(g/mol)$	$cmc/(mol/L)$	$\Delta G_{mic}/(k_BT)$
$C_{14}H_{39}(CH_3)_2NO$	0.897	$-1.96 \cdot 10^{-5}$	257.46	$1.2 \cdot 10^{-4}$ [63]	−9.0
$C_5F_{11}CO_2Li$	2.019	$4.25 \cdot 10^{-4}$	319.98	$2.3 \cdot 10^{-1}$ [105]	−1.5
$C_6F_{13}CO_2Li$	1.947	$4.11 \cdot 10^{-4}$	369.99	$9 \cdot 10^{-2}$ [105]	−2.4
$C_7F_{15}CO_2Li$	1.922	$4.07 \cdot 10^{-4}$	420.00	$3.34 \cdot 10^{-2}$ [107]	−3.4

2.2 Phase Behaviour

As a first step the macroscopic phase behaviour at 25°C as a function of the mixing ratio for a given total surfactant concentration of 50mM for mixtures of TDMAO with various anionic perfluoro surfactants of different chain lengths was studied. In addition the case was studied, where TDMAO becomes slightly charged by protonation with HCl, thereby moving our system from a zwitanionic surfactant mixture, where the TDMAO can easily be protonated, to one that has more catanionic properties. The phase behaviour of the mixtures was studied by visual inspection and further corroborated by means of measurements of electric conductivity, pH, viscosity, and hydrodynamic radius as determined by DLS.
The electric conductivity can be taken as an indication for vesicle formation. If vesicles are formed in the solution, a substantial part of the ions becomes entrapped, thereby reducing the ion mobility. Therefore the measured conductivity κ_C significantly deviates from the expected linear behaviour of the conductivity $\kappa_{C,0}$ with the composition α of a surfactant mixture without vesicles. From this reduced conductivity κ_C one can calculate the volume fraction of the contained vesicles, ϕ_V, and the radius R of the vesicles can then be estimated

from the volume fraction of the surfactant $\phi_{\text{amph.}}$ and the volume fraction of the vesicles ϕ_V in the solution[116]:

$$\phi_V = \frac{1 - \frac{\kappa_C}{\kappa_{C,0}}}{\frac{\kappa_C}{2\kappa_{C,0}} + 1} \tag{2.2.1}$$

$$R = \frac{3D\phi_V}{\phi_{\text{amph.}}} \tag{2.2.2}$$

This calculation is valid under the assumption that the vesicles are unilamellar and monodisperse and that the vesicle radius is much larger than the thickness of the bilayer. The shell thickness D was determined from SANS measurements to be 2.3-2.7 nm (see later).
An increased viscosity could indicate formation of vesicles but this becomes only significant for volume fractions approaching dense packing. In contrast, a pronounced increase of viscosity can be expected for the case of formation of long cylindrical micelles already at low concentrations below or around 1 wt%[123]. Once they overlap the solutions become viscous and for higher concentrations these micelles can form loose networks, where the knots in the network consist of entanglements of the micelles. They can be broken under shear stress but cause a high zero shear viscosity, when the entanglements stay intact[25]. Whether vesicles or rod-like micelles are present can be further differentiated by means of DLS measurements, as vesicle formation leads to a pronounced increase of the hydrodynamic radius while the presence of cylindrical micelles leads only to moderately larger values.

TDMAO/$C_5F_{11}CO_2Li$. First we studied the surfactant lithium perfluorohexanoate with the shortest chain in order to see whether it is possible to form vesicles with such a rather weak amphiphile, whose cmc is much higher than the concentration investigated here (see Table 2.1.1). All samples are clear and optically isotropic and the conductivity increases linearly with the amount of ionic surfactant in the solution. This indicates the formation of micelles. The pH is higher in the mixtures than in the pure surfactant solutions (Fig. A.2.8). This can be attributed to the fact, that the presence of the anionic perfluoro surfactant stabilizes the protonation of the weakly basic amine oxide group and therefore enhances its degree of protonation, thereby raising the pH. This effect confirms the formation of mixed aggregates and is similarly observed for the longer chain analogues. The viscosity (Fig. 2.2.1) increases with increasing amount of perfluoro surfactant up to a maximum at α(TDMAO) = 0.5 and decreases again for higher content of perfluoro surfactant. This indicates formation of rodlike micelles.
From DLS (Fig. 2.2.1) for the pure TDMAO solution a hydrodynamic radius R_h of 7.6 nm is observed (deduced from a cumulant analysis). Upon addition of perfluoro surfactant a

decrease of R_h at $\alpha(\text{TDMAO}) = 0.9$ is observed, in agreement with the SANS measurements (see later). They show that the decrease of the hydrodynamic radius R_h, measured by DLS, arises from the fact that TDMAO forms cylindrical micelles with a length of 20nm and addition of small amounts of $C_5F_{11}CO_2Li$ leads to a decrease of the apparent R_h, which is presumably due to the charging effect. With further increase of the fraction of perfluoro surfactant the micelles apparently become elongated and form long cylindrical micelles, which leads to a higher hydrodynamic radius again.

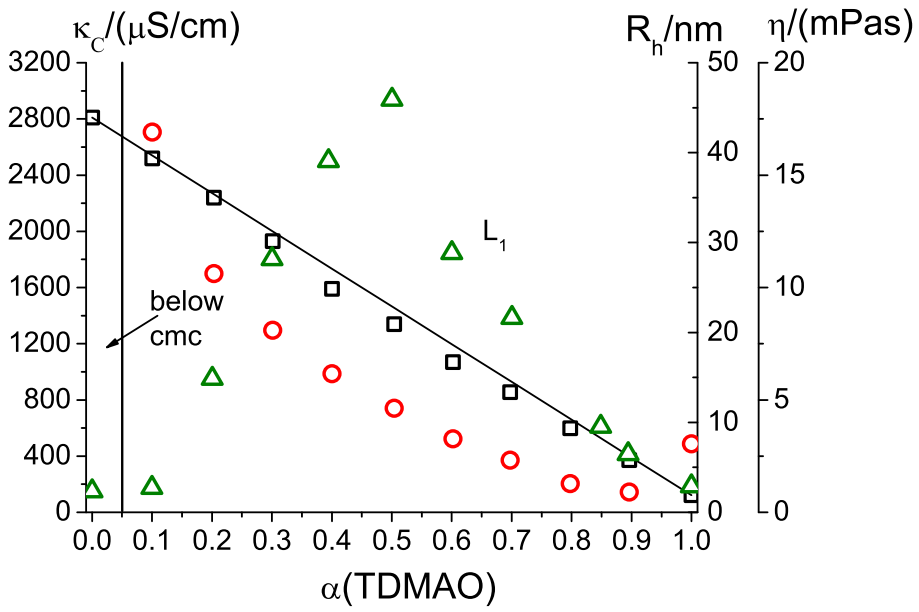

Figure 2.2.1: TDMAO/$C_5F_{11}CO_2Li$, 50 mM, $T = 25$ °C; conductivity (κ_C) □, hydrodynamic radius (R_h) ◯, and zero-shear viscosity (η_0) △

TDMAO/ HCl/$C_5F_{11}CO_2Li$. As the admixture of pure perfluorohexanoate does not lead to the formation of vesicles in zwitanionic mixtures with TDMAO, we were interested in seeing how a change towards a catanionic mixture might facilitate vesicle formation. For that purpose we charged the originally uncharged TDMAO by addition of HCl, thereby introducing cationic $TDMAOH^+$ into the system. Due to the fact that $TDMAOH^+$ is a weak acid with a pKa-value of 5[(90)] this is rather easily possible and for our investigation we chose a degree of charging of 10%, i. e. $c(\text{HCl})/c(\text{TDMAO}) = 0.1$. The addition of HCl reduces the pH of the TDMAO solution from 7.9 to 6. Upon admixture of perfluoro surfactant solution the pH rises again like in mixtures in the system TDMAO/$C_5F_{11}CO_2Li$ (Fig. A.2.9). This rise in pH indicates again the formation of mixed aggregates and further

protonation of TDMAO in the anionic environment of $C_5F_{11}CO_2Li$. The pH of the samples was not adjusted to a fixed value, but the effective pKa of the surfactant mixtures, and thereby the extent of protonation, will anyway depend on the mixing ratio. This means that the real degree of protonation of the TDMAO will be somewhat higher than the 10 mol% of added HCl. However, in total this effect will be rather small as can be estimated from the pH increase observed from pH $\sim$ 6 to pH $\sim$ 9, which corresponds to less than a relative change of 1% in the extent of the degree of protonation.

For α(TDMAO) = 1 − 0.9 the samples were transparent and optically isotropic and the conductivity (Fig. 2.2.2) increases linearly with the perfluoro surfactant content, thereby indicating the formation of mixed micelles. At α(TDMAO) = 0.4 − 0.8 a second lower turbid, flow birefringent phase of condensed large vesicles appears in addition to the micellar phase. In the range of α(TDMAO) = 0.1 − 0.3 the samples are monophasic and show a bluish shimmer. In the turbid and the two-phase areas the conductivity (Fig. 2.2.2) is significantly lower compared to the linear behaviour, from which the presence of vesicles could be concluded.

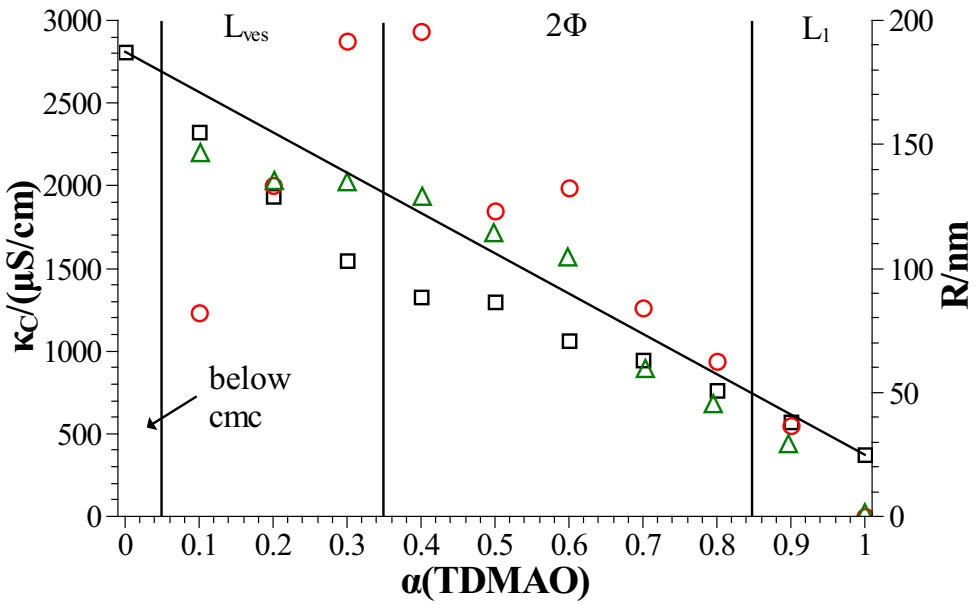

Figure 2.2.2: TDMAO/HCl/$C_5F_{11}CO_2Li$, 50 mM, T = 25 °C, (c(HCl)/c(TDMAO) = 0.1); conductivity (κ_C) □, and particle radius (R) determined by DLS measurements (hydrodynamic radius) △ and from the decrease of conductivity ◯

DLS measurements (Fig. 2.2.2) confirm the presence of vesicles and the radii of 100-150nm obtained from DLS and from conductivity measurements are similar in the mono- and biphasic region, the DLS data being more reliable. Comparing the phase behaviour of the systems TDMAO/ $C_5F_{11}CO_2Li$ and TDMAO/ HCl/ $C_5F_{11}CO_2Li$ one observes that already the pres-

ence of this fairly small amount of 10 mol% cationic surfactant changes the aggregation behaviour of this systems drastically, while having only a rather small effect on the solutions pH (see Figs. A.2.8 and A.2.9). The L_1-phase, which is the only one present in the system TDMAO/ $C_5F_{11}CO_2Li$, is drastically reduced and formation of vesicles is induced due to stronger head group interactions between the cationic $TDMAOH^+$ and the anionic $C_5F_{11}CO_2^-$ thereby increasing the packing parameter $p = v/(a_H l_C)$, where v is the volume of the surfactant, a_H the head group area, and l_C length of the hydrophobic chain.[76]

TDMAO/ $C_6F_{13}CO_2Li$. As a next step we increased the chain length of the anionic surfactant in order to see how this parameter influences the aggregation behaviour in the zwitanionic mixtures with TDMAO. For $\alpha(\text{TDMAO}) > 0.6$ a transparent, optically isotropic, micellar phase appears. In the region $\alpha(\text{TDMAO}) = 0.1 - 0.3$ the samples are transparent with a bluish shimmer indicating the formation of vesicles. A two-phase area appears for $\alpha(\text{TDMAO}) = 0.4 - 0.6$ after a time of two weeks at 25°C. The samples were optically isotropic and transparent directly after preparation. The upper phase is transparent and optically isotropic. The lower phase is white and shows flow birefringence. This lower phase only has a very small volume and presumably consists of a condensed vesicle phase (Figs. A.2.10 and A.2.11).

DLS experiments show an increase of the hydrodynamic radius R_h at the phase boundary between the micellar phase and the two-phase region (see Fig. 2.2.3). In the micellar region R_h lies between 2 and 7 nm. The polydispersity calculated from the cumulant fit is quite high (see Fig. A.2.12 and Table A.2.1). At $\alpha(\text{TDMAO}) = 0.6$ close to the phase boundary in the two-phase area the intensity autocorrelation function can better be described with a double exponential fit (see Fig. A.2.13). One radius can be identified as the radius of micellar aggregates while the other radius is the hydrodynamic radius of large vesicles. The radii of the vesicles in the two-phase area lie between 75 and 165 nm. In the homogeneous vesicle area the aggregates are much more monodisperse and the vesicles are smaller. The vesicle radii lie between 50 and 60 nm which is in good agreement with the radii calculated from the decrease of the conductivity. The polydispersity is around 0.3 (see Table A.2.1).

It is very interesting to note that the phase behaviour in this mixture is rather asymmetric. On the TDMAO rich side one starts from a micellar solution, where the rodlike micelles become increasingly longer until at a certain point the packing parameter has changed so much that bilayers are formed. This structural transition occurs via a two-phase situation. On the $C_6F_{13}CO_2Li$ rich side one starts from a solution below the cmc but upon addition of TDMAO one immediately forms vesicles. Apparently the perfluoro surfactant here is below the cmc but its packing parameter is such that it forms bilayers easily and accordingly

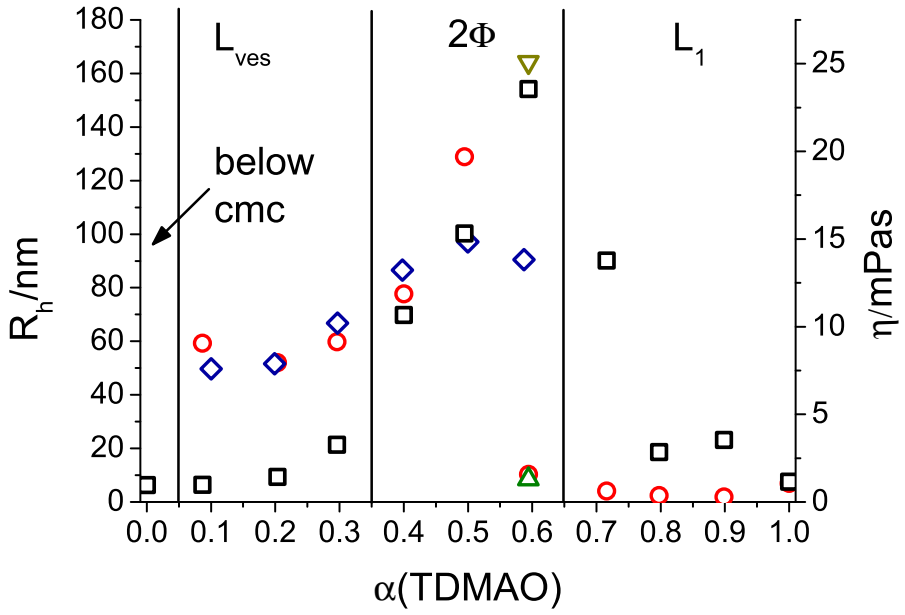

Figure 2.2.3: TDMAO/$C_6F_{13}CO_2Li$, 50 mM, T = 25 °C; viscosity (η) □, hydrodynamic radius (R_h) determined with cumulant analysis ◯ and for α(TDMAO) = 0.6 with a bi-exponential fit of $g^{(2)}$ △ and ▽, and vesicle radius determined from the decrease of the conductivity ◊

the first aggregate structure formed is directly that of vesicles. On the perfluoro surfactant rich side it can easily take up TDMAO to form vesicles while on the TDMAO rich side the TDMAO micelles incorporate the perfluoro surfactant. In the two-phase area it can be assumed from the vesicle area and the micellar area in the phase diagram, that the micelles and the vesicles do not have the same composition, but that the vesicles are rich in anionic perfluoro surfactant and the micelles are rich in TDMAO. It is also interesting to note that the viscosity maximum occurs just upon entering the biphasic region from the TDMAO rich side (Fig. 2.2.3), as the largest amount of long rodlike micelles will be present.

TDMAO/HCl/ $C_6F_{13}CO_2Li$. As before we studied the effect of changing from the purely zwitanionic system to a partly catanionic one by protonating the TDMAO by HCl to an extent of 10 mol%. The samples for α(TDMAO) = 0.1 − 0.5 are all transparent with a bluish shimmer and low viscosity, i.e. here one has a largely extended vesicle region compared to the system without added HCl. The vesicle phase is shifted towards the TDMAO rich side. This is due to the packing parameter in mixtures with $TDMAOH^+$, which is higher and favours bilayer formation. For the sample with α(TDMAO) = 0.5 sedimentation was

observed. Since catanionic mixtures show crystallisation and here the system is partly catanionic, the sediment quite likely consists of surfactant crystals but was not further investigated here. A broad two-phase area for $\alpha(\text{TDMAO}) = 0.5 - 0.9$ is observed, with a transparent optically isotropic upper micellar phase and a turbid flow birefringent lower phase consisting of condensed vesicles. In the turbid areas and in the two-phase areas the conductivity is decreased compared to the linear interpolation of the conductivity from the pure surfactant solutions (Fig. 2.2.4). This decrease was even stronger than that in the system without $TDMAOH^+$ (Fig. A.2.8).

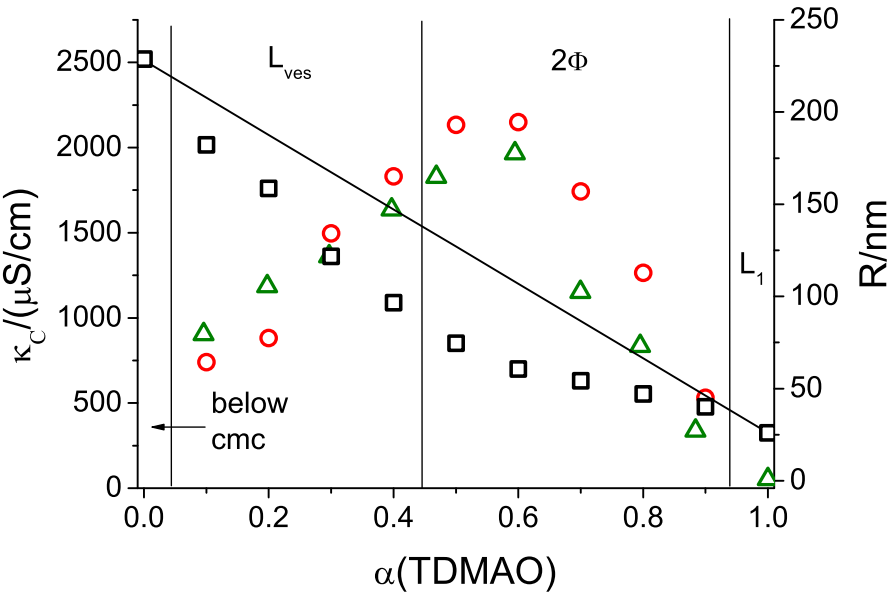

Figure 2.2.4: TDMAO/HCl/$C_6F_{13}CO_2Li$, 50mM, $T = 25°C$; conductivity (κ_C) □, and particle radius (R) determined by DLS measurements (hydrodynamic radius) △ and from the decrease of conductivity ◯

From the decrease of the conductivity vesicle radii between 60 and 170 nm were calculated (eqn (2.2.2) and Fig. 2.2.4) in good agreement with the DLS measurements. This structural picture is furthermore corroborated by the cryo-SEM picture (Fig. 2.2.5) of the sample with $\alpha(\text{TDMAO}) = 0.5$ that shows spherical objects with a diameter of about 120-180 nm. Compared to the pure zwitanionic system already the addition of 10 mol% HCl leads to a pronounced enlargement of the vesicle phase and a substantial shift towards the TDMAO rich side of the phase diagram, thereby almost completely suppressing the L_1-phase.

TDMAO/$C_7F_{15}CO_2Li$. The system TDMAO-$C_7F_{15}CO_2Li$ was previously analysed by Wolf et al. and therefore shall only be briefly compared here to the counterparts with

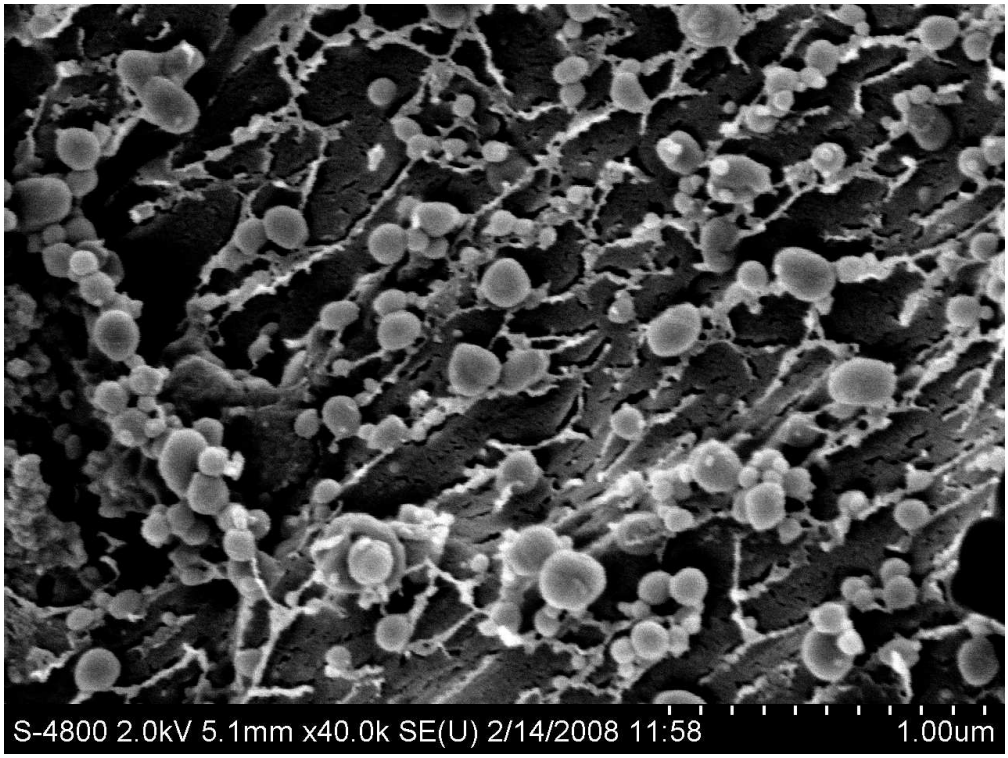

Figure 2.2.5: Cryo-SEM micrograph of a mixture of TDMAO-$C_6F_{13}CO_2Li$ with 50mM, α(TDMAO) = 0.5 and c(HCl) = 2.5mM; mostly vesicles with a radius of 140nm are formed

shorter perfluoro chains. The two systems consisting of TDMAO-$C_6F_{13}CO_2Li$ and TDMAO-$C_7F_{15}CO_2Li$ show some similarities but as well some very important differences. Both systems show a vesicle area at low TDMAO content but in comparison the vesicle area is moved to larger fractions of TDMAO and is found for $\alpha(\text{TDMAO}) = 0.2 - 0.6$ in the system with $C_7F_{15}CO_2Li$. In contrast to the system with $C_6F_{13}CO_2Li$ for lower $\alpha(\text{TDMAO}) = 0 - 0.1$ micellar solutions of low viscosity are observed, where short cylindrical or nearly spherical micelles are present, and for higher $\alpha(\text{TDMAO}) > 0.6$ no two-phase area is seen. So far it remains unclear, why no macroscopic phase separation is observed, but it was verified, that it neither occurs for extended periods of waiting nor upon centrifugation. The size of the vesicles determined by DLS varies between 25 and 80 nm. The radii obtained from the decrease of the conductivity are larger as determined by the DLS measurements. Like in the system with $C_6F_{13}CO_2Li$ at higher molar ratios of $\alpha(\text{TDMAO}) > 0.6$ a second micellar region with higher viscosity can be found. The zero-shear viscosity reaches a maximum at $\alpha(\text{TDMAO}) = 0.7$ with 33.2 mPas close to the phase boundary (Fig. 2.2.6). Accordingly here, similar as in the systems TDMAO-$C_5F_{11}CO_2Li$ and TDMAO-$C_6F_{13}CO_2Li$, at higher TDMAO content networks of long cylindrical micelles are present.

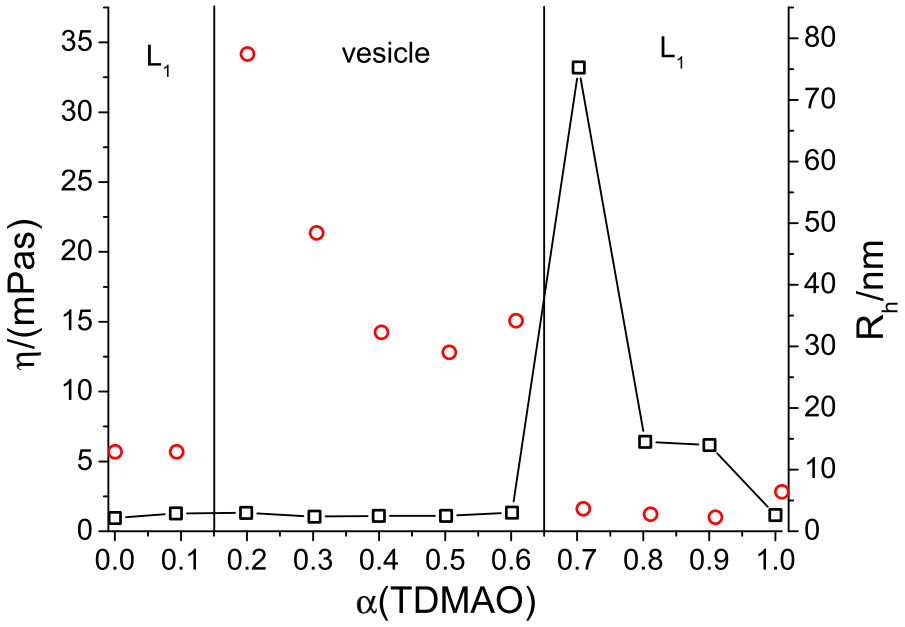

Figure 2.2.6: TDMAO/$C_7F_{15}CO_2Li$, 50 mM, T =25°C; hydrodynamic radius (R_h) ◯ and viscosity (η) □

2.3 Small Angle Neutron Scattering (SANS)

In order to obtain a more detailed picture regarding the mesoscopic structural progression in the mixtures of zwitterionic TDMAO with anionic perfluoro surfactants of different chain length SANS measurements were performed as a function of the mixing ratio. Measurements on the systems TDMAO-$C_5F_{11}CO_2Li$ and TDMAO-$C_6F_{13}CO_2Li$ were performed at the HZB (Berlin) on V4 and measurements on the system TDMAO-$C_7F_{15}CO_2Li$ were performed at the JCNS (operating at FRMII, Munich, Garching) on KWS-2 (see section 10.1.3)
Pure TDMAO is known to form short cylindrical micelles at the given concentration[62,120]. An analysis of our data with a model for polydisperse cylindrical micelles with a cylinder radius R and a log-normal distributed cylinder length with the mean length L and the polydispersity $\sigma_{rel.}$ yields a length of the cylinders of about 20 nm and a radius of 1.8 nm. These values are in good agreement with previous SANS work from Gorski and Kalus[44].

TDMAO/$C_5F_{11}CO_2Li$. SANS experiments confirm, that at 50 mM total concentration in the whole mixing range of the system TDMAO-$C_5F_{11}CO_2Li$ cylindrical micelles are present except for very low TDMAO content, where no micelles are formed (Fig. 2.3.1a).
Pure TDMAO micelles show no interaction peak but the addition of small amounts of $C_5F_{11}CO_2Li$ already leads to a repulsion between the micelles, which is visible as a cor-

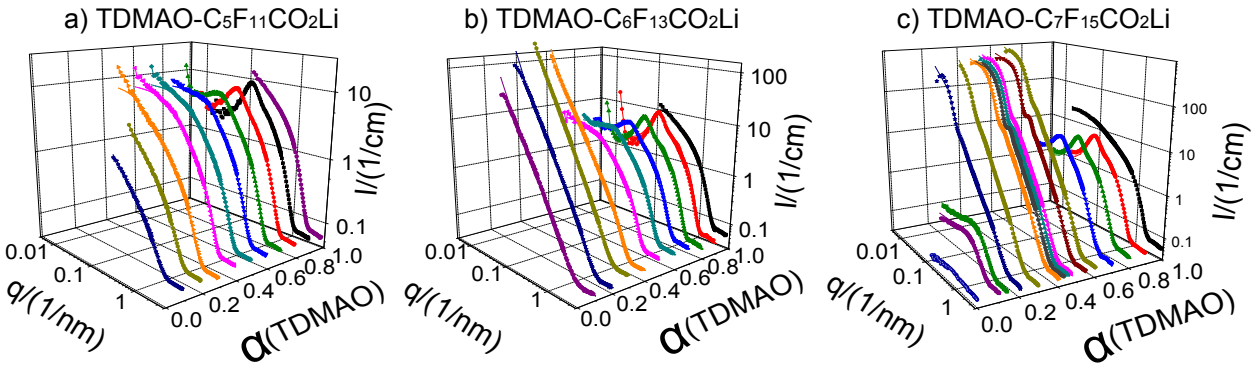

Figure 2.3.1: Small Angle Neutron Scattering (SANS) measurements of mixtures of TDMAO with various perfluoro surfactants (50 mM, 25°C) a) $C_5F_{11}CO_2Li$, b) $C_6F_{13}CO_2Li$, c) $C_7F_{15}CO_2Li$. For TDMAO-$C_5F_{11}CO_2Li$ and TDMAO-$C_6F_{13}CO_2Li$ at α(TDMAO) = 0 no measurement is shown since here one is below the *cmc*, 2-dimensional plots are given in Figs. A.2.14 to A.2.16

relation peak (see Fig. 2.3.1a), thereby indicating the incorporation of the $C_5F_{11}CO_2Li$ and the formation of mixed micelles. The repulsive electrostatic interaction of the micelles becomes stronger with increasing content of $C_5F_{11}CO_2Li$. The SANS data were described with a model of interacting cylindrical micelles for which the scattering intensity as an approximation can be written as:

$$I_{\text{cylinder,RPA}}(q) = I_{\text{cylinder}}(q) \cdot S(q) \tag{2.3.1}$$

where $I_{\text{cylinder}}(q)$ is the scattering intensity for polydisperse cylindrical micelles given in eqn (10.2.8). $S(q)$ is the structure factor that accounts for inter-particle interferences (see eqn (10.2.27)). In our case we employed for $S(q)$ an approximation as it is obtained based on the well-known hard sphere Percus-Yevick approximation[(7)] and modified for electrostatic repulsion described by a classical DLVO potential in a random phase approximation (RPA)[(8)], as it has been employed successfully before for the description of charged mixed micelles[(43)]. The analysis worked quite well here despite the fact, that the structure factor is only strictly valid for spherical particles and here we are studying significantly elongated micelles. The additional parameters introduced by $S(q)$ are the effective electrostatic potential (ζ-potential), and the effective hard-sphere radius $R_{\text{eff.}}$, while the particle number density for the structure factor was fixed by the volume fraction of amphiphilic material as calculated in eqn (10.2.3) and the form factor. The fit parameters are summarised in Table 2.3.1 and it is interesting to note that the electrostatic potential increases with increasing TDMAO content up to 55mV due to the decreasing concentration of Li and weaker counterion binding. The electrostatic repulsion in the pure TDMAO micelles is only caused by the slight protonation

of the TDMAO and therefore with 11mV significantly lower than for the mixed micelles.
The fit parameters show that the cylinder length increases with increasing amount of the anionic $C_5F_{11}CO_2Li$ in the mixture, while the radius decreases. This is due to the increasing head group interactions and the increasing amount of short but bulky perfluoro surfactant chains, thereby increasing the packing parameter and decreasing the radius. That causes an increasing slope at low q which compensates the influence of the structure factor. For that reason the structure factor seems to vanish at low q with decreasing α(TDMAO). Due to the limited q-range the length of the cylinders could not be determined for $\alpha(\text{TDMAO}) < 0.4$. The cylinder length for those measurements was fixed to a value of 40 nm as an upper limit of detection in our experiment. The elongation of the micelles correlates for $\alpha(\text{TDMAO}) = 0.5 - 1$ with the increase in viscosity (see Fig. A.2.17) and is due to entanglements of the cylindrical micelles.
The hydrodynamic radius calculated from the DLS measurements is in good agreement with the hydrodynamic radius calculated from the length L and the radius R of the cylinders as obtained from the SANS measurements (Table 2.3.1) via[54]:

$$\begin{aligned} R_\text{h} = &(1.0304 + 0.0193x + 0.06229x^2 + 0.00476x^3 \\ &+0.00166x^4 + 2.66 \cdot 10^{-6}x^7) \cdot \sqrt[3]{\frac{3}{4}R_\text{cyl}^2 L} \\ \text{with} \quad x = &\ln\left(\frac{L}{2}R_\text{cyl}\right) \end{aligned} \tag{2.3.2}$$

TDMAO/$C_6F_{13}CO_2Li$. In the system TDMAO-$C_6F_{13}CO_2Li$ cylindrical micelles with repulsive interactions, resulting in a pronounced correlation peak (Fig. 2.3.1b), are observed for $\alpha(\text{TDMAO}) = 0.9 - 0.7$. This behaviour at high TDMAO content is similar to that of the system TDMAO-$C_5F_{11}CO_2Li$. The micelles are charged and show the same repulsive interaction and screening effect from the Li counterions.
The increasing content of perfluoro surfactant in the solution leads to structural changes. The length of the micelles increases (as evidenced from the increase of the scattering intensity at low q) and cylindrical micelles with a length of about 40 nm are formed, as obtained by fitting the experimental data with eqn (10.2.8). At the same time the polydispersity of the length of the cylindrical micelles increases. The elongation of the micelles correlates with the increase in viscosity and is apparently due to entanglements of the cylindrical micelles (Fig. A.2.17)). Here it is interesting to note that for a similar length of the micelles the longer the perfluoro chain of the anionic surfactant the higher the viscosity. This can be explained by an increased thickness and stiffness of the cylindrical micelles with increasing

Table 2.3.1: SANS fit parameters for a model of cylindrical micelles with electrostatic repulsion modelled with the RPA structure factor in the system TDMAO-$C_5F_{11}CO_2Li$ (50mM, 25°C, molar fraction of TDMAO α(TDMAO), cylinder radius R, cylinder length L, aggregation number of micelles $N_{\text{agg, mic.}}$, hydrodynamic radius $R_{\text{h,SANS}}$ calculated from SANS-parameters, hydrodynamic radius $R_{\text{h,DLS}}$ determined from DLS, effective hard-sphere radius R_{eff}, and electrostatic potential ζ used in the RPA structure factor)

α(TDMAO)	R /nm	L /nm	$N_{\text{agg, mic.}}$	$R_{\text{h,SANS}}$ /nm	$R_{\text{h,DLS}}$ /nm	R_{eff} /nm	$\lvert\zeta\rvert$ /mV
1.0	1.8	20	428	6.7	7	4	10
0.9	1.9	14	351	5.6	2	7	55
0.8	1.9	16	399	5.9	3	8	53
0.7	1.9	27	735	8.8	6	8	49
0.6	1.9	30	839	9.3	8	7	37
0.5	1.8	40	1125	11	12	8	31
0.4	1.8	40	1282	12	15		
0.3	1.8	(40)	1176		20		
0.2	1.8	(40)	1258		27		
0.1	1.5	(40)	994		42		

length of the perfluoro chain. This results in a larger structural relaxation time of the system and correspondingly higher viscosity.

From the cylinder length and radius, obtained by SANS, hydrodynamic radii of these cylinders were calculated which are in good agreement with those from DLS (Table 2.3.2).

The number of charges in the micelles increases with increasing amount of anionic perfluoro surfactant. The fit parameters for the ζ-potential here show a maximum for $\alpha(TDMAO) = 0.8$ while it could be expected that the ζ-potential increases with the number of charges. On the other hand the RPA structure factor is valid for spherical particles while the micelles here become more and more elongated. So the decrease in the ζ-potential is probably an artefact due to the increase in the micellar length, that results in an enhanced effective repulsive interaction.

In the two-phase region at α(TDMAO) = 0.5 the scattering curve shows a combination of cylindrical micelles and large spherical shells (i.e. vesicles). By SANS measurements the phase transition could be detected in the same area of the phase diagram as by DLS measurements and the scattering data was then described by a structural two-state system for which the scattering intensity is given by:

$$I(q) = A_1 \cdot I_{\text{cylinder}}(q) + (1 - A_1) \cdot I_{\text{ves.}}(q) \tag{2.3.3}$$

When subdividing the scattering contributions from the micelles and the vesicles the total volume fraction was kept fixed to be the one of dispersed amphiphilic material and their relative content in form of cylinders or vesicles is described by the parameter A_1. Here $I_{\text{cylinder}}(q)$ and $I_{\text{ves.}}(q)$ for polydisperse vesicles (spherical shells) with a log-normal distributed intermediate radius R with a mean radius R_0 and a relative standard deviation σ_{rel} are given by eqns (10.2.8) and (10.2.14), respectively.
In mixtures with a high perfluoro surfactant content ($0 < \alpha(\text{TDMAO}) < 0.4$) the scattering intensity follows a q^{-2} law that indicates the presence of locally planar structures. From the slope a thickness of the bilayer of $\sim$ 2.5nm can be deduced. This value can be compared with twice the length of the TDMAO-chain estimated from the number of C-atoms n_C in the TDMAO-chain[137]:

$$d = 2 \cdot (1.5\text{Å} + 1.265\text{Å} \cdot n_C) \tag{2.3.4}$$

This value of 3.6nm is significantly higher than the thickness deduced from SANS measurements. This estimation only holds for fully stretched hydrocarbon chains but here we have to take into account that in the vesicle region TDMAO is only the minority component. Accordingly an interdigitation with the much shorter perfluoro chains takes place. d calculated from eqn (2.3.4) for this case would be 2.8 nm (length of TDMAO plus length of perfluoro surfactant[135]), in good agreement with the experimental data.
The phase study and DLS indicate that for $0 < \alpha(\text{TDMAO}) < 0.4$ vesicles of a radius of 50 nm with a polydispersity index of $\sim$ 0.3 are formed. The SANS measurements showed no minimum due to the high polydispersity of the vesicles. Therefore the vesicle radius could not be determined from the SANS measurements, due to its restricted q-range.
As observed before the hydrodynamic radii calculated from the radius and the length of the cylindrical micelles and from the DLS measurements are in good agreement for $\alpha(\text{TDMAO}) <$ 0.5 (Table 2.3.2).

TDMAO/ $C_7F_{15}CO_2Li$. SANS-measurements in the system TDMAO-$C_7F_{15}CO_2Li$ confirm the phase behaviour already published by us before[143] (see Fig. 2.3.1c). It should be noted that the samples studied were all about two days old, in difference to the previously published study in which the systems studied were typically four weeks old. This may lead to some differences as slow ageing of the vesicles will occur, which leads to an increase of

Table 2.3.2: SANS fit parameters for a model of cylindrical micelles with electrostatic repulsion and vesicles in the system TDMAO-$C_6F_{13}CO_2Li$ (50mM, 25°C, molar fraction of TDMAO α(TDMAO), volume fraction of scattering material in micelles A_1, cylinder radius R, cylinder length L, aggregation number of micelles $N_{\text{agg, mic.}}$, lamellar thickness of the vesicles D, hydrodynamic radius $R_{\text{h,SANS}}$ calculated from SANS-parameters, hydrodynamic radius $R_{\text{h,DLS}}$ determined from DLS, effective hard-sphere radius R_{eff}, and electrostatic potential ζ used in the RPA structure factor)

α(TDMAO)	A_1	R /nm	L /nm	$N_{\text{agg, mic.}}$	D /nm	$R_{\text{h, SANS}}$ /nm	$R_{\text{h, DLS}}$ /nm	R_{eff} /nm	$\lvert\zeta\rvert$ /mV
1.0	1	1.8	20	428		6.7	7	4.1	10
0.9	1	1.9	10	246		4.4	1.8	7.7	58
0.8	1	1.9	11	298		4.9	2.5	8.3	61
0.7	1	1.9	17	471		6.4	4.1	8.5	48
0.6	0.97	1.9	24	685		8.0	10	9.0	48
0.5	0.95	1.8	33	926		9.7	130	9.4	42
0.4	0.47	1.6	15	334	2.5		78		
0.3	0				2.4		60		
0.2	0				2.3		52		
0.1	0				2.4		59		

the average size with time. A vesicle phase is observed for $\alpha(\text{TDMAO}) = 0.2 - 0.6$, which is marked by a scattering pattern with pronounced oscillations around $q = 0.1$ nm^{-1} as they are typical for spherical shells. A quantitative analysis with fitting of eqn (10.2.14) to the experimental data yields vesicle radii of 27 to 40 nm and polydispersity indices of about 0.3 (see Table 2.3.3). This means that for the longest perfluoro surfactant one has much more well-defined unilamellar vesicles than for the shorter perfluoro counterparts.

The volume fraction of scattering material in the micelles (A_1) shows that at α(TDMAO) = 0.2 micelles and vesicles are present at the same time in the solution (Table 2.3.3). However, a macroscopic phase separation could not be observed over a long time range and also not be enforced by centrifugation.

Between $\alpha(\text{TDMAO}) = 0.05-0.15$ and $\alpha(\text{TDMAO}) = 0.65-1$ cylindrical and for α(TDMAO) = 0 nearly spherical micelles are observed. The scattering patterns of repulsive micelles are similar to those of the shorter chain perfluoro surfactant but the oscillations become more pronounced with increasing content of $C_7F_{15}CO_2Li$, indicating a lower polydispersity. At high TDMAO content long cylindrical micelles are found. The length of these micelles in-

creases with increasing $C_7F_{15}CO_2Li$ content. The presence of long wormlike micelles close to the phase boundary is as well indicated by the increase of the viscosity that correlates with the cylinder length derived from the SANS-fits (Fig. A.2.17).

Table 2.3.3: SANS fit parameters for a model of cylindrical micelles with electrostatic repulsion and vesicles with a log-normal distributed radius in the system TDMAO-$C_7F_{15}CO_2Li$ (50mM, 25°C, molar fraction of TDMAO α(TDMAO), volume fraction of scattering material in micelles A_1, cylinder radius R, cylinder length L, aggregation number of micelles $N_{\text{agg, micelle}}$, mean vesicle radius R_{vesicle}, lamellar thickness of the vesicles D, vesicle polydispersity index PDI_{vesicle}, effective hard-sphere radius R_{eff}, and electrostatic potential ζ used in the RPA structure factor)

α(TDMAO)	A_1	R /nm	L /nm	$N_{\text{agg, micelle}}$	R_{vesicle} /nm	D /nm	PDI_{vesicle}	R_{eff} /nm	$\lvert\zeta\rvert$ /mV
1	1	1.8	20	428				4.1	10
0.9	1	2.0	12	340				8.1	57
0.8	1	2.1	14	437				8.9	63
0.7	1	2.3	24	949				9.0	65
0.6	0				32	2.6	0.29		
0.55	0				32	2.7	0.19		
0.47	0				29	2.7	0.26		
0.45	0				28	2.6	0.28		
0.43	0				28	2.6	0.20		
0.4	0				29	2.5	0.26		
0.3	0				30	2.5	0.41		
0.21	0.41	3.3	2	278		2.1	0.31		
0.14	1	1.8	6	204				0.9	52
0.1	1	1.8	6	227				0.7	63
0	1	1.2	1	13				2.6	98

2.4 Comparison of the Systems with Tetradecyldimethylamine Oxide (TDMAO) and Lithium Perfluoroalkanoates

The comparison of the phase diagrams of the three perfluoro surfactants with different chain length shows that the vesicle region in the phase diagram moves to smaller molar fractions of TDMAO with decreasing chain length of the perfluoro surfactant, vanishing completely

for $C_5F_{11}CO_2Li$ (Fig. 2.4.1). Only for the system with $C_7F_{15}CO_2Li$ a second micellar phase at low TDMAO content exists, while for the shorter perfluoro surfactants at 50 mM total concentration one is below the cmc. For $C_6F_{13}CO_2Li$ the vesicle area extends to the pure perfluoro surfactant solution. This means for the shorter chain perfluoro surfactants, which then are below the cmc, one observes directly the formation of unilamellar vesicles as the first aggregation state upon the admixture of TDMAO. For increasing chain length of the perfluoro surfactant one finds an increased tendency for bilayer formation. At the same time the polydispersity of the vesicles decreases, and for all cases unilamellar vesicles are observed. The changes in the phase diagram can be explained by the change of the packing parameter with the perfluoro surfactant chain length. The bulkier the perfluoro surfactant chain the larger is the packing parameter of the TDMAO-$C_nF_{2n+1}CO_2Li$ pair and the higher is the tendency for vesicle formation. On the other hand a higher anionic perfluoro surfactant content in the micelle leads to an increased repulsive interaction of the head groups and to a decreasing packing parameter. This can explain why a second micellar phase can be observed at lower TDMAO content in the system TDMAO-$C_7F_{15}CO_2Li$, which is not found for TDMAO-$C_5F_{11}CO_2Li$ and TDMAO-$C_6F_{13}CO_2Li$. For the latter two cases the cmc of the pure perfluoro surfactant is to low so that the perfluoro surfactant can only be incorporated into the TDMAO micelles.

All vesicles formed are unilamellar and long-time stable. This can be attributed to the interaction parameter that has been shown to have a constant contribution of about $-20k_BT$ for the head group and becomes less attractive by about $1.1k_BT$ per CF_2 group in the perfluoro surfactant.

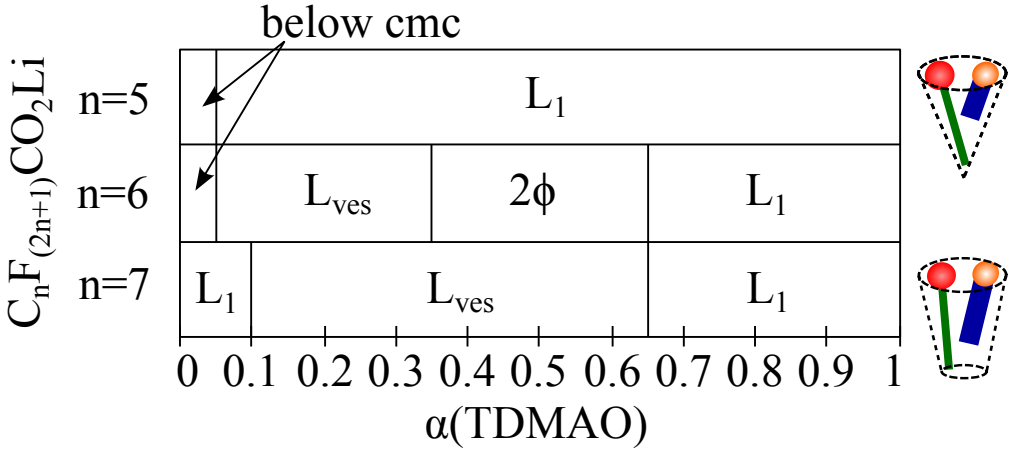

Figure 2.4.1: Comparison of the phase behaviours of the systems TDMAO/$C_nF_{2n+1}CO_2Li$ with n=5,6,7, $c_{tot} = 50mM$ (At 50mM one is below the *cmc* for $C_5F_{11}CO_2Li$ and $C_6F_{13}CO_2Li$. The molar ratio, where a *cmc* of 50mM is reached was not determined here and lies between 0 and 0.1)

It is interesting to observe that a slight shift from the zwitanionic system with TDMAO to a more catanionic system containing 10 mol% $TDMAOH^+$ (relative to the total amount of TDMAO) has a very substantial effect on the phase behaviour. The synergistic interactions and the tendency for vesicle formation become much more pronounced. For instance, for the shortest chain $C_5F_{11}CO_2Li$, that does not form any vesicles with TDMAO, a relatively extended vesicle region is observed upon HCl addition. A similar shift is observed for $C_6F_{13}CO_2Li$. A comparison between the systems TDMAO/HCl/$C_5F_{11}CO_2Li$ and TDMAO/HCl/$C_6F_{13}CO_2Li$ (Fig. 2.4.2) shows again the shift of the vesicle region to lower TDMAO contents for $C_5F_{11}CO_2Li$ compared to $C_6F_{13}CO_2Li$ and the influence of the volume of the perfluoro surfactant. Compared to the systems without HCl the effect of the chain length on the phase behaviour is less pronounced, as in general apparently the effect of the charging (moving from zwitanionic to catanionic) has a much more pronounced effect on the phase and structural behaviour compared to changing the alkyl chain length by one or two CF_2 groups. This may be attributed such that the charging of the head group leads to a substantial reduction of the head group area of the mixed systems.
An interesting point is that for the shorter perfluoro surfactants always a macroscopic two-phase region is observed between the TDMAO rich micellar phase and the vesicle phase. This is observed with or without the addition of HCl but not for the case of the longer chain $C_7F_{15}CO_2Li$, where only microscopically the presence of two different types of aggregates could be confirmed. This discrepancy is so far still unaccounted for.
Apparently the electrostatic conditions and chain length of the surfactants have a very pronounced effect on the packing parameter and therefore on the propensity of the given surfactant mixtures to form unilamellar vesicles. This all occurs in perfect agreement with the packing parameter paradigm.[76]

In the systems TDMAO-$C_6F_{13}CO_2Li$ and TDMAO-$C_7F_{15}CO_2Li$ for a TDMAO content higher than in the vesicle phase a region with cylindrical micelles is observed. The length of the micelles increases with decreasing amount of TDMAO in the solution and leads to an increased viscosity of the solutions. For the system TDMAO-$C_5F_{11}CO_2Li$ the maximum viscosity is found in the middle of the phase diagram at $\alpha(\text{TDMAO}) = 0.5$, indicating that here the longest micelles are present. The maximum of viscosity increases systematically with the chain length of the perfluoro surfactant. This may be due to an increase of the structural relaxation time that should be related to an increasing stiffness and thickness of the cylinders, and being in agreement with the SANS-measurements. In addition, the viscosity maximum shifts to higher TDMAO content with increasing chain length of the perfluoro surfactant.
In summary, it can be stated that zwitanionic surfactant mixtures composed of TDMAO

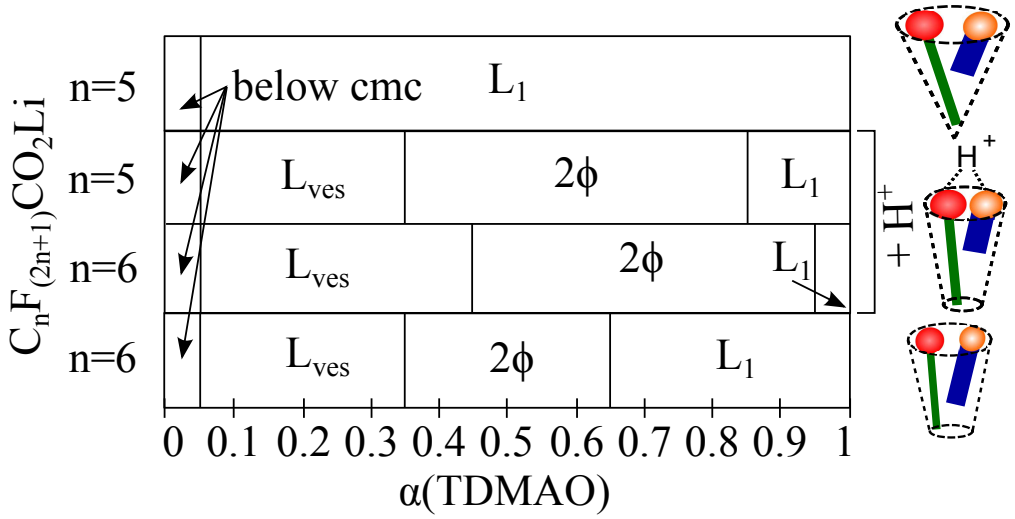

Figure 2.4.2: Comparison of the phase behaviours of the systems TDMAO/HCl/$C_nF_{2n+1}CO_2Li$ with n=5,6, influence of addition of HCl, $c_{tot} = 50mM$ (At 50mM one is below the *cmc* for $C_5F_{11}CO_2Li$ and $C_6F_{13}CO_2Li$. The molar ratio, where a *cmc* of 50mM is reached was not determined here and lies between 0 and 0.1)

and lithium perfluoro alkanoates are structurally versatile systems in which vesicle formation can be tuned by changing the chain length of the perfluoro alkanoate. Even stronger structural control can be exerted by changing the pH as already a relatively small degree of protonation of the TDMAO, thereby moving towards a catanionic system, affects the aggregation behaviour largely, transforming rod-like micelles directly to vesicles. This means that spontaneous formation of vesicles can be achieved by proper choice of its composition and vesicle formation can easily be tuned by pH.

Crystal Formation in Mixtures of Hydrocarbon and Perfluoro Surfactants

Mixtures of TDMAO and perfluoro surfactants do not only lead to the formation of mixed micelles and vesicles, but in equimolar mixtures of tetradecyltrimethylammonium bromide TTABr and lithium perfluorooctylsulfonate LiPFOS, equimolar mixtures of $TDMAOH^+Cl^-$ and $C_6F_{13}CO_2Li$, and TDMAO and $C_6F_{13}CO_2H$ as it could be expected from catanionic mixtures, to the formation of mixed crystals. In the mixtures TDMAO-$C_5F_{11}CO_2H$, TDMAO-$C_7F_{15}CO_2H$, and $TDMAOH^+Cl^-$-LiPFOS no macroscopical crystals could be observed, but a second phase of condensed vesicles. To study mixed crystals from cationic hydrocarbon surfactants and anionic perfluoro surfactants crystals obtained from spontaneous formation like in the case of TTABr-LiPFOS, $TDMAOH^+Cl^-$-$C_6F_{13}CO_2Li$, and TDMAO-$C_6F_{13}CO_2H$ and crystals obtained from freeze-drying equimolar mixtures of both surfactants were observed in a neutron diffractometer. The crystals, that formed spontaneously, were freeze-dried as well to remove water that might swell the crystals.

Fig. 3.0.1 shows the neutron diffraction data measured on the systems TDMAO-$C_5F_{11}CO_2H$, TDMAO-$C_6F_{13}CO_2H$, and TDMAO-$C_7F_{15}CO_2H$ at the HZB in Berlin on V1 (see section 10.1.5).

In these data several characteristics can be observed, that show up in all measured data. First there is a strong peak at about 0.2 1/Å with a secondary peak at about 0.4 1/Å marked with A. Under the assumption that the crystals consist of stacked bilayers of mixed surfactants, than the crystal is isotropic on a larger length scale in two dimensions and shows a periodicity perpendicular to the bilayers with a periodical length linked to the repeating distance between the bilayers. Diffraction peaks linked to that length scale show up at $q_z = 2\pi n/\Delta z$. That leads to the sum of the bilayer thickness and the distance between the bilayers of 2.95nm for the mixture with TDMAO and $C_5F_{11}CO_2H$, of 3.13nm for the mixture with TDMAO and $C_6F_{13}CO_2H$, and of 3.26nm for the mixture with TDMAO and $C_7F_{15}CO_2H$ (see Fig. 3.0.1). As expected the longer the perfluoro surfactant the thicker the observed bilayer. The bilayer is thicker in the crystals than in the vesicles. This is not surprising since in the vesicle case zwitanionic systems were observed and in the crystals consist of catanionic pairs. Due to their stronger head group interactions those bilayers are expected to be stiffer and in addition some crystal water can be expected to be bound at the surfactant head groups. That means their internal pressure is higher and the chains should be more stretched. In addition in the crystal the chains are frozen and thereby more stretched and in the vesicles they are fluid and there might still some water in between the

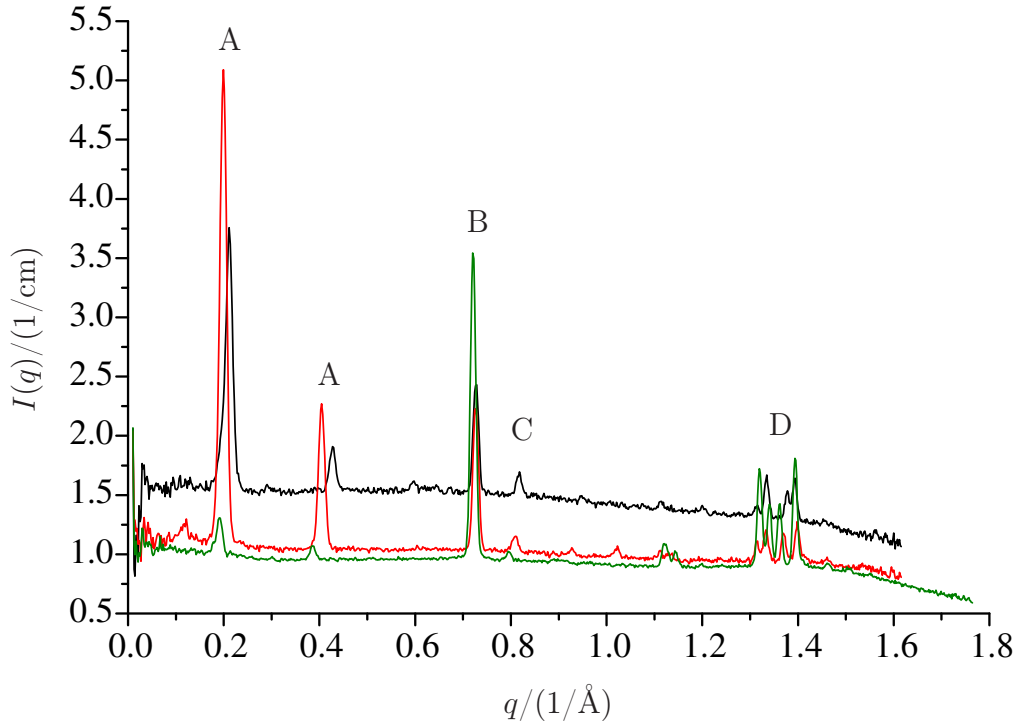

Figure 3.0.1: Neutron diffraction measured at crystals obtained from equimolar mixtures of TDMAO with 1) $C_5F_{11}CO_2H$ (black line), 2) $C_6F_{13}CO_2H$ (red line), and 3) $C_7F_{15}CO_2H$ (green line)

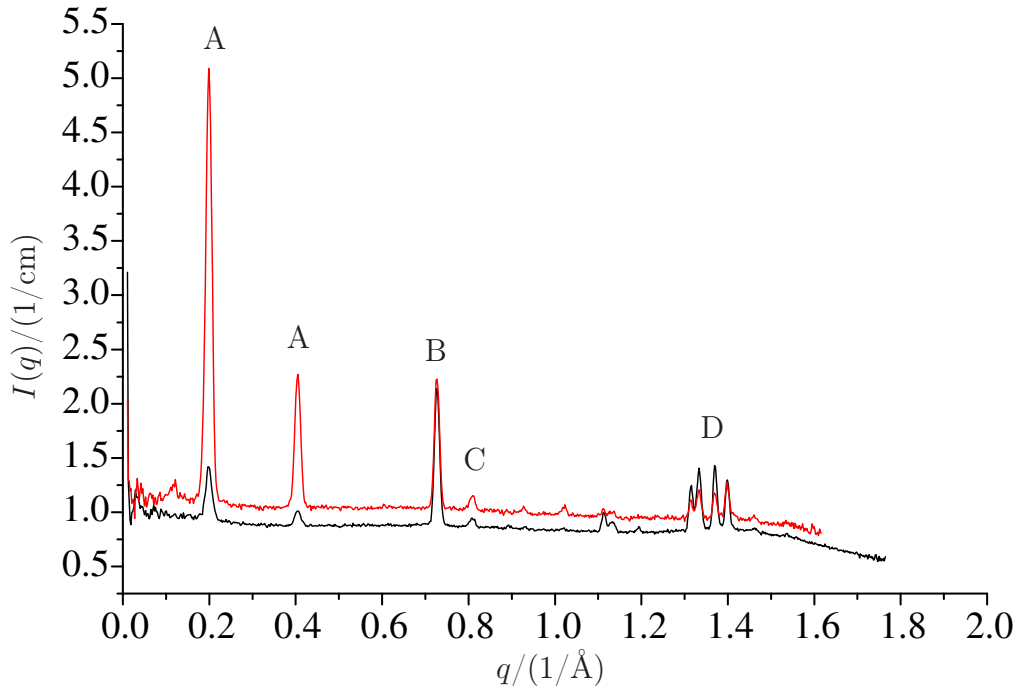

Figure 3.0.2: Neutron diffraction measured at crystals obtained from equimolar mixtures of with 1) $TDMAOH^+Cl^-$ with $C_6F_{13}CO_2Li$ (black line) and 2) TDMAO with $C_6F_{13}CO_2H$ (red line)

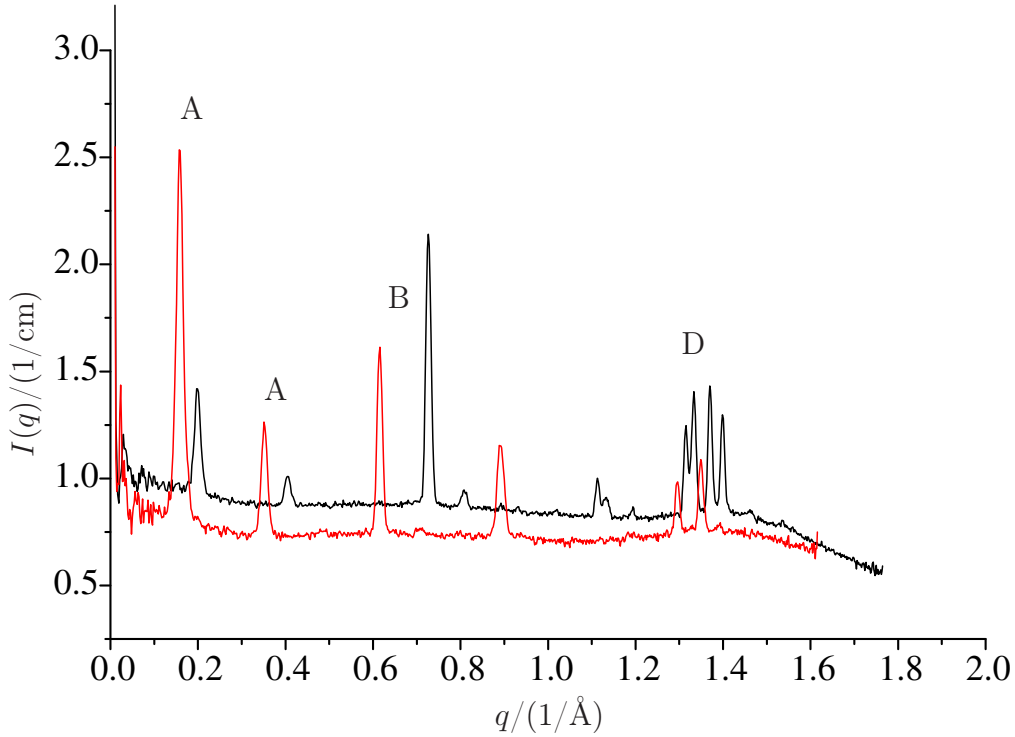

Figure 3.0.3: Neutron diffraction measured at crystals obtained from equimolar mixtures of $TDMAOH^+Cl^-$ with a) $C_6F_{13}CO_2Li$ (black line) and b) LiPFOS (red line)

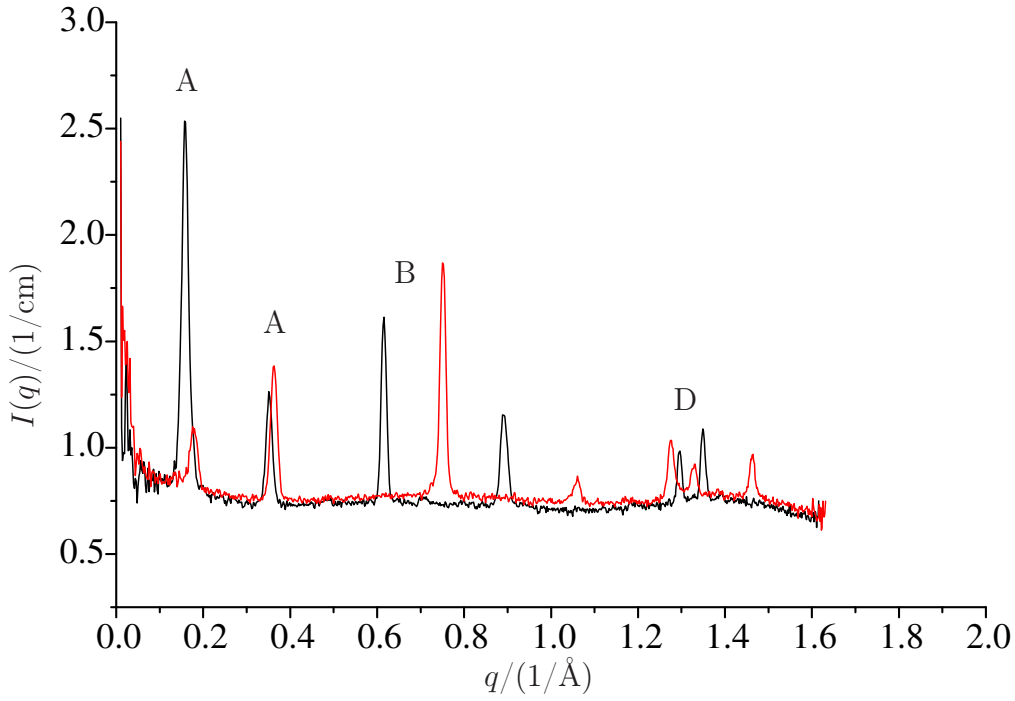

Figure 3.0.4: Neutron diffraction measured at crystals obtained from equimolar mixtures of LiPFOS with 1) $TDMAOH^+Cl^-$ (black line) and 2) TTABr (red line)

surfactant bilayers.

Additional salt, that means going from the system TDMAO-$C_6F_{13}CO_2H$ to the system $TDMAOH^+Cl^-$-$C_6F_{13}CO_2Li$ does not have an effect on the structure of the crystals (see Fig. 3.0.2) but by exchanging $C_6F_{13}CO_2Li$ with LiPFOS the bilayer thickness increases from 3.13nm to 3.5nm and is thereby thicker than in the mixture of TDMAO and $C_7F_{15}CO_2H$ due to the longer chain of the LiPFOS. The same bilayer thickness can be observed in the mixture TTABr-LiPFOS which is not surprising since the hydrocarbon chain has the same length for TDMAO and TTABr. Zemb et al. and Carrière et al. studied crystals from catanionic surfactant mixtures of cetyltrimethylammonium hydroxide (CTAOH) and myristic acid.[24,147] Below the chain melting temperature they found crystals in the shape of facettet hollow capsules similar to the vesicles found above the chain melting temperature and disc-like crystals. In SANS studies they found oscillations characteristic for single surfactant bilayers while in our case we find sharp peaks in the same q-range. That means in their case the crystals consisted only of one surfactant bilayer while we have a series of stacked bilayers that result in macroscopical crystals and a sharp peak.

Second around 1.4 1/Å a peak quartet appears for the mixtures with perfluoro alkanoic acid and TDMAO while for mixtures with LiPFOS and $TDMAOH^+Cl^-$ or TTABr only a doublet can be observed around 1.3 1/Å (marked with D). These peaks correlate with distances of 4.5Å or 4.8Å respectively. A similar feature was always observed in the scattering results observed by Carrière et al.. Carrière et al. observe a single reflection close to 1.5 1/Å and in this study peaks close to 1.4 1/Å were observed as well. The difference between the mixture of CTAOH-myristic acid and the mixture of perfluoro surfactant and hydrocarbon surfactant is that in the pure hydrocarbon case only a single peak could be observed while in our study always a doublet or a quartet could be found. The reason has to be due to distortions in a regular two dimensional hexagonal packing of the surfactants along the bilayer and due to perfluoro-perfluoro, perfluoro-hydrocarbon, and hydrocarbon-hydrocarbon interactions and the contrast between hydrocarbon and perfluoro surfactants. In mixtures of CTAOH and myristic acid only hydrocarbon-hydrocarbon interactions have to be considered. The position of the correlation peaks assigned to the (110) reflection around 1.4 1/Å leads to a head group area of $a_H = \frac{2}{\sqrt{3}}\left(\frac{2\pi}{q_{110}}\right)^2 = 23\text{Å}^2$. Carrière et al. give the distortion in the hexagonal packing as the reason for the smaller than expected head group area that should be larger than 25Å^2 in a regular hexagonal lattice.

Third there is a strong peak at about 0.7 1/Å marked with B. This peak corresponds to lengths of 8.65Å for TDMAO-$C_5F_{11}CO_2H$, 8.65Å for TDMAO-$C_6F_{13}CO_2H$, and 8.72Å for TDMAO-$C_7F_{15}CO_2H$. These lengths hardly change with the perfluoro surfactant chain length but going from $TDMAOH^+Cl^-$-LiPFOS to TTABr-LiPFOS the corresponding length

changes from 10Å to 8.37Å. The fact that the position of these peaks strongly changes with the system, leads to the conclusion that they originate from two dimensional lateral ordering in the bilayer. Carrière et al. observe a broad area of peaks in the same q-range and associate these peaks to long range order in the distorted hexagonal lattice. In our case we observe only two single sharp peaks marked with B and C, which could correspond to lattice planes within the two dimensional hexagonal lattice. In the mixtures of TDMAO and the perfluorocarboxylic acids and the mixture $TDMAOH^+Cl^-$-$C_6F_{13}CO_2Li$ the peak marked with B could as well be a fourth order peak from A, but in that case it remains unclear why no third order peak can be observed.

As shown in section 2 there are strong synergistic interactions between anionic perfluoro and nonionic hydrocarbon surfactants and even stronger interactions in the case of a catanionic system. These interactions may lead to the formation of mixed crystals of stacked bilayers and equally distributed hydrocarbon and perfluoro surfactant within the bilayer. Characteristics found in these crystal bilayers are quite likely similar to the structure of vesicle bilayers, where in the latter case one is in the fluid state and therefore has a correspondingly less ordered state.

The System TDMAO (Tetradecyldimethylamine Oxide) - LiPFOS (Lithium Perfluorooctylsulfonate) - Dependence on the Composition

4.1 Static Behaviour

Section 2 shows, that among the systems with TDMAO and lithium perfluoroalkanoates the system with $C_7F_{15}CO_2Li$ showed the most well defined vesicles and a broad vesicle area in the middle of the phase diagram. Weiss et al. studied the kinetics of vesicle formation in the systems TDMAO-$C_7F_{15}CO_2Li$ and TDMAO-LiPFOS (Lithium Perfluorooctylsulfonate, $C_8F_{17}SO_3Li$) at equimolar mixing and found similar results concerning the mechanism and kinetics of vesicle formation.[141,142] Since the system TDMAO-LiPFOS seems to be another suitable system for our studies, this system was characterised here and the kinetics where investigated in dependence on the mixing ratio.

Mixtures of TDMAO and LiPFOS show a strong synergistic behaviour. The cmc measurements reveal an interaction parameter of $-8.7k_BT$ (see section A.4), so that formation of mixed aggregates can be expected in solutions. After mixing a TDMAO stock solution with a LiPFOS stock solution a rise in the pH can always be observed in comparison to the pure surfactants solutions which indicates as well the formation of mixed aggregates. The rise in pH can be explained by the slightly higher basicity of the TDMAO in the anionic environment of the LiPFOS head groups which leads to a partial protonation of the TDMAO head groups by water.

In pure 50mM TDMAO solutions rod-like micelles can be found with a radius of 1.83nm and a length of 20nm and in pure 50mM LiPFOS solutions ellipsoidal micelles can be found with a major axis of 2.26nm and a minor axis of 1.31nm (see later). From these aggregates it can be deduced that the packing parameter p of the pure TDMAO and the pure LiPFOS is $1/3 < p < 1/2$. cmc measurements on a similar system with TDMAO and lithium perfluorocarboxylates[20] showed that the synergistic behaviour is due to the head group interactions while the interaction between the hydrocarbon chains and the perfluorinated chains is repulsive. The attractive interactions of the head groups lead to a decreased head group area while the repulsive interactions of the chains lead to an increased surfactant chain volume and as a result to a slightly increased packing parameter that should lead to the formation of locally planar objects.

Indeed in the middle of the phase diagram vesicle formation can be observed. The formation

of large closed objects is indicated by the change in conductivity and by a bluish shimmer in the solution, while the conductivity shows a linear behaviour with the LiPFOS content in the micellar phases at the edges of phase diagram. These micellar phases are transparent, colourless and optically isotropic. At higher TDMAO contents a two-phase area appears. In this area vesicles are formed shortly after mixing indicated by the bluish shimmer, which sediment after some days and form a second white flow birefringent phase at the bottom of the sample.

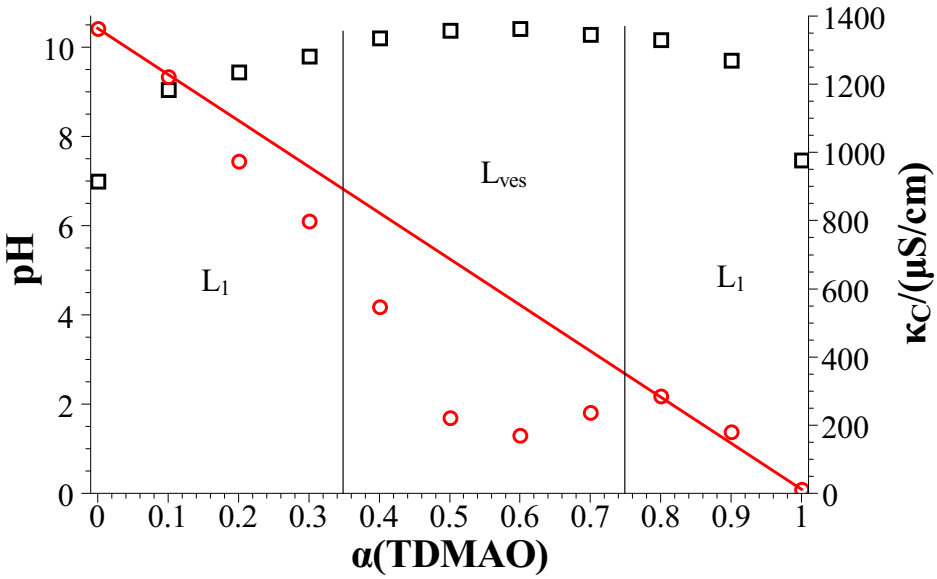

Figure 4.1.1: pH (□) and conductivity κ_C (◯) in the system TDMAO-LiPFOS at 50mM, 25°C; the red line shows the interpolation of κ_C between the pure surfactant solutions

To gain a better inside into the aggregate structures, SANS measurements were performed at the HZB Berlin on V4 (see section 10.1.3).

The sample age was two days. The scattering patterns show that the aggregate structure changes significantly with the mixing ratio (Fig. 4.1.2a). At low α(TDMAO) (Fig. 4.1.2b) and at high α(TDMAO) (Fig. 4.1.2d) a pronounced correlation peak can be observed. This correlation peak is due to electrostatic repulsion between the micelles. For low α(TDMAO) the form factor of the aggregates is that of ellipsoidal micelles. For these aggregates the correlation peak shifts to smaller q values while the total intensity increases at low q. These changes can be explained by a growth of these aggregates with increasing TDMAO content. The major axis of these ellipsoidal micelles increases and the micelles become more and more elongated and the micellar shape approaches that of rod-like micelles. For $0.4 \leq \alpha(\text{TDMAO}) \leq 0.75$ locally planar objects are formed. This is indicated by a $I \propto q^{-2}$ law for the mid-q area. In addition oscillations can be found around $q = 0.1/nm$ that indicate spherical objects, in this case the vesicles, that have a locally planar bilayer. At

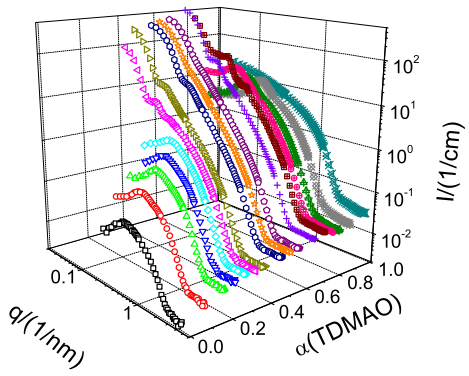

(a) Whole phase diagram

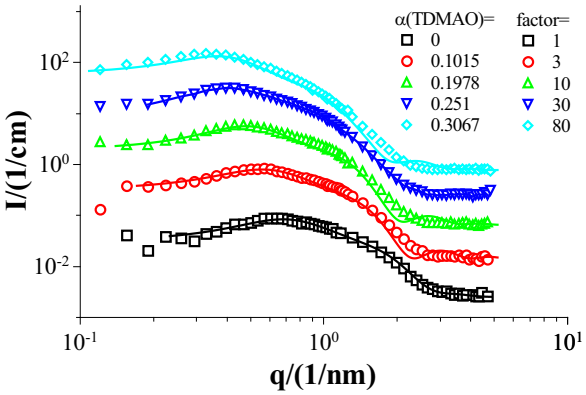

(b) Prolate ellipsoidal micelles at low TDMAO content

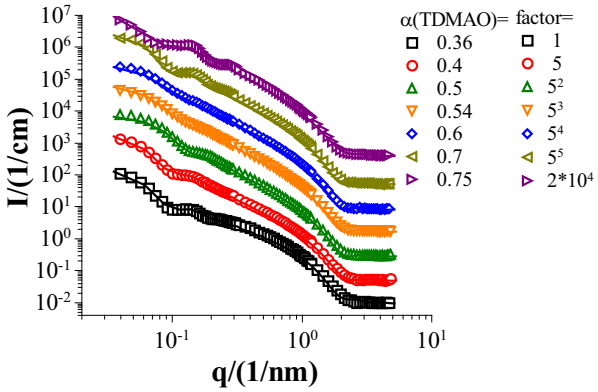

(c) Vesicles at centre of the phase diagram

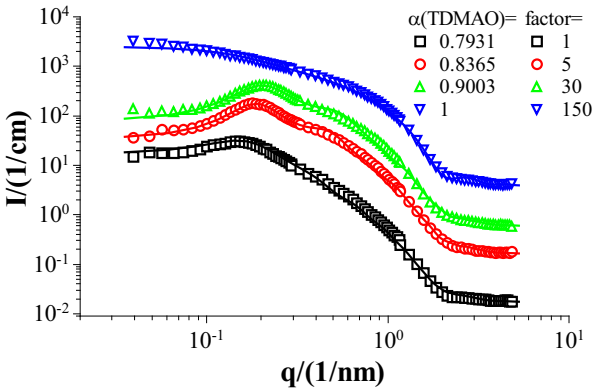

(d) Oblate ellipsoidal micelles at high TDMAO content, pure TDMAO forms short rod-like micelles

Figure 4.1.2: Small-angle neutron scattering (SANS) intensity as a function of the magnitude of the scattering vector q for various mixtures of TDMAO-LiPFOS at a total surfactant concentration of 50mM at 25°C; in Figs. 4.1.2b to 4.1.2d the scattering intensity of the scattering patterns was multiplied with a factor for better clarity; symbols represent measurements while lines represents fits

α(TDMAO) = 0.5 these oscillations are rather smeared out, while they are more pronounced at the edges of the vesicle area. So the polydispersity of the vesicle radius $R_{\text{ves.}}$ is higher at the centre of the vesicle phase than on the edges. At α(TDMAO) =0.7-0.75 where after some time phase separation takes place additional sharp peaks appear that might indicate the formation of multilamellar vesicles.

The analysis of the scattering patterns provides more detailed information about the structure of the aggregates. For the analysis of the scattering patterns the scattering contrast and therefore the scattering density length SLD of the aggregates and of the solvent is

needed. These values for the solvent D_2O and the two surfactants TDMAO and LiPFOS were determined as described in section 10.1.6. The scattering length densities of TDMAO, LiPFOS and D_2O are $SLD_{\mathrm{TDMAO}} = -1.96 \cdot 10^{-5} nm^{-2}$, $SLD_{\mathrm{LiPFOS}} = 4.15 \cdot 10^{-4} nm^{-2}$ and $SLD_{\mathrm{D_2O}} = 6.37 \cdot 10^{-4} nm^{-2}$, respectively. The following analysis was done under the simplifying assumption that all mixed aggregates are homogeneous, and that if two types of aggregates are formed in the solution, like micelles in equilibrium with vesicles, these two aggregate types have the same composition.

The results of the analysis of the SANS data are summarized in Table 4.1.1. Analysis of the scattering data showed that the micelles in the micellar regions had elliptical or disc-like architecture. The scattering intensity $I_{\mathrm{ell.}}$ arising from elliptical micelles is described in eqn (10.2.5) with the rotational axis of the ellipsoid $R_{\mathrm{maj.}}$ and the minor axis $R_{\mathrm{min.}}$. The scattering intensity I_{disc} arising from disc like micelles is described in eqn (10.2.7) with the disc radius R_{disc} and the thickness D. The same form factor can be used for short rod-like micelles while D would then be replaced by the length L of the rod and R_{disc} will be named R_{cyl}.

Pure TDMAO forms short rod-like micelles with a radius R_{cyl} of 1.83nm and a length L of 20nm.[120] Pure LiPFOS forms small ellipsoidal micelles and in the whole micellar area of the mixed surfactant systems the micelle have as well ellipsoidal structure. For pure LiPFOS and the micellar region with low TDMAO content the micelles are prolate and become more and more elongated with increasing α(TDMAO). In the micellar region with high TDMAO content the micelles have the structure of oblate ellipsoids or discs. The radius of these discs increases with increasing LiPFOS content. Here it is important to note that the structure changes drastically from the pure TDMAO micelles, which are cylindrical, upon admixture of LiPFOS to small oblate ellipsoids. This is as well an indication for the formation of mixed micelles and the change of the packing parameter p. The parameters are summarized in Fig. 4.1.3.

In the middle of the phase diagram ($0.3559 \leq \alpha(\mathrm{TDMAO}) \leq 0.7499$) vesicle formation can be observed. For the analysis of the SANS data the vesicles were modelled as polydisperse spherical shells with a homogeneous shell with the scattering length density $SLD_{\mathrm{agg.}}$. The scattering intensity $I_{\mathrm{ves.}}$ arising from vesicles is described in eqn (10.2.14).

Close to the phase boundaries micelles can be observed in equilibrium with vesicles. The scattering intensity is then a volume weighted sum of the scattering intensity I_{micelles} arising from the micelles and of the scattering intensity I_{vesicles} arising from the vesicles. The weighting factor $A = \phi_{\mathrm{micelles}}/\phi_{\mathrm{amph.}}$ describes the transition between both phases as shown in Fig. 4.1.4.

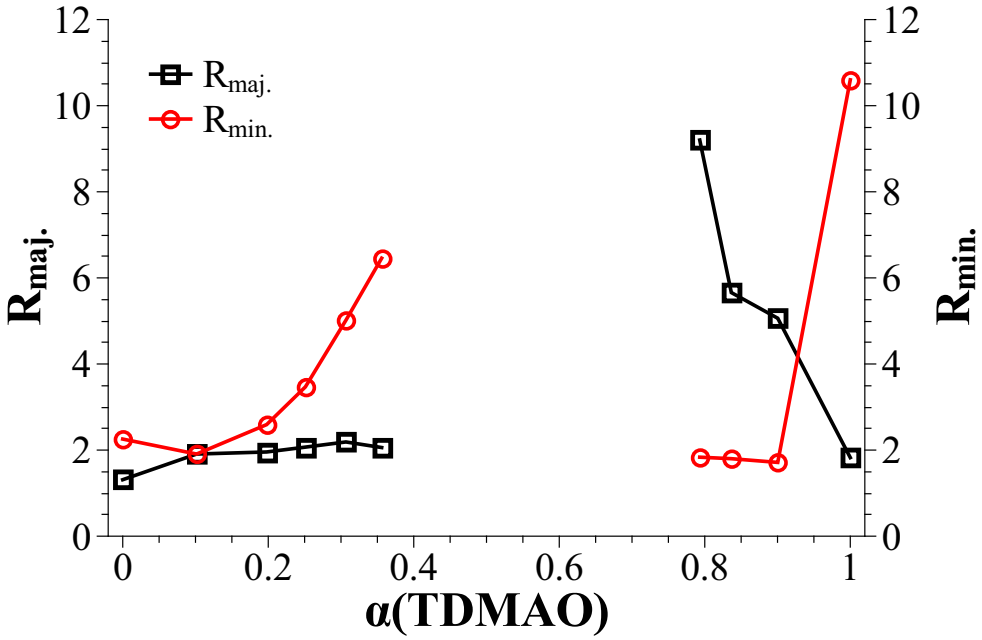

Figure 4.1.3: Dependence of the major (□) and the minor axis (◯) of the ellipsoidal micelles in the micellar area on the composition

$$I = A \cdot I_{\text{micelles}} + (1 - A) \cdot I_{\text{vesicles}} \tag{4.1.1}$$

For $0.36 \leq \alpha(\text{TDMAO}) \leq 0.7$ unilamellar vesicles can be observed while at α(TDMAO) =0.75 additional peaks appear that might indicate the formation of multilamellar vesicles. The observed vesicles had vesicle radii between 20nm and 30nm and a size minimum around equimolar mixing of TDMAO and LiPFOS, while the size increased when approaching the phase boundaries. This size range is similar to the sizes observed in the system TDMAO-$C_7F_{15}CO_2Li$.[20,142] The polydispersity shows the opposite behaviour with a maximum of 0.33 at α(TDMAO) =0.6 and decreasing polydispersity when approaching the phase boundaries to values of 0.23. The bilayer thickness of the vesicles increases slightly with the TDMAO content from 2.4nm to 2.9nm due to the higher chain length of TDMAO in comparison with LiPFOS.

4.2 Kinetic Behaviour

In order to gain a better inside into the driving forces that lead to vesicle formation kinetic experiments were performed. Hence stopped-flow mixing was used in combination with SANS detection. The stopped-flow method is described in section 10.1.1. These time-resolved SANS measurements were carried out on D22 at the ILL in Grenoble and the method and

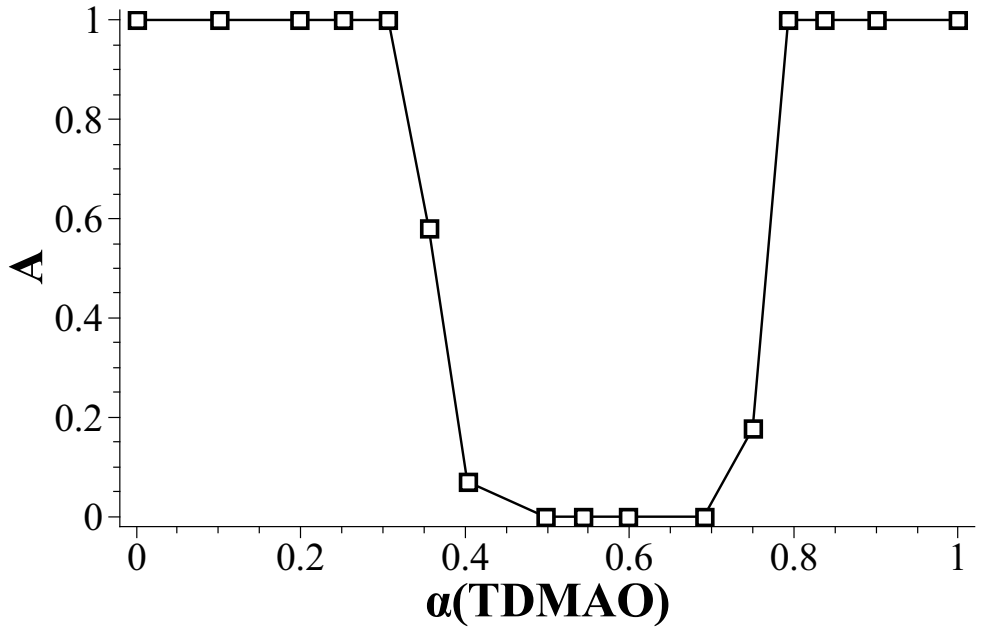

Figure 4.1.4: The parameter $A = \phi_{\text{micelles}}/\phi_{\text{amph.}}$ describes the transition between micelles and vesicles.

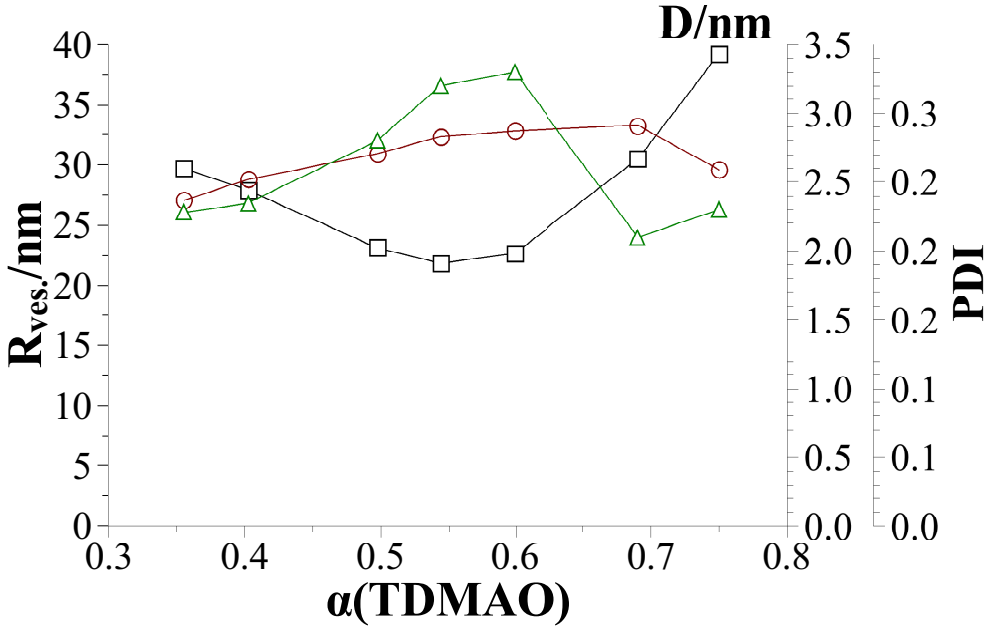

Figure 4.1.5: Vesicle radius $R_{\text{ves.}}$- □, bilayer thickness D - ◯ and polydispersity index PDI - △ in the vesicle areas

Table 4.1.1: Fit parameters from SANS measurements

α(TDMAO)	0.0000	0.1015	0.1978	0.2510	0.3067	0.3559	0.4027	0.4973
$R_{\text{maj.}}$/nm	2.26	1.91	2.59	3.47	5.01	6.46		
$R_{\text{min.}}$/n	1.31	1.91	1.96	2.07	2.19	2.06		
$R_{\text{ves.}}$/nm						29.69	27.90	23.13
D/nm						2.37	2.52	2.71
PDI						0.23	0.23	0.28
A	1.00	1.00	1.00	1.00	1.00	0.58	0.07	0.00

α(TDMAO)	0.5440	0.5987	0.6904	0.7499	0.7931	0.8365	0.9003
$R_{\text{maj.}}$/nm					1.84	1.80	1.71
$R_{\text{min.}}$/nm					9.20	5.66	5.06
$R_{\text{ves.}}$/nm	21.83	22.68	30.50	39.20			
D/nm	2.83	2.87	2.91	2.59			
PDI	0.32	0.33	0.21	0.23			
A	0.00	0.00	0.00	0.18	1.00	1.00	1.00

measurement parameters are described in section 10.1.3.
In this experiment a 50mM solution of TDMAO was mixed with a 50mM solution of LiPFOS to achieve molar fractions of α(TDMAO) =0.5-0.65. Due to the anionic character of LiPFOS the electrostatic conditions were altered with the composition. All mixtures were monitored over a total time range of 30min. On this time range the vesicle formation and first ageing processes can be observed. Later results show that the ageing process proceeds on a much larger time scale than observed here.
A representative example for such a time resolved SANS measurement is given in Fig. 4.2.1 for a mixture of α(TDMAO) =0.55. During the first second the scattering intensity increases at low q indicating the growth of aggregates. Analysis of the scattering intensity leads to structures of disc-like micelles at the earliest accessible measurement time. After about 1s very pronounced oscillations appear, which indicate the formation of monodisperse, unilamellar vesicles. With increasing time these oscillations blur out while the vesicles age and become more polydisperse. At the same time the first order minimum shifts to lower q due to an increase in the vesicle size.

The scattering data were analysed with a weighted model for a mixture of disc-like micelles and vesicles as described in eqns (4.1.1), (10.2.7) and (10.2.14). Taking into account the absolute intensity, it was possible to distinguish between the contribution to the scattering

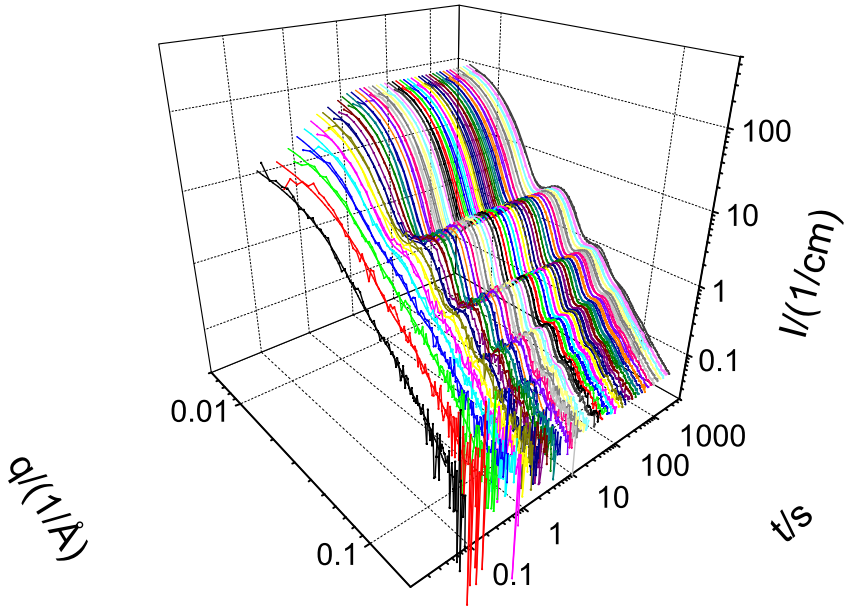

Figure 4.2.1: Time-resolved small angle neutron scattering (SANS) for TDMAO-LiPFOS (55:45), 50mM 25°C, fits are included as solid lines

arising from disc-like micelles and from vesicles keeping the volume fraction of amphiphilic material constant as depicted in Fig. 4.2.2. The polydispersity can be determined by the number of oscillations in the scattering contribution coming from the vesicles and the depths of the minima are flattened by the contribution of the discs to the scattering. The process of transformation between both can be described by the parameter A, that was introduced above (eqn (4.1.1)).

The analysis of the first measurement at $t = 0.084s$ shows that only mixed disc-like micelles are formed with a radius of 8.7nm and a thickness of 3.2nm. Taking into account the absolute intensity leads to the conclusion that the amount of monomeric surfactant is low compared to the amount of amphiphilic material in the micelles and can not be determined by this measurement. While the time t increases the scattering intensity increases at low q and the plateau range is shifted to lower q-values due to a growth process of the discs. The discs grow up to a radius of 20nm at 2.68s while the thickness of the discs does not change much (see Fig. 4.2.3). At the same time the formation of vesicles can be observed indicated by the appearance of oscillations and by the change in the parameter A. Obviously the disc-like micelles are transformed into vesicles. This process was already observed before on the system TDMAO-$C_7F_{15}CO_2Li$ at a ratio of 1:1.[(141)] These vesicles are with 12nm a factor of

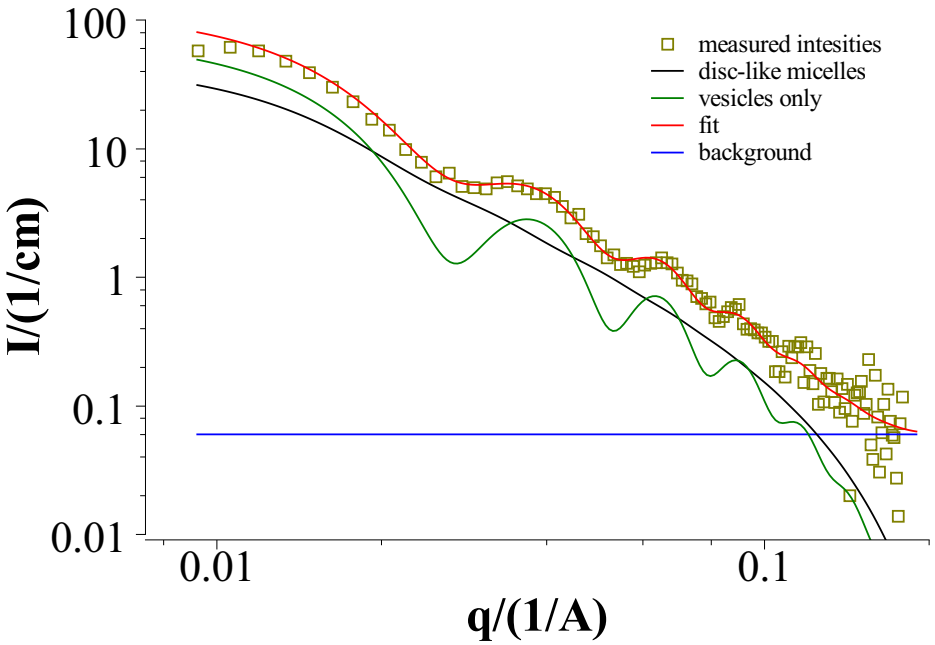

Figure 4.2.2: Analysis of the SANS data with a model for a mixture of micelles and vesicles taking into account the absolute intensity (α(TDMAO) = 0.55, t=1.734s, A=0.54072, R_{disc} =18nm, $R_{\text{ves.}}$ =12nm, PDI=0.045)

about 1.7 smaller than the discs and have a bilayer thickness of 3.1nm and a polydispersity index of 5%. That means that these vesicles are very monodisperse and the scattering curves show sharp oscillations at the moment of formation. Here the number of secondary oscillations helps to determine the PDI while the depth of the minima and the absolute intensity determine the fraction of vesicles $(1 - A)$ in the mixture. Hence the temporal evolution of A describes the transformation process from disc-like micelles to vesicles.
Since the growth of the disc-like micelles does not slow down until the vesicle formation starts, it can not be expected that the discs reach an equilibrium size and that the vesicle formation takes place as an absolutely unrelated process, but that vesicles are formed, if the discs reach a certain maximum size. The relation between the maximum disc size and the minimum vesicle size indicates, that vesicles are directly formed from discs and that one disc closes to form one vesicle.

After the formation process of the vesicles is finished ageing processes can be observed. These ageing processes are significantly slower than the disc growth and the vesicle formation and are probably unrelated to those two processes. In order to obtain more information about the ageing process, time dependent DLS measurements were performed. The time dependent DLS measurement is described in section 10.1.2. Time dependent DLS measurements show a slow increase in the vesicle size. That process continues over a long time range and does not

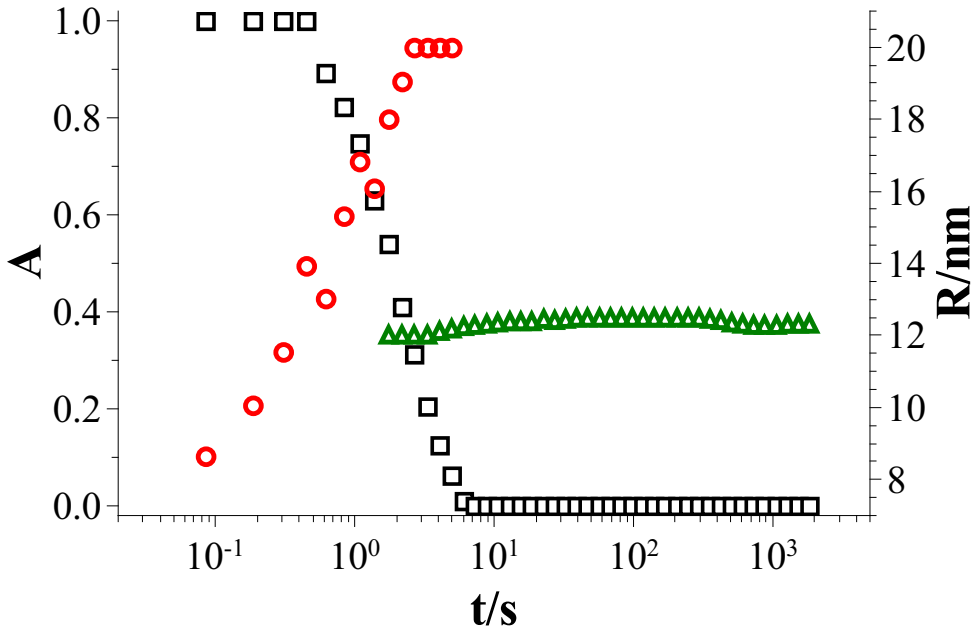

Figure 4.2.3: Temporal evolution of the fraction A (□) of disc-like micelles in the mixture, the radius of the discs R_{disc} (◯) and the vesicle radius $R_{\text{ves.}}$ (△) for TDMAO-LiPFOS (55:45), 50mM 25°C

finish within weeks. In this time range the vesicles reach sizes of more than 60nm (Fig. 4.2.4). From the analysis of the temporal development of the disc radius R_{disc} (see Fig. 4.2.5) and the transition parameter A (see Fig. 4.2.6) characteristic times for the disc growth and for the vesicle formation can be determined by describing the development of these parameters y by a monoexponential fit with the characteristic time t_{vesicle} and and onset time t_0 for the start of the process.

$$y(t) = y_0 \cdot \exp\left(-\frac{t - t_0}{t_{\text{vesicle}}}\right) \tag{4.2.1}$$

From these fits a characteristic time for the disc growth t_{disc}, an initial disc radius $R_{\text{disc,min}}$, a maximum disc radius $R_{\text{disc,max.}}$ and a characteristic time t_{vesicle} for the vesicle formation in dependence on α(TDMAO) can be determined.

The characteristic time t_{disc} for the disc growth is in the time range of 0.24-1.17s and decreases with α(TDMAO) (see Fig. 4.2.7). The electrostatic repulsion increases with increasing LiPFOS content and therefore slows down the growth process of the discs. The comparison between the smallest and the largest t_{disc} leads to an increase in the activation energy of $1.6k_{\text{B}}T = k_{\text{B}}T \ln\left(\frac{1.17}{0.24}\right)$. This might be an indication that the disc growth proceeds via a fusion mechanism. For the disc growth process no onset t_0 could be determined.

The characteristic time t_{vesicle} for the vesicle formation is in the time range of 1.46-4.53s and

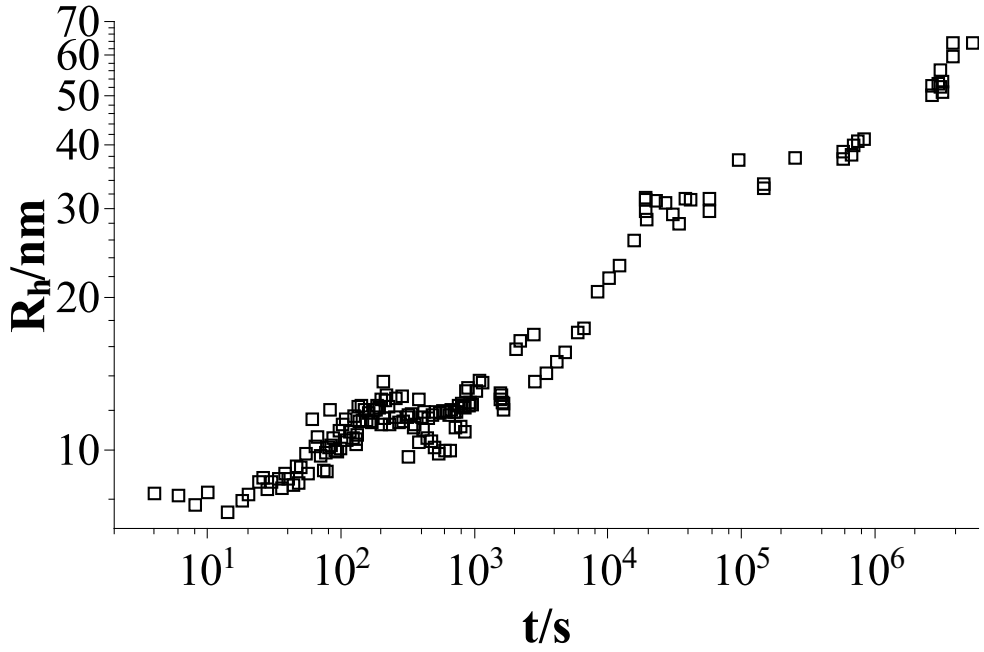

Figure 4.2.4: Ageing process of vesicles as seen from the hydrodynamic radius (DLS) for α(TDMAO) =0.55; c_{tot} =50mM, 25°C

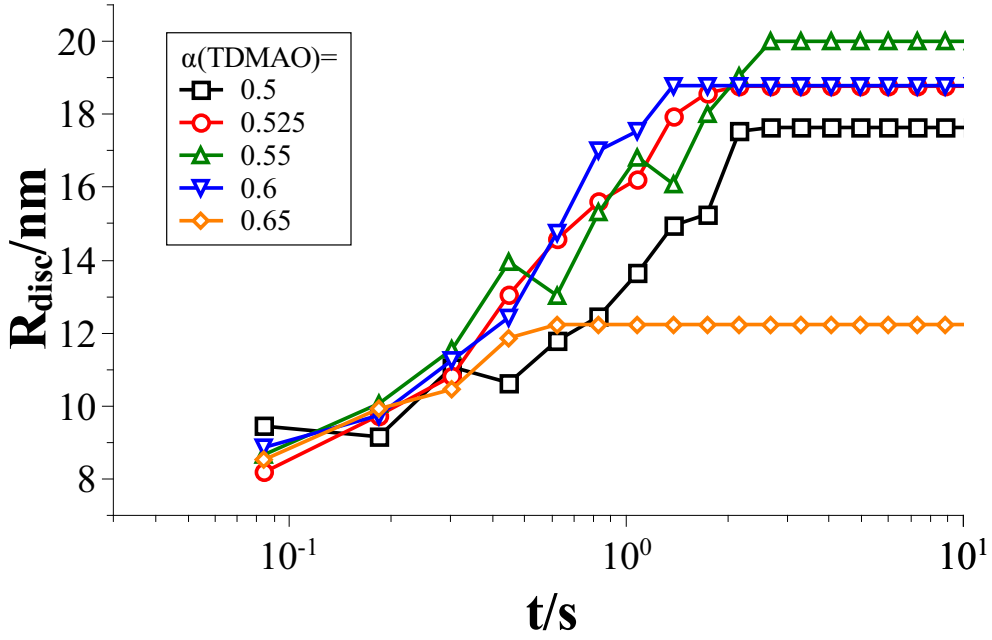

Figure 4.2.5: Time dependent development of the radius R_{disc} of the disc-like micelles

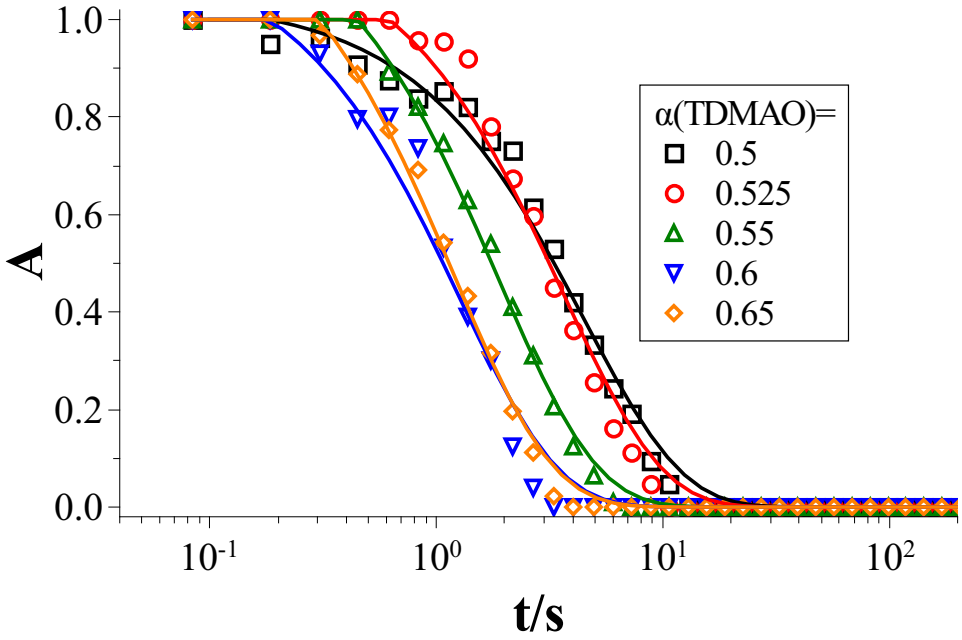

Figure 4.2.6: Time dependent development of the fraction A of disc-like micelles in the mixture

shows as well a decrease with α(TDMAO). In addition an onset time t_0 could be found that is in the same time range as the characteristic time for the disc growth. As a result one can say that there must be a relation between the disc growth and the vesicle formation. That supports the theory that the vesicle formation is a consequence of the disc radius reaching a maximal cut-off radius. On the other hand a dependence of the maximum disc radius $R_{\text{disc,max.}}$ on α(TDMAO) could be observed with a maximum at α(TDMAO) =0.55. If the discs become unstable at a certain cut-off radius $R_{\text{disc,max.}}$ and then close to form vesicles of a minimum vesicle radius $R_{\text{ves.,min.}}$, the minimum vesicle radius has always to be significantly smaller than the maximum disc radius. This behaviour could be observed in the area of $\alpha(\text{TDMAO}) = 0.5 - 0.6$ while the disc growth and the vesicle formation for α(TDMAO) =0.65 was with $t_{\text{disc}} = 0.24s$ and $t_{\text{vesicle}} = 1.46s$ to small to obtain reliable values for $R_{\text{disc,max.}}$.

4.3 Theoretical Description

The measurements showed that discs become unstable at a certain size $R_{\text{disc,max.}}$ and then close to form vesicles of the size $R_{\text{ves.,min.}}$. That means that the vesicle formation has to be energetically favoured at that point. To transform a disc into a vesicle this disc has then to go through a cup-like state of a bend disc. Then to the free energy F of the system a contribution from the free energy of the disc rim F_{l} as well as contribution from the free bending energy F_{b} have to be taken into account. F_{b} is described in eqn (4.3.1) with the

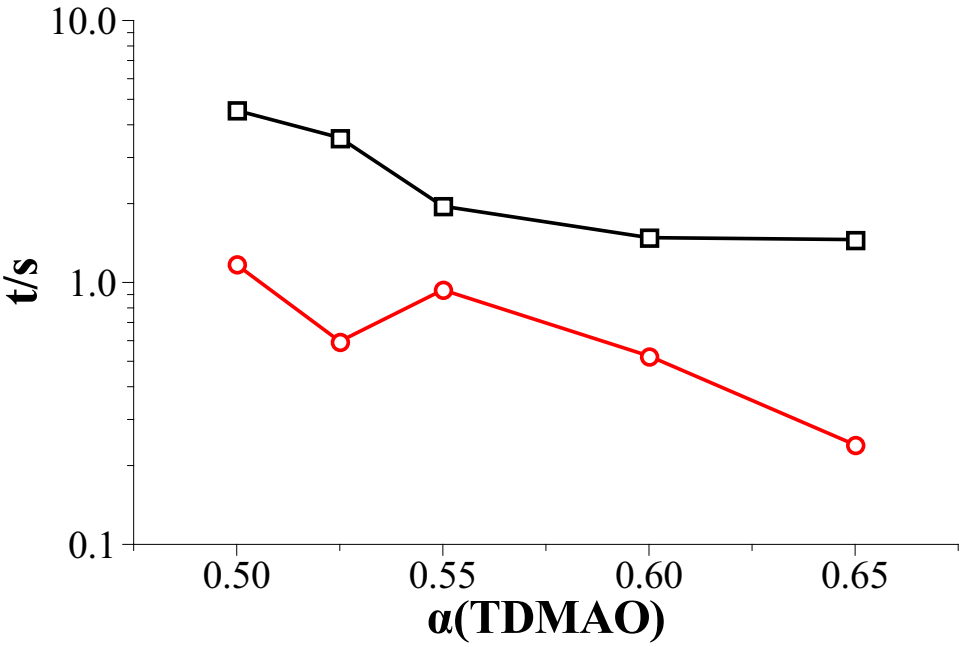

Figure 4.2.7: Characteristic times for the disc growth t_{disc} (◯) and the vesicle formation t_{vesicle} (□) in dependence on the the TDMAO content in the mixture

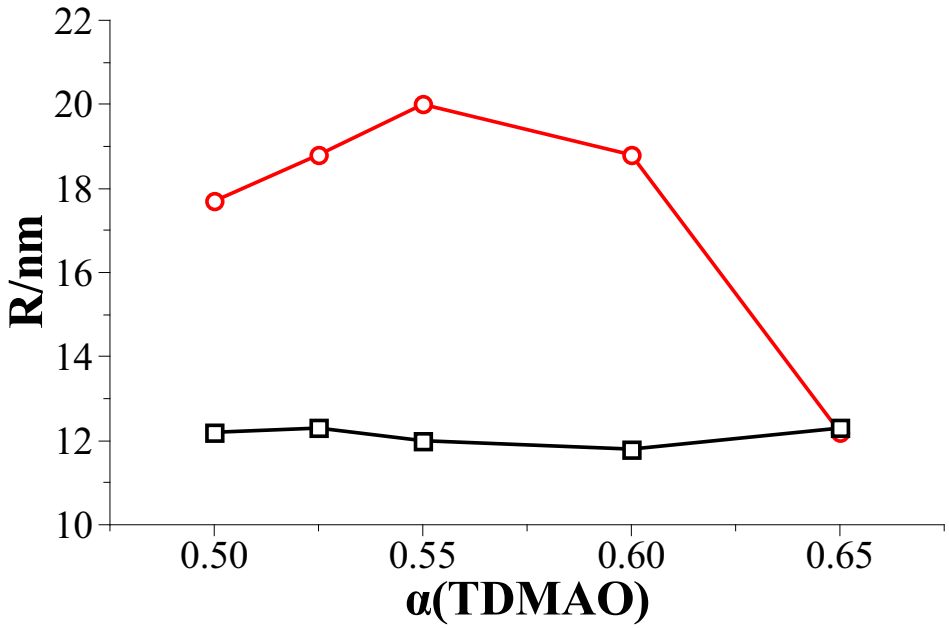

Figure 4.2.8: Maximum disc radius (◯) and minimum vesicle radius (□) in dependence on the the TDMAO content in the mixture

two principal curvatures c_1 and c_2, the spontaneous curvature c_0, the bending rigidity κ, the elastic modulus $\overline{\kappa}$, and the surface of the bilayer A. In the case of perfectly spherical vesicles $c_1 = c_2$ and the principal curvature c is the inverse of the vesicle radius $c = 1/R_{\text{ves.}}$. Then eqn (4.3.1) reduces to eqn (4.3.2).

$$F_{\text{b}} = \int_A \left(\kappa/2 \cdot (c_1 + c_2 - 2c_0)^2 + \overline{\kappa} c_1 c_2\right) dA \tag{4.3.1}$$

$$F_{\text{b}} = \int_A \left(\kappa/2 \cdot (2c - 2c_0)^2 + \overline{\kappa} c^2\right) dA \tag{4.3.2}$$

F_{l} is described in eqn (4.3.3) with the line tension λ and the length of the disc rim l.

$$F_{\text{l}} = \int_l \lambda dl \tag{4.3.3}$$

The total free energy F of a bend disc is then described in eqn (4.3.5).

$$F = F_{\text{b}} + F_{\text{l}} \tag{4.3.4}$$

$$= \left(\kappa/2 \cdot (2c - 2c_0)^2 + \overline{\kappa} c^2\right) \cdot A + \lambda l \tag{4.3.5}$$

The equality between the area of the disc A_{disc} (eqn (4.3.6)) and the area of bend disc $A_{\text{bend disc}}$ (eqn (4.3.7)) leads to a relation between the length of the disc rim l, the disc radius R_{disc} and the curvature c (eqn (4.3.12)). The situation in the bend disc is visualized in Fig. 4.3.1.

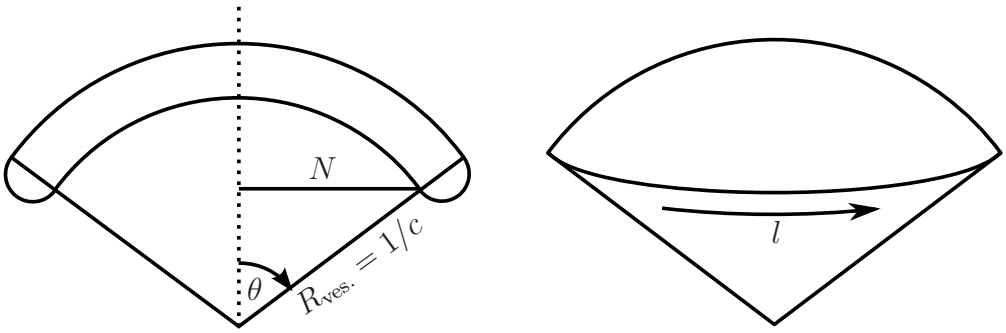

Figure 4.3.1: Scheme of a flexible disc-like micelle

$$A_{\text{disc}} = \pi R_{\text{disc}}^2 \tag{4.3.6}$$

$$A_{\text{bend disc}} = \frac{2\pi}{c^2}(1 - \cos(\theta)) \tag{4.3.7}$$

$$\cos^2(\theta) = 1 - R_{\text{disc}}^2 c^2 + \frac{R_{\text{disc}}^4 c^4}{4} \tag{4.3.8}$$

$$N = \frac{\sin(\theta)}{c} \tag{4.3.9}$$

$$l = 2\pi N \tag{4.3.10}$$

$$l = \frac{2\pi}{c}\sqrt{R_{\text{disc}}^2 c^2 - \frac{R_{\text{disc}}^4 c^4}{4}} \tag{4.3.11}$$

$$l = 2\pi R_{\text{disc}}\sqrt{1 - \left(\frac{R_{\text{disc}} c}{2}\right)^2} \tag{4.3.12}$$

The free energy per disc area F/A can then be expressed in dependence on the curvature c and the disc radius R_{disc} by eqn (4.3.14).

$$F = \left(\kappa/2 \cdot (2c - 2c_0)^2 + \overline{\kappa} c^2\right) \cdot A + \lambda \cdot 2\pi R_{\text{disc}}\sqrt{1 - \left(\frac{R_{\text{disc}} c}{2}\right)^2} \tag{4.3.13}$$

$$\frac{F}{A} = 2\kappa \cdot (c - c_0)^2 + \overline{\kappa} c^2 + \frac{2\lambda}{R_{\text{disc}}}\sqrt{1 - \left(\frac{R_{\text{disc}} c}{2}\right)^2} \tag{4.3.14}$$

$$= \frac{2\kappa + \overline{\kappa}}{R_{\text{disc}}^2} \cdot (2 - 2\cos(\theta)) - \frac{4\kappa c_0}{R_{\text{disc}}}\sqrt{2 - 2\cos(\theta)} + 2\kappa c_0^2 + \frac{2\lambda}{R_{\text{disc}}}\sqrt{\frac{1}{2} + \frac{1}{2}\cos(\theta)} \tag{4.3.15}$$

The energy per aggregate F increases with the disc size, but while the disc size increases the number of aggregates is reduced. To evaluate the stability of the whole system the overall energy of the system has to be considered. The overall energy of the system is proportional to the energy density which can be calculated from the energy of the aggregate and the number density $N_{\text{V}} = \phi_{\text{amph}}/D$ of the system with ϕ_{amph} being the volume fraction of amphiphilic material in the system and D being the thickness of the disc. The energy density of the whole ensemble F_{en} is then described by eqn (4.3.17).

$$F_{\text{en}} = N_{\text{V}} \cdot F \tag{4.3.16}$$

$$= \frac{\phi_{\text{amph}}}{D} \cdot \left(\kappa/2 \cdot (2c - 2c_0)^2 + \overline{\kappa} c^2\right) + \frac{2\phi_{\text{amph}}\lambda}{D R_{\text{disc}}} \cdot \sqrt{1 - \left(\frac{R_{\text{disc}} c}{2}\right)^2} \tag{4.3.17}$$

The derivative of the free energy F_{en} with the disc radius R_{disc} is always negative independent of the curvature (eqn (4.3.18)). That means that the disc growth is always energetically

favoured and the driving force here is the decreasing energy of the disc rim that decreases in total, if disc fusion takes place and the overall length of the disc rim is decreased.

$$\left(\frac{\partial F_{\mathrm{A}}}{\partial R_{\mathrm{disc}}}\right)_{\mathrm{c}} = -\frac{\phi_{\mathrm{amph}}\lambda c^2}{D\cdot\sqrt{1-\frac{R_{\mathrm{disc}}^2 c^2}{4}}} - \frac{2\phi_{\mathrm{amph}}\lambda}{DR_{\mathrm{disc}}^2}\sqrt{1-\frac{R_{\mathrm{disc}}^2 c^2}{4}} < 0 \tag{4.3.18}$$

During the vesicle formation the particle number density does not change and therefore does not have to be considered in the change of the free energy. To evaluate whether vesicle formation takes place the thermodynamic situation has to be considered as well as the kinetic situation. If the area specific free energy of the flat disc $F_{\mathrm{A}}(\theta = 0)$ is lower than the energy of the corresponding vesicle $F_{\mathrm{A}}(\theta = \pi)$ with the same surface, than the vesicles are thermodynamically unstable. If $F_{\mathrm{A}}(\theta = 0) \geq F_{\mathrm{A}}(\theta = \pi)$, than vesicles are thermodynamically stable but the formation can be kinetically hindered. The energy difference $F_{\mathrm{A}}(\pi) - F_{\mathrm{A}}(0)$ between the vesicle and the flat disc is given in eqn (4.3.21).

$$F_{\mathrm{A}}(0) = 2\kappa c_0^2 + \frac{2\lambda}{R_{\mathrm{disc}}} \tag{4.3.19}$$

$$F_{\mathrm{A}}(\pi) = \frac{4\cdot(2\kappa+\overline{\kappa})}{R_{\mathrm{disc}}^2} - \frac{8\kappa c_0}{R_{\mathrm{disc}}} + 2\kappa c_0^2 \tag{4.3.20}$$

$$F_{\mathrm{A}}(\pi) - F_{\mathrm{A}}(0) = \frac{4\cdot(2\kappa+\overline{\kappa})}{R_{\mathrm{disc}}^2} - \frac{8\kappa c_0}{R_{\mathrm{disc}}} - \frac{2\lambda}{R_{\mathrm{disc}}} \tag{4.3.21}$$

Vesicles are thermodynamically stable if the energy difference is smaller than zero. That leads to a maximum disc radius $R_{\mathrm{disc,max,therm.}}$ where discs are no longer thermodynamically stable.

$$\frac{4\cdot(2\kappa+\overline{\kappa})}{R_{\mathrm{disc}}^2} \geq \frac{2\lambda + 8\kappa c_0}{R_{\mathrm{disc}}} \tag{4.3.22}$$

$$R_{\mathrm{disc}} \leq \frac{2(2\kappa+\overline{\kappa})}{\lambda + 4\kappa c_0} \tag{4.3.23}$$

$$R_{\mathrm{disc,max,therm.}} = \frac{2(2\kappa+\overline{\kappa})}{\lambda + 4\kappa c_0} \tag{4.3.24}$$

Eqn (4.3.24) shows that even, if the spontaneous curvature is zero a cut-off radius $R_{\mathrm{disc,max,therm.}}$ can be expected, where vesicles are thermodynamically favoured over discs. The energy barrier for the vesicle formation is the difference between $F_{\mathrm{A}}(0)$ and the energy maximum where $((\partial F_{\mathrm{A}})/(\partial\theta))_{R_{\mathrm{disc}}} = 0$. This equation is fulfilled for $\theta = 0$, where a minimum is indicated by $((\partial^2 F_{\mathrm{A}})/(\partial\theta^2))_{R_{\mathrm{disc}}} > 0$, and for $\cos(\theta) = \frac{\lambda^2 R_{\mathrm{disc}}^2}{8(2\kappa+\overline{\kappa})^2} - 1$, where a maximum is indicated by $((\partial^2 F_{\mathrm{A}})/(\partial\theta^2))_{R_{\mathrm{disc}}} < 0$. This leads to the area specific activation energy given in eqn (4.3.26).

$$E_{\mathrm{A,A}} = F_{\mathrm{A,maximum}} - F_{\mathrm{A}}(0) \tag{4.3.25}$$

$$= \frac{4(2\kappa + \overline{\kappa})}{R_{\mathrm{disc}}^2} + \frac{\lambda^2}{4(2\kappa + \overline{\kappa})} - \frac{2\lambda}{R_{\mathrm{disc}}} \tag{4.3.26}$$

Since there is a relation between the maximum disc radius $R_{\mathrm{disc,max,therm.}}$ and the line tension λ (eqn (4.3.24)), λ can be replaced in eqn (4.3.26).

$$E_{\mathrm{A,A}} = \frac{4(2\kappa + \overline{\kappa})}{R_{\mathrm{disc}}^2} - \frac{4(2\kappa + \overline{\kappa})}{R_{\mathrm{disc}} R_{\mathrm{disc,max,therm.}}} + \frac{2\kappa + \overline{\kappa}}{R_{\mathrm{disc,max,therm.}}^2} \tag{4.3.27}$$

The area specific activation energy reduces to eqn (4.3.28), when R_{disc} approaches $R_{\mathrm{disc,max,therm.}}$.

$$E_{\mathrm{A,A}} = \frac{2\kappa + \overline{\kappa}}{R_{\mathrm{disc,max,therm.}}^2} \tag{4.3.28}$$

That leads to the activation energy for the formation of one vesicle from one disc then given in eqn (4.3.29) and does neither depend on the line tension nor on the maximum disc radius since these two parameters together with the bending energy are not independent.

$$E_{\mathrm{A}} = \pi(2\kappa + \overline{\kappa}) \tag{4.3.29}$$

During the vesicle formation process not only the thermodynamic stability but as well the kinetics have to be considered. The time constant for the closure process described in eqn (4.3.30) is a product of the Boltzmann factor and an oscillation frequency of the bending mode of the disc. Leng et al. [91] assumed that the viscous dissipation in the liquid media is the dominant contribution to this oscillation frequency which is the described by the "Zimm time" $\tau_{\mathrm{Z}} = 6\pi\eta R_{\mathrm{disc}}^3/(k_{\mathrm{B}}T)$. The closure time τ_{c} is then described in eqn (4.3.30) with eqn (4.3.27) and can be regarded as a function of R_{disc}.

$$\tau_{\mathrm{c}}(R_{\mathrm{disc}}) = \frac{6\pi\eta R_{\mathrm{disc}}^3}{k_{\mathrm{B}}T} \exp\left(\frac{E_{\mathrm{A}}(R_{\mathrm{disc}})}{k_{\mathrm{B}}T}\right) \tag{4.3.30}$$

Fig. 4.3.3 shows the dependence of the closure time τ_{c} and the opening time τ_{o} on the disc radius for different thermodynamic cut-off radii $R_{\mathrm{disc,max,therm.}}$ for a fixed $2\kappa + \overline{\kappa}$. The equilibrium is shifted to the formation of vesicles, if the closing process is faster than the vesicle opening process, that means if τ_{c} is smaller than τ_{o}. τ_{c} crosses τ_{o} at $R_{\mathrm{disc,max,therm.}}$. If only these two processes of opening and closing had to be considered an equilibrium

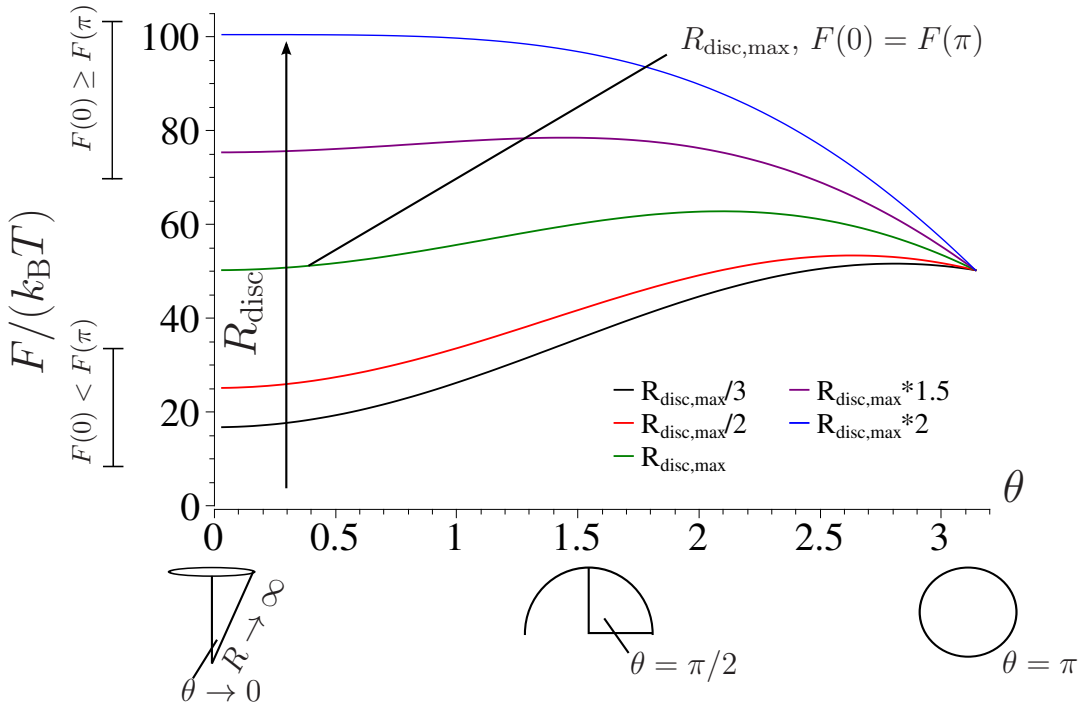

Figure 4.3.2: Free energy F in dependence on the closing angle θ (see Fig. 4.3.1) for different disc radii R_{disc}, c_0, λ, and $2\kappa + \overline{\kappa}$ were set to arbitrary values of 0, $0.4k_BT/nm$, and $3k_BT$ respectively

between discs and vesicles could be achieved with vesicles being favoured over discs for $R_{\text{disc}} > R_{\text{disc,max,therm.}}$. Though a side process has to be considered since discs of the size $R_{\text{disc,max,therm.}}$ might still grow. Whether the vesicle formation after this point is kinetically hindered, simply depends on the value of τ_c. If the closure process is significantly slower than the micellar growth process, the formed vesicles can be expected to be larger than $0.5 \cdot R_{\text{disc,max,therm.}}$. The observed cut-off radius $R_{\text{disc,max,kin.}}$ is then kinetically determined. On the other hand, if τ_c is low, it can be expected that a thermodynamic equilibrium between micelles and vesicles exists. Especially systems with a small $R_{\text{disc,max,therm.}}$, that did not yet reach the cut-off radius, show a fast conversion between discs and vesicles. Here it can be expected that there is already a small fraction of aggregates p, that is in the vesicle state below $R_{\text{disc,max,therm.}}$, depending on the Boltzmann factor (eqn (4.3.32)).

$$p = \frac{\exp\left(\frac{-F(\theta)}{k_BT}\right)}{\exp\left(\frac{-F(0)}{k_BT}\right) + \exp\left(\frac{-F(\theta)}{k_BT}\right)} \tag{4.3.31}$$

$$= \frac{\exp\left(\frac{-(F(\theta)-F(0))}{k_BT}\right)}{1 + \exp\left(\frac{-(F(\theta)-F(0))}{k_BT}\right)} \tag{4.3.32}$$

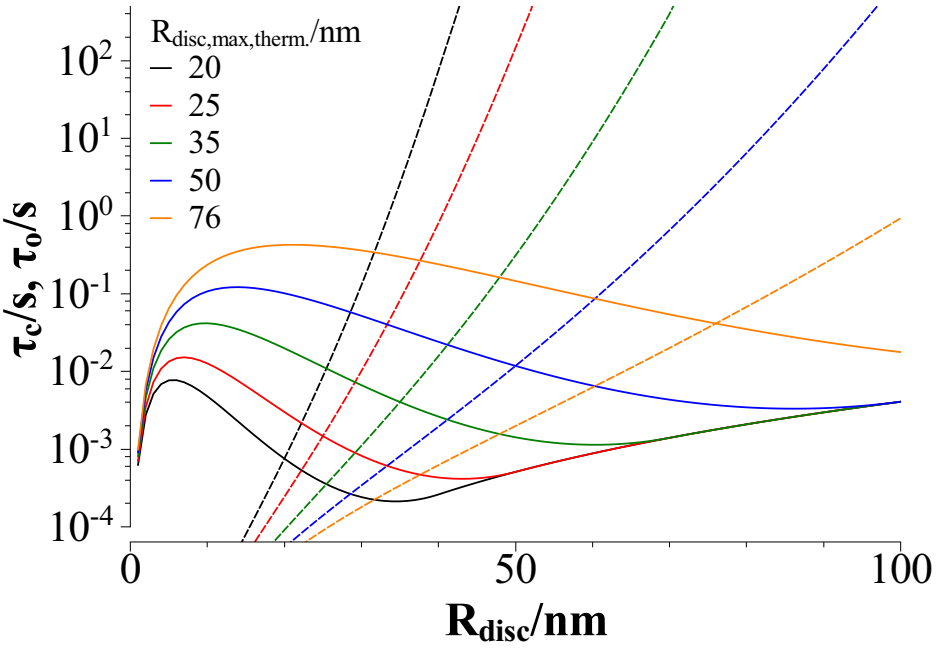

Figure 4.3.3: Closure time τ_c (solid line) and opening time τ_o (dashed lines) in dependence on the disc radius R_{disc} for different thermodynamic cut-off radii $R_{disc,max,therm.}$; c_0 and $2\kappa+\overline{\kappa}$ were set to arbitrary values of 0 and k_BT respectively

The other influence on $R_{disc,max,kin.}$ besides $R_{disc,max,therm.}$ is $2\kappa+\overline{\kappa}$ for a given $R_{disc,max,therm.}$ (see Fig. 4.3.4). τ_c increases strongly with $2\kappa+\overline{\kappa}$. So the vesicle formation in systems with rigid bilayers may be kinetically hindered and the vesicle formation may be delayed until sizes are reached where the closure time is small enough. That means depending on $2\kappa+\overline{\kappa}$ either $R_{disc,max,kin.}$ or $R_{disc,max,therm.}$ defines the maximum disc size $R_{disc,max.}$ and therefore the minimum vesicle size $R_{ves.,min.}$.

For $(\partial F/\partial\theta)_{R_{disc}} \geq 0$ the free energy decreases monotonically during closure and the activation energy vanishes. This is fulfilled for $R_{disc} \geq \frac{4(2\kappa+\overline{\kappa})}{\lambda}$.

For vesicles there is no energetical contribution from a rim since there is none and only the bending energy F_b has to be considered. The curvature c is then the inverse of the vesicle radius $R_{ves.}$.

$$F_b = 8\pi\kappa\left(1-\frac{c_0}{c}\right)^2 + 4\pi\overline{\kappa} \tag{4.3.33}$$

The equilibrium vesicle radius $R_m = 1/c_m$ can be determined over the energy minimum. Since it was assumed that the bending energy has the form of a harmonic potential with a minimum at the spontaneous curvature, c_0 can be set to $c_0 = c_m = 1/R_m$ and with the vesicle radius $R_{ves.} = 1/c$ eqn (4.3.35) follows.

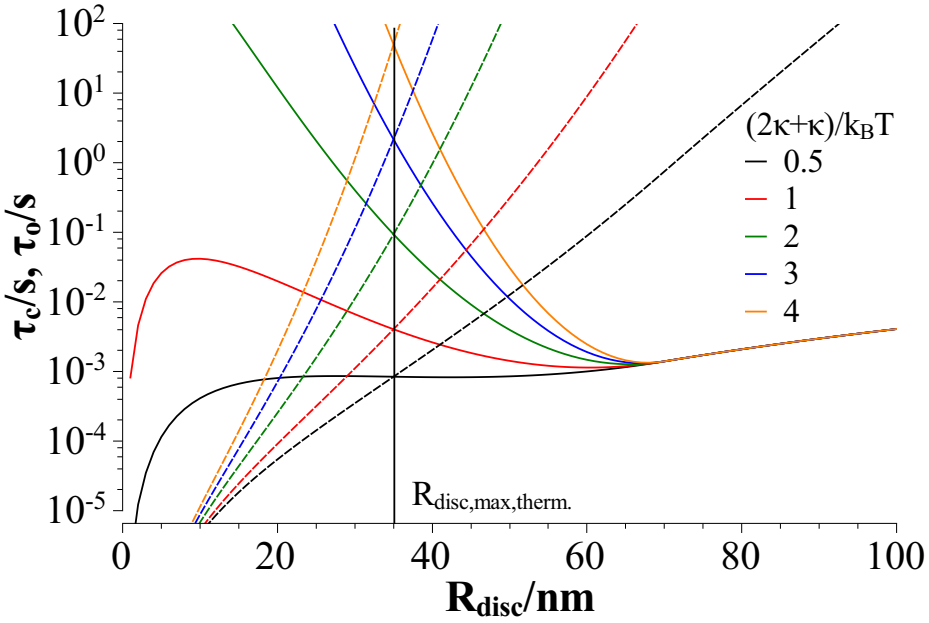

Figure 4.3.4: Closure time τ_c (solid line) and opening time τ_o (dashed lines) in dependence on the disc radius R_{disc} for different $2\kappa + \overline{\kappa}$ at an arbitrary thermodynamic cut-off radius $R_{disc,max,therm.} = 35nm$; c_0 was set to an arbitrary value of 0

$$F_b = A \cdot \left(\frac{\kappa}{2}(2c - 2c_0)^2 + \overline{\kappa}c^2\right) \tag{4.3.34}$$

$$= \frac{8\pi\kappa}{R_m^2}\left(R_m - R_{ves.}\right)^2 + 4\pi\overline{\kappa} \tag{4.3.35}$$

In equilibrium the probability f that a vesicle has the bending energy F_b is given by the Boltzmann factor $f \propto exp(-F_b/(k_BT))$ described in eqn (4.3.36).

$$f \propto \exp\left(-\frac{8\pi\kappa}{k_BTR_m^2}\left(R_m - R_{ves.}\right)^2\right) \cdot \exp\left(-\frac{4\pi\overline{\kappa}}{k_BT}\right) \tag{4.3.36}$$

This Boltzmann factor has the form of a Gauss distribution (see eqn (4.3.37)) of the vesicle radius $R_{ves.}$ with a mean radius of R_m and the standard deviation σ.

$$f(R_{ves.}) = \frac{1}{\sigma\sqrt{2\pi}} \exp\left(-\frac{(R_{ves.} - R_m)^2}{2\sigma^2}\right) \tag{4.3.37}$$

Comparison of the Boltzmann factor with the Gauss function leads to the expression for σ given in eqn (4.3.38).

$$\sigma = R_m\sqrt{\frac{k_BT}{4\pi\kappa}} \tag{4.3.38}$$

Similar expressions have been calculated by other authors.[27,58,78,84] κ can then be calculated over the polydispersity $PDI = \sigma/R_{\mathrm{m}}$ (eqn (4.3.39)).

$$\kappa = \frac{k_{\mathrm{B}}T}{4\pi PDI^2} \tag{4.3.39}$$

Table 4.3.1: Values for the mean bending modulus of the bilayer κ and the line tension λ estimated from the polydispersity PDI and the maximum disc radius $R_{\mathrm{disc,max.}}$

α(TDMAO)	0.5	0.525	0.55	0.6	0.65
PDI	0.238	0.238	0.259	0.322	0.333
$\kappa/(k_{\mathrm{B}}T)$	1.40	1.40	1.19	0.77	0.72
$R_{\mathrm{disc,max}}/nm$	17.7	18.8	20	18.8	12.2
$\lambda/(k_{\mathrm{B}}T)\cdot nm$	0.16	0.15	0.12	0.08	0.12

The values calculated here for κ are quite low. For phospholipids, a typical value is $\kappa \approx 20k_{\mathrm{B}}T$.[95] Nevertheless Jung et al. reported values of $2\kappa + \overline{\kappa} = 1.4k_{\mathrm{B}}T$ for vesicles of cetyltrimethylammonium bromide and sodium octylsulfonate (2wt% , 3:7 by weight) and $2\kappa + \overline{\kappa} = 12k_{\mathrm{B}}T$ for vesicles of cetyltrimethylammonium bromide and sodium perfluorooctanoate (2wt% , 2:8 by weight).[78] This shows on the one hand that vesicles with such a low bending rigidity exist but are polydisperse. On the other hand for perfluoro surfactant vesicles with the bulky chain perfluoro chain higher bending rigidities than observed in this study could be expected. One difference between the investigated system TDMAO-LiPFOS and the system investigated by Jung et al. lies within the head group charges. For zwitanionic surfactant pairs much more flexible membranes can be expected than for catanionic surfactant pairs. For catanionics the head group interactions are so attractive that they lead to a denser packing of the alkyl chains, thereby to a higher lateral pressure within the membrane, which then leads to a larger bending moduli. So this then explains the differences.
Under the assumption that $2\kappa + \overline{\kappa}$ is closer to $k_{\mathrm{B}}T$ than to $10k_{\mathrm{B}}T$ it is not unlikely that vesicles are formed in thermodynamic equilibrium and the vesicle formation is not kinetically hindered. Nonetheless the bilayer closure time τ_{c} is strongly dependent on the bending rigidity as shown in Fig. 4.3.4 and for slightly higher bending rigidities a delayed vesicle formation can be expected. Then the initial vesicle radius can not be described by eqn (4.3.24). In section 5 temperature dependent measurements are described in order to determine the bending rigidity from the activation energy. This method is more reliable than calculating the bending rigidity from the polydispersity since here thermal fluctuations or smearing may indicate a higher polydispersity than the actual polydispersity.

4.4 Comparison Between the Systems TDMAO-Lithium Perfluoralkanoate and TDMAO-LiPFOS

In general in mixtures of TDMAO and perfluoroalkanoates as well as in the system TDMAO-LiPFOS vesicle formation can be observed, where the ability to form vesicles depends on the perfluoro surfactant chain length. In mixtures of TDMAO and perfluoro alkanoates vesicle formation was facilitated with increasing perfluoro chain length. For lithium perfluorooctaneoate (LiPFO) and LiPFOS well defined unilamellar vesicles are formed. In the TDMAO-LiPFOS system the vesicle area lies in the centre of the phase diagram and is even shifted to higher TDMAO content while in the TDMAO-LiPFO system the vesicle area is found at lower TDMAO content like in the other TDMAO perfluoralkanoate systems with shorter perfluor chains. The vesicles in both systems are of comparable size of 20-30nm and the polydispersities were with 0.2-0.3 similar two days after mixing. In both systems micellar phases could be found at the edges of the phase diagram. In the TDMAO-LiPFO case at low TDMAO content the micelles are spherical and at high TDMAO content they are rod-like. In the TDMAO-LiPFOS case at low TDMAO content spherical micelles can be observed that transform into rod-like micelles with increasing TDMAO content, while at higher TDMAO content disc-like micelles are found close to the phase boundary. So both phase diagrams and as well the formed vesicles are quite similar.

Kinetic measurements show that in both systems the mechanism of vesicle formation follows the same path over disc-like micelles (see section 4.2 and Weiss et al.[142] (2005)). The time constants for the micellar growth and for the vesicle formation are with 0.2-1.2s and 1.4-4.6s in the same order of magnitude.

In the system TDMAO-LiPFOS the kinetics of formation were investigated in dependence on the mixing ratio between TDMAO and LiPFOS. Here it could be observed that the most well defined vesicles with the lowest polydispersity were formed in the centre of the vesicle area around $\alpha(\text{TDMAO}) = 0.55$.

Since the systems TDMAO-LiPFO and TDMAO-LiPFOS show both formation of well defined vesicles and the same mechanism of vesicle formation, both systems are suitable for further experiments and variations of previously performed experiments. In the following parts the aim was to use the knowledge about the vesicle formation process to gain control about the size and polydispersity of the formed vesicles. Since the size of the vesicles is controlled by the balance between the line tension of the micellar disc-rim and the bending energy of the bilayer. At this point it is possible to intervene with this process by e.g. by lowering the line tension. This can be achieved by incorporating a third component that will preferably accumulate into the disc-rim. This component can locally decrease the packing

parameter and increase the spontaneous curvature in the disc-rim. Thereby the disc-rim can be stabilised, with the desired effect that the vesicle size increases and that the vesicle size can be controlled by the concentration of the additive.

Temperature Dependent Vesicle Formation in the System TDMAO-LiPFOS

Section 4 showed the dependence of the vesicle radius on the balance between the line tension and the rigidity of the membrane. The bending energy of the membrane is linked to the activation energy of the vesicle formation (eqn (4.3.29)) and therefore it is possible to determine the bending energy from temperature dependent measurements.
Here a 50mM TDMAO solution and a 50mM LiPFOS solution were mixed at temperatures between 20°C and 45°C in a stopped-flow device in a 55:45 ratio and structural changes were monitored by SAXS measurements. These measurements were performed on ID02 of the ESRF in Grenoble (see section 10.1.4).
The measurements performed at 25°C were already discussed in section 4.2. Measurements at other temperatures showed in principal a similar behaviour. That means that rod-like TDMAO micelles and spherical LiPFOS micelles fuse into disc-like mixed micelles, that grow and transform into vesicles at a certain point. The data analysis was performed similar to the data analysis in section 4.2.
Fig. 5.0.1 shows the development of the disc radius with the time. To gain an idea about the time scale the data were fitted with a monoexponential function, that is not connected to the mechanism of the growth process but gives a characteristic time t_{disc} for the overall process. The discs grow rather fast for temperatures above 35°C, so here the resolution of the measurement is not sufficient to follow the process.
The ratio A_1 of scattering material in the disc-like micelles was determined by fitting the scattering curves with a model that takes into account the absolute scattering intensity coming from the micelles and the vesicles (eqn (4.1.1)). So A_1 is a measure for the transformation of discs into vesicles. Fig. 5.0.2 shows the time dependent development of A_1. As to be expected the vesicle formation slows down with decreasing temperature. Under the assumption that discs directly transform into vesicles after a certain initial time the parameter development could be fitted according to eqn (4.2.1).
First the fits in Fig. 5.0.2 provide the starting time of the vesicle formation t_0. This time is linked to the time when the first discs reach the maximum disc radius and is therefore in the same range as t_{disc}. Second these fits give the characteristic time for the overall vesicle formation process t_{vesicle} (Fig. 5.0.3).
If the vesicle formation takes place in equilibrium the characteristic time t_{vesicle} determined from the fits in Fig. 5.0.2 has to be identical to the closure time τ_{c} as defined in eqn (4.3.30). To achieve a linear dependence on the temperature eqn (4.3.30) was written in the form

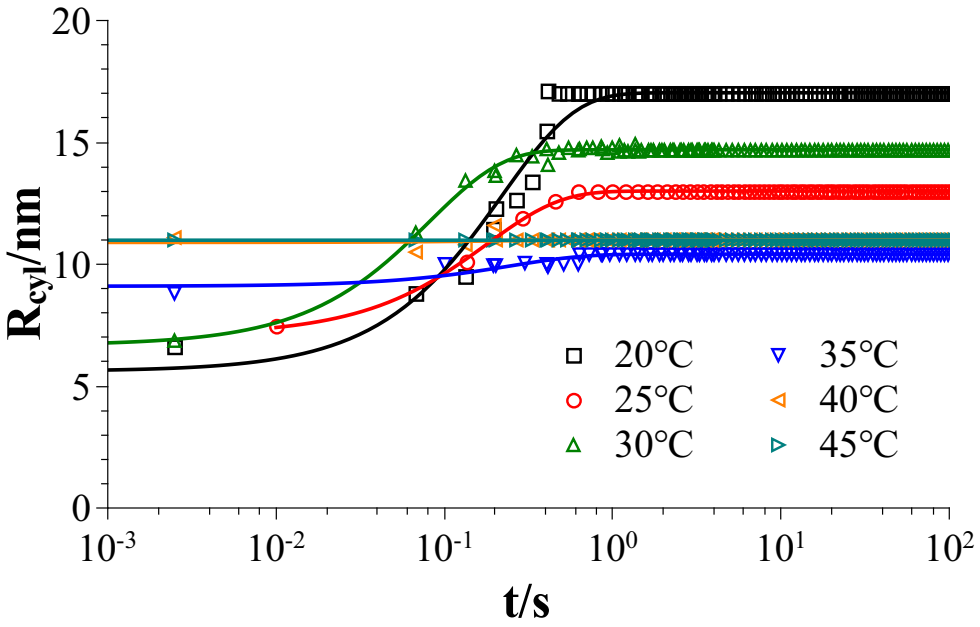

Figure 5.0.1: Time dependent development of the disc radius R_{disc} at different temperatures in the mixture TDMAO-LiPFOS (55:45), 50mM

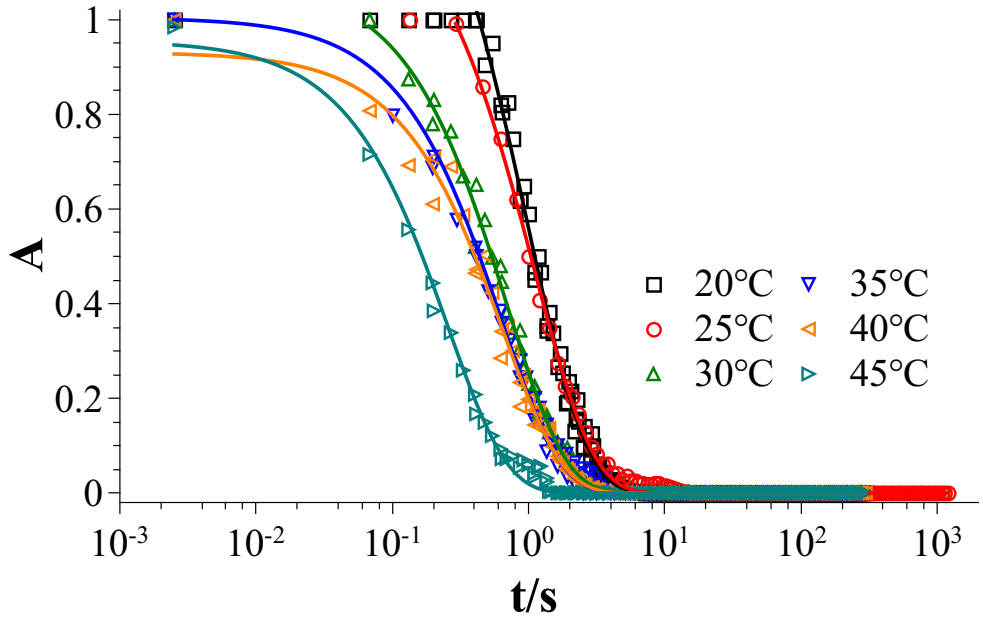

Figure 5.0.2: Temporal evolution of the fraction A_1 of disc-like micelles in the mixture at different temperatures in the mixture TDMAO-LiPFOS (55:45), 50mM

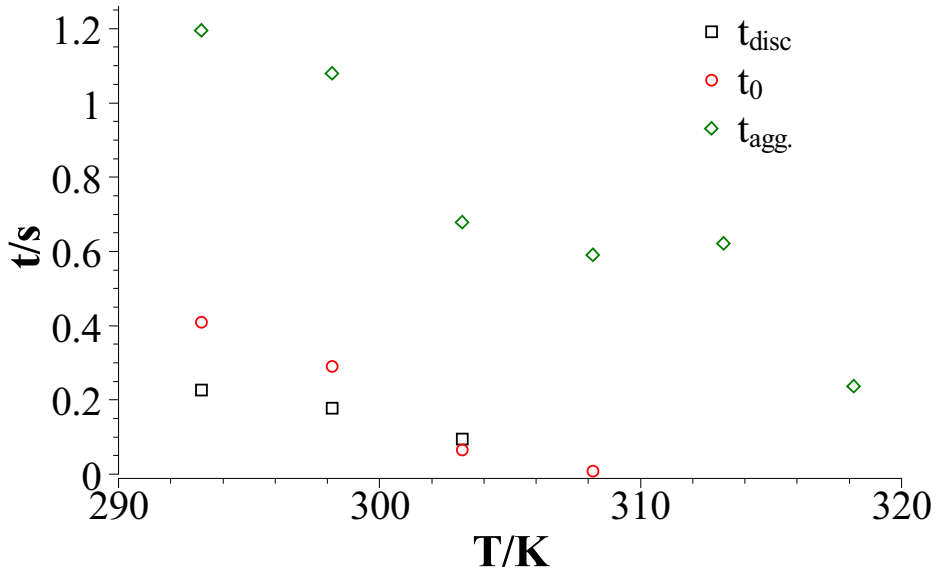

Figure 5.0.3: Characteristic time for disc growth t_{disc}, for starting time of the vesicle formation process t_0, and for the vesicle formation process t_{vesicle} in the mixture TDMAO-LiPFOS (55:45), 50mM

shown in eqn (5.0.1) and $\ln(\tau_c) + \ln(T)$ was plotted versus $1/T$ as shown in Fig. 5.0.4.

$$\ln(\tau_c/s) + \ln(T/K) = \ln\left(\frac{6\pi\eta R^3_{\text{disc,max,therm.}}}{k_B}\right) + \frac{E_A}{k_B}\cdot\frac{1}{T} \tag{5.0.1}$$

From the linear fit (eqn (5.0.2)) to the data shown in Fig. 5.0.4 the expected maximum disc radius $R_{\text{disc,max,therm.}}$ can be determined from the intercept A (eqn (5.0.3)) and the activation energy E_A can be determined from the slope B. In fact since the bilayer stiffness should weaken with increasing temperature, $R_{\text{disc,max,therm.}}$ is not a constant regarding the temperature and eqn (5.0.1) is a function of $1/T$ and $R_{\text{disc,max,therm.}}(T)$. Fig. 5.0.4 shows nearly linear behaviour of $\ln(\tau_c/s) + \ln(T/K)$ with $1/T$. So the temperature dependence of $R_{\text{disc,max,therm.}}$ can be neglected in the observed interval.

$$\ln(\tau_c) + \ln(T) = A + B\cdot\frac{1}{T} \tag{5.0.2}$$

$$R_{\text{disc,max,therm.}} = \sqrt[3]{\frac{\exp(A)k_B}{6\pi\eta}} \tag{5.0.3}$$

$$\Delta R_{\text{disc,max,therm.}} = \frac{dR_{\text{disc,max,therm.}}}{dA}\Delta A \tag{5.0.4}$$

From the fit an activation energy of $E_A = (11 \pm 3)k_BT$ could be determined. This activation energy comes from a membrane rigidity of $2\kappa + \overline{\kappa} = (3 \pm 1)k_BT$ (see eqn (4.3.29)). With this

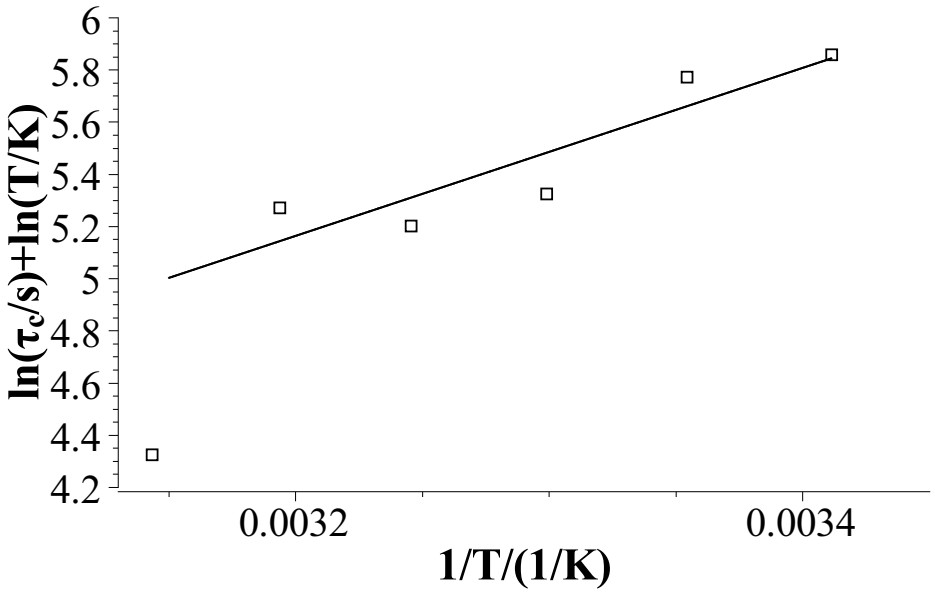

Figure 5.0.4: Linearisation of the Arrhenius law according to eqn (5.0.1)

method the determination of the bending energy is more reliable than the determination from the polydispersity in section 4.3 because in the SANS fits in section 4.3 it was assumed, that the vesicles were in thermodynamic equilibrium and thermal fluctuations from the vesicle membrane were neglected. As a result the determined polydispersities might differ from the polydispersity of the vesicles in equilibrium.

In section 4.2 the maximum disc radius $R_{\text{disc,max,therm.}}$ was determined with 20nm and the temperature dependent measurements and their analysis lead to an expected maximum disc radius of $R_{\text{disc,max,therm.}} = (20 \pm 16)nm$ ($A = -5.14 \pm 2.83$). These two values are in good agreement. From the values determined for $2\kappa + \overline{\kappa}$ here and from the maximum disc radius the line tension λ can be determined with $(0.3 \pm 0.34)k_{\text{B}}T/nm$. The error bars here are quite large due to the logarithmic dependence of the maximum disc radius on the intercept of the fit in Fig. 5.0.4.

Fig. 5.0.5 shows the kinetic situation in a system with the parameters as determined above. The resulting maximum disc radius in equilibrium is with 20nm the same for all temperatures and the expected closing time is below 0.5s for all temperatures. This is in the same range as t_{disc}. So the vesicle formation time is slow compared to the disc growth process. This might lead to a situation where the vesicle formation is kinetically hindered and where the vesicles are not formed in equilibrium as assumed. As a result the equilibrium cut-off radius for the discs would be lower and the resulting line tension would be higher. A dependence of the initial vesicle radius on the temperature might be expected since the closure time

decreases with the temperature. On the other hand the disc growth is as well accelerated with increasing temperature so that both effects might cancel out.

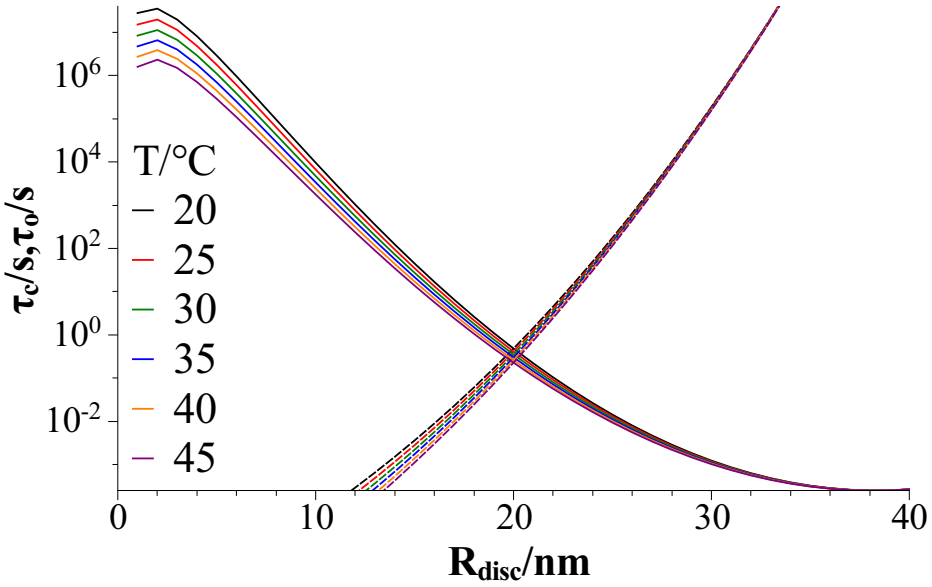

Figure 5.0.5: Closing time τ_c and opening time τ_o for $2\kappa + \overline{\kappa} = 3k_BT$ and $\lambda = 0.3k_BT/nm$

Fig. 5.0.6 shows indeed a slight dependence of the initial vesicle radius on the temperature. This might be due to a kinetic determined process. On the other hand as shown in Fig. 5.0.7 the polydispersity of the initial vesicles increases with the temperature so that the decrease in radius could be as well an artefact from the fits with increasing polydispersity. With incresing temperature the energy of the system increases and therefore the probability increases that particles can overcome the energy barrier for vesicle formation before the cut-off radius is reached. So the size distribution on the initial vesicle radius becomes broader, i.e. the initial polydispersity for the vesicle radius increases.

As a result the rigidity of the membrane could be determined from the temperature dependent measurements and analysis of the disc growth process and the kinetic situation showed that in this situation it can not ultimately be decided whether the vesicle formation takes place in equilibrium, so that the initial vesicle radius is only determined by the balance between the line tension and the bending energy, or whether the vesicle formation is kinetically hindered.

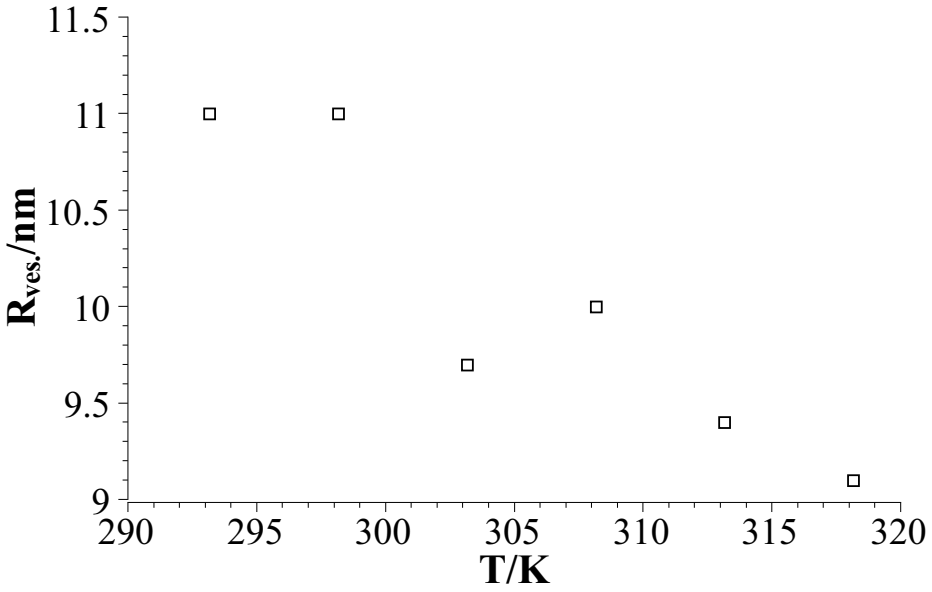

Figure 5.0.6: Initial vesicle Radius $R_{\text{ves.}}$ in dependence on the temperature T in the mixture TDMAO-LiPFOS (55:45), 50mM

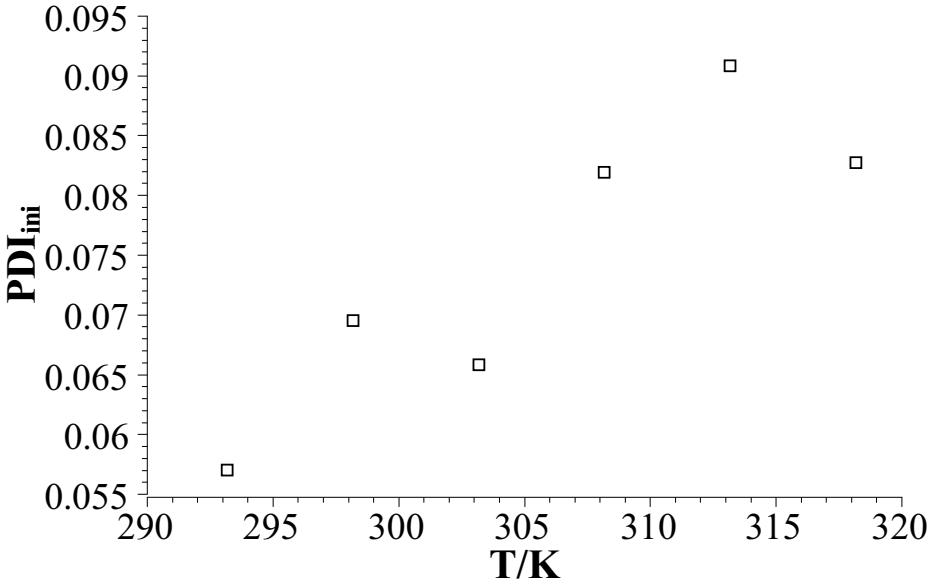

Figure 5.0.7: Polydispersity of the vesicles in dependence on the temperature in the mixture TDMAO-LiPFOS (55:45), 50mM

Influence of the Amphiphilic Polymer Pluronic L35 on the System TDMAO-LiPFOS

The use of vesicles in pharmaceutical or cosmetic applications depends on the control over vesicle structure and stability. The admixture of nano particles has been shown to allow for enhanced stability and to prevent vesicles from vesicle-vesicle fusion or precipitation but is not suited to control structural features like size and polydispersity.[129] Another possibility is the addition of small quantities of amphiphilic polymers, what has been applied in the case of phospholipids where the size was controlled in a range of 15-150nm[77]. Nevertheless the mechanism that leads to different vesicle sizes was not fully resolved. In the mentioned cases especially the effect of additives on the equilibrium vesicle size[77] was investigated or the additives were introduced after the formation of non equilibrium vesicles in order to stabilise the formed structures.[129] Since vesicles are often non-equilibrium structures another possibility is to interfere with intermediate structures, that appear during the formation process, and in this way to influence the final structure. The pathway of vesicle formation for catanionic or zwitanionic surfactant mixtures was investigated before[60,91,92,130,132,141,142] and corroborated by the studies with TDMAO and LiPFOS (see section 4).[19]

It was shown that the vesicles are formed via a state of disc-like micelles. These micelles are formed within milliseconds after mixing two pure surfactant solutions but do not constitute an equilibrium state. Due to their line tension these micelles show a subsequent growth that results in a decrease of the disc-rim energy. At the same time the disc-like micelles are in equilibrium with a vesicle state that they can reach by deformation over a cup state. The transformation is controlled by the balance between the energy of the disc-rim and the energy of the corresponding vesicles. The bending energy of the vesicle bilayer decreases with decreasing curvature and increasing corresponding disc-rim. At a certain point where the energy of the bilayer goes below the energy of the disc-rim the discs become unstable and vesicle formation appears. During this process it is possible to add amphiphilic polymer and to effect the formation and gain kinetic control over the balance between line-tension and bending-energy and thereby control the size of the formed vesicles. When adding amphiphilic polymers to the surfactant system then these polymers may be expected to accumulate preferably in the rim of the disc-like micelles. Due to their bulky head group that leads to a reduction of the line tension and equality between disc-rim energy and bending energy will be reached at a later point so that the resulting vesicle size is larger than in the case without polymer.

The polymer chosen in the following investigation was a polymer of the EOn−POm−EOn

type, the Pluronic L35 (average formula: $EO_{11}-PO_{16}-EO_{11}$). It can be assumed that the polypropylene part is hydrophobic enough to become incorporated within the surfactant bilayer. The hydrophobic part with sixteen PO units has a stretched length of about 5.6nm (3.5Å per repeat unit[51]) and is in the same range as the thickness of the bilayer with 3nm, especially when considering that in reality the PO_{16} will not really be fully stretched. The hydrophilic parts are relatively short so that Pluronic L35 has a relatively low diffusive constant what results in a short relaxation time for the incorporation into the micelles.

6.1 Vesicle Formation in the Presence of Pluronic L35

Like in the system TDMAO-LiPFOS without Pluronic L35 (see section 4.2) stopped-flow measurements were performed to investigate the kinetics and the vesicle formation process. In this system the measurements were performed at the ESRF in Grenoble and the detection method was Small Angle X-ray Scattering using the radiation from the synchrotron source (see section 10.1.4). To vary the Pluronic L35 concentration in the mixture 50 mM TDMAO solutions with different Pluronic L35 concentrations were mixed with a pure 50mM LiPFOS solution in the stopped-flow apparatus in a volume ratio of 55:45. This mixing ratio lies in the middle of the vesicle area and here very monodisperse vesicles compared to those at the edges of the vesicle area could be found (see section 4.2). The polymer concentration is always given as percentage with respect to the molar TDMAO concentration. That means at a TDMAO concentration of 27.5mM and a polymer concentration of 0.275mM the polymer concentration is given as 1 mol%. Since in 50mM TDMAO solutions with Pluronic L35 like in the pure 50mM TDMAO solution rod-like micelles are present, the mixing process is again mixing of nearly spherical LiPFOS micelles with rod-like TDMAO micelles.

The principal scattering patterns and the general mechanism of vesicle formation over disc-like micelles is observed in the mixtures with Pluronic L35 (Fig. 6.1.2) as well as without added polymer (Fig. 6.1.1).

The scattering patterns show at the beginning scattering arising from disc-like micelles with a typical radius of 6-7nm and a thickness of 3.2nm. It can be observed that these discs grow with time. The growth process in the pure surfactant system only lasts for less than a second before vesicle formation can be observed while in the system with polymer oscillations arising from vesicle formation do not occur during the first 20s seconds (for 1 mol% L35). That means the vesicle formation is hindered by the polymer and the polymer interacts with the disc-like micelles and stabilises them so that the point of instability is reached at larger disc sizes.

After about 1s in the system without polymer and after about 20s in the system with 1mol%

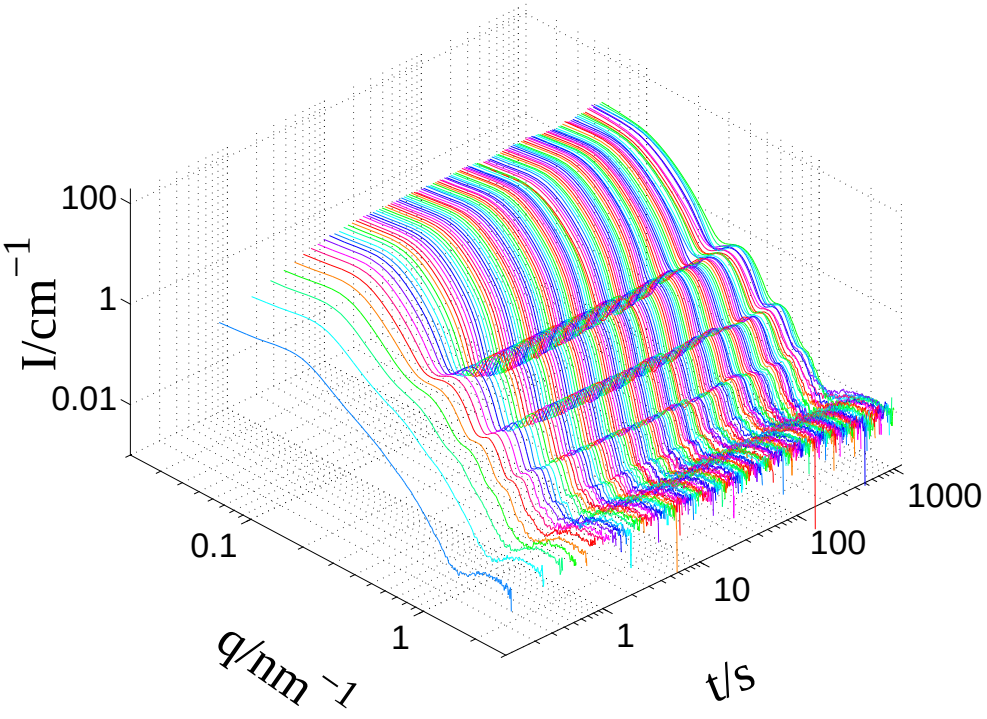

Figure 6.1.1: Evolution of the aggregates in the system TDMAO-LiPFOS (55:45)

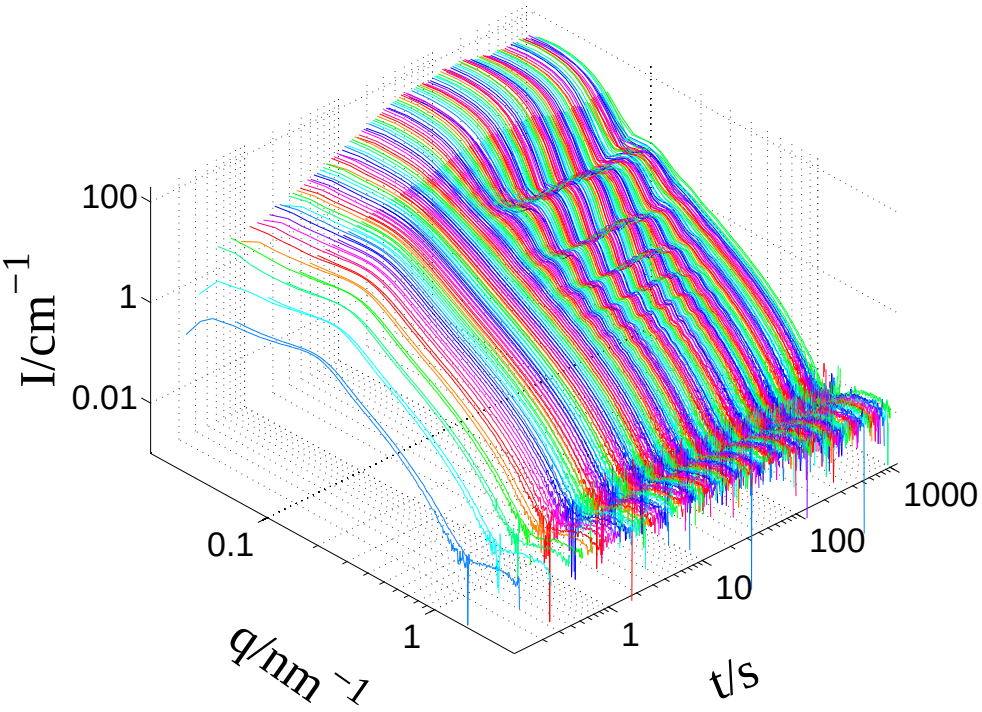

Figure 6.1.2: Evolution of the aggregates in the system TDMAO-LiPFOS (55:45) + 1 mol% Pluronic L35 (0.275mM) (here two measurements at two different configurations are plotted together, demonstrating very good reproducibility)

Pluronic L35 oscillation appear that can be identified with the formation of vesicles. This vesicle formation takes place when the first disc-like micelles reach the maximum radius and become unstable. With progressing time these oscillations become more pronounced as the fraction of vesicles in the mixture increases. The large number of higher order oscillations in the form factor indicates a very low polydispersity of about 5%. In the system without polymer the vesicles are formed with a radius of 10nm and in the presence of 1 mol% Pluronic L35 the initial vesicle radius is 35nm. That means not only the time for the vesicle formation but as well the initial size of the vesicles is influenced by the polymer content. The stopped-flow measurements show, that with increasing time the sharp oscillations in the scattering curve blur due to an increasing polydispersity and ageing processes of the vesicles. The time scale for the ageing processes exceeds the time scale of the stopped-flow SAXS measurements, but it was followed by time resolved DLS measurements.
Since a transformation from disc-like micelles to vesicles can be observed, the scattering intensity was modelled with a weighted sum of the scattering that arises from the micelles and the scattering that arises from the vesicles (see eqn (4.1.1)).

$$I = A \cdot I_{\text{micelles}} + (1 - A) \cdot I_{\text{vesicles}}$$

From these fits the volume fraction of scattering material that is in the micelles A and the volume fraction of scattering material that is in the vesicles $1 - A$ was determined. Thereby the average radius of the disc-like micelles R_{disc}, the mean vesicle radius $R_{\text{ves.}}$ and the polydispersity of the vesicles PDI can be described. These parameters are discussed in the following. The evolution of these parameters with the time allows us to draw conclusions about the mechanism of the micellar growth and about the vesicle formation.
The time dependent development of the disc size with the polymer content is shown in Fig. 6.1.3.
The fit parameter disc radius always follows the same development. It increases up to a maximum value where it was set constant. For polymer concentrations from 0-1mol% Pluronic L35 the disc size is similar for short times but the maximum disc size increases with increasing polymer content. That means the rate of the growth process does not change much but it stops later at larger sizes and the growth process is prolonged.
In the fit an average disc size was determined with a fixed standard deviation of the disc size of 10%. The aim is now to draw a conclusion from the size development and the kinetics about the mechanism of disc growth. If the discs grow by incorporating free surfactant monomers into the overall surface (assuming this is the rate determining step), then the rate for the disc growth would be proportional to the surface of the micelle:

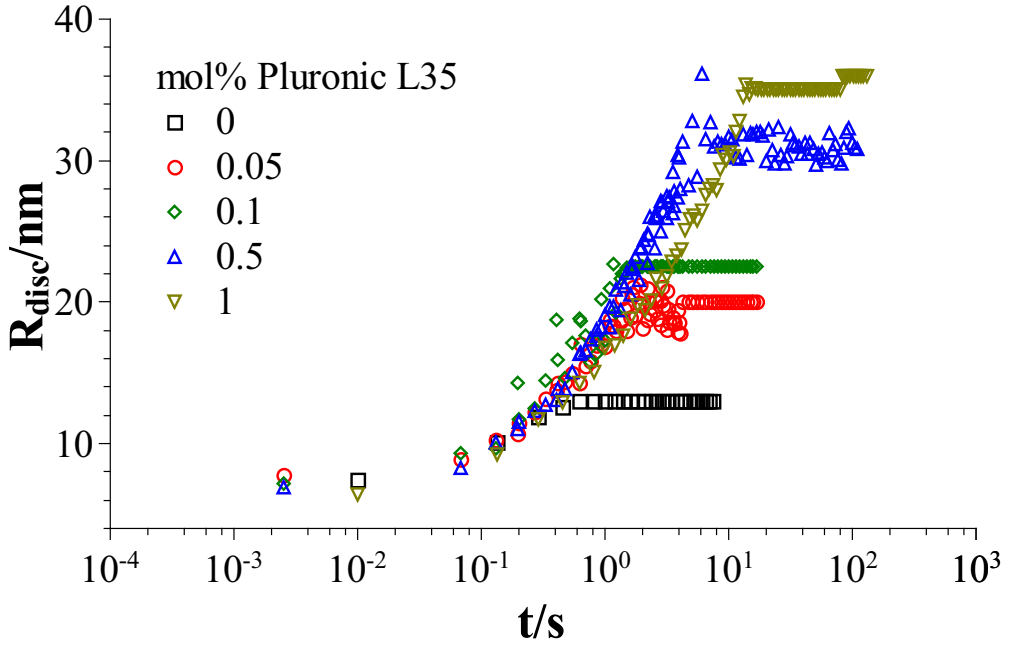

Figure 6.1.3: Time dependent development of the mean radius of the disc-like micelles R_{disc} with the molar percentage of Pluronic L35 with respect to the TDMAO concentration

$$\frac{dV(t)}{dt} = k \cdot \left(2\pi R_{\text{disc}}^2(t) + 2\pi R_{\text{disc}}(t) D\right) \tag{6.1.1}$$

$$2\pi D R \frac{R(t)}{dt} = k \cdot \left(2\pi R_{\text{disc}}^2(t) + 2\pi R_{\text{disc}}(t) D\right) \tag{6.1.2}$$

$$0 = R_{\text{disc}}(t) - \frac{D}{k}\frac{dR_{\text{disc}}(t)}{dt} + D \tag{6.1.3}$$

$$R_{\text{disc}}(t) = (R_{\text{disc},0} + D)\exp\left(\frac{k \cdot t}{D}\right) - D \tag{6.1.4}$$

Another possibility would be, that the surfactant monomer is only incorporated over the disc-rim:

$$\frac{dV(t)}{dt} = 2\pi k R_{\text{disc}}(t) \tag{6.1.5}$$

$$R_{\text{disc}}(t) = \frac{k}{D}t + R_{\text{disc},0} \tag{6.1.6}$$

In contrast to that mechanism, that is similar to an Ostwald ripening process, the micelles can as well grow by a micelle fusion process. In that case, if we assume no dependence of the energy barrier for the fusion on the disc radius, the growth is mainly controlled by the diffusion of the micelles. This kind of mechanism was described by von Smoluchowski [134]

and it was applied to a similar process by Shioi and Hatton.[132] The time dependent development of the Z-average of the disc radius R_Z can be described by eqn (6.1.7) with the radius of the smallest micelle R_0, the number density at the beginning N_0, the rate constant for the fusion K, that does not depend on the disc radius, and the time t.

$$R_Z = R_0 \sum_{n=1}^{\infty} \frac{(KN_0t)^{n-1}}{(1+KN_0t)^{n+1}} \cdot n^{5/2} \Bigg/ \sum_{n=1}^{\infty} \frac{(KN_0t)^{n-1}}{(1+KN_0t)^{n+1}} \cdot n^2 \tag{6.1.7}$$

This model for the fusion mechanism leads to a disc size distribution described in eqn (6.1.8) with n peaks at $R_n = \sqrt{n+1}R_0$.

$$N_n = N_0 \cdot \frac{(KN_0t)^{n-1}}{(1+KN_0t)^{n+1}} \tag{6.1.8}$$

In the present process we assume that there is a maximum disc radius, where disc-like micelles are stable, that is determined by the balance between the line tension of the discs and the bending energy of the corresponding vesicles. At this radius the discs close to form vesicles. That means that the sum to describe the mean disc radius and the sum to describe the size distribution can not be treated as an infinite sum but that there is a maximum n_{max} and therefore a maximum disc radius $R_{disc,max} = \sqrt{n_{max}} \cdot R_0$. From that maximum disc radius a minimum vesicle radius $R_{vesicle,min} = R_{disc,max}/2$ can be calculated. The Z-average of the mean disc radius is then described by eqn (6.1.9).

$$R_Z = R_0 \sum_{n=1}^{n_{max}} \frac{(KN_0t)^{n-1}}{(1+KN_0t)^{n+1}} \cdot n^{5/2} \Bigg/ \sum_{n=1}^{n_{max}} \frac{(KN_0t)^{n-1}}{(1+KN_0t)^{n+1}} \cdot n^2 \tag{6.1.9}$$

The mean disc radius achieved from the fits of the scattering data was compared to the predictions by the fusion model and by the models with Ostwald ripening (see Fig. 6.1.4). Comparison of the three models in Fig. 6.1.4 shows that the fusion model is the best model to describe the evolution of the disc radius. Eqn (6.1.9) can as well be described in terms of t_{disc} for the disc fusion (see eqn (6.1.10)). This time constant is the characteristic time for the fusion and for the growth process of the micelles. Since K is the kinetic constant for the fusion between two discs and N_0 is the particle number density at the beginning of the fusion process, t_{disc} describes the characteristic time for the whole ensemble to grow from R_0 to R_1. Since vesicles are formed, when a certain minimum radius is reached, this time also influences the time, when the vesicle formation starts. From the minimum disc radius R_0 and the upper limit for the sum n_{max} the maximum disc radius $R_{disc,max} = \sqrt{n_{max}} \cdot R_0$ and the theoretical minimum vesicle radius $R_{vesicle,min} = R_{disc,max}/2$ can be calculated.

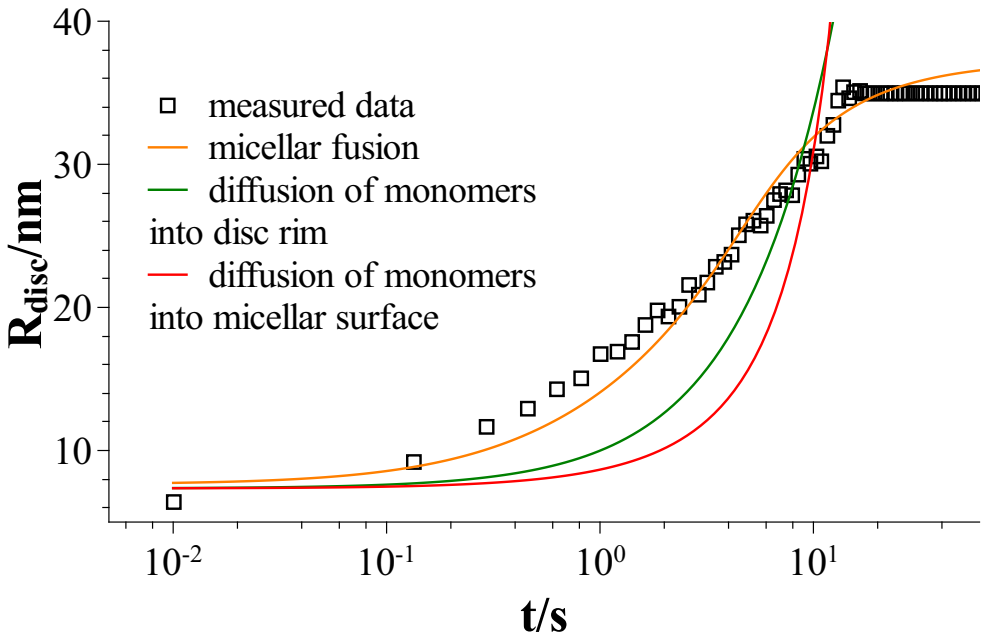

Figure 6.1.4: Comparison of the description of the time dependent evolution of the mean radius of disc-like micelles with predictions a) by a model for an Ostwald ripening process and monomer incorporation into the disc rim (green line), b) by a model for and Ostwald ripening process and monomer incorporation into the micellar surface (red line) and c) by a model that describes micellar fusion (yellow line) (mixture: TDMAO:LiPFOS (55:45) 50mM + 0.275mM Pluronic L35 (1mol% Pluronic L35))

$$R_Z = R_0 \sum_{n=1}^{n_{max}} \frac{\left(\frac{t}{t_{disc}}\right)^{n-1}}{\left(1+\frac{t}{t_{disc}}\right)^{n+1}} \cdot n^{5/2} \Bigg/ \sum_{n=1}^{n_{max}} \frac{\left(\frac{t}{t_{disc}}\right)^{n-1}}{\left(1+\frac{t}{t_{disc}}\right)^{n+1}} \cdot n^2 \qquad (6.1.10)$$

$$\text{with} \quad t_{disc} = \frac{1}{K \cdot N_0}$$

To gain an overall characteristic time for the micellar growth process, the development of the radius can as well be described with an exponential function given in eqn (6.1.11). This exponential function gives a characteristic time τ_{disc} for the overall growth process but is not linked to a mechanism for the growth process.

$$R_{disc} = R_{disc,E} - (R_{disc,E} - R_{disc,A}) \cdot \exp\left(\frac{-t}{\tau_{disc}}\right) \qquad (6.1.11)$$

The description of the measured parameters with the model for disc fusion results in the parameters listed in Table 6.1.1 and results in the listed predicted values for $R_{disc,max}$ and $R_{vesicle,min}$. τ_{disc} gives a characteristic time for the overall growth process.

Table 6.1.1: Parameters determined from the disc fusion model; minimum disc radius R_0, number of smallest discs in largest disc-like micelle $n_{\max}$, kinetic constant for the fusion process K, particle number density at the beginning of the aggregation process N_0, characteristic time for the aggregation process t_{disc}, predicted maximum disc radius $R_{\text{disc,max}}$, predicted minimum vesicle radius $R_{\text{vesicle,min}}$, distance between polymer molecules in disc rim of largest disc d_{pol}

mol% Pluronic L35	R_0/ nm	$n_{\max}$	K/ $(m^3 \cdot mol^{-1} \cdot s^{-1})$	N_0/ $(mol \cdot m^{-3})$	t_{disc}/ s	$R_{\text{disc,max}}$/ nm	$R_{\text{vesicle,min}}$/ nm	τ_{disc}/ s	d_{pol}/ nm
0	7.1	5	66.7	38.6	0.39	16.0	8.0	0.18	
0.05	7.8	9	60.5	32.5	0.51	23.3	11.7	0.55	43.8
0.1	7.3	16	72.1	37.2	0.37	29.0	14.5	0.58	17.6
0.5	6.9	32	49.2	40.7	0.50	39.3	19.6	1.73	2.6
1	8.7	25	22.1	26.2	1.73	43.3	21.6	5.33	1.2

The total length of the disc rim over all micelles in the solution decreases with time. At the beginning the length of the disc rim of the individual micelles is rather short but the number of micelles is much higher than at the end of the process. During the disc growth the number of micelles decreases and is proportional to R_{disc}^{-2} while the length of the disc rim for each individual micelle is proportional to R_{disc}. So the increase in the disc rim for each disc can not compensate for the decrease in the number of micelles and the overall length of the disc rim decreases. As a result the distance d_{pol} between the polymer molecules, that are incorporated into the disc rim, decreases with time and decrease as well with increasing polymer content from 44nm at 0.05mol% to 1nm at 1mol%. At low polymer content no interaction between the polymer molecules can be expected, while they are densely packed at high polymer contents. So quite likely at high polymer contents the polymer is not mainly situated in the disc rim but as well in the disc surface and in the solution. The given values are calculated for monodispers distributions for the given disc radius. In reality the size distributions are large at the end of the growth process. That means, that still many smaller micelles are present and as a result the distance between the polymers is smaller than calculated for a monodispers distribution.

Upon the formation of vesicles oscillations can be observed that arise from the form factor of the vesicles. These oscillations become more pronounced with increasing vesicle content. The parameter A is a measure for the conversion from micelles to vesicles. Fig. 6.1.5 shows the time dependent development of A.

The development of the parameter A shows an exponential decay with the time. That can be explained with the mechanism of vesicle formation, where each vesicle is formed from one disc-like micelle that has grown by fusion to a size beyond the maximum size stable for a disc-like micelle, and thereby spontaneously closing to form a vesicle. The parameter A then

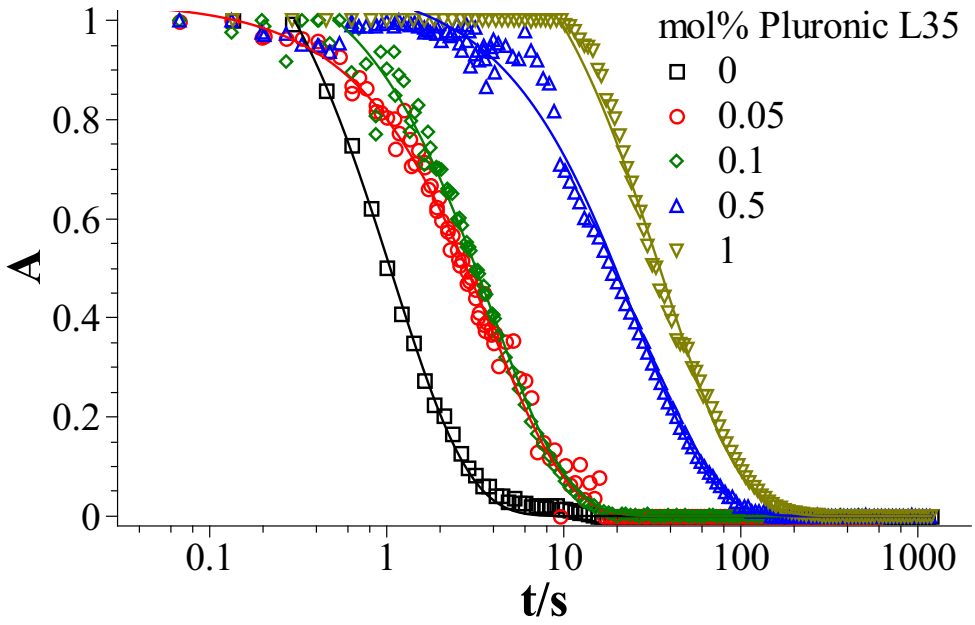

Figure 6.1.5: The parameter A represents the conversion of disc-like micelles to vesicles (mixture TDMAO:LiPFOS (55:45) 50mM + Pluronic L35, symbols are fit parameter to the SAXS data, lines are mono-exponential fits to the data points)

decreases in a monoexponential function with a characteristic decay time t_{vesicle}:

$$A(t) = \exp\left(\frac{-(t-t_0)}{t_{\text{vesicle}}}\right) \tag{6.1.12}$$

Fig. 6.1.6 shows that t_0 and τ_{disc} have a congruent behaviour. Since t_0 is the time when vesicle formation starts and τ_{disc} is the characteristic time for the overall disc growth process, this could be expected since vesicle formation can only start, when the first disc like micelles reach the cut-off radius. τ_{disc}, t_0 and t_{vesicle} all increase systematically and significantly with the polymer content. Since the disc growth is prolonged and vesicles are formed later τ_{disc} and t_0 are increased.

The characteristic time for the vesicle formation t_{vesicle} is equivalent to the closure time of the discs τ_c and is not related to τ_{disc} or t_0. According to Leng et al. the closure time from discs to vesicles τ_c depends on the energy barrier E_A and on the "Zimm time", which is the rotational diffusion of a disc in a viscous media. It is given in eqn (4.3.30). The free energy for a bend disc with the radius R_{disc} and a curvature $c = 1/R_{\text{disc}}$ can be described by eqn (4.3.14). The energy barrier E_A then results from the energy difference at zero curvature and at the energetic maximum (see eqn (4.3.26)). Since the maximum disc radius $R_{\text{disc,max}}$, the line tension λ and the bending rigidity $(2\kappa+\overline{\kappa})$ are related with $\lambda = 2(2\kappa+\overline{\kappa})/R_{\text{disc,max}}$ the energy barrier can be described by eqn (4.3.27). The energy barrier reduces to $E_A = \pi(2\kappa + \overline{\kappa})$,

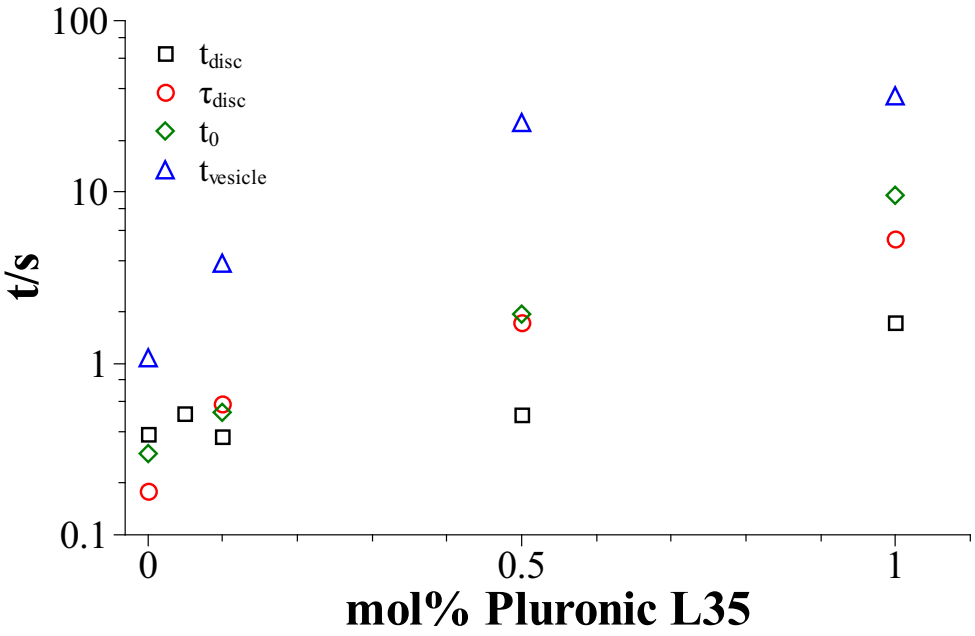

Figure 6.1.6: Characteristic time for the disc growth and the vesicle formation; t_{disc} is the characteristic time for the whole ensemble of micelles to grow from the initial radius R_0 to the next disc radius $R_1 = \sqrt{2}R_0$, τ_{disc} is the characteristic time for the overall disc growth process determined from a monoexponential fit to the disc radius, t_0 is the starting time for the vesicle formation and t_{vesicle} is the characteristic time for the vesicle formation process i.e. the characteristic time for the decay of A

when R_{disc} approaches $R_{\mathrm{disc,max}}$, so that the closure time τ_{c} is proportional to $R^3_{\mathrm{disc,max}}$ and as a result the characteristic time for the vesicle formation t_{vesicle} increases with $R^3_{\mathrm{disc,max}}$.
The size and polydispersity of the initially formed vesicles can be determined from the fit of the form factor of the vesicles (see Fig. 6.1.7). Here the minimum size of the vesicles determined from the vesicle form factor was compared to the minimum vesicle size, that was calculated from the maximum disc size in the micellar fusion model over $R_{\mathrm{vesicle,min}} = R_{\mathrm{disc,max}}/2$ (see Fig. 6.1.8).
Fig. 6.1.8 shows that the calculated vesicle radius is lower than the radius determined from the fit parameters under the assumption, that one disc forms one vesicle. If each vesicle was formed from two discs, than the ratio between the maximum disc radius and the minimum vesicle radius was $\sqrt{2}$. Similar results would be observed, if two large discs would fuse and then would immediately transform into vesicles. Under the assumption, that the fusion rate was independent from the disc size, this scenario would be unlikely, because then the size distribution would be broad. That would lead to a more continuous disc growth with a broad size distribution, where disc fusion between discs of different size was as likely as fusion

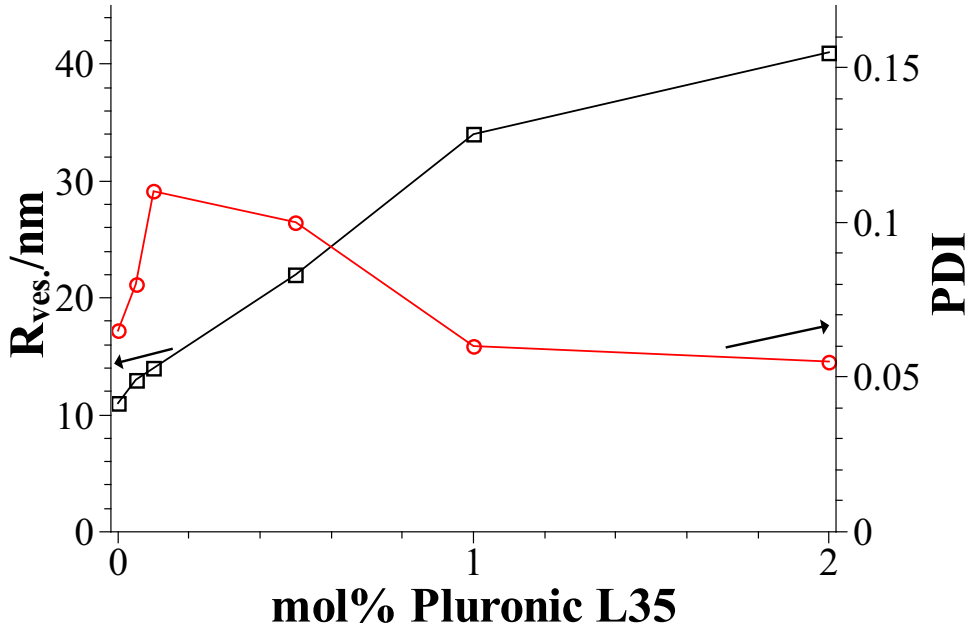

Figure 6.1.7: Initial vesicle radius $R_{\text{ves.}}$ (□) and initial polydispersity PDI (◯)

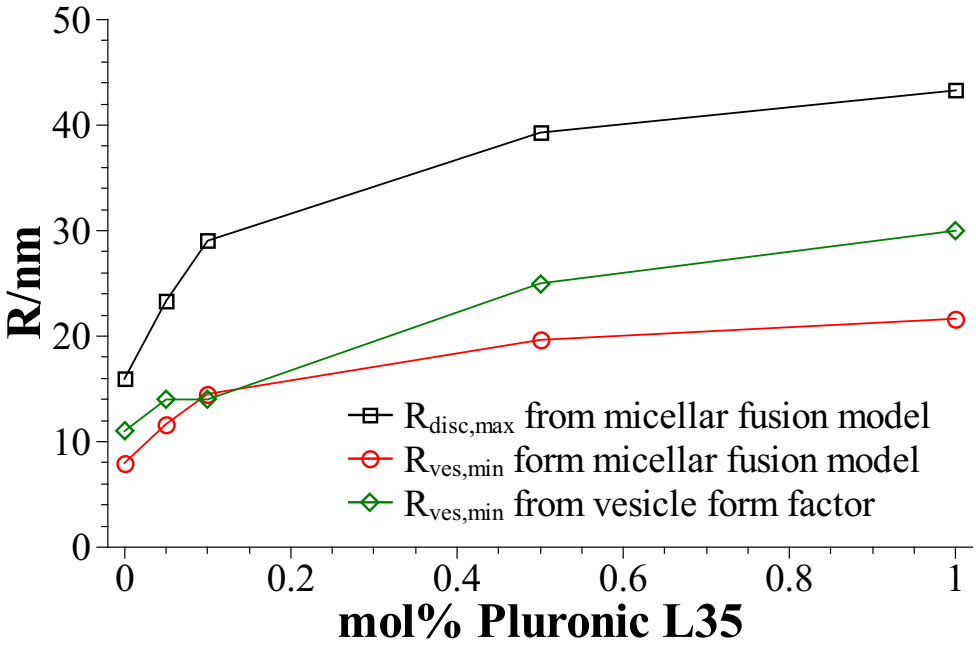

Figure 6.1.8: The maximum radius of the disc-like micelles R_{disc} as well as the minimum radius of the corresponding vesicles R_{vesicle} can be calculated form the micellar fusion model and can be compared to the minimum vesicle radius that was determined from the vesicle form factor (mixture: TDMAO:LiPFOS (55:45) 50mM + Pluronic L35)

between discs of equal size, in contrast to a more step-wise mechanism with a narrow size distribution, where the fusion rate was the higher the smaller the discs were. In the later case small discs would disappear faster and in the end fusion between large discs, would be more likely. Fig. 6.1.9 shows the minimal vesicle radius calculated from $R_{\text{vesicle,min}} = R_{\text{disc,max}}/\sqrt{2}$, $R_{\text{disc,max}}$ determined from the disc fusion model and the vesicle radius $R_{\text{vesicle,min}}$ determined from the SAXS fits. Here the vesicle radius determined from the disc fusion model and from SAXS fits are in good agreement. Table 6.1.2 shows the values for the vesicle radius calculated with $R_{\text{vesicle,min}} = R_{\text{disc,max}}/\sqrt{2}$.

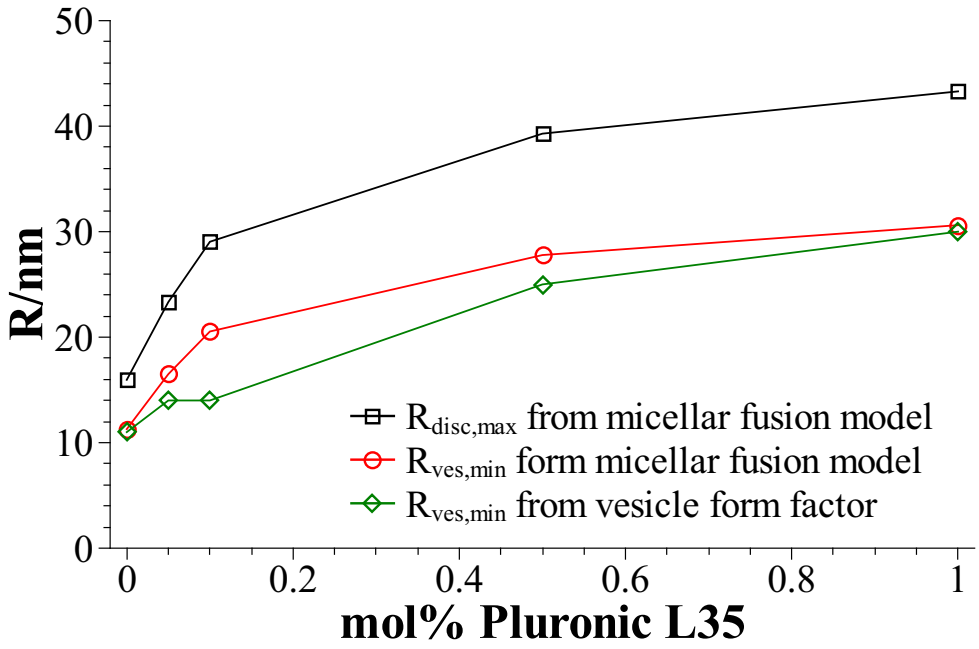

Figure 6.1.9: The maximum radius of the disc-like micelles R_{disc} as well as the minimum radius of the corresponding vesicles R_{vesicle} can be calculated form the micellar fusion model and can be compared to the minimum vesicle radius that was determined from the vesicle form factor (mixture: TDMAO:LiPFOS (55:45) 50mM + Pluronic L35)

6.2 Surface Dilatational Rheology

Since the initial size is influence by the bending energy of the bilayer, the mechanic properties of the bilayer are quite important. The dilatational rheological properties of the corresponding monolayer can be determined by oscillatory measurements in a pendant drop tensiometer (see section 10.1.9). They describe the interaction forces within an adsorption layer at the surface of a pendant drop. These measurements were performed in dependence on the molar percentage of Pluronic L35 with respect to the TDMAO concentration.

Table 6.1.2: The disc fusion model gives the minimum disc radius $R_{\text{disc,min.}}$, the maximum disc radius $R_{\text{disc,max.}}$, and the characteristic time for the disc fusion t_{disc}. The minimum vesicle radius $R_{\text{ves.,min.}}$ can be predicted from the maximum disc radius obtained from the disc fusion model and from the form factor at the moment of vesicle formation. t_{vesicle} is the characteristic time for the transformation from micelles to vesicles. (mixture: TDMAO:LiPFOS (55:45) 50mM + Pluronic L35)

	from disc fusion model				from form factor		
c(Pluronic L35) /mol%	$R_{\text{disc,min.}}$ /nm	$R_{\text{disc,max.}}$ /nm	$R_{\text{ves.,min.}}$ /nm	t_{disc} /s	$R_{\text{ves.,min.}}$ /nm	t_{vesicle} /s	$(2\kappa+\overline{\kappa})/\lambda$ /nm
0.00	7.1	16.0	11.3	0.39	11	1.1	4
0.05	7.8	23.3	16.5	0.51	14	3.9	5.8
0.10	7.3	29.0	20.5	0.37	14	3.8	7.3
0.50	6.9	39.3	27.8	0.50	25	25.4	9.8
1.00	8.7	43.3	30.4	1.73	30	36.5	10.8

Figs. 6.2.1 and 6.2.2 show the viscous modulus $\Im(E)$ and the elastic modulus $\Re(E)$ in dependence on the oscillatory frequency f. Both values decrease systematically with the polymer content, where the decrease is more pronounced for the elastic modulus. Frømyr et al. describe the dependence of the elastic and the viscous modulus on the oscillatory frequency f or the angular frequency $\omega = 2\pi f$ for two types of processes. If diffusion of surface active components between the bulk and the surface is the main process, that takes place during the volume and surface changes of the droplet, than the elastic modulus should be higher than the viscous modulus. That is not the case in the performed measurements. So it can be expected that reorganisation within the membrane is the dominating process.

The surface dilatational modulus $E^{\star}$ depends on the phase angle δ (eqn (6.2.2)).

$$E^{\star} = \Re(E) + i\Im(E) \tag{6.2.1}$$

$$= |E| \cdot \cos(\delta) + i|E| sin(\delta) \tag{6.2.2}$$

For a process during the surface oscillation of the droplet, where diffusion of surface active components between bulk and droplet surface have to be taken into account as well as reorganisation processes within the surface, the surface dilatational modulus can be described by eqn (6.2.3).

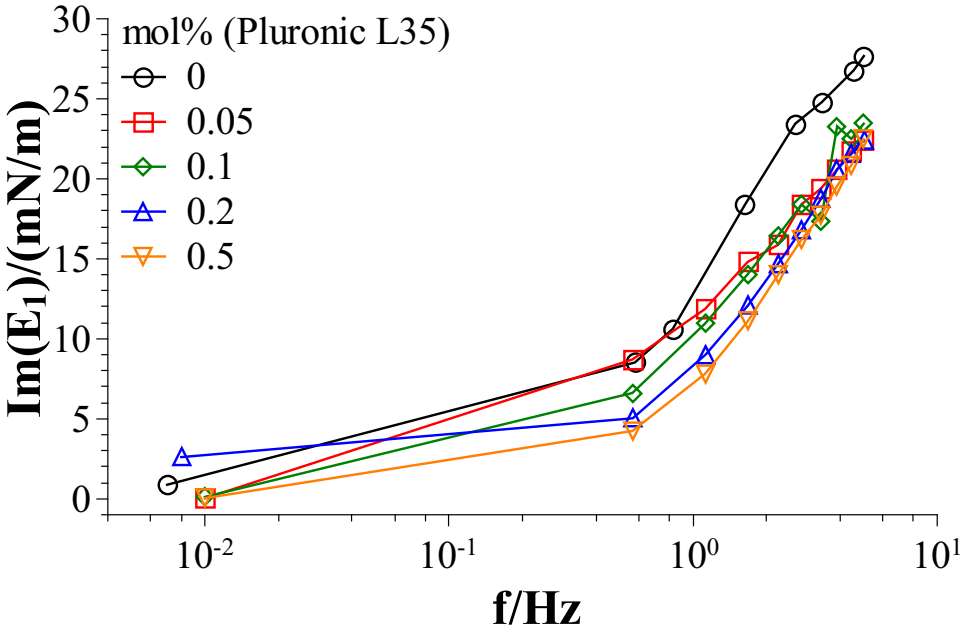

Figure 6.2.1: Viscous modulus $\Im(E)$ in dependence on the excitational frequency ω and the polymer content in mol% with respect to the TDMAO concentration

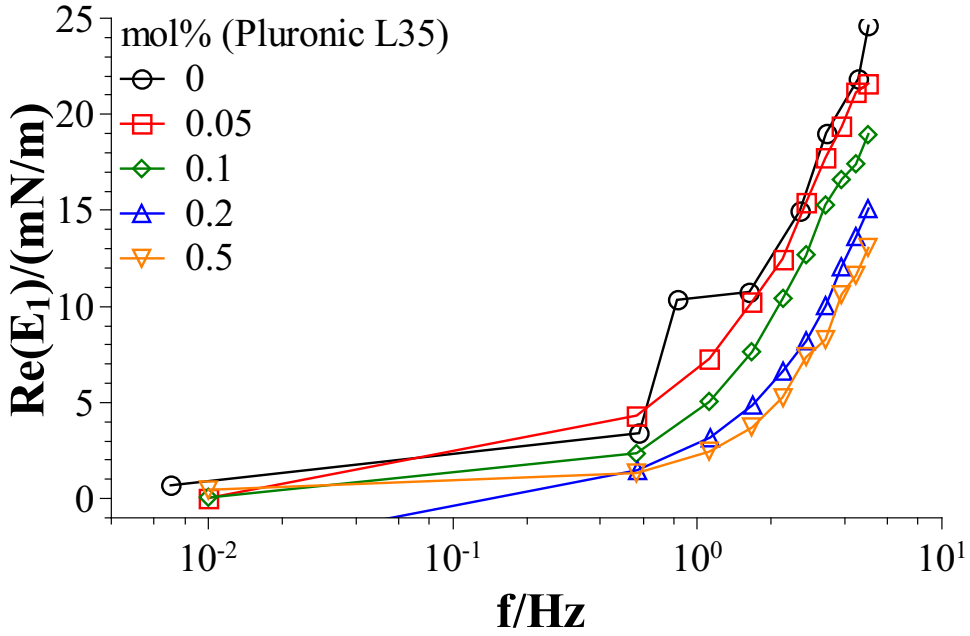

Figure 6.2.2: Elastic modulus $\Re(E)$ in dependence on the excitational frequency ω and the polymer content in mol% with respect to the TDMAO concentration

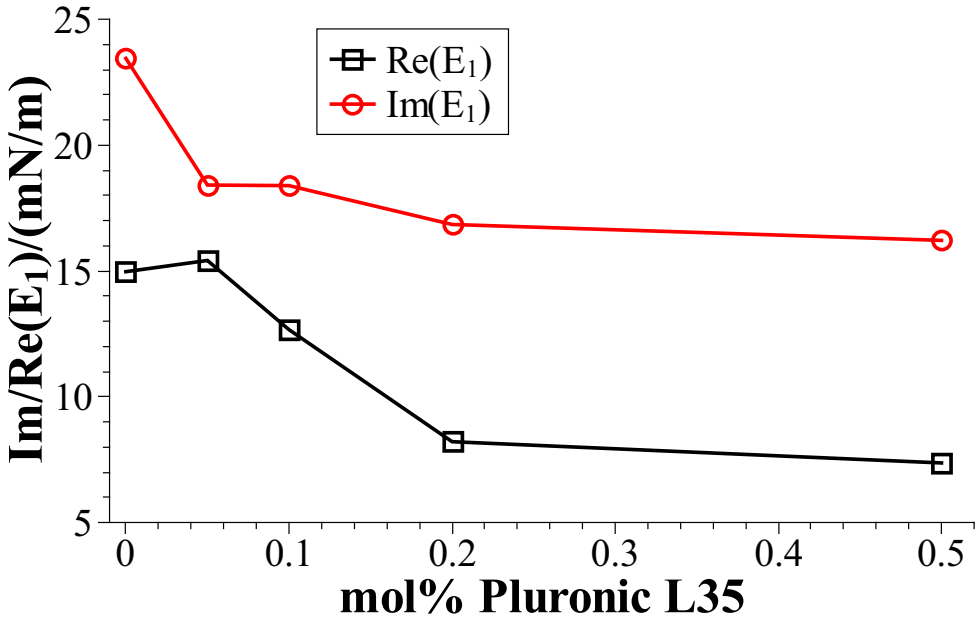

Figure 6.2.3: Elastic modulus $\Re(E)$ and viscous modulus $\Im(E)$ in dependence on the polymer content at a fixed frequency of $\omega = 2.8$ 1/s

$$E^{\star} = E_0 \cdot \frac{1 + \xi + i \cdot \left(\xi + \left(\frac{\omega\chi}{E_0} \right)^2 (1 + 2\xi + 2\xi^2)^2 \right)}{1 + 2\xi + 2\xi^2} \tag{6.2.3}$$

with
$$|E| = E_0 \sqrt{\frac{1 + 2\xi \left(\frac{\omega\chi}{E_0} \right)^2 (1 + 2\xi + 2\xi^2)}{1 + 2\xi + 2\xi^2}} \tag{6.2.4}$$

and
$$\tan(\delta) = \frac{\xi}{1 + \xi} + \frac{\omega_0 \chi}{E_0} \cdot \frac{1 + 2\xi + 2\xi^2}{\xi^2 (1 + \xi)} \tag{6.2.5}$$

The dimensionless value ξ is described by the angular frequency ω and the characteristic angular frequency ω_0 by $\xi = \omega/\omega_0$. χ is the surface dilatational viscosity and E_0 is the elastic modulus in equilibrium and therefore constitutes an upper limit for $E^{\star}$ at high frequencies. The elastic and the viscous modulus were then fitted simultaneously according to $\Re(E) = |E| \cos(\delta)$ and $\Im(E) = |E| \sin(\delta)$. Data plots and fits are shown in Figs. 6.2.4 to 6.2.8. The elastic modulus is always lower than the viscous modulus and the elastic modulus decreases relatively to the viscous modulus with increasing polymer content. According to theory the viscous modulus crosses the elastic modulus at ω_0. The performed measurements are always in an angular frequency area below ω_0 and measurements with 1 mol% Pluronic L35 did not show enough characteristic features in the accessible frequency region to be analysed, so that the series ends at 0.5 mol%.

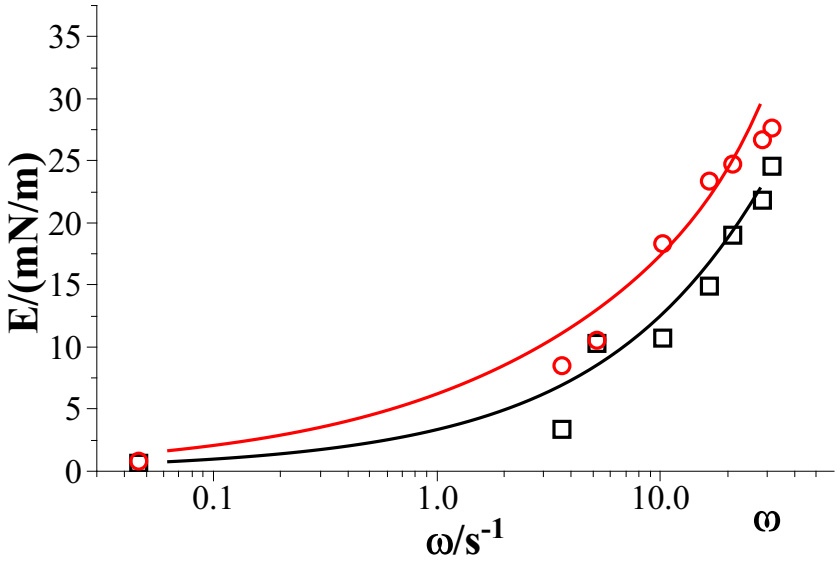

Figure 6.2.4: Elastic modulus $\Re(E)$ (black squares: data and black line: fit) and viscous modulus $\Im(E)$ (red circles: data and red line: fit), mixture TDMAO:LiPFOS (55:45) 50mM

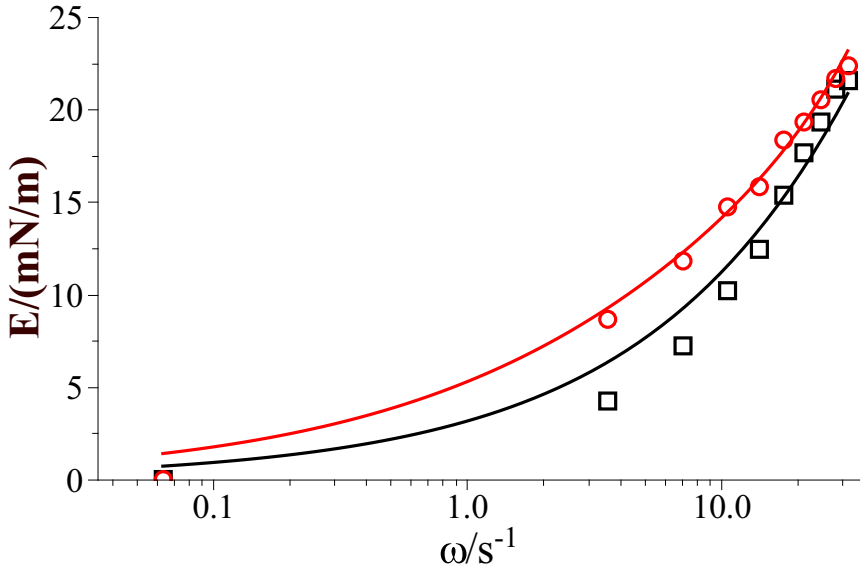

Figure 6.2.5: Elastic modulus $\Re(E)$ (black squares: data and black line: fit) and viscous modulus $\Im(E)$ (red circles: data and red line: fit), mixture TDMAO:LiPFOS (55:45) 50mM + 0.01375mM Pluronic L35 (0.05 mol%)

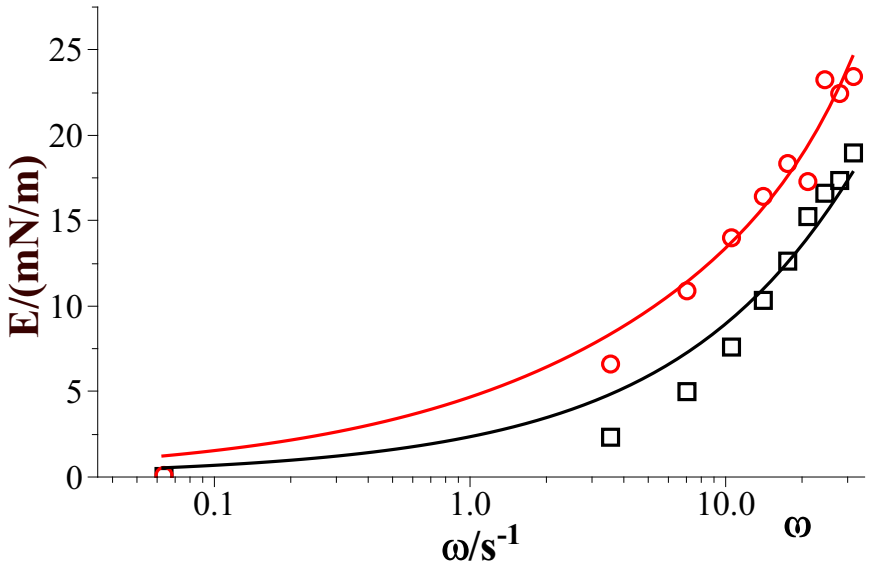

Figure 6.2.6: Elastic modulus $\Re(E)$ (black squares: data and black line: fit) and viscous modulus $\Im(E)$ (red circles: data and red line: fit), mixture TDMAO:LiPFOS (55:45) 50mM + 0.0275mM Pluronic L35 (0.1 mol%)

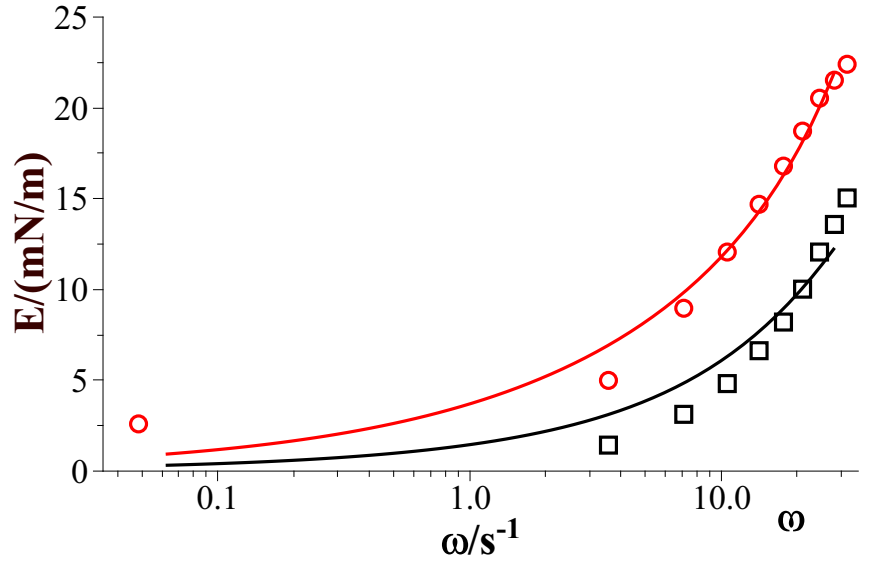

Figure 6.2.7: Elastic modulus $\Re(E)$ (black squares: data and black line: fit) and viscous modulus $\Im(E)$ (red circles: data and red line: fit), mixture TDMAO:LiPFOS (55:45) 50mM + 0.055mM Pluronic L35 (0.2 mol%)

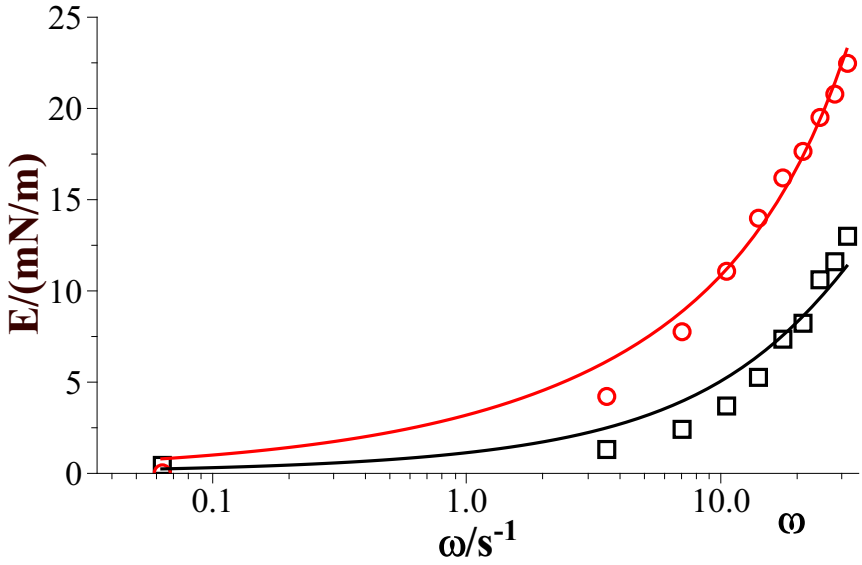

Figure 6.2.8: Elastic modulus $\Re(E)$ (black squares: data and black line: fit) and viscous modulus $\Im(E)$ (red circles: data and red line: fit), mixture TDMAO:LiPFOS (55:45) 50mM + 0.1375mM Pluronic L35 (0.5 mol%)

The fit parameters E_0, ω_0, χ and a characteristic time t determined from ω_0 in dependence on the polymer content are shown in Figs. 6.2.9 and 6.2.10. ω_0, χ and t show no characteristic changes with the polymer content, while E_0 decreases systematically with polymer content. This shows that mainly the elastic properties of the surfactant/polymer layer change while the viscous properties remain constant. That means the layer softens probably due to decreasing surfactant interactions. The polymer, when incorporated into the surfactant layer, decreases the head group interactions.
As a result it can be expected that as well the bending energy of a surfactant bilayer is decreased and that the initial vesicle radius of vesicles formed from disc-like micelles as described above is not only controlled by the decrease in the micellar line-tension but as well by the decrease in the bending energy.

In section 5 the membrane rigidity was determined with $2\kappa + \overline{\kappa} = (3 \pm 1)k_{\mathrm{B}}T$ for the system 27.5mM TDMAO and 22.5mM LiPFOS. The measurements of the elastic properties of the surface suggest, that it is weakened by the polymer. Now we assume that the bending rigidity decreases to the same extent in percentage as the elastic modulus of the membrane according to $2\kappa + \overline{\kappa} = 3k_{\mathrm{B}}T \cdot E_0(c(\text{Pluronic L35}))/E_0(c(\text{Pluronic L35}) = 0)$. Table 6.1.1 gives the maximum radius of the disc-like micelles as determined from the disc fusion model. From the calculated bending rigidity and the maximum disc radius the line tension of the disc rim can be calculated according to eqn (4.3.24). Fig. 6.2.11 shows the modified bending rigidity and the line tension calculated via eqn (4.3.24) from a constant bending rigidity

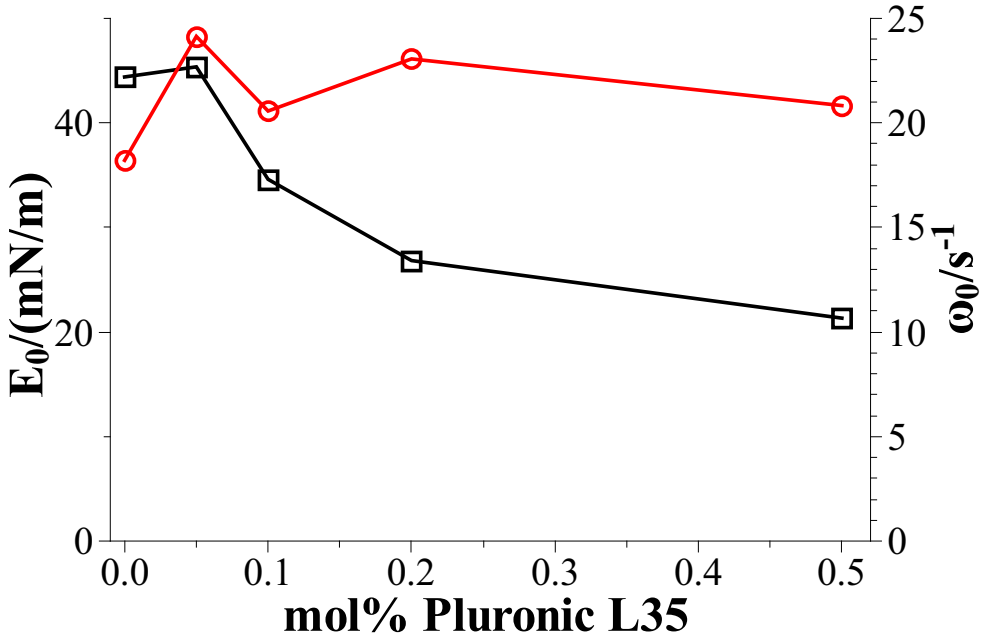

Figure 6.2.9: Elastic modulus in equilibrium E_0 (□) and characteristic angular frequency ω_0 (◯) in dependence on the Pluronic L35 content

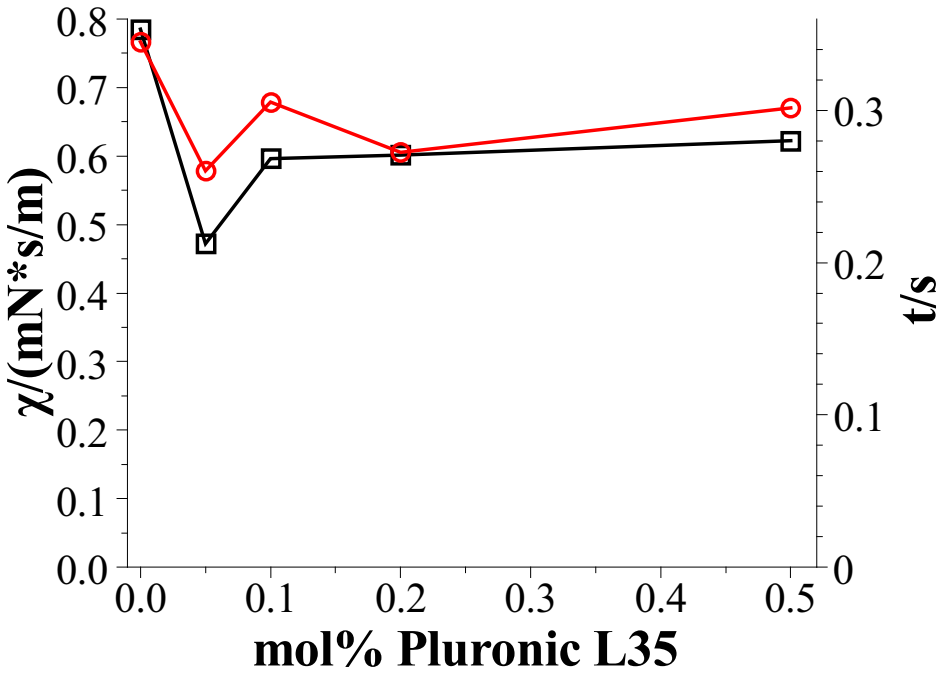

Figure 6.2.10: Surface dilatational viscosity χ (□) and characteristic time t (◯) in dependence on the Pluronic L35 content

with $2\kappa+\overline{\kappa} = (3\pm1)k_BT$ and from the modified bending rigidity. Since the bending rigidity decreases with increasing polymer content, it can be assumed that the polymer effect on the line tension is even more pronounced as it could be assumed from a constant bending elasticity and from the determined maximum disc radius. While the polymer concentration in the rim of the disc-like micelles increases during the growth process, the line tension decreases at the same time. The line tension determined here is the line tension at the end of the growth process.

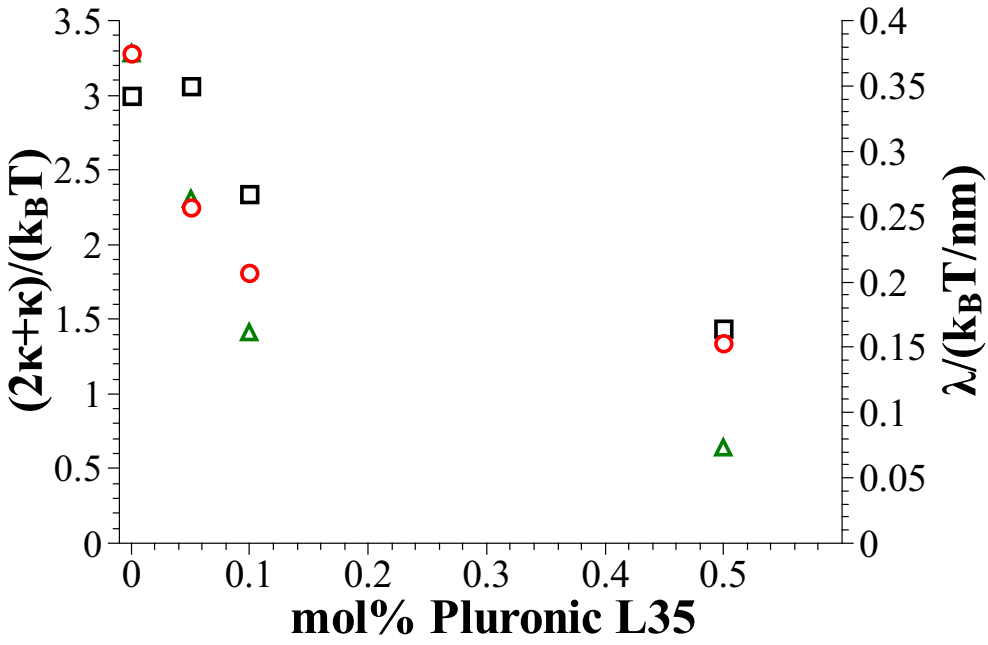

Figure 6.2.11: Modified values for $2\kappa+\overline{\kappa}$ (□), line tension λ calculated from a constant $2\kappa+\overline{\kappa} = (3\pm1)k_BT$ (◯) and line tension λ calculated from the modified values for $2\kappa+\overline{\kappa}$ (△) in dependence on the Pluronic L35 content with respect to the TDMAO concentration in a system with TDMAO-LiPFOS (55:45), 50mM, 25°C

6.3 Stabilisation of Vesicles against Ageing

By Dynamic Light Scattering (DLS) we recorded the time dependent development of the average hydrodynamic radius of all aggregates in the sample (Fig. 6.3.1). The samples were ones prepared by the stopped-flow technique and in addition by mixing adequate volumes of both surfactant solutions by hand to achieve a good time resolution and to cover a wide time range. In these measurements we see a sum of the scattering that arises from the disc-like micelles and the scattering that arises from the vesicles and we can not distinguish between both contributions. As a result for the higher polymer contents the scattering is mostly dominated by the scattering of the micelles during the first 60s. Directly after the vesicle

formation, we can observe a plateau in the development of the hydrodynamic radius R_h with the time. For polymer contents larger than 0.5mol% Pluronic L35 this plateau exceeds the experiment time (which is already longer than 10 days). The aggregates in these mixtures are long-time stabilised by the addition of polymer. If the polymer content is lower, a subsequent increase in the hydrodynamic radius is observed. The increase of the hydrodynamic radius is the less and the slower the higher the the polymer content is.

A probable reason for the stabilisation is that the polymer is incorporated into the vesicle membrane with its hydrophobic part and that the hydrophilic parts cover the vesicle like hairs. This would lead to a repulsion between the vesicles due to steric interactions between the polymers. In that way fusion processes can be slowed down and kinetic stabilisation of the vesicle size can be achieved.

As a result we can say, that the addition of polymers of the Pluronic type can not only control the kinetics and size of the polymers, but higher polymer contents can as well stabilise the vesicles for many days compared to the situation without added polymer, where ageing occurs already after a few minutes.

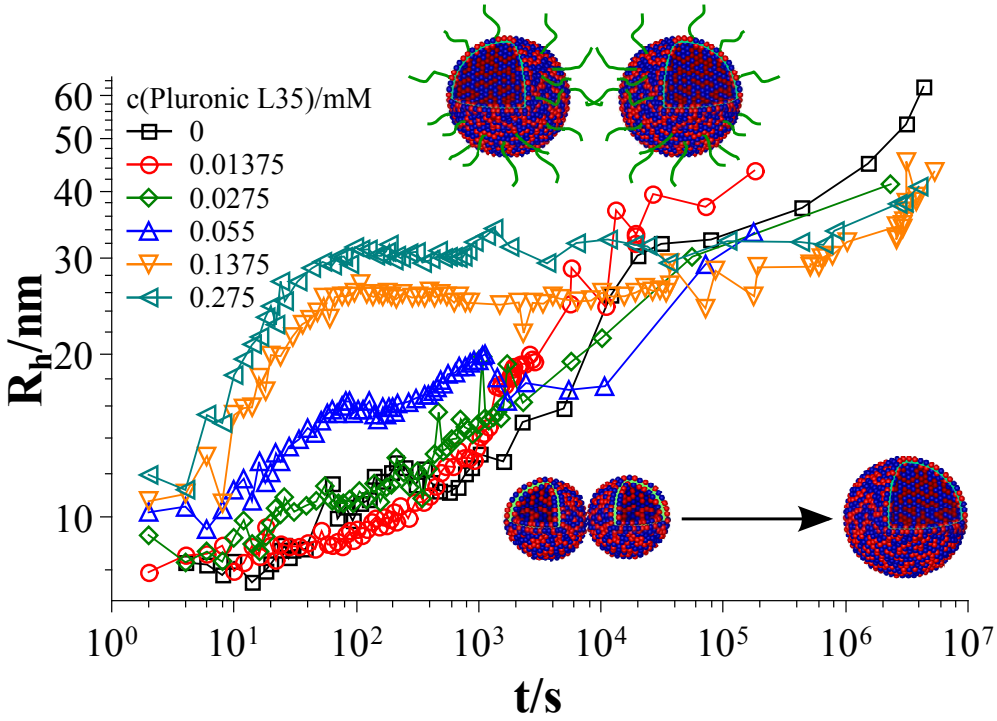

Figure 6.3.1: Time dependent development of the average hydrodynamic radius R_h (mixture: TDMAO:LiPFOS (55:45) 50mM + Pluronic L35)

Influence of the Polymer Architecture

Section 6 showed that adding a polymer to the surfactant mixture TDMAO-LiPFOS during the vesicle formation process influences the process and in the end the resulting structures. The growth process of the micellar discs as well as the vesicle formation process are significantly slowed down where the effect is the stronger the higher the polymer concentration. Since the effect can be seen during the formation process, it can be assumed that the observed polymer effect is not primarily due to thermodynamic reasons but due to the kinetic process. As presumed in section 6 the polymer effects the vesicle formation process by incorporating into the disc rim of intermediately formed disc-like micelles and thereby changes the kinetics. From these findings it can be assumed that the ability of the polymer to incorporate into the disc-rim has to have an effect on the kinetics and the end products as well. For that reason the vesicle formation process was followed with different polymers of the Pluronic type in order to see the relevance of the polymer architecture for the process of vesicle formation.

7.1 Pluronic L35 versus Pluronic 10R5

A comparison of Pluronic L35 and Pluronic 10R5 shows the effect of the architecture of the polymer. Both polymers have the same number of PO and EO units, but while Pluronic L35 has a hydrophobic core and two hydrophilic chains, in the case of Pluronic 10R5 this architecture is reversed. Pluronic L35 has the average structure $EO_{11}-PO_{16}-EO_{11}$ and Pluronic 10R5 has the average structure $PO_8-EO_{22}-PO_8$. For the Pluronic L35 the length of the stretched hydrophobic part is about 6nm. This is close to the thickness of the vesicle bilayer of 3.2nm so that the polymer can be incorporated into the bilayer. A stretched length of 3nm for Pluronic 10R5 is too short to cover the whole disc thickness but the hydrophobic part fits into the bilayer anyway. It can be expected that Pluronic 10R5 works as good as Pluronic L35.

In a concentration dependent series a LiPFOS solution was mixed in the stopped-flow with a TDMAO solution with varying polymer content. The total surfactant concentration in the mixture was 50mM and the ratio between TDMAO and LiPFOS was 55:45 since this ratio provided very monodisperse vesicles in the solution as described in section 4. The stopped-flow device was combined with DLS to monitor the time dependent hydrodynamic radius.

Figs. 7.1.1 and 7.1.2 show the time dependent development of aggregates in the systems TDMAO-LiPFOS + Pluronic L35 and TDMAO-LiPFOS + Pluronic 10R5 for different polymer concentrations. Both systems show an increase of the hydrodynamic radius with the polymer content as already described in section 6 and for both systems the hydrodynamic

radius increases shortly after mixing and reaches a plateau after about 100s for polymer contents of 0.5-2 mol% with respect to the TDMAO content. That means for polymer contents of 0.5-2 mol% the expected vesicles can be stabilised by the polymer. For Pluronic L35 the vesicle radius stays constant for a period of about 12d while for Pluronic 10R5 after reaching the plateau still a slight increase of the vesicle radius can be observed, i.e., the long term stability is somewhat reduced.

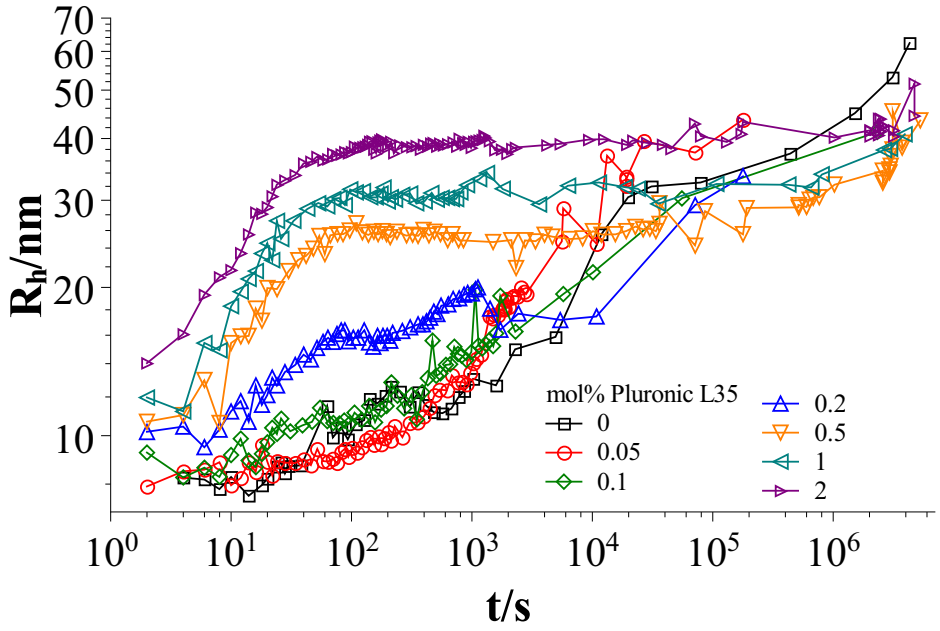

Figure 7.1.1: Time dependent hydrodynamic radius R_h in the system TDMAO-LiPFOS + Pluronic L35

Fig. 7.1.3 shows the hydrodynamic radius of the aggregates in solution for all polymer contents after 100s where the plateau region begins for polymer contents of 0.5-2 mol%. In the graph two regions can be observed. In the area for a polymer content <0.5 mol% the slope is steeper than in the area 0.5-2 mol%. The first area is the area where fast ageing can be observed while the vesicles in the second area stay stable for about 12d. In total it can be observed that Pluronic L35 and Pluronic 10R5 show no significant difference in their behaviour. While having the same polymer content and the same number of monomer units the architecture does not seem to have an influence on the particle size and the stabilisation.

7.2 Pluronic L35 versus Pluronic F38

The two polymers Pluronic L35 and Pluronic F38 have the same architecture and the same length for the PPO block of 16 monomer units but with 46 EO units on each side the

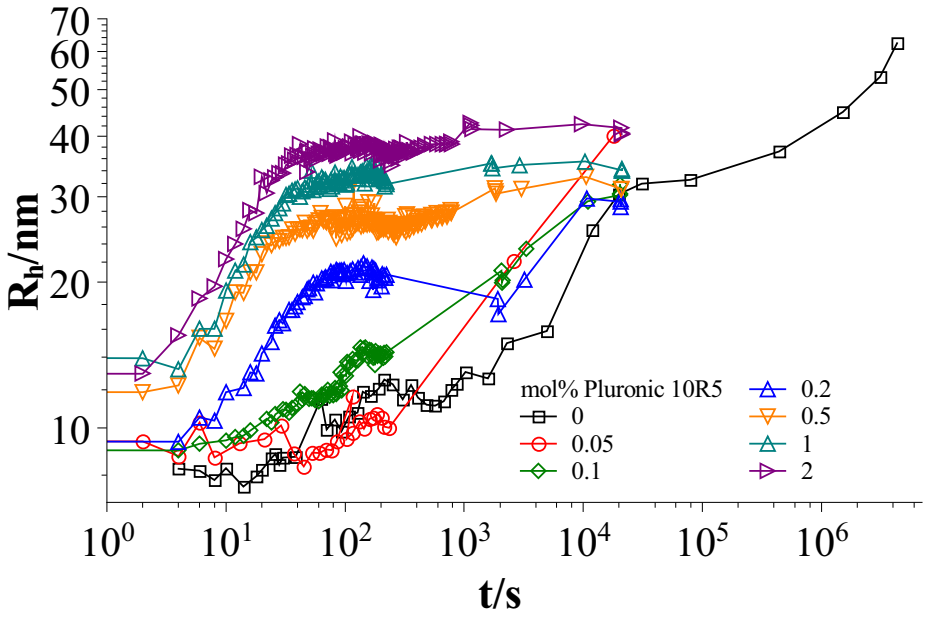

Figure 7.1.2: Time dependent hydrodynamic radius R_h in the system TDMAO-LiPFOS + Pluronic 10R5

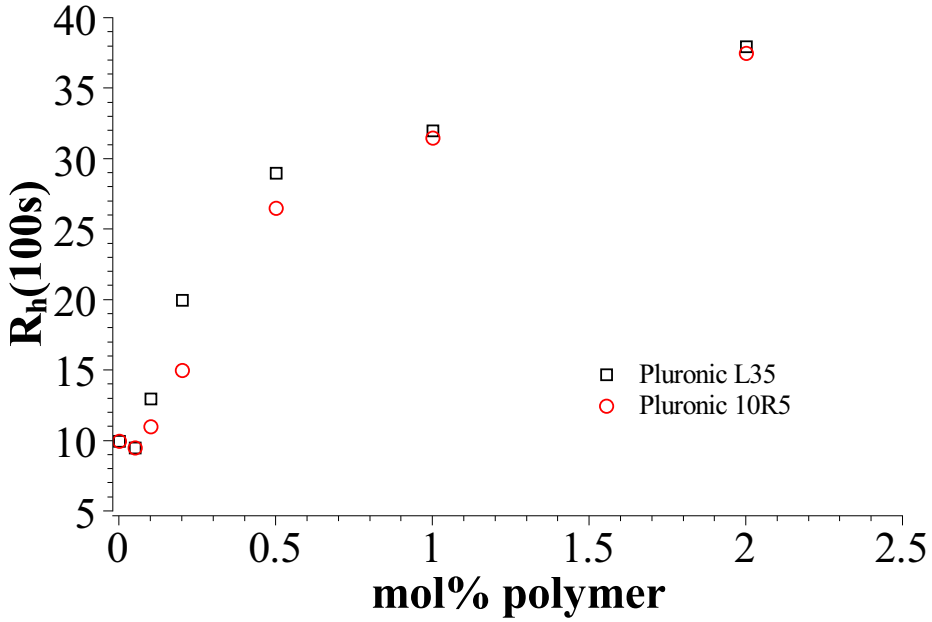

Figure 7.1.3: Hydrodynamic radius at 100s in dependence on the polymer content

hydrophilic part of the Pluronic F38 is significantly longer.
In a stopped-flow device a TDMAO/polymer solution was mixed with a LiPFOS solution and the evolution of the system was followed by SAXS measurements. The total surfactant concentration was 50mM and the TDMAO:LiPFOS ratio was 55:45.
The overall behaviour that can be observed during the vesicle formation process is similar to that observed with Pluronic L35 so we can compare the characteristic times derived from SAXS-stopped-flow measurements as already described in section 6.1 in both systems and as well the maximum sizes for the disc like micelles and the initial vesicle sizes.

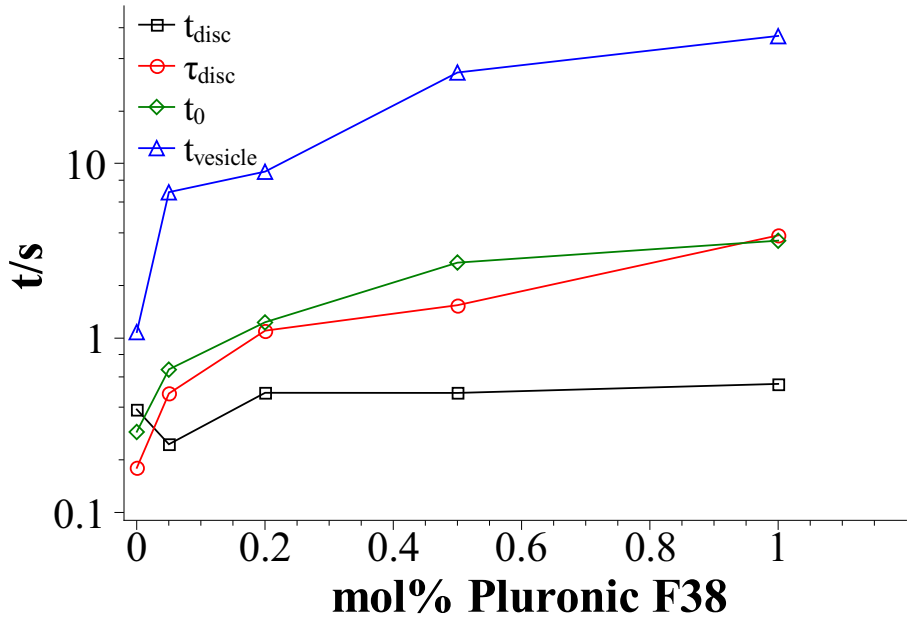

Figure 7.2.1: Characteristic time in the system TDMAO-LiPFOS + Pluronic F38

Fig. 7.2.1 shows again like in Fig. 6.1.6 a short time t_{disc} for a disc growth step from R_0 to R_1 which is significantly lower than the characteristic time of the overall micellar growth process τ_{disc} and a starting time for the vesicle formation t_0 that is very similar to τ_{disc} but slightly larger. The time for vesicle formation is by an order of magnitude larger than the time for the disc growth and slightly larger than in the system TDMAO-LiPFOS + Pluronic L35 (see Fig. 7.2.4).
t_{disc} is the characteristic time that describes the disappearance of the initial disc-like micelles and for a micellar fusion process the characteristic time for the fusion of two micelles is independent of their size as proposed by the model described in eqn (6.1.7). This time constant does not describe the overall growth process because the characteristic time for the overall process depends on the cut-off radius and the number of growth steps before this cut-off radius is reached. This value is independent of the polymer content.

The characteristic time for the overall disc growth process τ_{disc} shows a clear dependence on the polymer content. There is no difference in the time for the disc fusion process but due to the decreasing line tension the cut-of radius for the disc size increases. The growth process includes more steps and the discs grow longer to larger sizes and as a result the overall time τ_{disc} is larger. We see a close correlation between the initial time for vesicle formation t_0 and τ_{disc}. This confirms again the assumption that vesicles are formed when a certain cut-off radius is reached and since τ_{disc} is linked to the cut-off radius over the number of growing steps τ_{disc} is as well correlated to t_0.

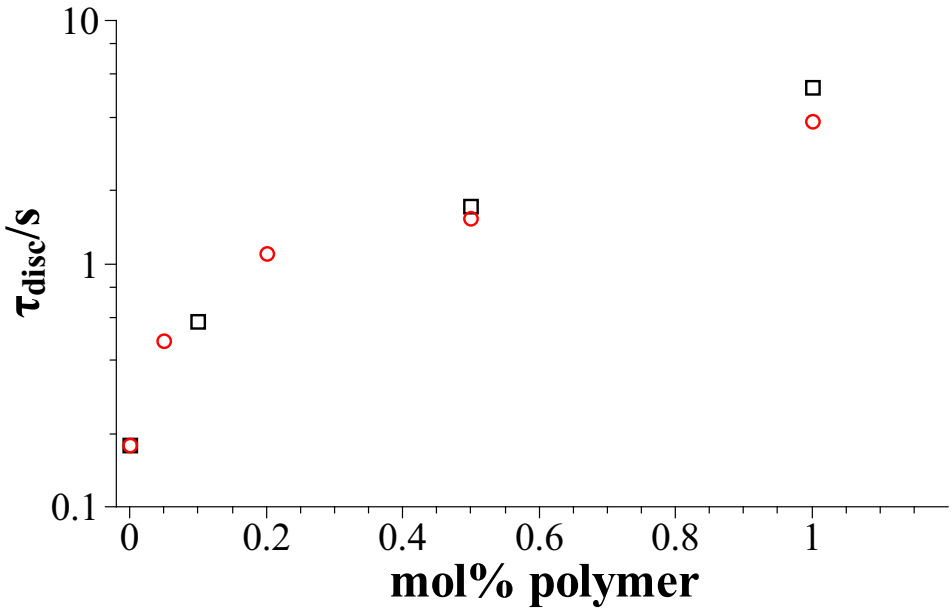

Figure 7.2.2: Characteristic time for the overall disc growth process in the systems TDMAO-LiPFOS + Pluronic L35 (□) and TDMAO-LiPFOS + Pluronic F38 (◯)

Fig. 7.2.2 compares the characteristic time for the overall disc growth process in the system with Pluronic L35 and Pluronic F38. In both systems the times are very similar which leads to the conclusion, that the decrease in the line tension is the same for Pluronic L35 and Pluronic F38 and as a result the initial vesicle radii derived from SAXS and DLS experiments are as well similar (see Fig. 7.2.3). This is not surprising since the hydrophobic parts in both polymers are the same and in the proposed mechanism the hydrophobic part of the polymer is supposed to be responsible for the decrease in the line tension.

The time for the vesicle formation is by an order of magnitude larger than τ_{disc} and t_0. t_{vesicle} increases strongly with the polymer content and is even higher than in the system with Pluronic L35 (see Fig. 7.2.4). The vesicle formation time is related to the closing time of the discs as described in section 4 by eqn (4.3.30). According to eqn (4.3.29) the activation

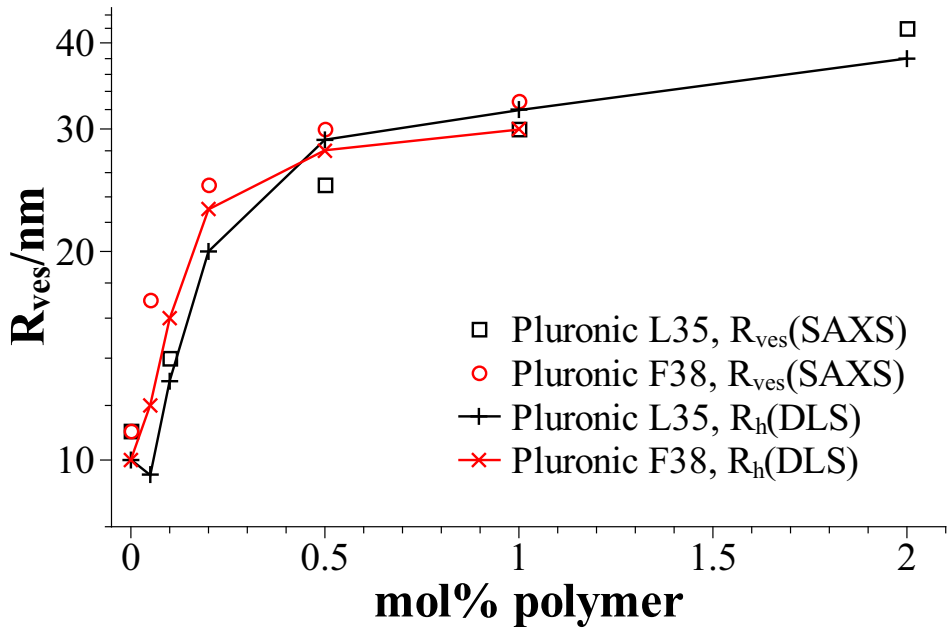

Figure 7.2.3: Initial vesicle radius and hydrodynamic radius 100s after mixing in the systems TDMAO-LiPFOS + Pluronic L35 and TDMAO-LiPFOS + Pluronic F38

energy does not depend on the disc size when R_{disc} reaches the cut-off radius, so that the closing time only depends on the "Zimm time", which describes the rotational diffusion of the disc in the medium. It can be assumed, that the hydrophilic part will be mainly located in the aqueous medium and might increase the friction in the medium and thereby slow down the rotational diffusion. Since the PEO chain of Pluronic F38 is significantly longer than that of Pluronic L35 this leads to a slower closing time for Pluronic F38 and therefore to larger t_{vesicle}.

The radii measured with SAXS and by DLS show a similar development and deviations are mainly seen at lower polymer contents. So at higher polymer contents >0.5 mol% the vesicles are very well stabilised, what can be seen in the time dependent DLS measurements (see Fig. 7.2.5). At the beginning for polymer contents >0.5mol% the hydrodynamic radius first strongly increases where still growing disc like micelles can be seen and than remains constant for about 12d. In the system with Pluronic L35 stabilisation can be observed for polymer contents larger than 0.5% while in the system with Pluronic F38 stabilisation can already be achieved for 0.2%. Since the hydrophilic chains are longer in Pluronic F38 than in Pluronic L35 they are more efficient in covering the vesicle and leading to steric stabilisation.

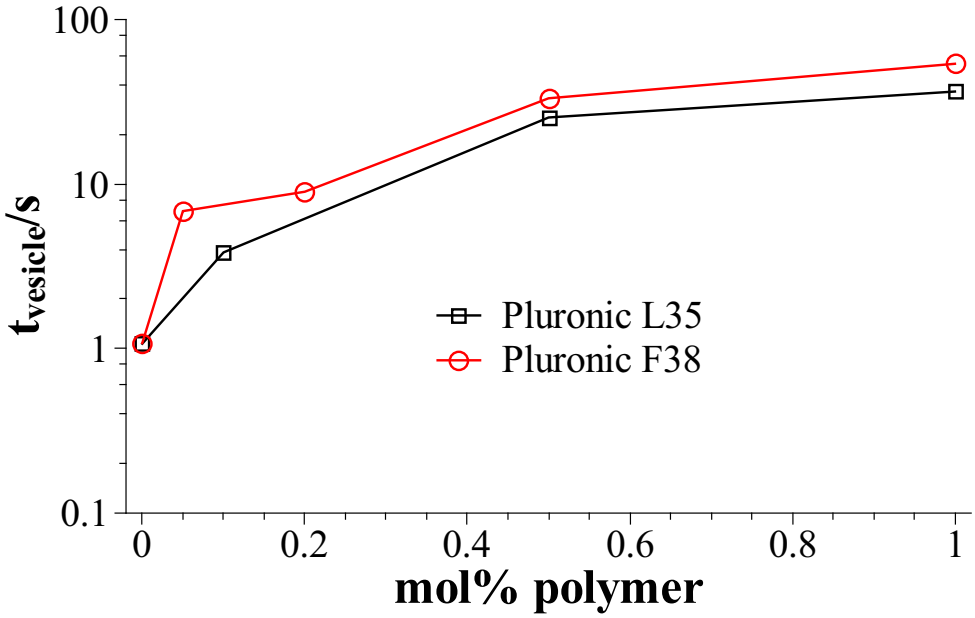

Figure 7.2.4: Characteristic vesicle formation time in the systems TDMAO-LiPFOS + Pluronic L35 and TDMAO-LiPFOS + Pluronic F38

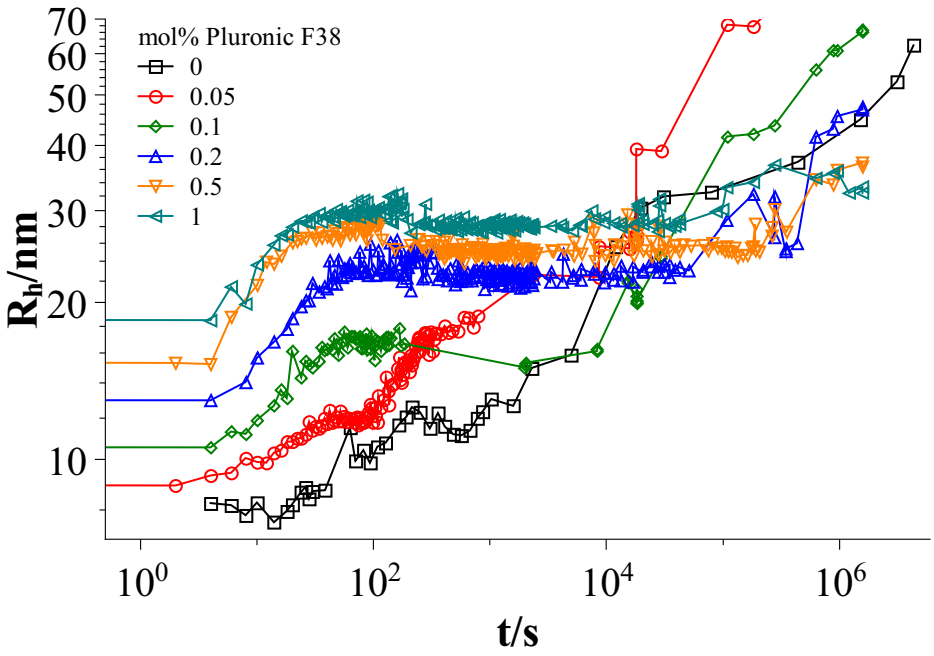

Figure 7.2.5: Time dependent DLS measurements in the system TDMAO-LiPFOS +Pluronic F38

7.3 Pluronic F38, Pluronic F88, Pluronic F108, Increasing the Polymer Chain Length

By comparing the polymers Pluronic F38, Pluronic F88 and Pluronic F108 we stay at a fixed ratio of PO and EO units (4:21) and vary the overall length of the polymer from 16 PO units to 52 PO units. Pluronic F38 has the structure $EO_{46}-PO_{16}-EO_{46}$, Pluronic F88 has the structure $EO_{102}-PO_{41}-EO_{102}$, and Pluronic F108 has the structure $EO_{132}-PO_{52}-EO_{132}$. Since by going from Pluronic L35 to Pluronic F38 there was no effect on the vesicle radius and mainly the vesicle formation time and the vesicle stability was affected, here mainly the length of the PPO block might play the important role.
A premixed TDMAO-polymer solution was mixed with a LiPFOS solution in a stopped-flow device. The evolution of the aggregates in the mixture was followed by DLS measurements and the average hydrodynamic radius was determined. The total surfactant concentration after mixing was 50mM and the ratio between TDMAO and LiPFOS was 55:45.
Figs. 7.2.5, 7.3.1 and 7.3.2 show the time dependent development of the hydrodynamic radius in the systems TDMAO-LiPFOS + Pluronic F38, TDMAO-LiPFOS + Pluronic F88, and TDMAO-LiPFOS + Pluronic F108.

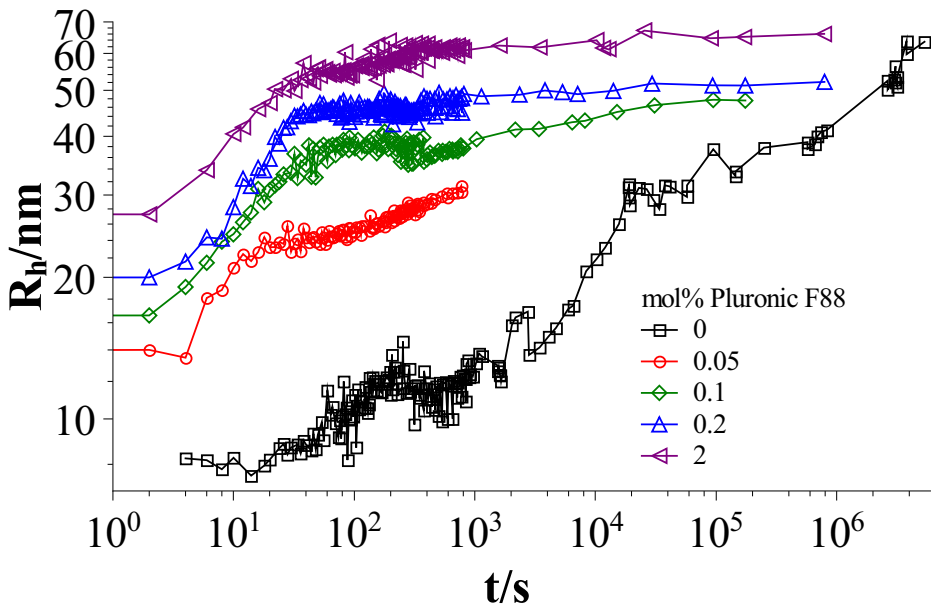

Figure 7.3.1: Time dependent DLS measurements in the system TDMAO-LiPFOS + Pluronic F88

Comparing the hydrodynamic radius 100s after mixing in the three different systems in dependence on the polymer content shows a strong increase of the hydrodynamic radius

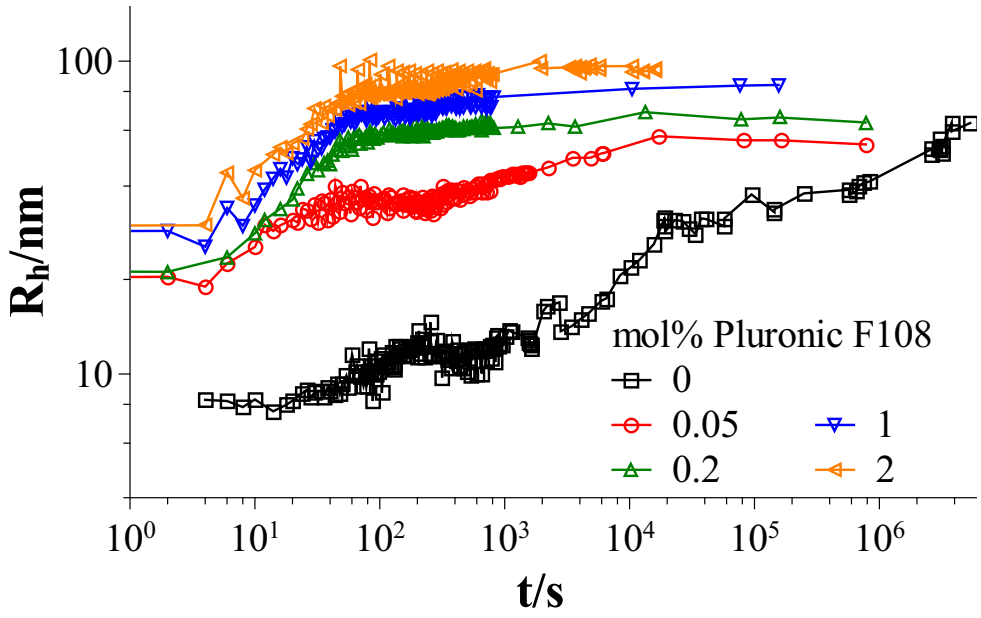

Figure 7.3.2: Time dependent DLS measurements in the system TDMAO-LiPFOS + Pluronic F108

with the polymer length (see Fig. 7.3.3). At the same amount of polymer molecules in the mixture the formed vesicles are the larger the longer the polymer chain is. That means a larger polymer leads to a stronger decrease in the line tension of the discs. Since an increase in the length of the hydrophilic chain did not have an effect on the vesicle radius, as seen by comparing Pluronic L35 and Pluronic F38, it is reasonable to assume, that the increase in the vesicle radius is caused by the hydrophobic part of the polymer. Here it might be that polymers with a longer hydrophobic part orientate themselves along the disc rim thereby causing a higher decrease of the line tension per polymer molecule. On the other hand comparing the time dependent development of the hydrodynamic radius in different systems with polymers of different hydrophilic chain length, than it can be seen that the longer the hydrophilic part is the lower is the polymer content that is needed to reach the plateau area in the DLS measurements. Comparing Pluronic L35 with 11 EO unit in the PEO chain, Pluronic F38 with 46 EO units, Pluronic F88 with 102 EO units, and Pluronic F108 with 132 EO units (see Fig. 7.3.4) leads to the conclusion that the line tension and thereby the vesicle size is mainly controlled by the length of the hydrophobic part while the stability is more due to the length of the hydrophilic chain.

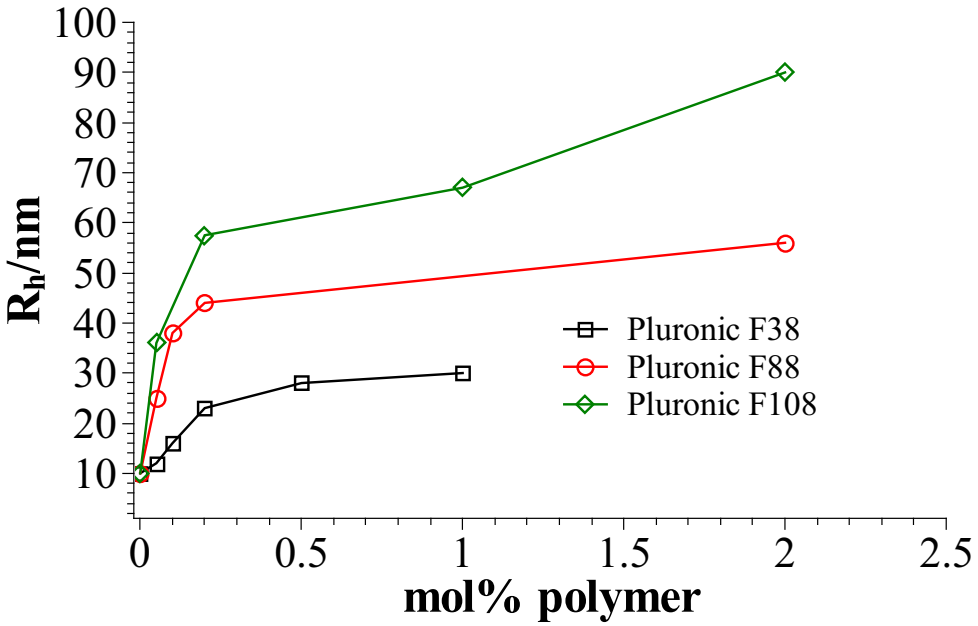

Figure 7.3.3: Hydrodynamic radius 100s after mixing in the systems TDMAO-LiPFOS + Pluronic F38, TDMAO-LiPFOS + Pluronic F88, and TDMAO-LiPFOS + Pluronic F108

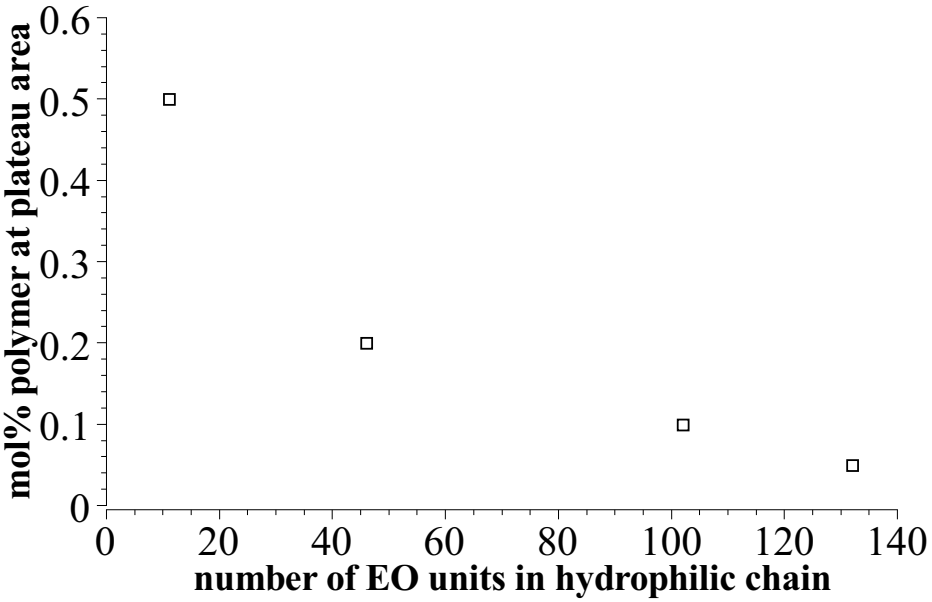

Figure 7.3.4: Polymer content where the plateau area in the DLS measurements is reached in dependence of the length of the hydrophilic part in the polymer

Conclusion and Outlook

8.1 Final Conclusion

In the presented work the mechanism of vesicle formation in mixtures of the hydrocarbon nonionic surfactant TDMAO with anionic perfluoro surfactants was studied. The principal mechanism was investigated [130,141–143] and theoretically described [60,91,92,109,127,128,132] before. The experiments show that the vesicle formation passes through a disc-like state, where the discs grow until the energy of the disc-rim exceeds the energy of the bend bilayer and discs become unstable. That results in the discs folding into spherical shells so vesicle formation takes place. In this work influences on the vesicle formation like charge, temperature and polymer additives were investigated.

In section 2 ternary systems of TDMAO and lithium perfluoroalkanoates in water with a surfactant concentration of 50mM were characterised in order to identify vesicle phases and to analyse, which parameters lead to vesicle formation. Structures in the observed mixtures were characterised by conductivity, viscosity, dynamic light scattering and small angle neutron scattering. Changes in the packing parameter allow to switch between micellar phases and vesicle phases. It is either possible to change the tail volume of the surfactant pair or the interactions between the head groups and thereby the head group area. In mixtures of TDMAO with $C_nF_{2n+1}CO_2Li$ the packing parameter increases with increasing perfluoro surfactant content due to the bulky perfluorocarbon chain at a constant total surfactant concentration. As a result the aggregates transform from short rod-like micelles in the pure TDMAO solution into longer micelles and finally, if the packing parameter is high enough, into vesicles. An increase in the perfluoro surfactant chain length increases the packing parameter as well and facilitates vesicle formation. While in a system with lithium perfluorohexanoate no vesicle formation can be observed, with lithium perfluorooctanoate already small volume fractions of $\alpha(C_7F_{15}CO_2Li) = 0.4$ lead to the formation of vesicles. A change in the head group interactions can be initiated by charging the TDMAO head group by lowering the pH. Shifting from a zwitanionic system to a partly catanionic system decreases the head group area and increases the packing parameter. As a result in the system TDMAO-$C_5F_{11}CO_2Li$, where no vesicle formation could be observed, charging 10% of the TDMAO molecules facilitates vesicle formation. Vesicle formation can be induced by increasing the packing parameter either by increasing the perfluoro surfactant chain length or by charging the TDMAO head group.

In section 3 neutron diffraction experiments on surfactant crystals consisting of catanionic and nonionic-anion mixtures of hydrocarbon and fluorocarbon surfactants were performed.

In these crystals stacked surfactant bilayers with hydrocarbon and perfluoro surfactant equally distributed along the bilayer were found. The bilayer thickness could be determined that increases with the surfactant chain length from 2.95nm in the system TDMAO and $C_5F_{11}CO_2H$ to 3.26nm in the system TDMAO and $C_7F_{15}CO_2H$ and further to 3.5nm when replacing $C_7F_{15}CO_2H$ with LiPFOS. Multiple peaks at around 1.4 1/Å indicate a distorted hexagonal packing within the bilayer. The distortion is caused by different hydrocarbon-hydrocarbon, hydrocarbon-perfluoro and perfluoro-perfluoro chain interactions. Since the structure of the bilayers in the crystals and in vesicle bilayers in similar systems are expected to be similar, neutron diffraction experiments on surfactant crystals give some information about the conditions in vesicle bilayers.

The system TDMAO-LiPFOS described in section 4 is quite similar to mixtures of TDMAO and perfluoroalkanoates. The phase behaviour was investigated with small angle neutron scattering and in the middle of the phase diagram around equimolar mixing of TDMAO and LiPFOS a vesicle area with well defined vesicles with polydispersities between 0.2 and 0.3 could be observed. Kinetic measurements performed in the stopped-flow and monitored with scattering methods confirm the mechanism described above. In this section the mixing ratio between TDMAO and LiPFOS was varied and it could be observed, that the characteristic time for the growth of the disc-like micelles and the characteristic time for the vesicle formation decreases with increasing TDMAO content. That means with decreasing number of charges per aggregates all processes are accelerated due to decreasing repulsive interactions between the aggregates. It could be observed that the initially formed vesicles have a very low polydispersity of 5% but age with increasing time and become larger and more polydisperse. Charge stabilisation was not sufficient to prevent vesicle fusion and further ageing.

Theoretical considerations show that the maximum disc radius, where disc-like micelles transform into vesicles, is the ratio between twice the sum of the bending moduli $2\kappa + \overline{\kappa}$ and the line tension λ (eqn (4.3.24)). If disc-like micelles reach this cut-off radius or grow larger, they become thermodynamically unstable and vesicle formation is favoured. Even if vesicles are thermodynamically stable still the activation energy can be too high and vesicle formation can be kinetically hindered. Eqn (4.3.27) shows that the activation energy depends as well on the bending energy, so if the vesicle membrane rigidity is too high, vesicle formation is not controlled by the thermodynamic cut-off radius but by the ratio between the disc-growth time and the vesicle formation time. As a result it is important to know the bending energy in order to distinguish between both situations.

In section 5 TDMAO and LiPFOS were mixed at a fixed ratio of 55:45 and the temperature was varied to gain information about the activation energy of vesicle formation. From the dependence of the time constant for vesicle formation on the temperature the activation energy

E_A and the cut-off radius $R_{disc,max,therm.}$ could be determined with $E_A = (11 \pm 3)k_BT$ and $R_{disc,max,therm.} = (20 \pm 16)nm$. That leads to a bending energy of $2\kappa + \overline{\kappa} = (3 \pm 1)k_BT$ and a line tension of $\lambda = (0.3 \pm 0.34)k_BT/nm$. The bending energy determined in eqn (4.3.27) from the temperature dependent measurements is significantly higher than the values determined in section 4 from the polydispersity of the vesicles. In the analysis in section 4 membrane fluctuations were not taken into account what might lead to a falsification of the determined polydispersity and as a result to lower values for the bending energy.

In section 6 the information about the vesicle formation process obtained in sections 4 and 5 was used to influence the process by adding a polymer of the Pluronic type. Incorporation of the polymer into the disc-rim lowers the line tension significantly. As a result the time period for disc growth is increased what leads to an increase in the initial vesicle radius and in the vesicle formation time. The initial vesicle size increases from about 10nm in solution without any polymer up to sizes of 35nm in a solution with a Pluronic L35 concentration of 0.275mM and the characteristic time for the vesicle formation increases from 1s in solutions without polymer up to 45s in a solution with a Pluronic L35 concentration of 0.55mM. That means even small amounts of polymer in the solution have a huge effect on the vesicle formation process and the resulting vesicles. The initial formed vesicles here had the same low polydispersity as in the system without polymer, but in addition it could be observed, that the stability of the initially formed vesicles increases with increasing polymer content. This might be due to steric stabilisation of polymer decorated vesicles.

In section 7 for different polymers of the same structural type the same tendency as in section 6 could be observed. Addition of polymer leads to an elongated period of disc growth resulting in larger initial vesicles. In this section the architecture of the polymer was varied, meaning the length of the EO-block and the PO-block and Pluronic L35 ($EO_{11}-PO_{16}-EO_{11}$) was compared to Pluronic 10R5 ($PO_8-EO_{22}-PO_8$). It could be observed that reversing the structure, that means exchanging Pluronic L35 with Pluronic 10R5, had hardly any effect on the vesicle formation, but increasing the number of hydrophilic EO units by exchanging Pluronic L35 with Pluronic F38 had a small effect on the vesicle size and a significant effect on the stability of the vesicles. Pluronic F38 slightly increased the vesicle size compared to Pluronic L35, but while in the system with Pluronic L35 a polymer concentration of 0.1375mM was needed to stabilise the vesicles, in the system with Pluronic F38 already a polymer concentration of 0.055mM was sufficient to obtain a stable vesicle size. So an increasing number of EO units, i.e. a longer hydrophilic part leads to a stabilisation of the vesicles.

By comparing measurements with Pluronic F38, Pluronic F88 ($PEO_{102}-PPO_{41}-PEO_{102}$) and Pluronic F108 ($PEO_{132}-PPO_{52}-PEO_{132}$) the molecular mass of the polymer was in-

creased while keeping the relation between PEO-chain and PPO-chain constant. Here a clear relation between the polymer molecular mass and the initial vesicle size could be observed and as well the number of polymer molecules in the mixture decreased, that was necessary to reach stabilisation of the vesicles. From this observation together with the comparison between Pluronic L35 and Pluronic F38 it can be concluded that the length of the hydrophilic part of the polymer leads to a stabilisation of the vesicles while the length of the hydrophobic part increases the initial vesicle size.
As a conclusion this study gives an insight on the phase behaviour in systems of zwitanionic hydrocarbon and anionic perfluoro surfactants with an emphasis on vesicle formation. Stopped-flow studies and theoretical considerations give further insight on the mechanism of vesicle formation and modifications with charges and polymer additives reveal possibilities to influence the vesicle formation process. Especially addition of polymers of the Pluronic type allowed for a control over the vesicle formation process and in consequence of this it was possible to control the size and stability of the resulting vesicles and to preserve the low polydispersity of the vesicles, that is otherwise increasing due to ageing processes.

8.2 Outlook

In this study a way was devised to control the size, polydispersity and stability of vesicles in mixtures of the nonionic TDMAO and anionic perfluoro surfactants. A similar mechanism of vesicle formation as observed here was as well found for other catanionic mixtures like TTAOH (tetradecyltrimethylammonium hydroxide) and Texapon N_{70} (sodium laureth sulfate).[49] Here, like in the systems studied in this work, two micellar solutions are mixed that form vesicles in equilibrium due to the packing parameter of the surfactant pair. So in principal it should as well be possible to control not only mixtures of TDMAO and anionic perfluoro surfactants but the same mechanism should apply to all mixtures, where the vesicle formation follows a mechanism, where two micellar solutions are mixed and form mixed disc-like micelles, that transform into vesicles. Preliminary experiments were performed in a mixture of 30mM DTABr (dodecyltrimethylammonium bromide) and 20mM Texapon N_{70} with Brij 97 ($C_{18}H_{35}EO_{10}$) by fusing a premixed DTABr/Brij 97 solution with a Texapon N_{70} solution and determining the hydrodynamic radius by dynamic light scattering.
A dependence of the hydrodynamic radius with the polymer content could be observed like in the system studied in this work. So future experiments on vesicle formation in hydrocarbon catanionic mixtures and the influence of suitable copolymers on the vesicle formation would be very interesting to extend the knowledge gained from model systems on commercially interesting surfactant mixtures and potentially also to other vesicle forming systems, like

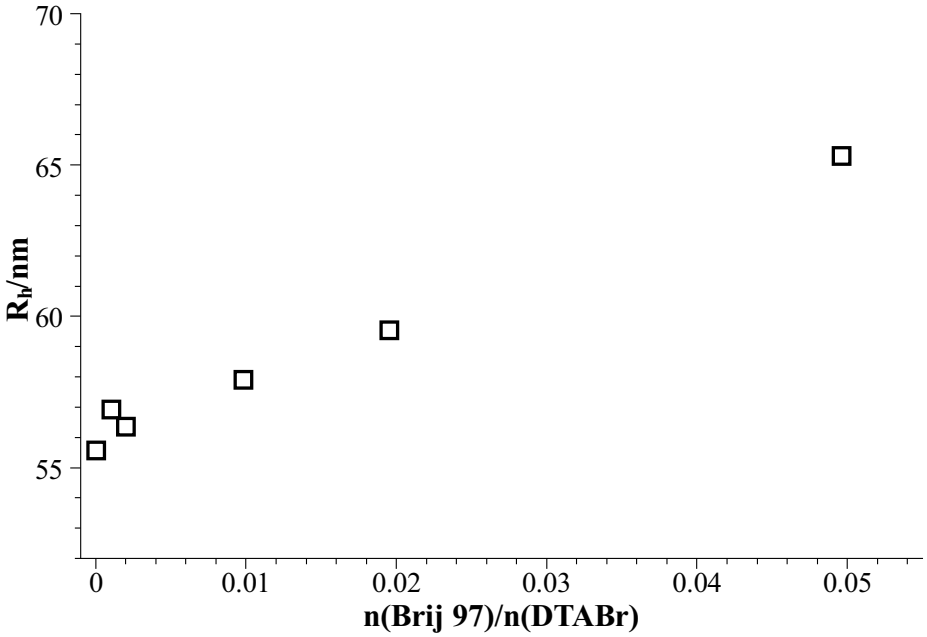

Figure 8.2.1: Influence of the polymer content on the hydrodynamic radius in mixtures of DTABr (30mM) and Texapon N_{70} (20mM)

phospholipids or esterquats.

Another interesting point is the possibility to use the initially formed monodisperse vesicles as templates. Templating vesicles in equilibrium is quite established in hydrocarbon/hydrocarbon and hydrocarbon/perfluorocarbon catanionic vesicle phases.[29,59,96,103,113] In preliminary studies the influence of admixing a certain amount of a styrene/divinylbenzene (3:1) mixture to a solution of 27.5mM TDMAO, 22.5mM LiPFOS and 0.275mM Pluronic L35, where stable, monodisperse vesicle with a radius of 31nm can be expected, on the hydrodynamic radius was studied by dynamic light scattering.

The measurements show that the structure of the vesicles can be preserved. Given the hydrophobicity of styrene and divinylbenzene it is quite likely that the monomers are incorporated into the vesicle membrane. Under this conditions it should be possible to start a polymerisation reaction and to form a polystyrene shell with divinylbenzene as cross linker in the vesicle shell. As future work it would be interesting to establish a procedure to use these vesicles as templates either by templating them in a suitable polymerisation reaction or by admixing a silica precursor like TMOS (tetramethoxysilane) and synthesis of hollow silica spheres via acid-catalysed hydrolysis. A problem here is the pH dependence of the TDMAO. That is the reason why TTABr (tetradecyltrimethylammonium bromide) could be a good replacement for TDMAO.

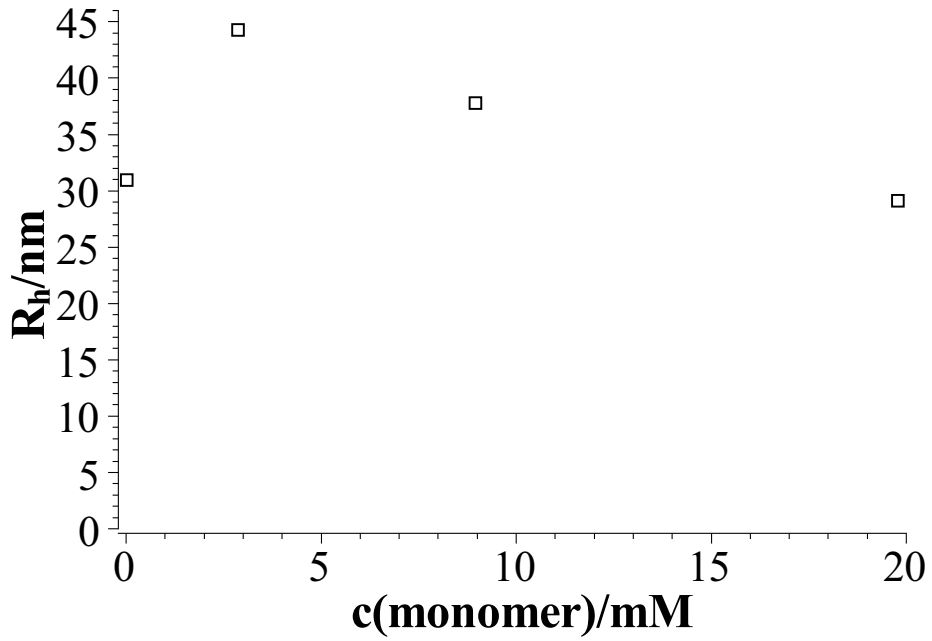

Figure 8.2.2: Influence of the concentration of a styrene/divinylbenzene (3:1) mixture on the hydrodynamic radius of vesicles formed in the system 27.5mM TDMAO, 22.5mM LiPFOS and 0.275mM Pluronic L35

Besides vesicle formation via the disc-like state vesicles can as well be formed via rod-like micelles like in the system TDMAO-$C_7F_{15}CO_2Li$ at a low total surfactant concentration of 8mM as described by Gummel et al. [52] where the TDMAO is above its cmc of 0.12mM and the perfluoro surfactant is below its cmc of 33mM or like in the system sodium oleate/octanol when adding 3.5 wt% octanol to a 100mM sodium oleate solution. [45,47] In the former case free $C_7F_{15}CO_2Li$ monomers are incorporated into existing rod-like TDMAO micelles, so that the rod-like micelles grow in length and finally transform into vesicles. In the latter case sodium oleate forms rod-like micelles in solution and the oil droplets vanish in a process similar to Ostwald ripening by diffusion of octanol monomers into the sodium oleate micelles, what leads to elongation of the micelles and finally vesicle formation. In this study a transition from a micellar phase of rod-like micelles to vesicles could be observed as well. In section section 2.2 mixtures of TDMAO and $C_5F_{11}CO_2Li$ at a total surfactant concentration of 50mM the influence of protonating TDMAO with HCl were studied. In the first case only rod-like micelles could be observed but after charging the TDMAO vesicle formation takes place. A detailed structural and kinetic study resolving this transformation should be carried out in the future and a model as discussed here and described before [60,91,92,109,127,128,132] should be developed.

Theoretical Background

9.1 Scattering Methods

Scattering is the interaction of an electromagnetic or matter wave with a medium. In elastic scattering processes the radiation just changes its direction without changing its energy while in inelastic scattering processes the interaction leads to a change in energy of the scattering beam. The measurable quantity in a scattering experiment is the differential scattering cross section $d\sigma/d\Omega$. This quantity describes the number of particles scattered per second into a solid angle $d\Omega$ in the direction ϕ and θ per $d\Omega$ divided by the flux of the incident beam Φ. The geometry of a typical scattering experiment is pictured in Fig. 9.1.1.

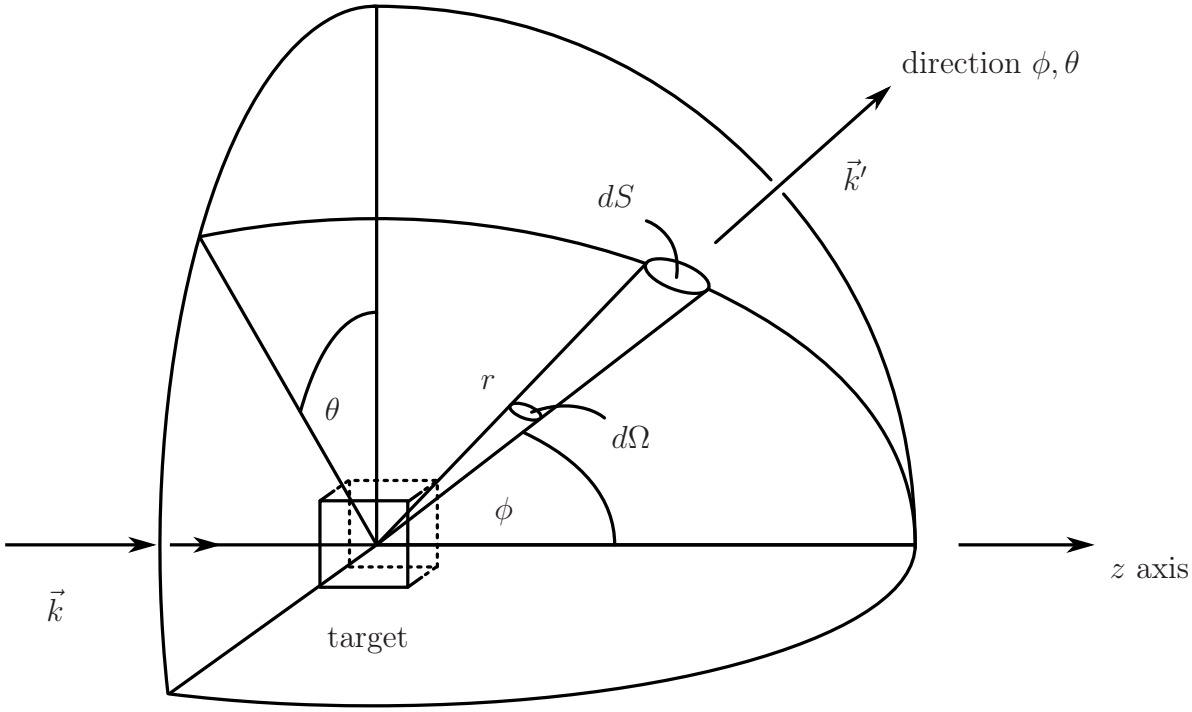

Figure 9.1.1: Geometry for scattering experiment

The radiation is described by the wave vector $\vec{k}$ which is related to its momentum $\vec{p}$ over:

$$\vec{p} = \hbar\vec{k} \tag{9.1.1}$$

$\vec{k}$ is the wave vector of the incident beam while the wave vector of the scattered beam is $\vec{k}'$. The scattering vector $\vec{q}$ is defined over the difference between $\vec{k}'$ and $\vec{k}$. For elastic scattering $|\vec{k}| = |\vec{k}'|$ and $|\vec{q}| = 4\pi/\lambda \cdot \sin(\phi/2)$.

A planar wave of the magnitude Ψ with the wavelength λ, the amplitude Ψ_0, and the

propagation speed v can be expressed in dependence on the position $\vec{r}$ and the time t by eqn (9.1.2). The direction of the wave vector is the direction of wave propagation and its magnitude is $|\vec{k}| = 2\pi/\lambda$. The circular frequency is defined over $\omega = 2\pi v/\lambda$.

$$\Psi(\vec{r}, t) = \Psi_0 \exp[\mathrm{i}(\vec{k} \cdot \vec{r} - \omega t)] \tag{9.1.2}$$

The interaction of an incoming wave at the position $\vec{r}$ with the material leads to scattering from each scattering centre j at the position $\vec{R}_\mathrm{j}$ in the material. $\vec{x}_\mathrm{j}$ is the difference between $\vec{r}$ and $\vec{R}_\mathrm{j}$. The scattering length (here b) is related to the interaction potential $\mathbf{V}(\vec{r} - \vec{R}_\mathrm{j}) \propto b(\vec{r} - \vec{R}_\mathrm{j})$ between the material and the radiation. The potential $\mathbf{V}$ determines the interaction between the radiation and the material. For neutron scattering it determines the interaction between the nuclei of the atoms of the material and the neutrons. For x-ray scattering and light scattering it determines the interaction between the electrons of the atoms of the material and the electromagnetic wave. In case of elastic scattering the material does not change its state but the radiation changes its wave vector from $\vec{k}$ to $\vec{k}'$ under the influence of the potential operator $\mathbf{V}$. The wave function Ψ_sc of the radiation scattered from the N scattering centres in the material is then described in eqn (9.1.5). N is the number of nuclei in the observed volume and D is the distance between the scattering centre and the observer.

$$\Psi_\mathrm{sc}(\vec{q}, t) = \sum_{\mathrm{j}=0}^{N} \langle \Psi^\star_\mathrm{out} | \mathbf{V} | \Psi_\mathrm{in} \rangle \tag{9.1.3}$$

$$= \frac{\Psi_0}{D} \sum_{\mathrm{j}=0}^{N} \int \exp(-i\vec{k}'\vec{r}) \exp(i\omega t) b(\vec{r} - \vec{R}_\mathrm{j}(t)) \exp(i\vec{k}\vec{r}) \exp(-i\omega t) d\vec{r} \tag{9.1.4}$$

$$= \frac{\Psi_0}{D} \sum_{\mathrm{j}=0}^{N} b_\mathrm{j}(\vec{q}, t) \exp(i\vec{q}\vec{R}_\mathrm{j}(t)) \tag{9.1.5}$$

$$\text{with } b_\mathrm{j}(\vec{q}, t) = \int_{V_\mathrm{j}} b_\mathrm{j}(\vec{x}_\mathrm{j}(t)) \exp(-\mathrm{i}\vec{q} \cdot \vec{x}_\mathrm{j}(t)) d\vec{x}_\mathrm{j} \tag{9.1.6}$$

In the far-field approximation the intensity I_sc is calculated over eqn (9.1.8) with b being real, if the pure scattering process is considered without any absorption.

$$I_\mathrm{sc}(\vec{q}, t) = |\Psi_\mathrm{sc}(\vec{q}, t)|^2 \tag{9.1.7}$$

$$= \frac{\Psi_0^2}{D^2} \sum_{\mathrm{j}=0}^{N} \sum_{\mathrm{j'}=0}^{N} b_\mathrm{j}(\vec{q}, t) b_\mathrm{j'}(\vec{q}, t) \exp(-\mathrm{i}\vec{q}(\vec{R}_\mathrm{j}(t) - \vec{R}_\mathrm{j'}(t))) \tag{9.1.8}$$

If the system is ergodic, that means if the time average is equal to the ensemble average, which gives no information of the individual scattering units and particles. Then the scattering intensity is described in eqn (9.1.9) with $I_0 = \Psi_0^2$.

$$I_{\mathrm{sc}}(\vec{q}) = \left\langle \frac{I_0}{D^2} \sum_{\mathrm{j}=0}^{N} \sum_{\mathrm{j'}=0}^{N} b_{\mathrm{j}}(\vec{q}) b_{\mathrm{j'}}(\vec{q}) \exp(-\mathrm{i}\vec{q}(\vec{R_{\mathrm{j}}} - \vec{R_{\mathrm{j'}}})) \right\rangle \tag{9.1.9}$$

The intensity I_{sc} of the scattered radiation is proportional to the differential cross section. The scattering intensity decreases with the square of the distance D between the scattering centre and the observer and increases with the scattering volume V and the intensity of the incident beam I_0 (eqn (9.1.10)).

$$I_{\mathrm{sc}}(\vec{q}) = \frac{I_0 V}{D^2} \cdot \frac{d\sigma}{d\Omega}(\vec{q}) \tag{9.1.10}$$

That leads to a differential cross section of:

$$\frac{d\sigma}{d\Omega}(\vec{q}) = \frac{I_{\mathrm{sc}}(\vec{q}) D^2}{I_0 V} \tag{9.1.11}$$

$$= \frac{1}{V} \left\langle \sum_{\mathrm{j}=0}^{N} \sum_{\mathrm{j'}=0}^{N} b_{\mathrm{j}}(\vec{q}) b_{\mathrm{j'}}(\vec{q}) \exp(-\mathrm{i}\vec{q}(\vec{R_{\mathrm{j}}} - \vec{R_{\mathrm{j'}}})) \right\rangle \tag{9.1.12}$$

In the case of radially isotropical, identical ($b_{\mathrm{j}}(\vec{q}) = b_{\mathrm{j'}}(\vec{q})$), and monodisperse particles the scattering cross section can be factorised.

$$\frac{d\sigma}{d\Omega}(\vec{q}) = \frac{1}{V} \left\langle b^2(\vec{q}) \right\rangle \left\langle \sum_{\mathrm{j}=0}^{N} \sum_{\mathrm{j'}=0}^{N} \exp(-\mathrm{i}\vec{q}(\vec{R_{\mathrm{j}}} - \vec{R_{\mathrm{j'}}})) \right\rangle \tag{9.1.13}$$

In this approximation the differential cross section is described as the product of the particle number density N/V, the square of the scattering length density at zero angle $b^2(0)$, the form factor $P(\vec{q}) = \langle b^2(\vec{q}) \rangle / b^2(0)$, that is basically the Fourier transform of the shape of one particle, and the structure factor $S(\vec{q})$ that is described in eqn (9.1.15) and that describes the particle-particle interactions.

$$\frac{d\sigma}{d\Omega}(\vec{q}) = \frac{N}{V} b^2(0) P(\vec{q}) S(\vec{q}) \tag{9.1.14}$$

$$\text{with } S(\vec{q}) = \frac{1}{N} \left\langle \sum_{\mathrm{j}=0}^{N} \sum_{\mathrm{j'}=0}^{N} \exp(-\mathrm{i}\vec{q}(\vec{R_{\mathrm{j}}} - \vec{R_{\mathrm{j'}}})) \right\rangle \tag{9.1.15}$$

In a system with isolated scattering centres the mass density function in real space and therefore the function for the scattering length density b can be described as a delta function with $b_{\mathrm{j}}(\vec{x}_{\mathrm{j}}, t) = b_{\mathrm{j}}(t) \cdot \delta(\vec{x}_{\mathrm{j}})$ and $b_{\mathrm{j}}(\vec{q}, t) = b_{\mathrm{j}}(t)$. In this case the sum can be split into two sums for the case that $j = j'$ and for $j \neq j'$. If the scattering lengths of the scattering centres are statistically uncorrelated, then $\langle b_{\mathrm{j}'} b_{\mathrm{j}} \rangle = \langle b^2 \rangle$ for the first case and $\langle b_{\mathrm{j}'} b_{\mathrm{j}} \rangle = \langle b \rangle^2$ for the second case.

$$\frac{d\sigma}{d\Omega}(\vec{q}) = \frac{1}{V} \left(\langle b \rangle^2 \left\langle \sum_{\mathrm{j}=0}^{N} \sum_{\mathrm{j'}=0}^{N} \exp(-\mathrm{i}\vec{q}(\vec{R}_{\mathrm{j}} - \vec{R}_{\mathrm{j}'})) \right\rangle \right.$$
$$\left. + (\langle b^2 \rangle - \langle b \rangle^2) \left\langle \sum_{\mathrm{j}=0}^{N} \exp(-\mathrm{i}\vec{q}(\vec{R}_{\mathrm{j}} - \vec{R}_{\mathrm{j}'})) \right\rangle \right) \tag{9.1.16}$$
$$= \frac{1}{V} \langle b \rangle^2 \left\langle \sum_{\mathrm{j}=0}^{N} \sum_{\mathrm{j'}=0}^{N} \exp(-\mathrm{i}\vec{q}(\vec{R}_{\mathrm{j}} - \vec{R}_{\mathrm{j}'})) \right\rangle + (\langle b^2 \rangle - \langle b \rangle^2) \frac{N}{V} \tag{9.1.17}$$
$$= \underbrace{\frac{1}{V} \langle b \rangle^2 \left\langle \sum_{\mathrm{j}=0}^{N} \sum_{\mathrm{j'}=0}^{N} \exp(-\mathrm{i}\vec{q}(\vec{R}_{\mathrm{j}} - \vec{R}_{\mathrm{j}'})) \right\rangle}_{\text{coherent}} + \underbrace{\Delta b \frac{N}{V}}_{\text{incoherent}} \tag{9.1.18}$$

The first term, which was referred to as structure factor before, is $\vec{q}$ dependent and is due to interference effects between scattering centres while the second term does not depend on the scattering angle. This term is called the incoherent scattering and is due to particle density fluctuations. It does not provide any information about the spacial order in the system. This incoherent scattering is the dominant background in small angle x-ray scattering. In small angle neutron scattering incoherent scattering comes as well from the incoherent part of the scattering length density which is not described by this formalism and which is due to interactions between the neutron and the nucleus spin, thereby lifting the principle of indistinguishability of particles required in order for having interference effects. These two effects add an internal background to the scattering intensity that has to be taken into account during data analysis. This internal background does not include effects from the instrument.

9.1.1 Small Angle Scattering (SAS)

The general experimental set-up is in the case of small angle scattering techniques like Small Angle Neutron Scattering (SANS), Small Angle X-ray Scattering (SAXS) or Small Angle Light Scattering (SALS) very similar. The sample is illuminated by a focused beam of radiation.

For SANS the neutron beam can be generated by a nuclear reactor or a spallation source.

These fast neutrons produced there have to be slowed down by a moderator, where often D_2O is used. The wavelength of these thermal neutrons is subject to the Maxwellian distribution. The deBroglie wavelength λ_T marks the maximum of this distribution with the temperature T of the moderator, the mass of the neutron m, the Planck constant h, and the Boltzmann constant k_B (eqn (9.1.19)).

$$\lambda_T = \frac{h}{\sqrt{2mk_BT}} \tag{9.1.19}$$

From this broad distribution a thin wavelength area is selected by a velocity selector, that consists of a rotating twisted bundle of absorbing plates (like a turbine) and allows only neutrons of a certain velocity to pass, and the divergent beam is focused in a pin-hole collimation by neutron collimators on the sample. For SAXS often synchrotrons or X-ray tubes are used as sources and the beam can be focused on the sample in different geometries depending on the flux of the source. For SALS lasers are used as radiation source.
Behind the sample the scattered radiation is collected on a detector that is usually planar. The primary beam is stopped by an absorbing material. Due to the small measurement angles, the relation between the magnitude q of the scattering vector $\vec{q}$ and the scattering angle θ can be linearised. Than q can be described by the distance between the sample and the detector D and over the distance r_{det} between the scattered beam and the primary beam on the detector (eqn (9.1.21)).

$$q = |\vec{q}| = \frac{4\pi}{\lambda} \cdot \sin\left(\frac{\theta}{2}\right) \tag{9.1.20}$$

$$= \frac{4\pi n}{\lambda} \cdot \frac{r_{det}}{D} \tag{9.1.21}$$

The general geometry of a SAS experiment is depictured in Fig. 9.1.2.

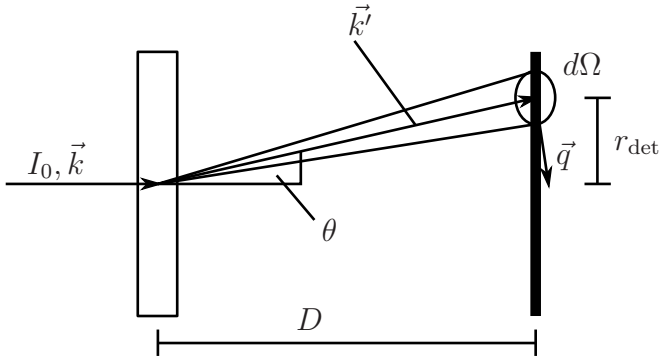

Figure 9.1.2: General geometry of a small angle scattering experiment (see as well Fig. 9.1.1)

In the ideal case the relation between the differential cross section and the scattering intensity is given in eqn (9.1.10). In reality the solid angle $d\Omega$, the detector efficiency $\epsilon(\lambda)$ and the transmition of the sample $T_\mathrm{s}(\lambda)$ have to be taken into consideration (eqn (9.1.22)).

$$I_{\mathrm{sc,real}}(\vec{q}) = \int_\Omega d\Omega \cdot I_0 V \cdot \epsilon(\lambda) \cdot T_\mathrm{s}(\lambda) \cdot \frac{d\sigma}{d\Omega}(\vec{q}) \tag{9.1.22}$$

In addition instrumental effects add a constant background B to the scattering intensity and an incoherent background coming from the sample can as well contribute to the differential cross section. In addition liquid samples can only be measured in an adequate sample container with a transmission T_c so that eqn (9.1.23) describes the measured scattering intensity.

$$I_{\mathrm{sc,real}}(\vec{q}) = \int_\Omega d\Omega \cdot I_0 V \epsilon(\lambda) \cdot \left[T_\mathrm{s}(\lambda) \left(\left(\frac{d\sigma}{d\Omega} \right)_{\mathrm{coh.,s}} (\vec{q}) + \left(\frac{d\sigma}{d\Omega} \right)_{\mathrm{inc.,s}} \right) + T_\mathrm{c}(\lambda) \left(\frac{d\sigma}{d\Omega} \right)_{\mathrm{inc.,c}} \right] + B \tag{9.1.23}$$

For the data reduction the measured intensity of the sample with the sample container $I_\mathrm{s,c}$ has to be corrected by the measured intensity coming from electronic effects of the detector I_d with the transmition determined from the sample together with the sample container $T_\mathrm{s,c}(\lambda)$ (eqn (9.1.24)). All measured intensities have to be corrected by the intensity of the incoming beam or the counts of a monitor $M = I_0$ at the time of measurement respectively.

$$I_{\mathrm{s,c,0}} = \frac{\frac{I_\mathrm{s,c}}{M_\mathrm{s,c}} - \frac{I_\mathrm{d}}{M_\mathrm{d}}}{T_\mathrm{s,c}(\lambda)} \tag{9.1.24}$$

The intensity measured from the empty sample container or the sample container containing the solvent I_b has to be treated in the same way with the transmition $T_\mathrm{b}(\lambda)$ to achieve the scattering coming from the sample container and the solvent or purely the sample container $I_\mathrm{b,0}$ (eqn (9.1.25)).

$$I_{\mathrm{b,0}} = \frac{\frac{I_\mathrm{b}}{M_\mathrm{b}} - \frac{I_\mathrm{d}}{M_\mathrm{d}}}{T_\mathrm{b}(\lambda)} \tag{9.1.25}$$

$I_\mathrm{s,c,0}$ and $I_\mathrm{b,0}$ lead to the scattering intensity purely coming from the sample $I_\mathrm{s,0}$ with $I_\mathrm{s,0} = I_\mathrm{s,c,0} - I_\mathrm{b,0}$. Electronic effects coming from the detector and the volume of the sample, that is proportional to the sample thickness t_s, have to be taken into account by comparing the scattering coming from the sample $I_\mathrm{s,0}$ with the scattering I_r coming from a homogeneous

scatter with a known scattering cross section $(d\sigma/d\Omega)_{\mathrm{r}}$ and thickness t_{r}. This leads to the scattering cross section of the sample $(d\sigma/d\Omega)_{\mathrm{s}}$(eqn (9.1.26)).

$$\left(\frac{d\sigma}{d\Omega}\right)_{\mathrm{s}} = \frac{I_{\mathrm{s},0}}{I_{\mathrm{r}}} \cdot \frac{t_{\mathrm{r}}}{t_{\mathrm{s}}} \cdot \left(\frac{d\sigma}{d\Omega}\right)_{\mathrm{r}} \tag{9.1.26}$$

9.1.2 Dynamic Light Scattering (DLS)

In Dynamic Light Scattering (DLS) not the angular dependent, stationary scattering is observed but the time dependence of the scattering intensity. A typical set up for a DLS experiment is depicted in Fig. 9.1.3. Monochromatic coherent laser light is focussed onto the sample that consists of a diluted solution of particles in a homogeneous medium to avoid multiple scattering. The scattering intensity is monitored by a photomultiplier that is connected to a photon counter and a correlator. The photomultiplier is mounted on a goniometer to allow for changes in the scattering angle θ.

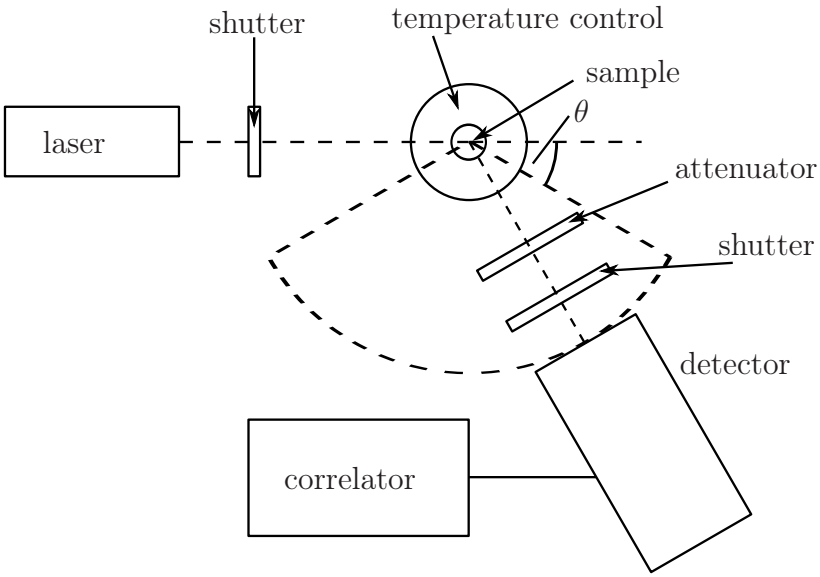

Figure 9.1.3: Set-up for dynamic light scattering

For independent particles eqn (9.1.8) can be applied. In DLS experiments time correlation functions are regarded. They describe how the intensity or the amplitude electric field of the scattered light changes due to particle diffusion in the scattering volume. Since the amplitude of the electric field Ψ_{sc} depends on the location $\vec{R}_j$ of a particle j, which shows pure diffusional, statistical behaviour in an homogeneous medium, Ψ_{sc} itself fluctuates in a statistical way (Fig. 9.1.4). The field autocorrelation function $G^{(1)}(\tau)$ describes the correlation of the amplitude of the scattered electric field at an arbitrary time $t = 0$ with the amplitude at a time $t = \tau$ (eqn (9.1.27)).

$$G^{(1)}(\tau) = \langle \Psi_{\mathrm{sc}}(0)\Psi^{\star}_{\mathrm{sc}}(\tau)\rangle \tag{9.1.27}$$

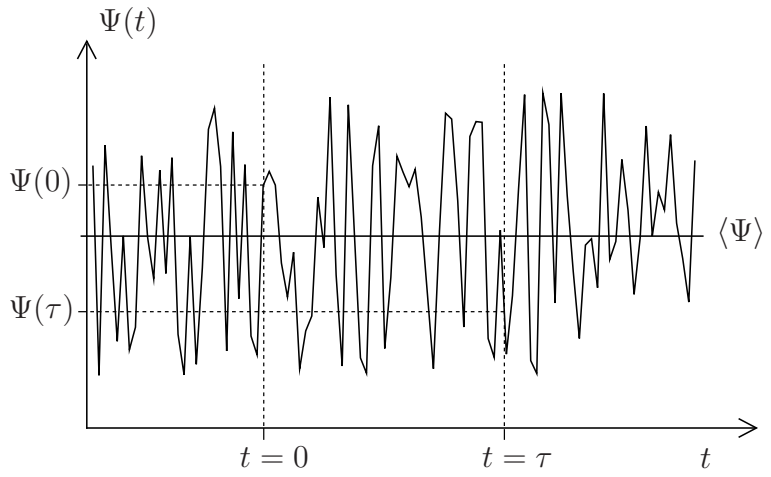

Figure 9.1.4: The electric field Ψ fluctuates with time t around its intermediate value $\langle\Psi\rangle$ due to diffusion of scattering particles in the medium

With eqn (9.1.5) follows eqn (9.1.28).

$$G^{(1)}(q,\tau) = \frac{\Psi_0^2}{D^2}\sum_{j=0}^{N}\sum_{j'=0}^{N} b_j(\vec{q},0)b^{\star}_{j'}(\vec{q},\tau)\exp[i\vec{q}(\vec{R}_j(0) - \vec{R}_{j'}(\tau))] \tag{9.1.28}$$

For radially isotropical, identical, and monodisperse particles eqn (9.1.28) can be factorised. Due to the long wavelength of the usually used visible light q is low and unless the particles are quite large the form factor $P(\vec{q}) = \langle b^2(\vec{q})\rangle / b^2(0)$ should be one. Then eqn (9.1.28) reduces to eqn (9.1.29).

$$G^{(1)}(\tau) = \frac{\Psi_0^2}{D^2}b^2(0)\sum_{j=0}^{N}\sum_{j'=0}^{N}\exp[i\vec{q}(\vec{R}_j(0) - \vec{R}_{j'}(\tau))] \tag{9.1.29}$$

For $\tau = 0$ all summands are one while for $\tau \to \infty$ the summand can have arbitrary negative and positive values due to the Brownian motion of the particles. As a result $G^{(1)}$ decays from $\langle\Psi^2_{\mathrm{sc}}\rangle = I_0/D^2 \cdot b^2(0)N$, which gives the scattering intensity $I_{\mathrm{sc}}(0)$ at zero angle according to eqns (9.1.10) and (9.1.14), to $\lim_{\tau\to\infty}\langle\Psi_{\mathrm{sc}}(0)\Psi^{\star}_{\mathrm{sc}}(\tau)\rangle = \langle\Psi_{\mathrm{sc}}(0)\rangle\langle\Psi_{\mathrm{sc}}(\tau)\rangle = \langle\Psi_{\mathrm{sc}}\rangle^2 = 0$. In the case of monodisperse, spherical particles that show Brownian motion $G^{(1)}$ decays monoexponentially with a decay rate τ_1 (eqn (9.1.30) and Fig. 9.1.5) as a direct result of Ficks second law of diffusion.

$$G^{(1)}(\tau) = \langle \Psi_{\mathrm{sc}} \rangle^2 + \left[\langle \Psi_{\mathrm{sc}}^2 \rangle - \langle \Psi_{\mathrm{sc}} \rangle^2 \right] \exp\left(\frac{-\tau}{\tau_1} \right) \tag{9.1.30}$$

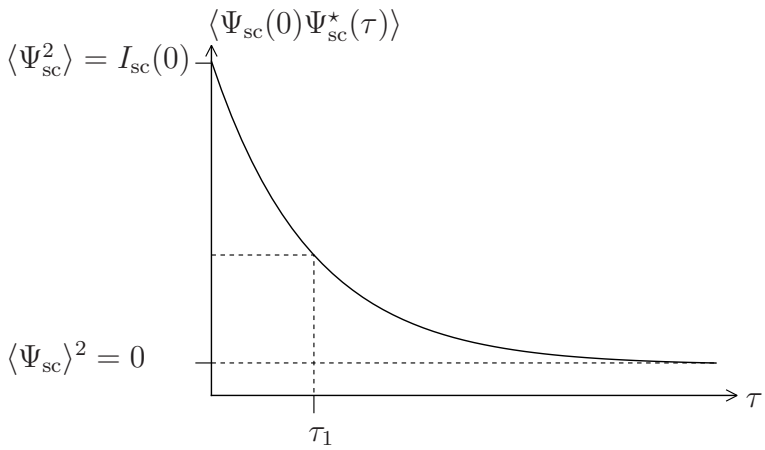

Figure 9.1.5: Time correlation function $G^{(1)} = \langle \Psi_{\mathrm{sc}}(0)\Psi_{\mathrm{sc}}^{\star}(\tau) \rangle$

Usually the electric field is not accessible as measurable quantity. Instead the intensity autocorrelation function $G^{(2)}$ can be calculated from the scattering intensity (eqn (9.1.31)).

$$G^{(2)}(\tau) = \langle I_{\mathrm{sc}}(0) I_{\mathrm{scc}}(\tau) \rangle \tag{9.1.31}$$

Under the assumption that Ψ_{sc} is a stochastic variable with a Gaussian distribution, the Siegert equation (eqn (9.1.35)) is valid.

$$G^{(2)}(\tau) = |G^{(1)}(0)|^2 + |G^{(1)}(\tau)|^2 \tag{9.1.32}$$

$$= \langle I_{\mathrm{sc}} \rangle^2 + |G^{(1)}(\tau)|^2 \tag{9.1.33}$$

$$\Leftrightarrow g^{(2)}(\tau) = \frac{G^{(2)}(\tau)}{\langle I_{\mathrm{sc}} \rangle^2} \tag{9.1.34}$$

$$= 1 + \beta_{\mathrm{s}} |g^{(1)}(\tau)|^2 \tag{9.1.35}$$

This is the case for pure translational diffusion of monodisperse, spherical particles without interaction in a diluted solution. Then the translational diffusion coefficient D_{T} and the absolute of the scattering vector $\vec{q}$ are linked to the relaxation time τ_1.

$$\Gamma = \frac{1}{\tau} \tag{9.1.36}$$

$$= D_{\mathrm{T}} q^2 \tag{9.1.37}$$

In a polydisperse system the field autocorrelation function $g^{(1)}$ has to be weighted with the relaxation rate distribution $dist$.

$$g^{(1)}(\tau) = \int_0^\infty dist(\Gamma) \exp(-\Gamma\tau) d\Gamma \tag{9.1.38}$$

The exponent can than be developed into a power series, where the coefficients K_m can be expressed by the ith moments μ_i of the distribution (cumulants).

$$g^{(2)}(\tau) = 1 + b \exp\left(-2 \cdot \sum_{m=1}^{\infty} K_m \frac{(-\tau)^m}{m!}\right) \tag{9.1.39}$$

$$\text{with} \quad K_1 = \langle\Gamma\rangle \tag{9.1.40}$$

$$K_2 = \mu_2 \tag{9.1.41}$$

$$K_3 = \mu_3 \tag{9.1.42}$$

$$K_4 = \mu_4 - 3\mu_2^2 \tag{9.1.43}$$

For small values of τ the summands starting from the third can be neglected which results in eqn (9.1.44).

$$g^{(2)}(\tau) = 1 + \beta_s \exp\left(-2\langle\Gamma\rangle\tau + \mu_2\tau^2\right) \tag{9.1.44}$$

μ_2 is the variance of the distribution and related to the standard deviation σ and the polydispersity index PDI by $\mu_2 = \sigma^2$ and $PDI = \sigma/\langle\Gamma\rangle$.
The Stokes-Einstein equation gives a relation between the thermal energy of a particle and the frictional energy during diffusion in a viscose medium of the viscosity η at the temperature T (eqn (9.1.45)). From this equation the hydrodynamic radius R_h can be calculated with the Boltzmann constant k_B.

$$R_h = \frac{k_B T}{6\pi\eta D_T} \tag{9.1.45}$$

9.2 Determination of the Critical Micelle Concentration (cmc)/Electrical Conductivity

In solutions amphiphilic molecules form micelles above a critical concentration at constant temperature or above a critical temperature at constant concentration. This critical concentration is called critical micelles concentration (cmc) and the critical temperature is called

critical micelles temperature (cmt)

In mixtures of to amphiphiles 1 and 2 the cmc of the mixture $c^\star$ can be calculated from the cmc of the pure components c_1 and c_2. In equilibrium the chemical potential μ_i of the monomers of the component i in the solution is equal to the chemical potential μ_i^M of the monomers of the component i in the mixed micelles. With the concentration c_i^M of the monomers of the component i, the activity coefficient γ_i of the monomer in the micelle, the molar fraction x_i of the monomer i in the micelle, and the standard potential μ_i^0 equation eqns (9.2.2) and (9.2.3) lead to eqn (9.2.4).

$$\mu_i = \mu_i^M \tag{9.2.1}$$

$$\mu_i = \mu_i^0 + rT \cdot \ln c_i^M \tag{9.2.2}$$

$$\mu_i^M = \mu_i^0 + RT \cdot \ln c_i + RT \cdot \ln \gamma_i x_i \tag{9.2.3}$$

$$\Rightarrow c_i^M = \gamma_i x_i c_i \tag{9.2.4}$$

If the monomer concentration is equal to the cmc in the mixture $c^\star$, then eqn (9.2.5) follows with the molar fraction α_i of the component i that exists in the overall solution.

$$\alpha_i c^\star = \gamma_i x_i c_i \tag{9.2.5}$$

The sum of the molar fractions $x_1 + x_2 = 1$ leads to eqn (9.2.6).

$$\frac{1}{c^\star} = \frac{\alpha_1}{\gamma_1 \cdot c_1} + \frac{\alpha_2}{\gamma_2 \cdot c_2} \tag{9.2.6}$$

In a binary mixture the activity coefficients γ_1 and γ_2 can be expressed by eqns (9.2.8) and (9.2.9) with the molar fraction x_i of the component i in the micelle and the interaction parameter β under the assumption, that the mixing enthalpy ΔH can be expressed by eqn (9.2.7) according to the regular solution theory for regular mixtures. The interaction parameter β describes the pairwise interaction of molecules in regular mixtures. That means β can be described by the interaction energies U_{11} and U_{22} between similar amphiphiles and by the interaction energy $U_{12} = U_{21}$ between different amphiphiles according to eqn (9.2.10) with the temperature T and the Boltzmann constant k_B.

$$\frac{\Delta H}{k_{\mathrm{B}}T} = \beta \cdot x_i(1 - x_i) \tag{9.2.7}$$

$$\gamma_1 = \exp\left(\beta(1 - x_1)^2\right) \tag{9.2.8}$$

$$\gamma_2 = \exp\left(\beta x_1^2\right) \tag{9.2.9}$$

$$\beta = \frac{U_{11} + U_{22} - 2U_{12}}{k_{\mathrm{B}}T} \tag{9.2.10}$$

Eqn (9.2.11) leads to an expression for the molar fraction x_1 of the component 1 in the micelle.

$$\frac{x_1^2 \ln\left(\frac{c^\star \alpha_1}{c_1 x_1}\right)}{(1 - x_1)^2 \ln\left[\frac{c^\star(1-\alpha_1)}{c_2(1-x1)}\right]} = 1 \tag{9.2.11}$$

Eqn (9.2.11) can be solved iteratively and with measured values for $c^\star$, c_1, and c_2 as well as with the known value for α_1 x_1 can be calculated. From x_1 the interaction parameter β can be calculated via eqn (9.2.12).

$$\beta = \frac{\ln\left(\frac{c^\star \alpha_1}{c_1(1-x_1)}\right)}{(1 - x_1)^2} \tag{9.2.12}$$

9.3 Surface Dilatational Rheology

In surface dilatational rheology the elastic and viscous properties of the surface are determined. In purely elastic surfaces the surface elasticity E is defined by Gibbs as the change in the surface tension ν with the change in the surface area A.

$$E = \frac{d\nu}{d\ln A} \tag{9.3.1}$$

If the surface has both elastic and viscous properties then E has to be referred to as surface dilatational modulus and will be different from the equilibrium surface elasticity E_0. The viscous contribution can be described by the surface dilatiational viscosity η_{d}, which only represents a true Newtonian type of surface viscosity.

$$\Delta\nu = \eta_{\mathrm{d}} \frac{d\ln A}{dt} \tag{9.3.2}$$

In a surface, where both processes take place, the storage modulus E' describes the elastic properties and the loss modulus E'' describes the viscous properties.

$$E^\star = E' + iE'' \tag{9.3.3}$$

Usually in an oscillatory experiment the surface area will be changed by an external force in an harmonic way.

$$\Delta \ln A \propto \exp(i\omega t) \tag{9.3.4}$$

Then the loss modulus is proportional to the surface dilatational viscosity.

$$E'' = \omega \eta_\mathrm{d} \tag{9.3.5}$$

A sinoidal change in the surface area leads to a sinoidal response in the surface tension with the phase angle δ.

$$\Delta A = A_0 - A \tag{9.3.6}$$
$$= A_\mathrm{a} \sin(\omega t) \tag{9.3.7}$$
$$\Delta \nu = \nu_\mathrm{a} \sin(\omega t + \delta) \tag{9.3.8}$$
$$= \nu_\mathrm{a} \sin(\omega t) \cos\delta + \nu_\mathrm{a} \sin(\omega t) \sin\delta \tag{9.3.9}$$

Then the complex surface dilatational modulus $E^\star$ can be expressed in the following way:[34,35,108]

$$E^\star = E' + iE'' \tag{9.3.10}$$
$$= |E| \cos\delta i |E| \sin\delta \tag{9.3.11}$$
$$\text{with} \quad |E| = \frac{\nu_\mathrm{a}}{A_\mathrm{a}/A_0} \tag{9.3.12}$$

Experimental

10.1 Methods

10.1.1 Stopped-Flow Mixing

A stopped-flow device is a rapid mixing device, where two, three (BioLogic SFM-300) or four (BioLogic SFM-400) solutions can be sequentially mixed in controlled ratios with a controlled volume flow. As depicted in Fig. 10.1.1 these solutions are stored in reservoirs and will be pushed by step motors through high efficiency mixers into the observation cell by high performance steperp motors. After mixing a defined volume at a defined flow rate and mixing ratio the flow is stopped by the hard-stop and the start of the measurement is electronically triggered by the hard stop, so that the measurement starts immediately after mixing. When reaching the cuvette the mixture already has a certain age due to the delay line. This dead time can be calculated from the filling volume between the last mixer, that is directly located under the observation cell, and the middle of the observation cell and from the flow rate of the mixture. To ensure for an efficient mixing the conventionally used Berger ball mixer right before the cuvette can be replaced by a high density mixer, which allows blockage of convection created by temperature and density effects.
Turbidity, fluorescence, conductivity, DLS, SANS and SAXS are among the conventional detection modes used in stopped-flow measurements. In the present work structural changes of aggregates of amphiphiles where observed by DLS (see section 10.1.2), SANS (see section 10.1.3) and SAXS (see section 10.1.4).

10.1.2 Kinetic Dynamic Light Scattering Measurements

In this study time dependent DLS measurements were performed as well as measurements in equilibrium.
Measurements with a high time resolution (2s) covering a time range of max. 30min were performed in a combined stopped-flow-DLS apparatus using the BioLogic SFM-400 with a rectangular Hellma QS quartz cell (FC-15 cell) with an inner diameter of 1.5mm provided by BioLogic. The flow rate was always set to 7mL/s and the dead volume in combination with the high density mixer is 51.3μL, which leads to a dead time of 7.3ms.
The sample was illuminated with a diode pumped Nd-Yag laser with a wavelength of 532nm and an output power of 20mW (Compass 215M-20, Coherent). The intensity of the scattered light was collimated under 90° by a combination of a fibre collimator (60FC, Schäfter + Kirchhoff) and a single mode glass fibre cable (SMC, Schäfter + Kirchhoff) and recorded

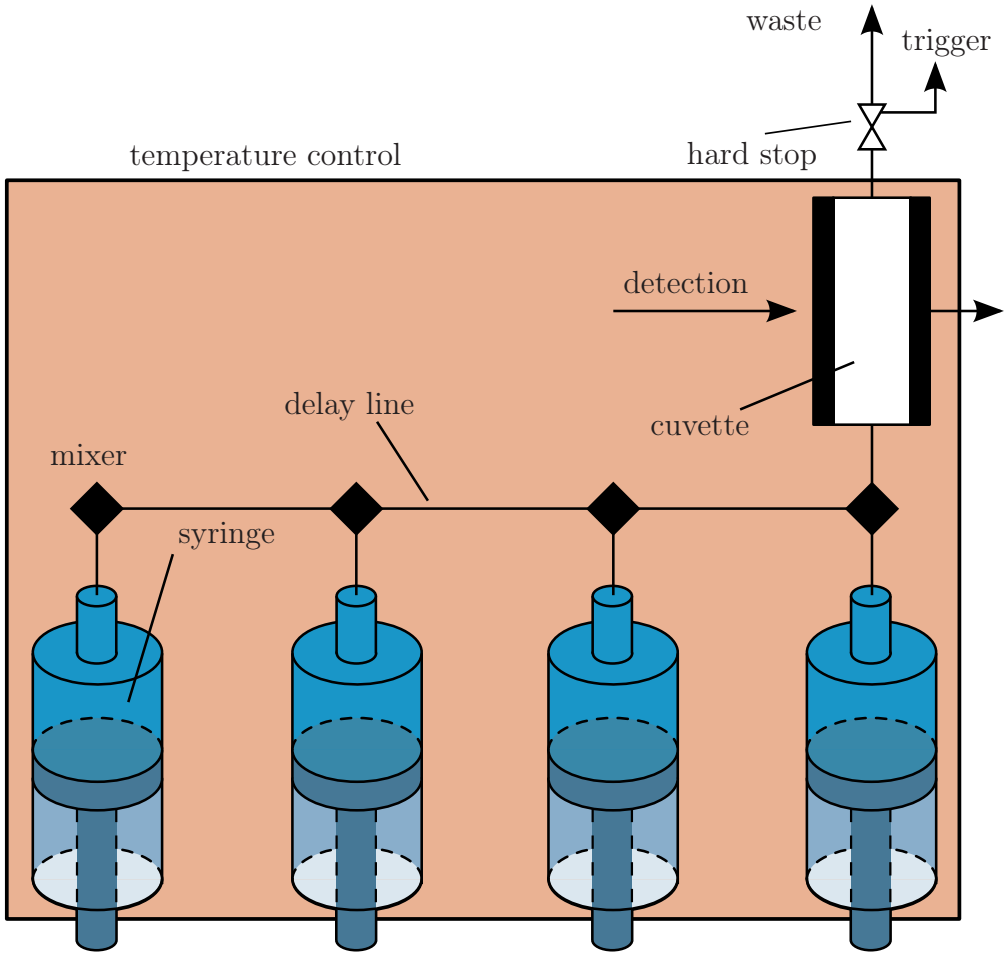

Figure 10.1.1: Schematic assembly of the SFM400/S stopped-flow apparatus

by an Avalanche photodiode (Count-250C-FC, Laser Components). T Flex02-1D digital correlator from correlator.com was used to process the signal.
Measurements with a low time resolution covering a large time range were performed with an ALV/CGS-3 Goniometer system with a 22 mW HeNe-Laser ($\lambda = 622.8$nm) and employing a pseudo cross-correlation under a scattering angle of 90°. The samples were prepared 30s before the first measurement by mixing of adequately chosen volumes of two surfactant stock solutions and homogenized by vigorous shaking. The samples were thermostated at 25°C in a toluene bath during the measurement.
To measure samples in equilibrium, these measurements were performed with the ALV/CGS-3 Goniometer system as described above.

10.1.3 Small Angle Neutron Scattering (SANS)

Kinetic Measurements Kinetic Small Angle Neutron Scattering (SANS) measurements using the stopped-flow technique as described in section 10.1.1 were performed. Here a Bio-

Logic SFM-300 apparatus was employed for the experiments. The dead time for mixing and for filling the observation cell is 25ms at a flow rate of 6mL/s. In order to achieve the time resolution of 25ms, it was required to repeat stopped-flow experiments 10-25 times and to accumulate the scattering intensities of these individual mixing events. The initial length of the measuring times was 50 or 100 ms, and it was increased in a geometric series with an increment of 1.1-1.2, thereby allowing for a good coverage of the scattering for the time range of 100ms to 30min.

The stopped-flow SANS data were obtained on D22 of the Institut Laue-Langevin (ILL) in Grenoble, France, using a 2D-^{3}He detector with 128x128 channels. The samples were measured using a Hellma QS quartz cuvette with a cell thickness of 1mm as stopped-flow cell, thermostated at 25°C. The sample-to-detector distance was 4m, the collimation length was 5.6m, and a wavelength of 0.8nm (FWHM 10%) was employed thereby covering a q-range of (0.01-0.18)nm^{-1}.

The experimentally obtained intensity was radially averaged and then corrected for the transmission and the detector efficiency. The absolute intensity was accounted for by comparison with the scattering from a 1 mm H_2O sample. Data reduction was performed with standard routines supplied by ILL. In these corrections also, the detector dead time and its electronic background were accounted for, and the finally used spectra were obtained by subtracting the scattering from the empty cell and the electronic background, which means that the scattering intensities given here still contain the scattering contribution of the solvent and the incoherent scattering.

Static Measurements Static Small Angle Neutron Scattering (SANS) measurements were performed at two different facilities on two different instruments. All measurements were performed using Hellma QS quartz cuvettes with a cell thickness of 1mm as sample containers.

On the instrument V4 of the Helmholtz-Zentrum Berlin (HZB, Germany) the measurements were performed with neutrons of a wavelength of $\lambda = 6.05$Å with a FWHM of 10.5% at sample-detector distances of 0.975, 4, and 15.865 m and corresponding collimation lengths of 4, 8, and 16 m, respectively. The scattering intensities were detected on a 2-D ^{3}He-detector. The 2-D images were corrected for the electronic background and for the detector efficiency with water as a homogeneous scatterer. The attenuated direct beam was used to determine the transmissions and therefore the absolute intensities.

On the instrument KWS-2 of JCNS (operating at FRMII, Munich, Germany) the measurements were performed with neutrons of a wavelength of $\lambda = 4.7$Å with a FWHM of 20% at

sample-detector distances of 1.4 and 8m, and in addition, with neutrons of a wavelength of $\lambda = 11.8$Å with a FWHM of 20% at a sample-detector distance of 8 m and a collimation length of 8 m. The scattering intensities were detected on a ^{6}Li-scintillation-detector. The 2-D images were corrected for the electronic background and for the detector efficiency with Plexiglas as a homogeneous scatterer. The tail of the unattenuated direct beam was measured by a detector placed on top of the beam stop. This intensity was used to determine the transmissions and therefore the absolute intensities.
The scattering intensity for the empty cell was subtracted and the two dimensional image was azimuthally averaged to obtain the scattering intensity as a function of q. These calculations were done using the data reduction software BerSANS[(85)]. The scattering length densities were determined by the Scattering Length Density Calculator provided by the NIST Center for Research (NIST).[(106)]

10.1.4 Small Angle X-ray Scattering (SAXS)

In this study kinetic measurements were performed using the stopped-flow technique monitoring structural changes with Small Angle X-Ray Scattering. These measurements were performed on ID02 at the European Synchrotron Radiation Facility (ESRF) in Grenoble. Here a BioLogic SFM-400 apparatus was employed for the experiments. The total mixing volume was 600μL and the flow rate 6mL/s. The dead volume was 50μL which leads to a dead time of 8.3ms.
Structural changes were followed in a highly time-resolved SAXS measurement series for a total time of up to 20 minutes. Here the acquisition time was always the same for all measurements but the waiting time between measurements was stretched obeying a geometric series. In addition each experiment consisted of more than one series of measurements to ensure reproducibility and to achieve a good time resolution. The scattering that arises from each mixture was first monitored over a short time range with a high time resolution and than again over a time range of 20 minutes with a lower time resolution. To achieve a higher time resolution each series was started with a different delay time. Measurements were started simultaneously with the mixing procedure so that the first acquisition was performed during mixing, which allowed to check on reprocibility of mixing. All measurement times are calculated relating to the time when the hard stop in the stopped-flow was closed.
To cover a large q-range each experiment was performed at two sample detector distances of 2m and 8m with corresponding q-ranges of (0.052-2.952) 1/nm and (0.012-0.732) 1/nm.
The energy of the X-Ray beam was 12.46keV, what corresponds to a wavelength of 0.996Å. The scattering was recorded on a FReLoN (Fast Readout, Low Noise) Kodak CCD detector, with an input field of 100mm x 100mm, a nominal dynamic range of 16bit, a 4x4 binning

(512x512 pixel) and a read out rate of 5 frames/s and with exposure times of 5 or 10 ms. All scattering patterns were corrected for electronic background, detector efficiency, and electronic effects of the ccd detector in a standard procedure at the ESRF. The azimuthal average of the two-dimensional images was calculated using the software BerSANS[(85)] and the background scattering from the solvent water was subtracted in a matlab application. The data analysis was done with the new developed Matlab based tool SASET for analysing series of small angle scattering data.
The scattering length densities SLD were calculated as described in section 10.1.6

10.1.5 Neutron Diffraction

Neutron diffraction experiments on surfactant crystals were performed on the membrane diffractometer V1 at the Helmholtz-Zentrum Berlin (HZB, Germany) with a wavelength of $\lambda = 5.23$Å. The detector was a 2-dimensional ^{3}He-detector mounted on a goniometer. The crystals were contained in a Hellma QS quartz cuvette with a cell thickness of 1mm. The data were treated in a standard procedure at the HZB and they were not corrected for background scattering or for the absolute intensity since mostly the peak position and not its height is interesting in such an experiment.

10.1.6 SLD-Determination

The scattering length density values used in the analysis of scattering data are always average values of the individual atoms in a molecule over the whole molecule. The scattering length density SLD for a molecule can be calculated from the bound coherent scattering lengths $b_{\mathrm{c,i}}$ of the individual atom by eqn (10.1.1).

$$SLD = \frac{\sum_{i=1}^{n} b_{\mathrm{c},i}}{v_{\mathrm{m}}} \tag{10.1.1}$$

This calculation can be performed with the Scattering Length Density Calculator provided by the NIST Center for Research (NIST).[(106)] Here the the molecular volume v_{m} or the density ρ of the employed compounds are required. Densities of solid components were determined by extrapolating the densities of diluted solutions to a solute content of 100 wt% assuming additivity of the volumes of all components. The densities of solutions with varying solute content were measured using an Anton-Paar DMA 4500 thermostated at 25.00°C. The inverse of the density of the solution $1/\rho$ was plotted over the mass fraction of the solute x_{S} (eqn (10.1.2)). The slope m of the line gives the density ρ_{S} of the pure solute by eqn (10.1.3). The intersect is the inverse of the solvent density $\rho_{\mathrm{solv.}}$

$$\frac{1}{\rho} = \underbrace{\left(\frac{1}{\rho_{\mathrm{S}}} - \frac{1}{\rho_{\mathrm{solv.}}}\right)}_{m} \cdot x_{\mathrm{S}} + \frac{1}{\rho_{\mathrm{solv.}}} \tag{10.1.2}$$

$$\frac{1}{\rho_{\mathrm{S}}} = m + \frac{1}{\rho_{\mathrm{solv.}}} \tag{10.1.3}$$

The surfactant density ρ_{S} and the molar mass M_{S} are connected to the molar volume $v_{\mathrm{m,S}}$ over $M_{\mathrm{S}}/\rho_{\mathrm{S}} = v_{\mathrm{m,S}}$.

10.1.7 Determination of the Critical Micelle Concentration (cmc)/Electrical Conductivity

The critical micelle concentration was determined by measuring the electric conductivity of a sample during dilution with Milli-Q-water. This was done with a Titrando 836 (Metrohm AG) and the conductivity was measured at 25°C by means of a conductometer 712 (Metrohm AG).
By plotting the conductivity versus the surfactant concentration two linear regions are observed. Those linear regimes were interpolated and the intersect marks the cmc. Usually the slope decreases when micelles are formed due to binding of counter ions to the micelles. However, in most micellar systems with an anionic perfluoro surfactant and TDMAO the slope increases above the cmc due to protonation of the TDMAO and the formation of hydroxide ions in the solution.

10.1.8 Viscosity

The viscosity was measured at (25±0.1)°C with an Ubbelohde-Viscosimeter (Schott 0a, recommended for 0.8-5mm^2/s) or an Ostwald-Viscosimeter (Schott Ic, recommended for 3-20mm^2/s). The values for the viscosity were determined from the average of three independent measurements.

10.1.9 Surface Dilatational Rheology

Surface dilatational rheology methods were performed using the oscillating drop tensiometer OCA 20 from Dataphysics. Here a pendant drop of the sample was prepared in air in a closed container over a solvent reservoir. The contour of the droplet was calculated using an axisymetric drop shape analysis by the program provided by Dataphysics. Using the Gauss-Laplace equation the interfacial tension can be calculated from the drop shape.

10.2 Analysis

10.2.1 Small Angle Scattering

The scattering length density of mixed material $SLD_{\text{agg.}}$ is a volume fraction weighted sum of the scattering length densities $SLD_{\text{mol,S}_1}$ and $SLD_{\text{mol,S}_2}$ of two components 1 and 2. The scattering length density contrast ΔSLD is the difference between the scattering length density of the particles $SLD_{\text{agg.}}$ and the average scattering length density of the solvent $SLD_{\text{solv.}}$. The scattering length density $SLD_{\text{agg.}}$ of these mixed aggregates is then described by eqn (10.2.1) and the scattering contrast ΔSLD by eqn (10.2.2) with the molar fraction x_{S_1} of surfactant 1 in the aggregates, with the molar volumes $v_{\text{mol,S}_1}$ and $v_{\text{mol,S}_2}$ of both surfactants and the scattering length densities $SLD_{\text{mol,S}_1}$ and $SLD_{\text{mol,S}_2}$ of both surfactants.

$$SLD_{\text{agg.}} = \frac{x_{\text{S}_1} v_{\text{mol,S}_1} SLD_{\text{mol,S}_1} + (1 - x_{\text{S}_1}) v_{\text{mol,S}_2} SLD_{\text{mol,S}_2}}{x_{\text{S}_1} v_{\text{mol,S}_1} + (1 - x_{\text{S}_1}) v_{\text{mol,S}_2}} \tag{10.2.1}$$

$$\Delta SLD = SLD_{\text{agg.}} - SLD_{\text{solv.}} \tag{10.2.2}$$

To obtain the correct scattering intensity it is important to know the correct number density of aggregates in the solution and therefore the volume fraction of dispersed material θ (see eqn (10.2.3)) with the total surfactant concentration c_{tot}, the molar fraction of surfactant 1 x_{S_1}, the molar masses of the surfactant 1 and 2 M_{S_1} and M_{S_2}, and the densities of the surfactants ρ_{S_1} and ρ_{S_2}.

$$\theta_{\text{amph.}} = c_{\text{tot}} \cdot \left(x_{\text{S}_1} \cdot \frac{M_{\text{S}_1}}{\rho_{\text{S}_1}} + (1 - x_{\text{S}_1}) \frac{M_{\text{S}_2}}{\rho_{\text{S}_2}} \right) \tag{10.2.3}$$

The scattering intensity $I_{\text{ell.}}$ for ellipsoidal aggregates with the form factor $P_{\text{ell.}}$, the rotational axis of the ellipsoid $R_{\text{maj.}}$, the minor axis $R_{\text{min.}}$, the volume fraction of scattering material $\theta_{\text{amph.}}$ and the scattering contrast compared to the surrounding medium ΔSLD is given by:[37]

$$P_{\text{ell.}}(q, R_{\text{maj.}}, R_{\text{min.}}) = \int_0^{\pi/2} \left(3\text{kForm}(q, R_{\text{ell.}}(R_{\text{maj.}}, R_{\text{min.}}, \theta))\right)^2 \cdot \sin(\theta) d\theta \tag{10.2.4}$$

$$I_{\text{ell.}}(q, R_{\text{maj.}}, R_{\text{min.}}) = \frac{\theta_{\text{amph.}} \cdot v_{\text{ell.}}^2(R_{\text{maj.}}, R_{\text{min.}})}{v_{\text{ell.}}(R_{\text{maj.}}, R_{\text{min.}})} \Delta SLD^2 \cdot P_{\text{ell.}}(q, R_{\text{maj.}}, R_{\text{min.}}) \tag{10.2.5}$$

$$\text{with} \quad \text{kForm}(z) = \frac{\sin(z) - z\cos(z)}{z^3} \quad ,$$

$$R_{\text{ell.}}(R_{\text{maj.}}, R_{\text{min.}}, \theta) = \sqrt{R_{\text{min.}}^2 \cos^2(\theta) + R_{\text{maj.}}^2 \sin^2(\theta)} \quad ,$$

$$\text{and} \quad v_{\text{ell.}}(R_{\text{maj.}}, R_{\text{min.}}) = \frac{4\pi}{3} R_{\text{maj.}} R_{\text{min.}}^2$$

The scattering intensity $I_{\mathrm{cyl}}(q)$ for monodisperse cylinders or discs with the form factor $P_{\mathrm{cyl}}(q)$, the length L, the radius R_{cyl}, the volume fraction of the scattering material $\theta_{\mathrm{amph.}}$ and the scattering contrast compared to the surrounding medium ΔSLD is given by:

$$P_{\mathrm{disc}}(q, R_{\mathrm{cyl}}, L) = 4 \int_0^{\pi/2} \left(\frac{\sin\left(\frac{qL}{2}\cos(\theta)\right)}{\frac{qL}{2}\cos(\theta)} \cdot \frac{J_1\left(qR_{\mathrm{cyl}}\sin(\theta)\right)}{\left(qR_{\mathrm{cyl}}\sin(\theta)\right)^2} \right)^2 \sin(\theta) d\theta \tag{10.2.6}$$

$$I_{\mathrm{disc}}(q, R_{\mathrm{cyl}}, L) = \frac{\theta_{\mathrm{amph.}} \cdot v_{\mathrm{cyl}}^2(R_{\mathrm{cyl}}, L)}{v_{\mathrm{cyl}}(R_{\mathrm{cyl}}, L)} \cdot \Delta SLD^2 \cdot P_{\mathrm{disc}}(q, R_{\mathrm{cyl}}, L) \tag{10.2.7}$$

$$\text{with} \quad v_{\mathrm{cyl}}(R_{\mathrm{cyl}}, L) = \pi R_{\mathrm{cyl}}^2 L$$

where J_1 is the Bessel function of the first order.
That leads to the following scattering intensity for the micelles with a log-normal distributed length L for cylindrical micelles:

$$I_{\mathrm{disc}}(q, R_{cyl}, L_0, \sigma) = \theta_{amph.} \cdot \frac{\int_0^\infty LogNorm(L, L_0, \sigma) \cdot v_{\mathrm{cyl}}^2(R_{\mathrm{cyl}}, L) \cdot \Delta SLD^2 \cdot P_{\mathrm{disc}}(q, R_{\mathrm{cyl}}, L) dL}{\int_0^\infty LogNorm(L, L_0, \sigma) v_{\mathrm{cyl}}(R_{cyl}, L) dL} \tag{10.2.8}$$

The log-normal distribution of a parameter t is given as:[21]

$$LogNorm(t, \mu, \sigma) = \frac{1}{t\sqrt{2\pi}\sigma_{\mathrm{L}}(\mu, \sigma)} \exp\left(\frac{-(\ln(t) - \mu_{\mathrm{L}}(\mu, \sigma))^2}{2\sigma_{\mathrm{L}}^2(\mu, \sigma)} \right) \tag{10.2.9}$$

The parameters μ_{L} and σ_{L} are linked to the mean μ of the distribution and the standard deviation σ:

$$\sigma_{\mathrm{L}}(\mu, \sigma) = \sqrt{\ln\left(\frac{\sigma^2}{\mu^2} + 1\right)} \tag{10.2.10}$$

$$\mu_{\mathrm{L}}(\mu, \sigma) = \ln(\mu) - \frac{\sigma_{\mathrm{L}}^2(\mu, \sigma)}{2} \tag{10.2.11}$$

In SANS measurements the scattering arising from vesicles was modelled as scattering coming from spherical shells with a homogeneous shell of the thickness D. For polydisperse vesicles (spherical shells) with a log-normal distributed (see eqn (10.2.9)) intermediate radius R, a mean radius $R_{\mathrm{ves.}}$ and a relative standard deviation $\sigma_{\mathrm{rel}} = \sigma/\mu$, here often referred to as polydispersity or polydispersity index PDI, the scattering intensity is given by:

$$f_1(R,D) = \frac{4\pi R_1^3(R,D)}{3}(SLD_{\text{solv.}} - SLD_{\text{agg.}}) \cdot \text{kForm}(qR_1(R,D)) \quad (10.2.12)$$

$$\text{with } R_1(R,D) = R - \frac{D}{2}$$

$$f_2(R,D) = \frac{4\pi R_2^3(R,D)}{3}(SLD_{\text{agg.}} - SLD_{\text{solv.}}) \cdot \text{kForm}(qR_2(R,D)) \quad (10.2.13)$$

$$\text{with } R_2(R,D) = R + \frac{D}{2}$$

$$I_{\text{ves.}}(R_{\text{ves.}}, D, PDI) = \frac{\theta_{\text{amph.}}}{\langle v_{\text{ves. shell}}\rangle(R_{\text{ves.}}, D, PDI)} \cdot \int_0^\infty \text{LogNorm}(R, R_{\text{ves.}}, PDI)(f_1(R,D) + f_2(R,D))^2 dR \quad (10.2.14)$$

In the analysis it was assumed that the bilayer thickness D of the vesicles does not change with the radius R. So the average volume $\langle v_{\text{ves. shell}}\rangle$ of the vesicle shell can be described by eqn (10.2.16).

$$v_{\text{ves. shell}}(R,D) = \frac{4\pi}{3}\left(R_2(R,D)^3 - R_1(R,D)^3\right) \quad (10.2.15)$$

$$\langle v_{\text{ves. shell}}\rangle(R_{\text{ves.}}, D, PDI) = \int_0^\infty \text{LogNorm}(R, R_{\text{ves.}}, PDI) v_{\text{ves. shell}}(R,D) dR \quad (10.2.16)$$

In SAXS measurements it proved necessary to refine the vesicle model and to take into account the scattering length density profile of the vesicle bilayer and the bilayer of disc-like micelles. In all measurements the aggregates consisted of mixed bilayers of two surfactant with different scattering length densities and different length, so that a step-wise SLD-profile along the bilayer can be expected. The maximal value that the overall thickness D can reach is twice the length of the longer surfactant. The inside of the bilayer with the length $D_{\text{core}} = D - 2 \cdot t$ consists only of the longer surfactant S_1 with a scattering length density of $SLD_{\text{core}} = SLD_{\text{S}_1}$. The outer parts of the bilayer are a mixture of both surfactants with a thickness t that correspondents to the length of the shorter surfactant S_2 and a scattering length density SLD_{shell} which is a volume weighted sum of the scattering length densities of both surfactants. Both parameters D and t are fit parameters and were not set equal to the length of the stretched chain of the two surfactants, because interdigitation can be expected. As a simplification the same SLD-profile was assumed for the disc bilayer and for the vesicle. As the only difference for the vesicles an asymmetry for the bilayer contrast was

introduced. That means it was assumed that the perfluoro surfactant was not distributed equally on the inner part of the bilayer and the outer part. The bilayer profile results in an oscillation at high q-values. The asymmetry in the bilayer causes the minimum of the oscillation to be smeared out but has no effect on the position of the minimum or on the slope of the scattering curve in the mid q-range.

10.2.1 shows a scheme of a disc-like micelle with a core-shell contrast. The scattering that arises from the micelles is described in eqn (10.2.19). R_{disc} is the radius of the discs. In reality the disc radius has a broad distribution. Here the polydispersity for the disc radius was set to a fixed value to reduce computational time.

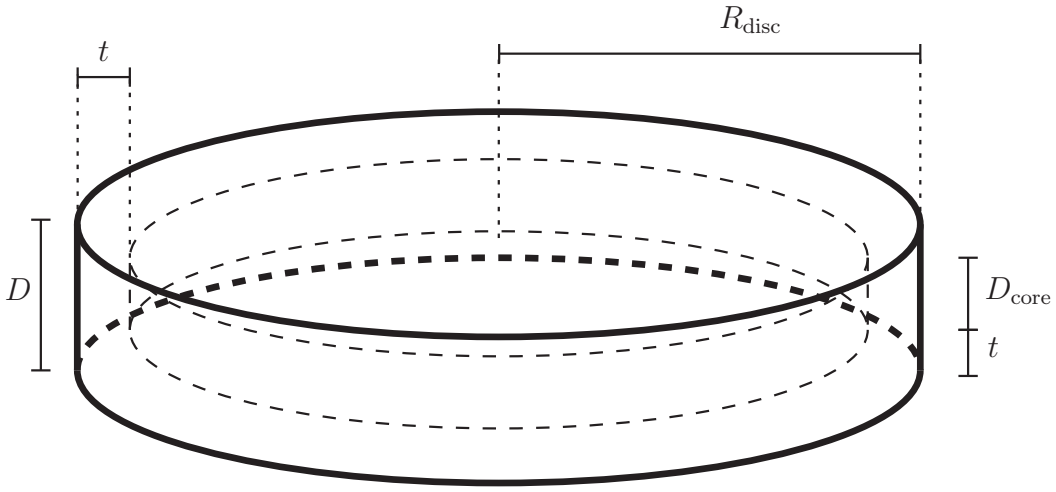

Figure 10.2.1: Disc-like micelle with core-shell contrast

$$f_1 = 2\left(SLD_{\text{core}} - SLD_{\text{shell}}\right)\pi\left(R_{\text{disc}} - t\right)^2 D_{\text{core}} \cdot \frac{\sin\left(\frac{D_{\text{core}}}{2}\cos(\theta)q\right)}{\frac{D_{\text{core}}}{2}\cos(\theta)q} \cdot \frac{J_1\left(q\left(R_{\text{disc}} - t\right)\sin(\theta)\right)}{q\left(R_{\text{disc}} - t\right)\sin(\theta)} \tag{10.2.17}$$

$$f_2 = 2\left(SLD_{\text{shell}} - SLD_{\text{medium}}\right)\pi R_{\text{disc}}^2 D \cdot \frac{\sin\left(\frac{D}{2}\cos(\theta)q\right)}{\frac{D}{2}\cos(\theta)q} \cdot \frac{J_1 q\left(R_{\text{disc}}\sin(\theta)\right)}{qR_{\text{disc}}\sin(\theta)} \tag{10.2.18}$$

$$I_{\text{core-shell disc}} = \int_0^{2\pi} \left(f_1 + f_2\right)^2 \sin(\theta) d\theta \tag{10.2.19}$$

10.2.2 shows a scheme of the SLD-profile of the vesicle in dependence of the distance to the vesicle centre R. The bilayer shows the same SLD-profile as the bilayer in the disc-like micelles except for an asymmetry in the vesicle bilayer that is indicated in the scheme with dotted lines. The size distribution of the vesicles is described by a LogNormial distribution eqn (10.2.9) with the mean radius $R_{\text{ves.}}$ and the relative standard deviation σ_{rel}. The bilayer thickness parameters D and t are assumed to be equal for all aggregates in the sample. The

average volume of the vesicle shell $\langle v_{\text{ves. shell}} \rangle$ is described in 10.2.25. The scattering intensity that arises from the vesicles is described in 10.2.26.

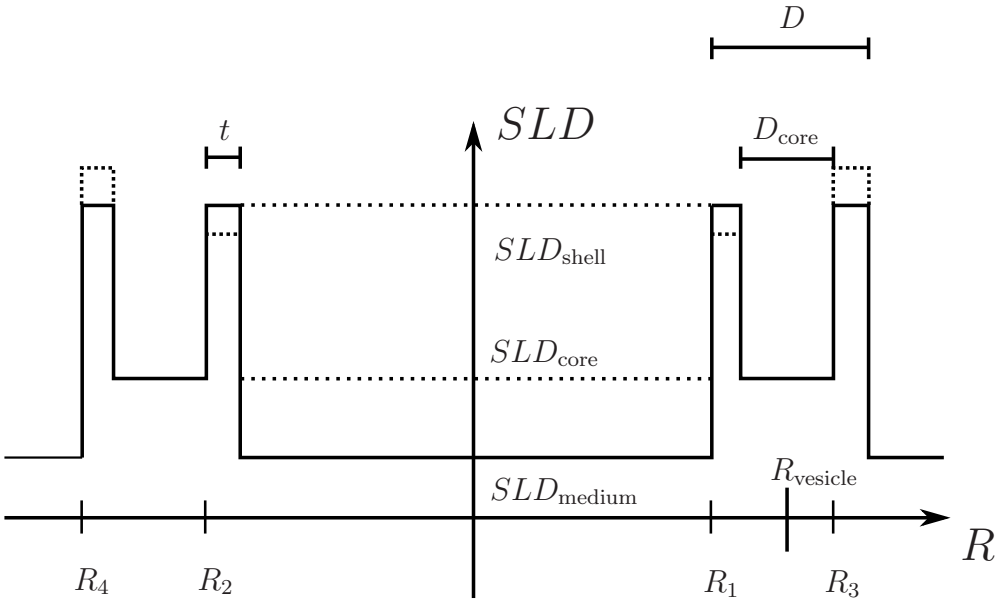

Figure 10.2.2: Scattering length density profile of the vesicle in dependence of the distance to the vesicle centre R

$$f_1(R) = 4\pi R_1^3 \cdot (SLD_{\text{sol}} - SLD_{\text{shell}}) \cdot \frac{\sin(qR_1) - qR_1\cos(qR_1)}{(qR_1)^3} \text{ with } R_1 = R - \frac{D}{2} \tag{10.2.20}$$

$$f_2(R) = 4\pi R_2^3 \cdot (SLD_{\text{shell}} - SLD_{\text{core}}) \cdot \frac{\sin(qR_2) - qR_2\cos(qR_2)}{(qR_2)^3} \text{ with } R_2 = R - \frac{D_{\text{core}}}{2} \tag{10.2.21}$$

$$f_3(R) = 4\pi R_3^3 \cdot (SLD_{\text{core}} - SLD_{\text{shell}}) \cdot \frac{\sin(qR_3) - qR_3\cos(qR_3)}{(qR_3)^3} \text{ with } R_3 = R + \frac{D_{\text{core}}}{2} \tag{10.2.22}$$

$$f_4(R) = 4\pi R_4^3 \cdot (SLD_{\text{shell}} - SLD_{\text{sol}}) \cdot \frac{\sin(qR_4) - qR_4\cos(qR_4)}{(qR_4)^3} \text{ with } R_4 = R + \frac{D}{2} \tag{10.2.23}$$

$$v_{\text{ves. shell}}(R,D) = \frac{4\pi}{3}\left(R_4(R,D)^3 - R_1(R,D)^3\right) \tag{10.2.24}$$

$$\langle v_{\text{ves. shell}}\rangle(R_{\text{ves.}},D,\sigma_{\text{rel}}) = \int_0^\infty \text{LogNorm}(R,R_{\text{ves.}},\sigma_{\text{rel}})v_{\text{ves. shell}}(R,D)dR \tag{10.2.25}$$

$$I_{\text{vesicle}} = \int_0^\infty \text{LogNorm}\left(R,R_{\text{vesicle}},\sigma_{\text{rel}}\right) \cdot \left(f_1(R)+f_2(R)+f_3(R)+f_4(R)\right)^2 dR \tag{10.2.26}$$

The RPA structure factor for electrostatic repulsion $S(q)$ is described by eqn (10.2.27) with the effective radius R_{eff} and the surface potential ζ as fit parameters and the inverse Debye screening length k_{D}, the Boltzmann constant k_{B}, the temperature T and the dielectric constant of the medium, here water, ι as constant parameters.

$$S(q) = \frac{1}{1-nC(q)} \tag{10.2.27}$$

$$nC_0(q) = \left[A(\sin(x)-x\cos(x)) + B\left[\left(\frac{2}{x^2}-1\right)x\cos(x)+2\sin(x)-\frac{2}{x}\right] -\frac{\theta_{\text{eff}}A}{2}\left[\frac{24}{x^3}+4\left(1-\frac{6}{x^2}\right)\sin(x)-\left(1-\frac{12}{x^2}+\frac{24}{x^4}\right)x\cos(x)\right]\right]x^{-3} \tag{10.2.28}$$

with $\quad x = 2qR_{\text{eff}}$

$$nC(q) = nC_0(q) - 48\frac{\theta_{\text{eff}}\pi\iota R_{\text{eff}}\zeta^2(x\cos(x)+2k_{\text{D}}R_{\text{eff}}\sin(x))}{k_{\text{B}}Tx(x^2+4k_{\text{D}}^2R_{\text{eff}}^2)} \tag{10.2.29}$$

with the factors

$$A = -24\theta_{\text{eff}}\frac{(1+2\theta_{\text{eff}})^2}{(1-\theta_{\text{eff}})^4} \quad \text{and} \quad B = 36\theta_{\text{eff}}^2\frac{(2+\theta_{\text{eff}})^2}{(1-\theta_{\text{eff}})^4}$$

The effective volume fraction of the particles θ_{eff} is calculated from the particle number density N_{V} which is determined from the form factor.

$$\theta_{\text{eff}} = N_{\text{V}}\pi\frac{4}{3}R_{\text{eff}}^3 \tag{10.2.30}$$

The particle number density N_{V} is described for the form factor as well as for the structure factor by eqn (10.2.31).

$$N_{\text{V}} = \frac{\theta_{\text{amph.}}}{V_{\text{aggregate}}} \tag{10.2.31}$$

In the case of polydisperse particles with a normalised distribution *dist* of a parameter t the particle number density is described by eqn (10.2.32).

$$N_{\mathrm{V}} = \frac{\theta_{\mathrm{amph.}}}{\int_0^\infty dist(t, t_0, \sigma) \cdot V_{\mathrm{aggregate}}(t) dt} \tag{10.2.32}$$

The volume of the aggregates $V_{aggregate}$ being the volume of scattering material in a single aggregate. For vesicles that would be only the vesicle shell.

10.2.2 Dynamic Light Scattering (DLS)

Data from DLS measurements can either be evaluated by a monoexponential fit to $g^{(2)}$ if the system is rather monodisperse or by a cumulant analysis in the case of moderate polydispersities or a biexponential fit if two relaxation rates can be observed. In the last case the polydispersity of both particle species can not easily be determined.
In a monoexponential relaxation the particle hydrodynamic radius R_{h} can simply be calculated from the relaxation time τ_1 as described in eqns (9.1.37), (9.1.45) and (10.2.33).

$$g^{(2)}(\tau) = 1 + \beta_{\mathrm{s}} \exp\left(-\frac{2\tau}{\tau_1}\right) \tag{10.2.33}$$

In a cumulant analysis an average hydrodynamic radius radius $\langle R_{\mathrm{h}} \rangle$ can be obtained from an average relaxation rate $\langle \Gamma \rangle$ as well as a polydispersity index (see eqns (9.1.37), (9.1.44) and (9.1.45)). In this study to analyse data with the cumulant method, the intensity autocorrelation function was described with eqn (9.1.44). For values far above $\tau = 1/\langle \Gamma \rangle$ the fit show strong deviations from the measured data because the cumulant analysis is only valid for small values of τ. As a result the fit area for the cumulant analysis only reaches to the relaxation time.
In a biexponential fit according to eqn (10.2.34) two average hydrodynamic radii $R_{\mathrm{h},1}$ and $R_{\mathrm{h},2}$ of two species can be obtain from eqns (9.1.37), (9.1.45) and (10.2.34)

$$g^{(2)}(\tau) = 1 + \beta_{\mathrm{s},1} \exp\left(-\frac{2\tau}{\tau_1}\right) + \beta_{\mathrm{s},2} \exp\left(-\frac{2\tau}{\tau_2}\right) \tag{10.2.34}$$

10.3 Materials

The tetradecyldimethylamine oxide (TDMAO, $C_{14}H_{39}(CH_3)_2NO$) was kindly given by Stepan (Stepan Company, Northfield, Illinois, USA) as a 25% TDMAO solution in water named Ammonyx M. This solution was freeze-dried and used without further purification. The cmc

measurements were done with TDMAO, kindly provided by Clariant (Germany), which was purified by recrystallizing twice from acetone. Both TDMAO batches (from Stepan and from Clariant) had very similar cmc values of 0.15mM and 0.14mM respectively determined by surface tension measurements. Perfluorohexanoic acid ($C_5F_{11}CO_2H$, 97%), perfluoroheptanoic acid ($C_6F_{13}CO_2H$, 95%) and lithium hydroxide ($LiOH \cdot H_2O$, $> 99\%$) were purchased from Fluka. Perfluorooctanoic acid ($C_7F_{15}CO_2H$, 96%) was purchased from Sigma-Aldrich. Lithium perfluorooctylsulfonate (LiPFOS $C_8F_{17}SO_3Li$, $> 96\%$) was purchased from TCI Europe and used without further purification. The characteristic parameters of the surfactants are summarized in Table 10.3.1.
Pluronic L35 ($EO_{11}PO_{16}EO_{11}$), Pluronic 10R5 ($PO_8EO_{22}PO_8$), Pluronic F38 ($EO_{46}PO_{16}EO_{46}$), Pluronic F88 ($EO_{102}PO_{41}EO_{102}$), and Pluronic F108 ($EO_{132}PO_{52}EO_{132}$) were kindly given by BASF (BASF SE, Ludwigshafen, Germany) and used without further purification. The characteristic parameters of the Pluronics are summarized in Table 10.3.2. Hydrochloric acid was purchased from Sigma-Aldrich as a 0.5N volumetric solution and used as supplied. Deuterium oxide ($D_2O > 99.96\%$) was purchased from Eurisotop.
The perfluoro carboxylate solutions were prepared by dissolving the acid in water and neutralizing with LiOH solution to the equivalence point. TDMAO and LiPFOS solutions were prepared by dissolving the surfactants in water. Stock solutions with TDMAO and polymers were prepared by dissolving TDMAO and the polymers in water and stock solutions with TDMAO and HCl were prepared by dissolving TDMAO in water together with the required amount of HCl solution. All surfactant solutions were prepared using water, that was filtered twice by a Millipore water filter. All SANS samples were prepared using D_2O instead of H_2O, in order to have enhanced contrast conditions and low incoherent background.
Samples were always prepared from stock solutions. Therefore pure perfluoro surfactant solutions were mixed with TDMAO solutions that contained the additives. Before mixing the required amounts of both solutions were determined by weight and then mixed at once. Samples used for measurements in equilibrium were prepared as mixtures of the stock solutions, homogenized by vigorous shaking by a vortex mixer, and then equilibrated at 25°C for at least two days before the measurement. For kinetic measurements adequate amounts of a pure perfluoro surfactant solution and a TDMAO solution with additives were determined by weight and mixed directly before the measurements. Samples for measurements performed in the stopped-flow were prepared by mixing the stock solutions in the stopped-flow at adequate ratios and with the chosen flow rate. Surfactant stock solutions and surfactant-polymer stock solutions were prepared by solubilising the solid surfactants and the polymer in water, that was filtered twice by a Millipore water filter.

Table 10.3.1: Density ρ, scattering length density SLD_{neutron} for neutrons, scattering length density $SLD_{\text{x-ray}}$ for x-rays with a wavelength of λ=0.1nm, critical micelle concentration *cmc* and molecular weight M_W of the used surfactants

molecular formular	ρ /(g/mL)	$SLD_{\text{neutron}}/(\text{nm}^{-2})$	$SLD_{\text{x-ray}}/(\text{nm}^{-2})$	M_W/(g/mol)	*cmc*/(mmol/L)
$C_{14}H_{29}(CH_3)_2NO$	0.897	$-1.96 \cdot 10^{-5}$	$8.64 \cdot 10^{-4}$	257.46	0.12 [63]
$C_5F_{11}CO_2Li$	2.019	$4.25 \cdot 10^{-4}$	$1.66 \cdot 10^{-3}$	319.98	230 [105]
$C_6F_{13}CO_2Li$	1.947	$4.11 \cdot 10^{-4}$	$1.6 \cdot 10^{-3}$	369.99	90 [105]
$C_7F_{15}CO_2Li$	1.922	$4.07 \cdot 10^{-4}$	$1.58 \cdot 10^{-3}$	420.00	33.4 [107]
$C_8F_{17}SO_3Li$	2.081	$4.15 \cdot 10^{-4}$	$1.71 \cdot 10^{-3}$	506.05	6.3 [131]

Table 10.3.2: Density ρ, scattering length density SLD_{neutron} for neutrons, scattering length density $SLD_{\text{x-ray}}$ for x-rays with a wavelength of λ=0.1nm, and average molecular weight M_W of the used Pluronics

Pluronic	molecular formular	ρ /(g/mL)	$SLD_{\text{neutron}}/(\text{nm}^{-2})$	$SLD_{\text{x-ray}}/(\text{nm}^{-2})$	M_W/(g/mol)
Pluronic 10R5	PO_8–EO_{22}–PO_8	1.058	$4.84 \cdot 10^{-5}$	$9.89 \cdot 10^{-4}$	1950
Pluronic L35	EO_{11}–PO_{16}–EO_{11}	1.06	$4.84 \cdot 10^{-5}$	$9.89 \cdot 10^{-4}$	1900
Pluronic F38	EO_{46}–PO_{16}–EO_{46}	1.07	$5.56 \cdot 10^{-5}$	$9.85 \cdot 10^{-4}$	4700
Pluronic F88	EO_{102}–PO_{41}–EO_{102}	1.06	$5.50 \cdot 10^{-5}$	$9.86 \cdot 10^{-4}$	11400
Pluronic F108	EO_{132}–PO_{52}–EO_{132}	1.06	$5.51 \cdot 10^{-5}$	$9.86 \cdot 10^{-4}$	14600

References

[1] Almgren, M. and Garamus, V., *J. Phys. Chem. B*, 2005, **109**(22), 11348–11353, doi:10.1021/jp0502510.

[2] Almgren, M., Garamus, V.M., Asakawa, T., and Jiang, N., *J. Phys. Chem. B*, 2007, **111**(25), 7133–7141, doi:10.1021/jp070271x.

[3] Almgren, M., Garamus, V.M., Nordstierna, L., Luc-Blin, J., and Stébé, M.J., *Langmuir*, 2010, **26**(8), 5355–5363, doi:10.1021/la903764u.

[4] Almgren, M., Wang, K., and Asakawa, T., *Langmuir*, 1997, **13**(17), 4535–4544, doi:10.1021/la970238+.

[5] Amato, M., Caponetti, E., Martino, D., and Pedone, L., *J. Phys. Chem. B*, 2003, **107**(37), 10048–10056, doi:10.1021/jp022697b.

[6] Ambühl, M., Bangerter, F., Luisi, P.L., Skrabal, P., and Watzke, H.J., *Langmuir*, 1993, **9**(1), 36–38, doi:10.1021/la00025a011.

[7] Ashcroft, N.W. and Lekner, J., *Phys. Rev.*, 1966, **145**(1), 83–90, doi:10.1103/PhysRev.145.83.

[8] Baba-Ahmed, L., Benmouna, M., and Grimson, M.J., *Phys. Chem. Liq.*, 1987, **16**(3), 235–238, doi:10.1080/00319108708078524.

[9] Baoukina, S., Monticelli, L., Risselada, H.J., Marrink, S.J., and Tieleman, D.P., *Proc. Nat. Acad. Sci. U.S.A.*, 2008, **105**(31), 10803–10808, doi:10.1073/pnas.0711563105.

[10] Barenholz, Y., Gibbes, D., Litman, B.J., Goll, J., Thompson, T.E., and Carlson, F.D., *Biochemistry-US*, 1977, **16**(12), 2806–2810, doi:10.1021/bi00631a035.

[11] Barthelemy, P., Tomao, V., Selb, J., Chaudier, Y., and Pucci, B., *Langmuir*, 2002, **18**(7), 2557–2563, doi:10.1021/la011600u.

[12] Baumgart, T., Hess, S.T., and Webb, W.W., *Nature*, 2003, **425**(6960), 821–824, doi:10.1038/nature02013.

[13] Bergmeier, M., Hoffmann, H., Witte, F., and Zourab, S., *J. Colloid Interface Sci.*, 1998, **203**(1), 1–15, doi:10.1006/jcis.1998.5486.

[14] Bergstrom, L., *Langmuir*, 2006, **22**(8), 3678–3691, doi:10.1021/la052800z.

[15] Bernheim-Groswasser, A., Zana, R., and Talmon, Y., *J. Phys. Chem. B*, 2000, **104**(17), 4005–4009, doi:10.1021/jp994301a.

[16] Betageri, G. and Parsons, D., *Int. J. Pharm.*, 1992, **81**, 235–241, doi:10.1016/0378-5173(92)90015-T.

[17] Boden, N., Clements, J., Jolley, K., Parker, D., and Smith, M., *J. Chem. Phys.*, 1990, **93**, 9096–9106, doi:10.1063/1.459200.

[18] Brasher, L.L., Herrington, K.L., and Kaler, E.W., *Langmuir*, 1995, **11**(11), 4267–4277, doi:10.1021/la00011a017.

[19] Bressel, K., Muthig, M., Prévost, S., Grillo, I., and Gradzielski, M., *Colloid. Polym. Sci.*, 2010, **288**(8), 827–840, doi:10.1007/s00396-010-2212-z.

[20] Bressel, K., Prévost, S., Appavou, M.S., Tiersch, B., Koetz, J., and Gradzielski, M., *Soft Matter*, 2011, **7**(23), 11232–11242, doi:10.1039/C1SM05618B.

[21] Bronstein, I.N. and Semendjajew, K.A., *Taschenbuch der Mathematik*, Verlag Harri Deutsch, Thun und Frankfurt am Main, 5 edn., 2000.

[22] Calero, N., Alfaro, C., García, C., Berjano, M., Lluch, A., and Muñoz, J., *Chem. Eng. Technol.*, 2011, **34**(9), 1473–1480, doi:10.1002/ceat.201100020.

[23] Calero, N., Alfaro, C., Lluch, A., Berjano, M., and Muñoz, J., *Chem. Eng. Technol.*, 2010, **33**(3), 481–488, doi:10.1002/ceat.200900496.

[24] Carrière, D., Belloni, L., Demé, B., Dubois, M., Vautrin, C., Meister, A., and Zemb, T., *Soft Matter*, 2009, **5**, 4983–4990, doi:10.1039/B912286A.

[25] Cates, M.E. and Candau, S.J., *J. Phys. Condens. Matter*, 1990, **2**(33), 6869–6892, doi:10.1088/0953-8984/2/33/001.

[26] Coldren, B., Warriner, H., van Zanten, R., Zasadzinski, J., and Sirota, E., *Langmuir*, 2006, **22**(6), 2474–2481, doi:10.1021/la052448p.

[27] Coldren, B., van Zanten, R., Mackel, M.J., Zasadzinski, J.A., and Jung, H.T., *Langmuir*, 2003, **19**(14), 5632–5639, doi:10.1021/la034311+.

[28] Coldren, B.A., Warriner, H., van Zanten, R., Zasadzinski, J.A., and Sirota, E.B., *Langmuir*, 2006, **22**(6), 2465–2473, doi:10.1021/la052447x.

[29] Cuomo, F., Lopez, F., Miguel, M.G., and Lindman, B., *Langmuir*, 2010, **26**(13), 10555–10560, doi:10.1021/la100584b.

[30] Danino, D., Talmon, Y., and Zana, R., *Langmuir*, 1995, **11**(5), 1448–1456, doi:10.1021/la00005a008.

[31] Dietrich, C., Bagatolli, L., Volovyk, Z., Thompson, N., Levi, M., Jacobson, K., and Gratton, E., *Biophys. J.*, 2001, **80**(3), 1417–1428, doi:10.1016/S0006-3495(01)76114-0.

[32] Dörfler, H.D., *Grenzflächen und kolloid-disperse Systeme*, Springer-Verlag Berlin, Heidelberg, 2002.

[33] Dubois, M., Demé, B., Gulik-Krzywicki, T., Dedieu, J.C., Vautrin, C., Desért, S., Perez, E., and Zemb, T., *Nature*, 2001, **411**(6838), 672–675, doi:10.1038/35079541.

[34] Dukhin, S.S., Kretzschmar, G., and Miller, R., *Dynamics of Adsorption at Liquid Interfaces*, vol. 1, Elsevier Science, 1995.

[35] Edwards, D.K., Brenner, H., and Wasan, D.T., *Interfacial Transport Processes and Rheology*, Butterworth-Heinemann Publischers, 1991.

[36] Egelhaaf, S.U. and Schurtenberger, P., *Phys. Rev. Lett.*, 1999, **82**(13), 2804–2807, doi:10.1103/PhysRevLett.82.2804.

[37] Feigin, L.A. and Svergun, D.I., *Structure Analysis by Small-Angle X-Ray and Neutron Scattering*, Plenum Press, New York, 233 Spring Street, New York, N. Y. 10013, 1987.

[38] Felgner, J.H., Kumar, R., Sridhar, C.N., Wheeler, C.J., Tsai, Y.J., Border, R., Ramsey, P., Martin, M., and Felgner, P.L., *J. Biol. Chem.*, 1994, **269**(4), 2550–2561.

[39] Frømyr, T., Hansen, F.K., Kotzev, A., and Laschewsky, A., *Langmuir*, 2001, **17**(17), 5256–5264, doi:10.1021/la001407k.

[40] Fukuda, H., Kawata, K., Okuda, H., and Regen, S.L., *J. Am. Chem. Soc.*, 1990, **112**(4), 1635–1637, doi:10.1021/ja00160a057.

[41] Ghoroghchian, P.P., Lin, J.J., Brannan, A.K., Frail, P.R., Bates, F.S., Therien, M.J., and Hammer, D.A., *Soft Matter*, 2006, **2**(11), 973–980, doi:10.1039/B604212K.

[42] Gonzalez-Perez, A., Schmutz, M., Waton, G., and Romero, M.J.and Krafft, M., *J. Am. Chem. Soc.*, 2007, **129**(4), 756–757, doi:10.1021/ja067228s.

[43] Gorski, N., Gradzielski, M., and Hoffmann, H., *Langmuir*, 1994, **10**(8), 2594–2603, doi:10.1021/la00020a018.

[44] Gorski, N. and Kalus, J., *J. Phys. Chem. B*, 1997, **101**(22), 4390–4393, doi:10.1021/jp9704776.

[45] Gräbner, D., Gradzielski, M., and Grillo, I., *ILL Annual Report*, 2001, pp. 74–75.

[46] Gradzielski, M., *Curr. Opin. Colloid In.*, 2003, **8**(4-5), 337–345, doi:10.1016/S1359-0294(03)00080-3.

[47] Gradzielski, M., *J. Phys. Condens. Matter*, 2003, **15**(19), R655–R697, doi:10.1088/0953-8984/15/19/202.

[48] Gradzielski, M., Bergmeier, M., Hoffmann, H., Muller, M., and Grillo, I., *J. Phys. Chem. B*, 2000, **104**(49), 11594–11597, doi:10.1021/jp0028913.

[49] Gradzielski, M., Grillo, I., and Narayanan, T., *Prog. Colloid Polym. Sci.*, 2004, **129**, 263–271, doi:10.1007/b100300.

[50] Gradzielski, M., Muller, M., Bergmeier, M., Hoffmann, H., and Hoinkis, E., *J. Phys. Chem. B*, 1999, **103**(9), 1416–1424, doi:10.1021/jp9833303.

[51] Grosberg, A.Y. and Kholokov, A.R., *Statistical physics of macromolecules*, AIP Series in Polymers and Complex Materials, AIP Press, New York, American Institute of Physics, 500 Sunnyside Boulevard, Woodbury, New York, 1994.

[52] Gummel, J., Sztucki, M., Narayanan, T., and Gradzielski, M., *Soft Matter*, 2011, **7**, 5731–5738, doi:10.1039/c1sm05354j.

[53] Guo, W., Guzman, E.K., Heavin, S.D., Li, Z., Fung, B.M., and Christian, S.D., *Langmuir*, 1992, **8**(10), 2368–2375, doi:10.1021/la00046a006.

[54] Hansen, S., *J. Chem. Phys.*, 2004, **121**(18), 9111–9115, doi:10.1063/1.1803533.

[55] Hao, J. and Hoffmann, H., *Curr. Opin. Colloid In.*, 2004, **9**(3–4), 279–293, doi:10.1016/j.cocis.2004.06.004.

[56] Hao, J., Hoffmann, H., and Horbaschek, K., *Langmuir*, 2001, **17**(14), 4151–4160, doi:10.1021/la0017779.

[57] Helfrich, W., *Zeitschrift für Naturforschung. Teil C: Biochemie, Biophysik, Biologie, Virologie*, 1973, **28c**, 693–703.

[58] Helfrich, W., *J. Phys.*, 1986, **47**, 321–329, doi:10.1051/jphys:01986004702032100.

[59] Hentze, H.P., Raghavan, S.R., McKelvey, C.A., and Kaler, E.W., *Langmuir*, 2003, **19**(4), 1069–1074, doi:10.1021/la020727w.

[60] Hernández-Zapata, E., Martìnez-Balbuena, L., and Santamaria-Holek, I., *J. Biol. Phys.*, 2009, **35**(3), 297–308, doi:10.1007/s10867-009-9169-5.

[61] Herrington, K.L., Kaler, E.W., Miller, D.D., Zasadzinski, J.A., and Chiruvolu, S., *J. Phys. Chem.*, 1993, **97**(51), 13792–13802, doi:10.1021/j100153a058.

[62] Hoffmann, H., Oetter, G., and Schwandner, B., *Prog. Colloid Polym. Sci.*, 1987, **73**, 95–106, doi:10.1007/3-798-50724-4_68.

[63] Hoffmann, H. and Pössnecker, G., *Langmuir*, 1994, **10**(2), 381–389, doi:10.1021/la00014a009.

[64] Hoffmann, H., Thunig, C., Schmiedel, P., and Munkert, U., *Langmuir*, 1994, **10**(11), 3972–3981, doi:10.1021/la00023a013.

[65] Hoffmann, H., Thunig, C., Schmiedel, P., and Munkert, U., *Faraday Discuss.*, 1995, **101**, 319–333, doi:10.1039/FD9950100319.

[66] Hoffmann, H., Witte, F., and Würtz, J., in F. Mallamace and H.E. Stanley (Eds.), 'Proceedings of the International School of Physics Enrico Fermi', vol. Course CXXXIV, IOS Press, Amsterdam, 1996 pp. 391–416.

[67] Hoffmann, H. and Würtz, J., *J. Mol. Liq.*, 1997, **72**(1-3), 191–230, doi:10.1016/S0167-7322(97)00039-1.

[68] Holland, P.M. and Rubingh, D.N., *J. Phys. Chem.*, 1983, **87**(11), 1984–1990, doi:10.1021/j100234a030.

[69] Hope, M., Bally, M., Webb, G., and Cullis, P., *BBA - Biomembranes*, 1985, **812**(1), 55–65, doi:10.1016/0005-2736(85)90521-8.

[70] Huang, C.H., *Biochemistry-US*, 1969, **8**(1), 344–352, doi:10.1021/bi00829a048.

[71] Huang, J.B. and Zhao, G.X., *Colloid. Polym. Sci.*, 1995, **273**(2), 156–164, doi:10.1007/BF00654013.

[72] Hubert, D.H.W., Jung, M., Frederik, P.M., Bomans, P.H.H., Meuldijk, J., and German, A.L., *Adv. Mater.*, 2000, **12**(17), 1286–1290, doi:10.1002/1521-4095(200009)12:17<1286::AID-ADMA1286>3.0.CO;2-7.

[73] Iampietro, D. and Kaler, E., *Langmuir*, 1999, **15**(25), 8590–8601, doi:10.1021/la990407l.

[74] Iijima, H., Kato, T., Yoshida, H., and Imai, M., *J. Phys. Chem. B*, 1998, **102**(6), 990–995, doi:10.1021/jp973048g.

[75] Israelachvili, J.N., Mitchell, D.J., and Ninham, B.W., *J. Chem. Soc., Faraday Trans. 2*, 1976, **72**, 1525–1568, doi:10.1039/F29767201525.

[76] Israelachvili, J.N., Mitchell, D.J., and Ninham, B.W., *BBA - Biomembranes*, 1977, **470**(2), 185–201, doi:10.1016/0005-2736(77)90099-2.

[77] Joannic, R., Auvray, L., and Lasic, D.D., *Phys. Rev. Lett.*, 1997, **78**, 3402–3405, doi:10.1103/PhysRevLett.78.3402.

[78] Jung, H.T., Coldren, B., Zasadzinski, J.A., Iampietro, D.J., and Kaler, E.W., *Proc. Nat. Acad. Sci. U.S.A.*, 2001, **98**(4), 1353–1357, doi:10.1073/pnas.98.4.1353.

[79] Jung, H.T., Lee, S.Y., Kaler, E.W., Coldren, B., and Zasadzinski, J.A., *Proc. Nat. Acad. Sci. U.S.A.*, 2002, **99**(24), 15318–15322, doi:10.1073/pnas.242374499.

[80] Kadi, M., Hansson, P., Almgren, M., and Furó, I., *Langmuir*, 2002, **18**(24), 9243–9249, doi:10.1021/la020579+.

[81] Kaler, E.W., Herrington, K.L., Murthy, A.K., and Zasadzinski, J.A.N., *J. Phys. Chem.*, 1992, **96**(16), 6698–6707, doi:10.1021/j100195a033.

[82] Kamenka, N., Chorro, M., Talmon, Y., and Zana, R., *Colloid. Surface.*, 1992, **67**, 213–222, doi:10.1016/0166-6622(92)80300-Q.

[83] Kegel, W.K. and Lekkerkerker, H.N.W., *J. Phys. Chem.*, 1993, **97**(42), 11124–11133, doi:10.1021/j100144a038.

[84] Kegel, W.K. and Reiss, H., *Ber. Bunsen-Ges. Phys. Chem.*, 1996, **100**(3), 300–312, doi:10.1002/bbpc.19961000316.

[85] Keiderling, U., *Appl. Phys. A*, 2002, **74**, 1455–1457, doi:10.1007/s003390201561.

[86] Khan, A. and Marques, E.F., *Curr. Opin. Colloid In.*, 2000, **4**(6), 402–410, doi:10.1016/S1359-0294(00)00017-0.

[87] Kunz, W., Testard, F., and Zemb, T., *Langmuir*, 2008, **25**(1), 112–115, doi:10.1021/la8028879.

[88] Langer, R., *Science*, 1990, **249**(4976), 1527–1533, doi:10.1126/science.2218494.

[89] Lasic, D.D., *Biochem. J.*, 1988, **256**(1), 1–11.

[90] Lawrence, S.A., *Amines: synthesis, properties and applications*, Cambridge University Press, The Edinburgh Building, Cambridge, CB2 2RU, UK, 2004.

[91] Leng, J., Egelhaaf, S., and Cates, M., *Biophys. J.*, 2003, **85**(3), 1624–1646, doi:10.1016/S0006-3495(03)74593-7.

[92] Leng, J., Egelhaaf, S.U., and Cates, M.E., *EPL-Europhys. Lett.*, 2002, **59**(2), 311, doi:10.1209/epl/i2002-00243-1.

[93] Li, X., Dong, S.L., Jia, X.F., Song, A.X., and Hao, J.C., *Chem.-a Eur. J.*, 2007, **13**(34), 9495–9502, doi:10.1002/chem.200700778.

[94] Lipowsky, R., *Nature*, 1991, **349**, 475–481, doi:10.1038/349475a0.

[95] Lipowsky, R., *Biophys. J.*, 1993, **64**(4), 1133–1138, doi:10.1016/S0006-3495(93)81479-6.

[96] Lootens, D., Vautrin, C., Van Damme, H., and Zemb, T., *J. Mater. Chem.*, 2003, **13**(9), 2072–2074, doi:10.1039/b305808p.

[97] MacDonald, R.C., MacDonald, R.I., Menco, B.P., Takeshita, K., Subbarao, N.K., and Hu, L.r., *BBA - Biomembranes*, 1991, **1061**(2), 297–303, doi:10.1016/0005-2736(91)90295-J.

[98] Marques, E., Khan, A., da Graça Miguel, M., and Lindman, B., *J. Phys. Chem.*, 1993, **97**(18), 4729–4736, doi:10.1021/j100120a028.

[99] Marques, E.F., Regev, O., Khan, A., da Graça Miguel, M., and Lindman, B., *J. Phys. Chem. B*, 1998, **102**(35), 6746–6758, doi:10.1021/jp980355t.

[100] Marques, E.F., Regev, O., Khan, A., da Graça Miguel, M., and Lindman, B., *J. Phys. Chem. B*, 1999, **103**(39), 8353–8363, doi:10.1021/jp990852p.

[101] Martini, G., Ristori, S., and Rossi, S., *J. Phys. Chem. A*, 1998, **102**(28), 5476–5480, doi:10.1021/jp9800315.

[102] Mayer, L., Hope, M., and Cullis, P., *BBA - Biomembranes*, 1986, **858**(1), 161–168, doi:10.1016/0005-2736(86)90302-0.

[103] McKelvey, C.A., Kaler, E.W., Zasadzinski, J.A., Coldren, B., and Jung, H.T., *Langmuir*, 2000, **16**(22), 8285–8290, doi:10.1021/la000569d.

[104] Mitchell, D.J., Tiddy, G.J.T., Waring, L., Bostock, T., and McDonald, M.P., *J. Chem. Soc., Faraday Trans. 1*, 1983, **79**(4), 975–1000, doi:10.1039/F19837900975.

[105] Moroi, Y., Take'uchi, M., Yoshida, N., and Yamauchi, A., *J. Colloid Interface Sci.*, 1998, **197**(2), 221–229, doi:10.1006/jcis.1997.5286.

[106] Munter, A., 'Scattering length density calculator', http://www.ncnr.nist.gov/resources/sldcalc.html, 11/2/2010, NIST Center for Neutron Research.

[107] Muzzalupo, R., Ranieri, G.A., and Lamesa, C., *Colloid. Surface. A*, 1995, **104**(2-3), 327–336, doi:10.1016/0927-7757(95)03268-7.

[108] Myrvold, R. and Hansen, F.K., *J. Colloid Interface Sci.*, 1998, **207**(1), 97–105, doi:10.1006/jcis.1998.5745.

[109] Noguchi, H. and Gompper, G., *J. Chem. Phys.*, 2006, **125**(16), 164908, doi:10.1063/1.2358983.

[110] Oberdisse, J., Couve, C., Appell, J., Berret, J.F., Ligoure, C., and Porte, G., *Langmuir*, 1996, **12**(5), 1212–1218, doi:10.1021/la950313l.

[111] Oda, R., Huc, I., Danino, D., and Talmon, Y., *Langmuir*, 2000, **16**(25), 9759–9769, doi:10.1021/la0008075.

[112] Oda, R., Huc, I., Homo, J.C., Heinrich, B., Schmutz, M., and Candau, S., *Langmuir*, 1999, **15**(7), 2384–2390, doi:10.1021/la9814889.

[113] Ojogun, V.A., Lehmler, H.J., and Knutson, B.L., *J. Colloid Interface Sci.*, 2009, **338**(1), 82–91, doi:10.1016/j.jcis.2009.06.022.

[114] Olson, F., Hunt, C., Szoka, F., Vail, W., and Papahadjopoulos, D., *BBA - Biomembranes*, 1979, **557**(1), 9–23, doi:10.1016/0005-2736(79)90085-3.

[115] Olson, F., Hunt, C.A., Szoka, F.C., Vail, W.J., and Papahadjopoulos, D., *BBA - Biomembranes*, 1979, **557**(1), 9–23, doi:10.1016/0005-2736(79)90085-3.

[116] Olsson, U., Nakamura, K., Kunieda, H., and Strey, R., *Langmuir*, 1996, **12**(12), 3045–3054, doi:10.1021/la9600560.

[117] Oppel, C., Preévost, S., Noirez, L., and Gradzielski, M., *Langmuir*, 2011, **27**(14), 8885–8897, doi:10.1021/la104972r.

[118] Pedersen, J.S., Egelhaaf, S.U., and Schurtenberger, P., *J. Phys. Chem.*, 1995, **99**(4), 1299–1305, doi:10.1021/j100004a033.

[119] Piculell, L. and Lindman, B., *Adv. Colloid Interfac.*, 1992, **41**(0), 149–178, doi:10.1016/0001-8686(92)80011-L.

[120] Pilsl, H., Hoffmann, H., Hofmann, S., Kalus, J., Kencono, A.W., Lindner, P., and Ulbricht, W., *J. Phys. Chem.*, 1993, **97**(11), 2745–2754, doi:10.1021/j100113a042.

[121] Prévost, S., Wattebled, L., Laschewsky, A., and Gradzielski, M., *Langmuir*, 2010, **27**(2), 582–591, doi:10.1021/la103976p.

[122] Regev, O. and Khan, A., *J. Colloid Interface Sci.*, 1996, **182**(1), 95–109, doi:10.1006/jcis.1996.0440.

[123] Rehage, H. and Hoffmann, H., *Mol. Phys.*, 1991, **74**(5), 933–973, doi:10.1080/00268979100102721.

[124] Rosen, M.J., *Surfactants and Interfacial Phenomena*, John Wiley & Sons, Inc., Hoboken, New Jersey, 3 edn., 2004.

[125] Rossi, S., Karlsson, G., Ristori, S., Martini, G., and Edwards, K., *Langmuir*, 2001, **17**(8), 2340–2345, doi:10.1021/la001444b.

[126] Safran, S., MacKintosh, F., Pincus, P., and Andelman, D., *Prog. Colloid Polym. Sci.*, 1991, **84**, 3–7, doi:10.1007/BFb0115925.

[127] Safran, S.A., Pincus, P., and Andelman, D., *Science*, 1990, **248**(4953), 354–356, doi:10.1126/science.248.4953.354.

[128] Safran, S.A., Pincus, P.A., Andelman, D., and MacKintosh, F.C., *Phys. Rev. A*, 1991, **43**(2), 1071–1078, doi:10.1103/PhysRevA.43.1071.

[129] Savarala, S., Ahmed, S., Ilies, M.A., and Wunder, S.L., *ACS Nano*, 2011, **5**(4), 2619–2628, doi:10.1021/nn1025884.

[130] Schmölzer, S., Gräbner, D., Gradzielski, M., and Narayanan, T., *Phys. Rev. Lett.*, 2002, **88**(25), 258301–1–258301–4, doi:10.1103/PhysRevLett.88.258301.

[131] Shinoda, K., Hato, M., and Hayashi, T., *J. Phys. Chem.*, 1972, **76**(6), 909–914, doi:10.1021/j100650a021.

[132] Shioi, A. and Hatton, T.A., *Langmuir*, 2002, **18**(20), 7341–7348, doi:10.1021/la020268z.

[133] Simonsen, A.C. and Bagatolli, L.A., *Langmuir*, 2004, **20**(22), 9720–9728, doi:10.1021/la048683+.

[134] von Smoluchowski, M., *Phys. Z.*, 1916, **17**, 585.

[135] Srinivasan, V. and Blankschtein, D., *Langmuir*, 2005, **21**(4), 1647–1660, doi:10.1021/la048304c.

[136] Szoka, F. and Papahadjopoulos, D., *Proc. Nat. Acad. Sci. U.S.A.*, 1978, **75**(9), 4194–4198, doi:10.1073/pnas.75.9.4194.

[137] Tanford, C., *J. Phys. Chem.*, 1972, **76**(21), 3020–3024, doi:10.1021/j100665a018.

[138] Tanford, C., *The Hydrophobic Effect: Formation of Micelles and Biological Membranes*, John Wiley & Sons Inc, New York, 1980.

[139] Vautrin, C., Dubois, M., Zemb, T., Schmölzer, S., Hoffmann, H., and Gradzielski, M., *Colloid. Surface. A*, 2003, **217**(1-3), 165–170, doi:10.1016/S0927-7757(02)00572-1.

[140] Watzke, H., *Prog. Colloid Polym. Sci.*, 1993, **93**, 15–21, doi:10.1007/BFb0118464, 10.1007/BFb0118464.

[141] Weiss, T., Narayanan, T., and Gradzielski, M., *Langmuir*, 2008, **24**(8), 3759–3766, doi:10.1021/la703515j.

[142] Weiss, T.M., Narayanan, T., Wolf, C., Gradzielski, M., Panine, P., Finet, S., and Helsby, W.I., *Phys. Rev. Lett.*, 2005, **94**(3), 038303, doi:10.1103/PhysRevLett.94.038303.

[143] Wolf, C., Bressel, K., Drechsler, M., and Gradzielski, M., *Langmuir*, 2009, **25**(19), 11358–11366, doi:10.1021/la901191a.

[144] Woodle, M.C. and Lasic, D.D., *BBA - Rev. Biomembranes*, 1992, **1113**(2), 171–199, doi:10.1016/0304-4157(92)90038-C.

[145] Yeh, Y.Q., Chen, B.C., Lin, H.P., and Tang, C.Y., *Langmuir*, 2005, **22**(1), 6–9, doi:10.1021/la052129y.

[146] Zana, R., *Adv. Colloid Interfac.*, 2002, **97**(1–3), 205–253, doi:10.1016/S0001-8686(01)00069-0.

[147] Zemb, T., Carrière, D., Glinel, K., Hartman, M., Meister, A., Vautrin, C., Delorme, N., Fery, A., and Dubois, M., *Colloid. Surface. A*, 2007, **303**(1-2), 37–45, doi:10.1016/j.colsurfa.2007.03.028.

[148] Zemb, T., Dubois, M., Demé, B., and Gulik-Krzywicki, T., *Science*, 1999, **283**(5403), 816–819, doi:10.1126/science.283.5403.816.

[149] Zourab, S., Kayali, I., and El-Astal, A., *J. Disper. Sci. Technol.*, 2001, **22**(5), 431–442, doi:10.1081/DIS-100107852.

Appendix

A.1 Introduction

To calculate the free energy of a bilayer that forms an ellipsoidal shape with the half axis R_1, R_2 and R_3 a cartesian coordinate system is set with its origin into the bilayer and with the normal to the bilayer along the z-axis. The ellipsoid can then be described by eqn (A.1.1).

$$\frac{(z+R_3)^2}{R_3^2}+\frac{y^2}{R_2^2}+\frac{x^2}{R_1^2}=1 \tag{A.1.1}$$

$$z=R_3\sqrt{1-\frac{y^2}{R_2^2}-\frac{x^2}{R_1^2}}-R_3 \tag{A.1.2}$$

The normal $\underline{n}$ to the bilayer in the origin of this coordinate system is then defined as in eqn (A.1.3).

$$\underline{n}=\frac{1}{\sqrt{1+\left(\frac{\partial z}{\partial x}\right)^2+\left(\frac{\partial z}{\partial y}\right)^2}}\begin{pmatrix}-\frac{\partial z}{\partial x}\\-\frac{\partial z}{\partial y}\\1\end{pmatrix} \tag{A.1.3}$$

Helfrich postulates that there are two contributions to the free energy of the membrane. One contribution accounts for changing the radius in an ellipsoidal shape and the other contribution describes the energy coming from a saddle in the bilayer. Here the energy coming from changing the radius is assumed to be similar to the energy of a harmonic oscillator and proportional to the square of the change of the layer normal during bending. The free energy as expressed by Helfrich is shown in eqn (A.1.4) with the surface area A.

$$F_\mathrm{b}=\int\left(\frac{\kappa}{2}\left(\frac{\partial n_\mathrm{x}}{\partial x}+\frac{\partial n_\mathrm{y}}{\partial y}-2c_0\right)^2+\overline{\kappa}\left(\frac{\partial n_\mathrm{x}}{\partial x}\frac{\partial n_\mathrm{y}}{\partial y}-\frac{\partial n_\mathrm{x}}{\partial y}\frac{\partial n_\mathrm{y}}{\partial x}\right)\right)dA \tag{A.1.4}$$

In the origin the derivatives of the layer normal are:

$$\frac{\partial n_\mathrm{x}}{\partial x}=\frac{R_3}{R_1^2} \tag{A.1.5}$$

$$\frac{\partial n_\mathrm{y}}{\partial y}=\frac{R_3}{R_2^2} \tag{A.1.6}$$

$$\frac{\partial n_\mathrm{x}}{\partial y}=0 \tag{A.1.7}$$

$$\frac{\partial n_\mathrm{y}}{\partial x}=0 \tag{A.1.8}$$

With the reduced radii $R_1' = R_1^2/R_3$ and $R_2' = R_2^2/R_3$ and the curvatures $c_1 = 1/R_1'$ and $c_2 = 1/R_2'$ the free energy can then be written as in eqn (A.1.9).

$$F_b = \int \left(\frac{\kappa}{2} (c_1 + c_2 - 2c_0)^2 + \overline{\kappa} c_1 c_2 \right) dA \tag{A.1.9}$$

c_0 accounts for a bilayer with a spontaneous curvature.

A.2 Zwitanionic Mixtures of Tetradecyldimethylamine Oxide and Lithium Perfluoroalkanoates

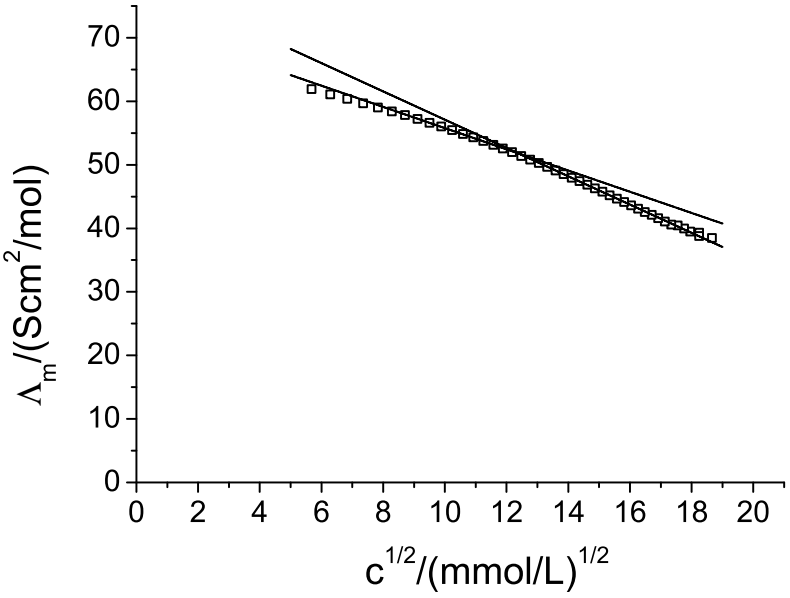

Figure A.2.1: Determination of the cmc by conductivity measurements on the system TDMAO-$C_5F_{11}CO_2Li$ at α(TDMAO) = 0 □, 25°C

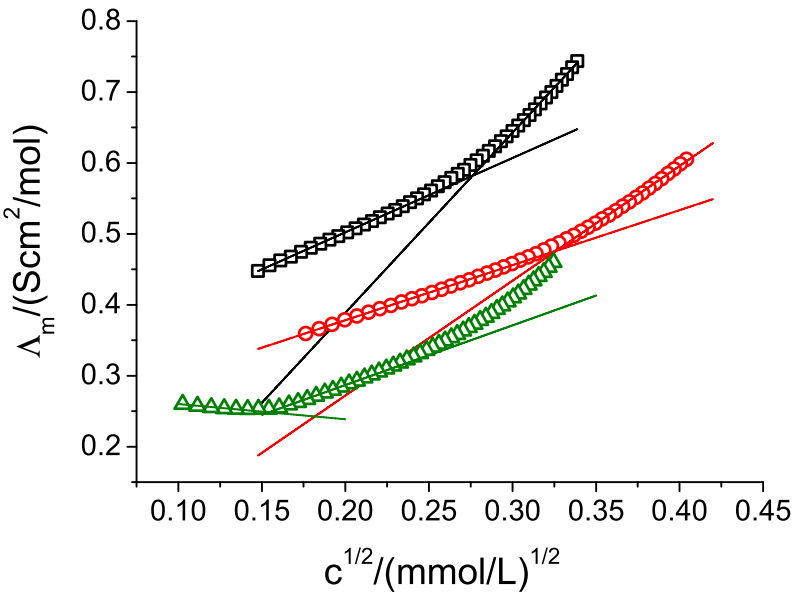

Figure A.2.2: Determination of the cmc by conductivity measurements on the system TDMAO-$C_5F_{11}CO_2Li$ at α(TDMAO) = 0.1 □, α(TDMAO) = 0.3 ◯, and α(TDMAO) = 0.5 △, 25°C

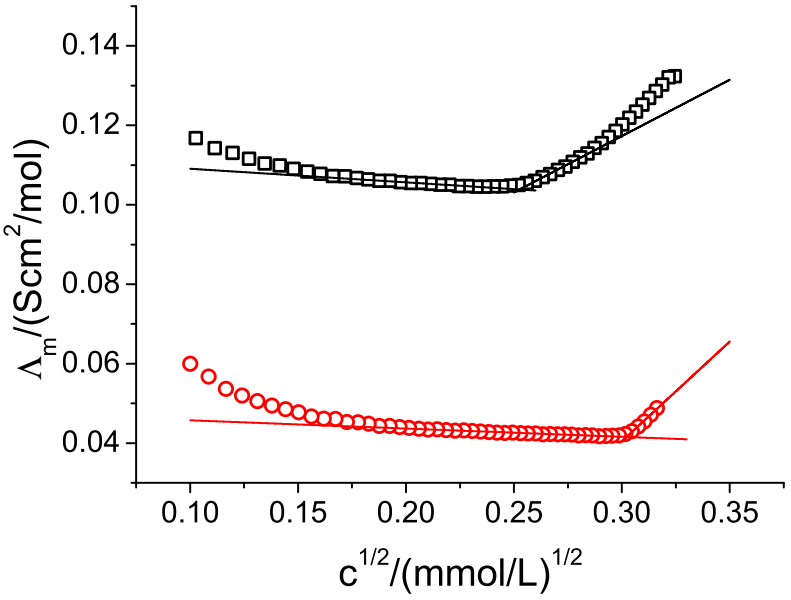

Figure A.2.3: Determination of the cmc by conductivity measurements on the system TDMAO-$C_5F_{11}CO_2Li$ at α(TDMAO) = 0.7 □ and α(TDMAO) = 0.9 ◯, 25°C

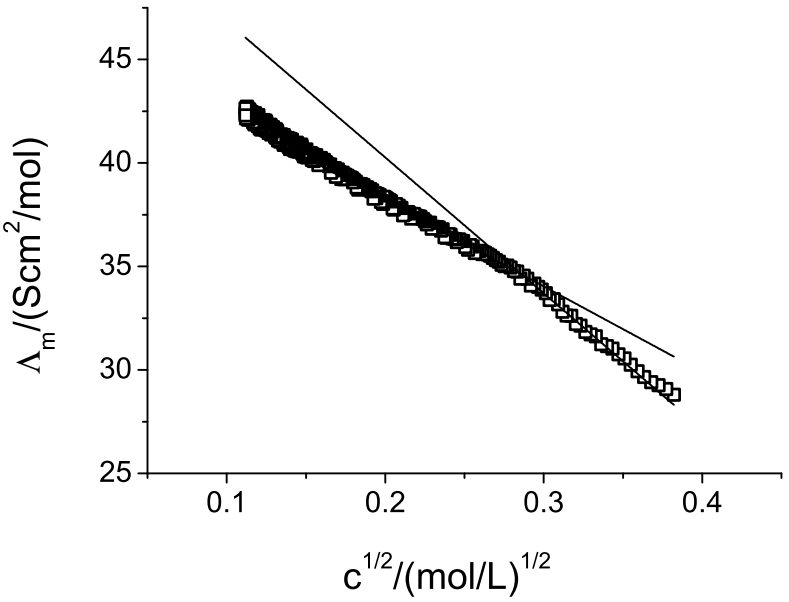

Figure A.2.4: Determination of the cmc by conductivity measurements on the system TDMAO-$C_6F_{13}CO_2Li$ at α(TDMAO) = 0 □, 25°C

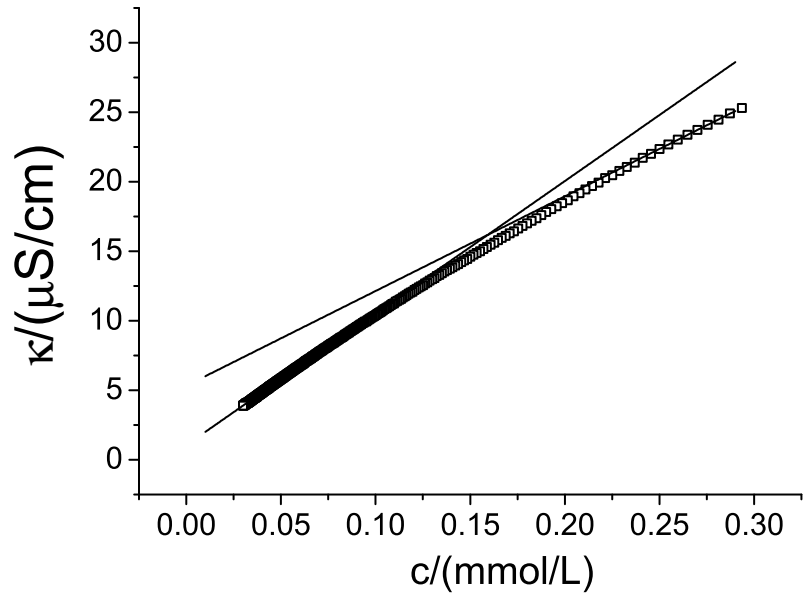

Figure A.2.5: Determination of the cmc by conductivity measurements on the system TDMAO-$C_6F_{13}CO_2Li$ at α(TDMAO) = 0.1 □, 25°C

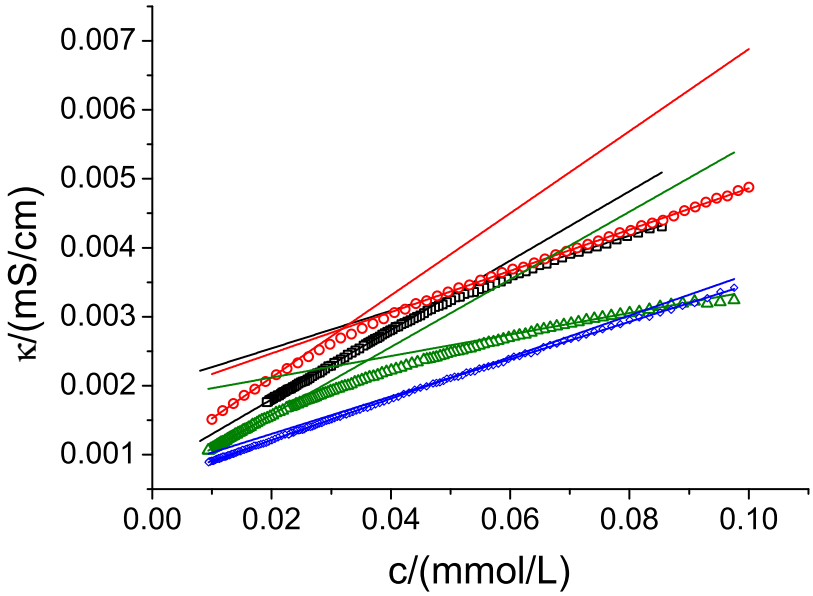

Figure A.2.6: Determination of the cmc by conductivity measurements on the system TDMAO-$C_6F_{13}CO_2Li$ at α(TDMAO) = 0.3 □, α(TDMAO) = 0.4 ◯, α(TDMAO) = 0.5 △, and α(TDMAO) = 0.7 ◊, 25°C

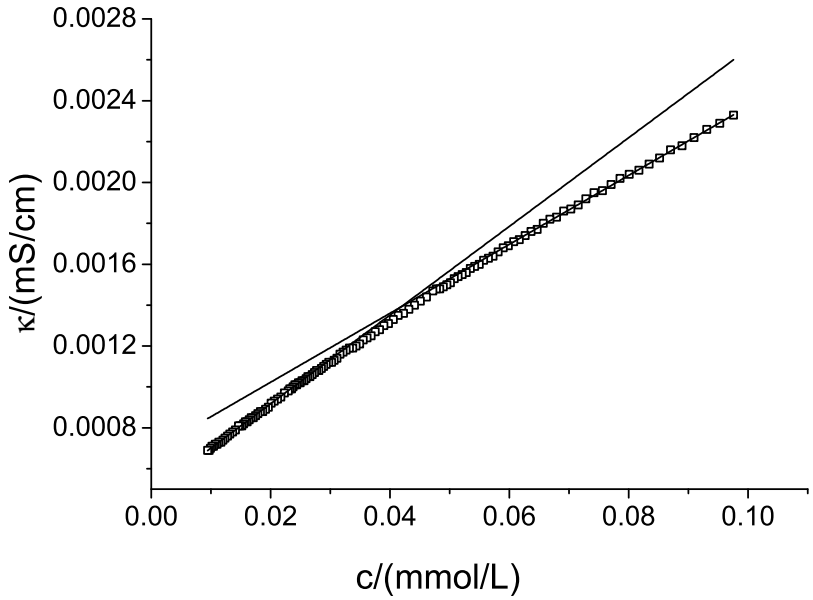

Figure A.2.7: Determination of the cmc by conductivity measurements on the system TDMAO-$C_6F_{13}CO_2Li$at α(TDMAO) = 0.9 □, 25°C

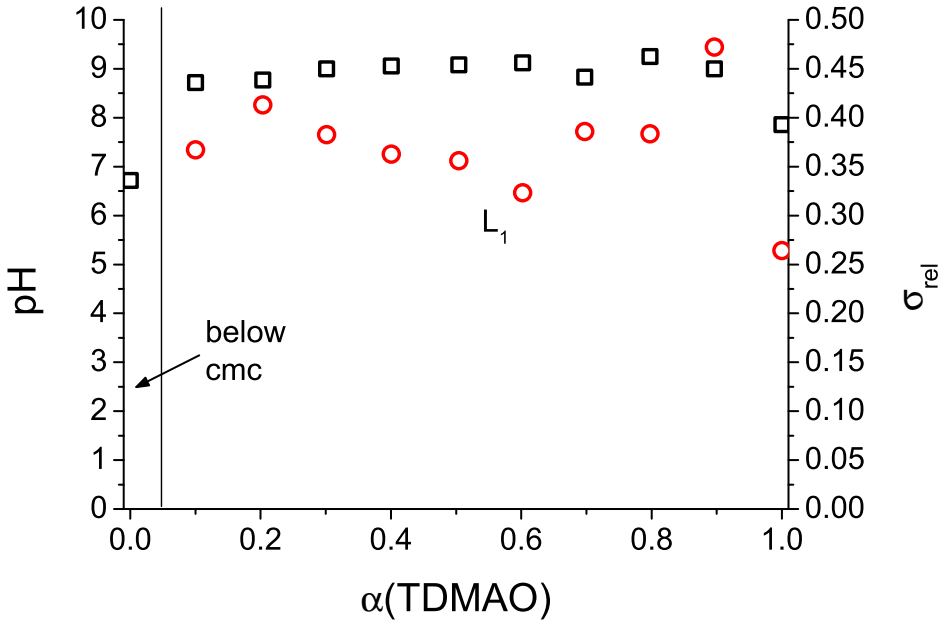

Figure A.2.8: pH □ and polydispersity index (σ_{rel}) from DLS ◯ as a function of the molar ratio of the TDMAO (α(TDMAO)) in the mixture TDMAO/$C_5F_{11}CO_2Li$ at 50mM total concentration (T = 25°C)

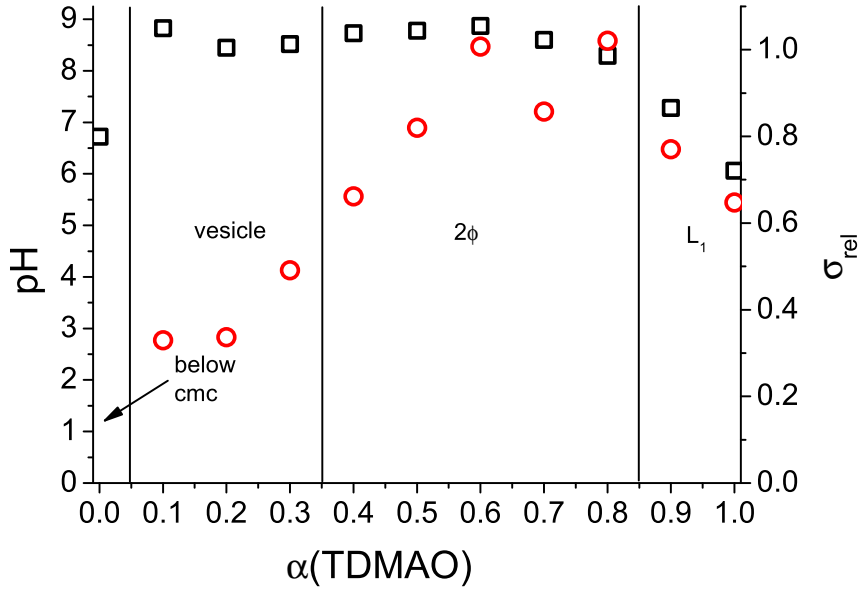

Figure A.2.9: pH □ and polydispersity index (σ_{rel}) determined by DLS measurements ◯ of the system TDMAO/HCl/$C_5F_{11}CO_2Li$ at 50mM total concentration (T=25°C) as a function of the molar ratio of the TDMAO (α(TDMAO))

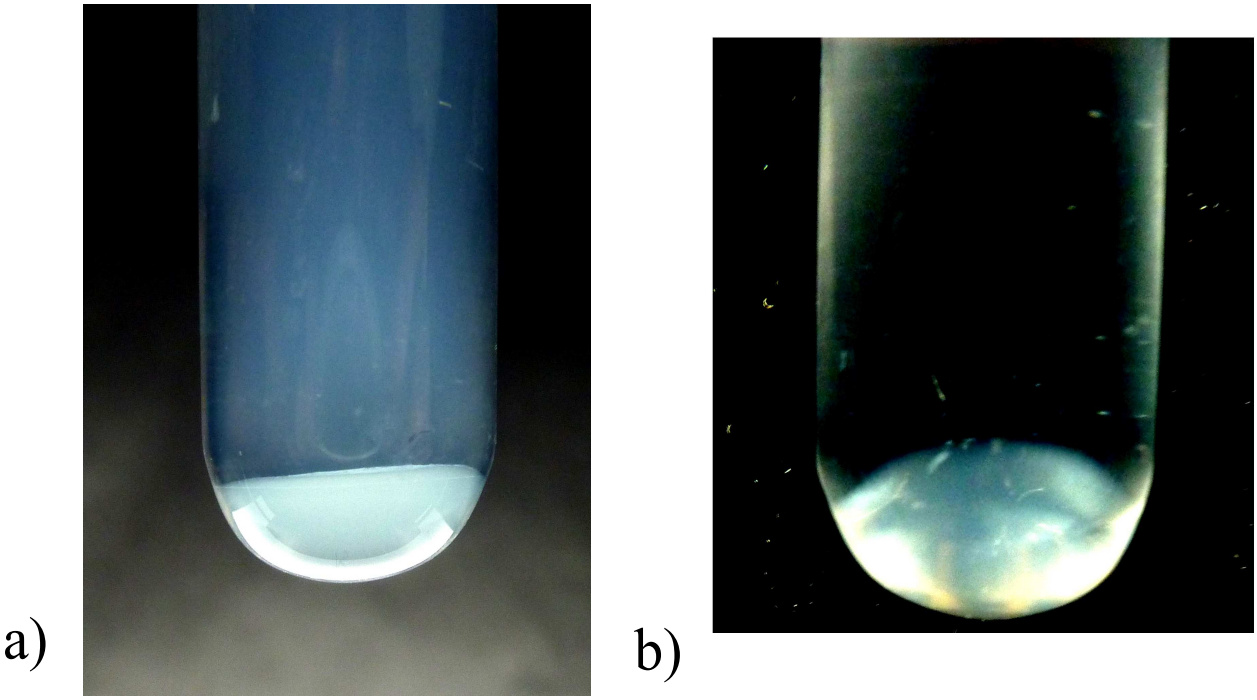

Figure A.2.10: Photo of a mixture of TDMAO-$C_6F_{13}CO_2Li$ with 50mM and α(TDMAO) = 0.5, 25°C, sample is between polarization filters in photo b)

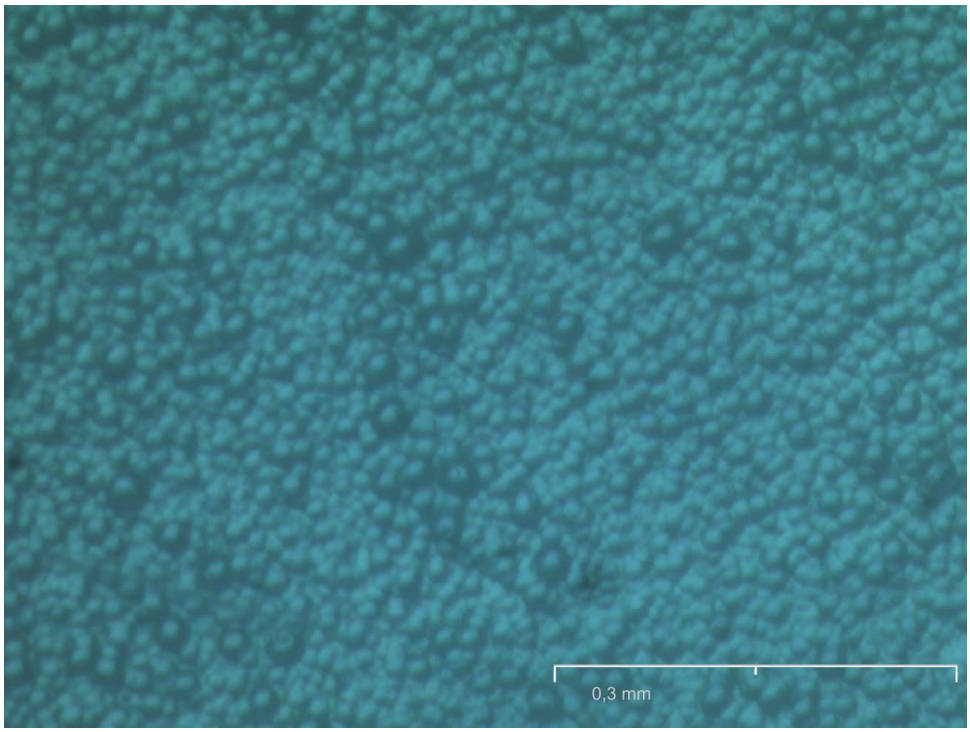

Figure A.2.11: Photo of a mixture of TDMAO-$C_6F_{13}CO_2Li$ with $50mM$ and α(TDMAO) = 0.5, 25°C, under a microscope with a tenfold magnification

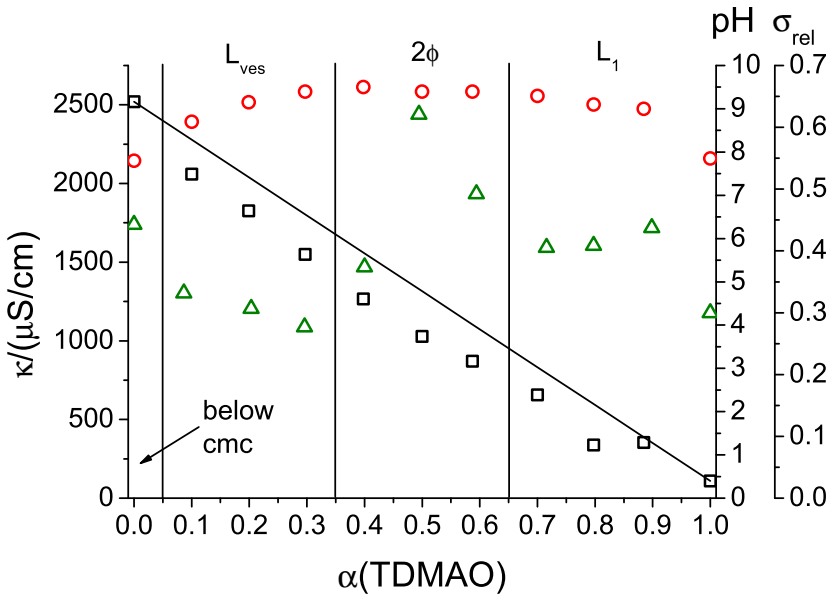

Figure A.2.12: Phase behaviour and corresponding conductivity (κ_C) □, pH ◯, and polydispersity index △ determined from cumulant analysis of the system TDMAO/$C_6F_{13}CO_2Li$ at a total concentration of 50mM (T=25°C) as a function of the molar ratio of the TDMAO (α(TDMAO))

Table A.2.1: Hydrodynamic Radii R_h determined from cumulant analysis and from biexponential fits, polydispersity index PDI determined from cumulant analysis, vesicle radius R determined from conductivity measurements and viscosity η as a function of the molar fraction a of the TDMAO in the system TDMAO-$C_6F_{13}CO_2Li$, 50mM (T=25°C)

α(TDMAO)	$R_{h,cumu.}/nm$	PDI	$\eta/mPas$	$R_{h1,biexp.}/nm$	$R_{h2,biexp.}/nm$	α(TDMAO)	$R_{cond.}/nm$
1.00	7	0.3	1.16			1.00	
0.90	2	0.44	3.54			0.88	
0.80	2	0.41	2.84			0.80	
0.72	4	0.41	13.78			0.70	
0.59	10	0.49	23.55	9	164	0.59	91
0.49	129	0.62	15.31			0.50	97
0.40	78	0.37	10.67			0.40	87
0.30	60	0.28	3.27			0.30	67
0.20	52	0.31	1.44			0.20	52
0.09	59	0.33	0.98			0.10	50
0.00			0.96			0.00	

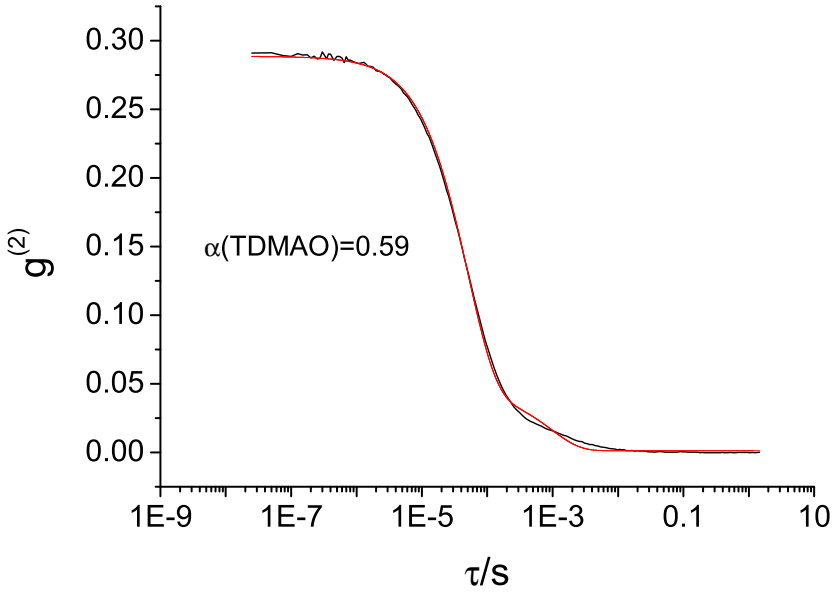

Figure A.2.13: Normalised intensity autocorrelation functions of the DLS measurement (symbols) and bi-exponential fit (lines) on the system TDMAO-$C_6F_{13}CO_2Li$ (0.59:0.41) with a total surfactant concentration of 50mM at a temperature of 25°C

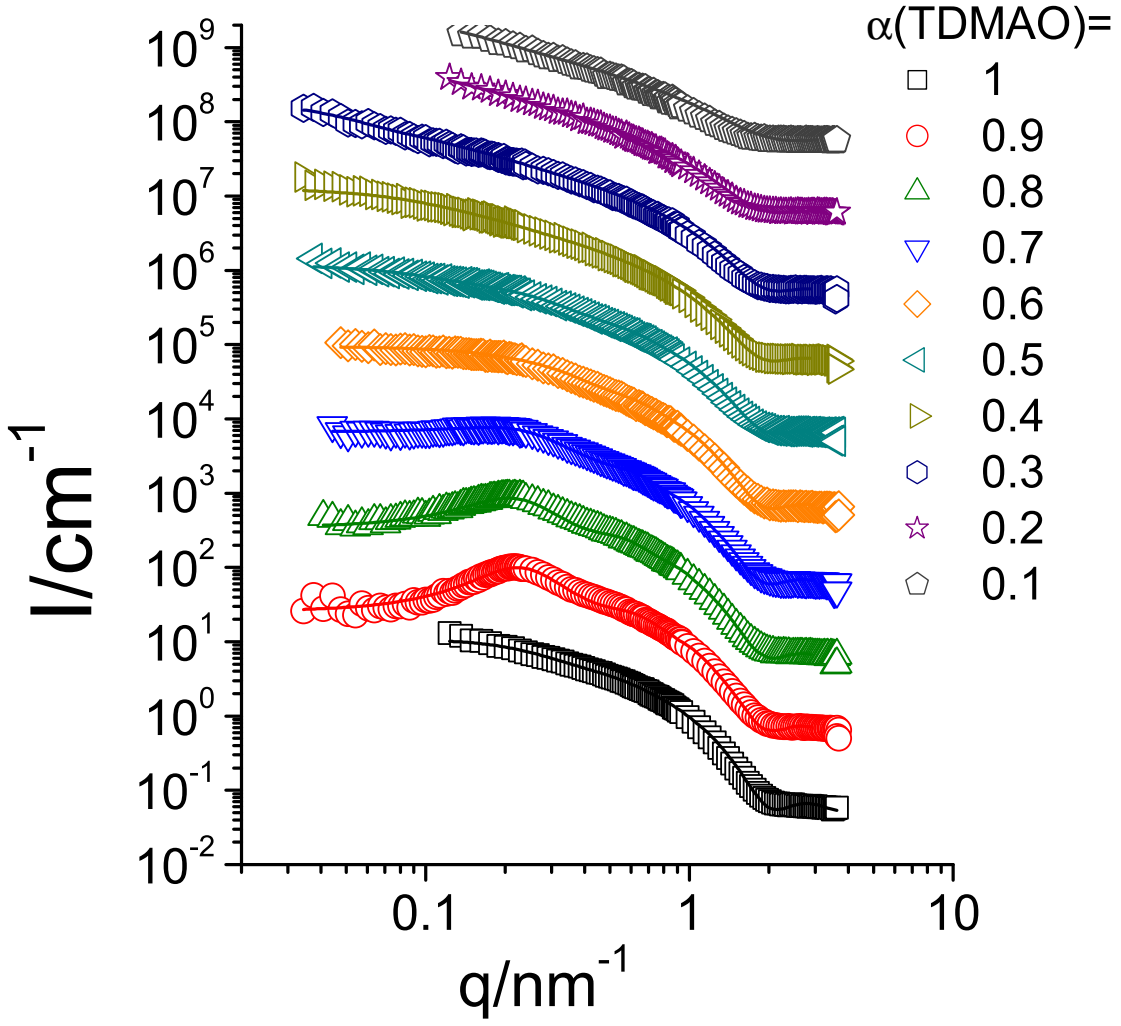

Figure A.2.14: Small Angle Neutron Scattering (SANS) measurements of mixtures of TDMAO-$C_5F_{11}CO_2Li$, (50 mM, 25°C, at α(TDMAO) = 0 no measurement is shown since here one is below the *cmc*, data are multiplied by multiples of 10 for clarification)

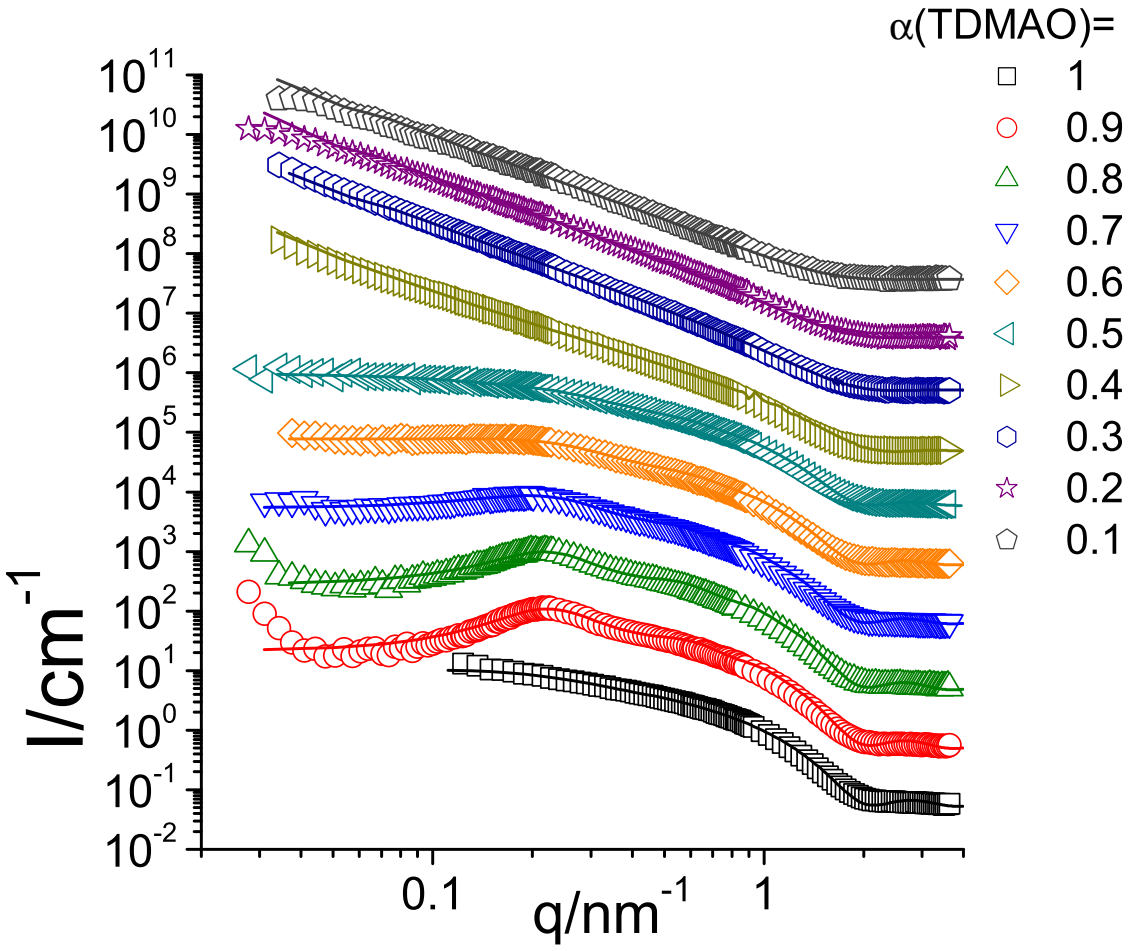

Figure A.2.15: Small Angle Neutron Scattering (SANS) measurements of mixtures of TDMAO-$C_6F_{13}CO_2Li$, (50 mM, 25°C, at α(TDMAO) = 0 no measurement is shown since here one is below the *cmc*, data are multiplied by multiples of 10 for clarification)

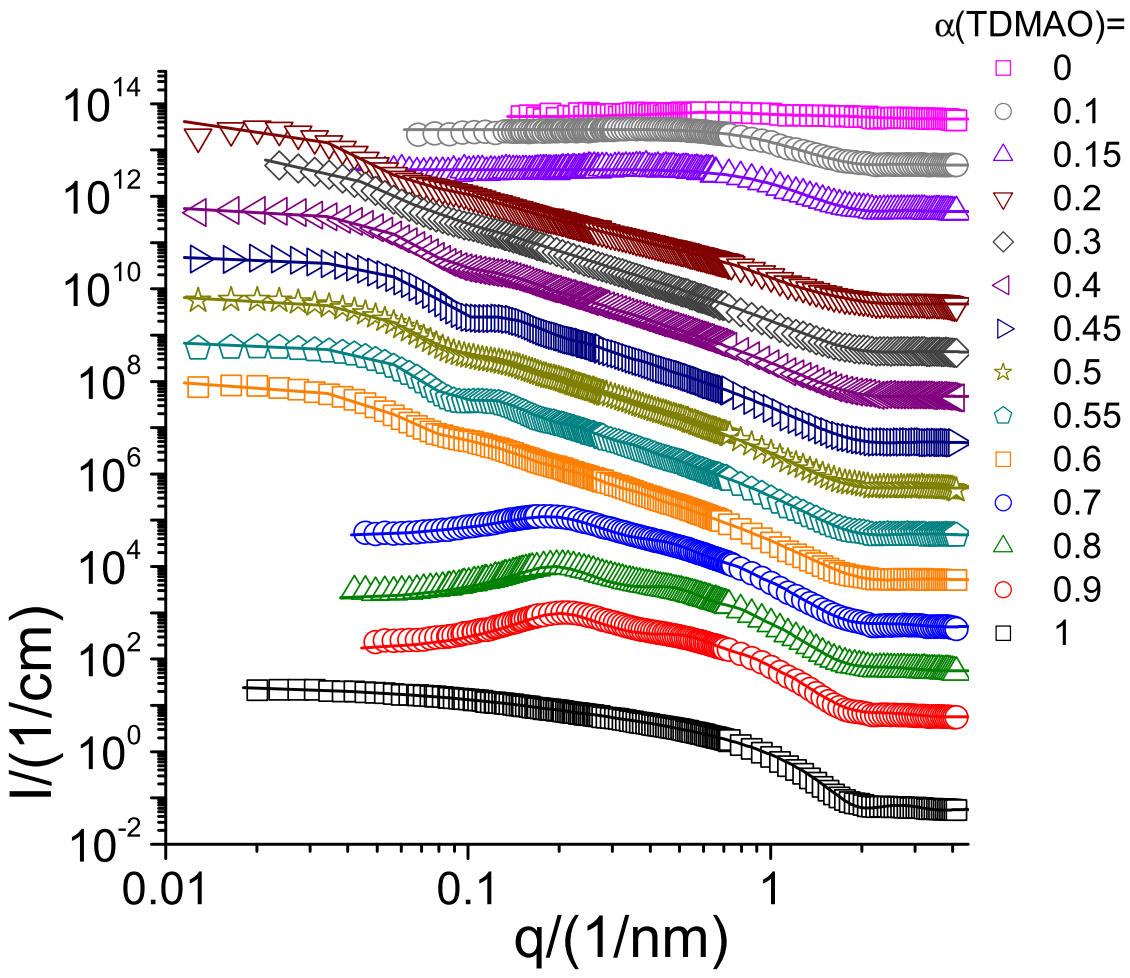

Figure A.2.16: Small Angle Neutron Scattering (SANS) measurements of mixtures of TDMAO-$C_7F_{15}CO_2Li$, (50 mM, 25°C, at α(TDMAO) = 0 no measurement is shown since here one is below the *cmc*, data are multiplied by multiples of 10 for clarification)

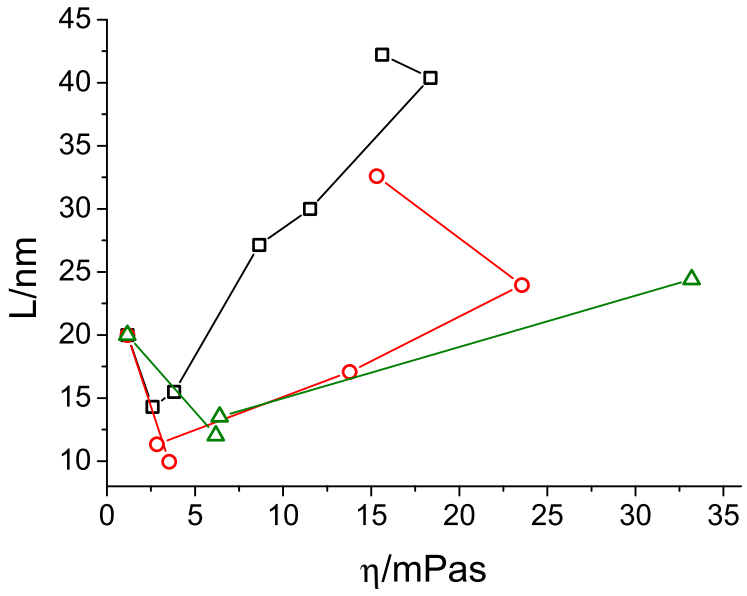

Figure A.2.17: Dependence of the length (L) of the micelles derived from SANS-measurements on the viscosity (η) of the sample in the system TDMAO-$C_nF_{2n+1}CO_2Li$ with a constant total concentration of 50mM at 25°C; n=5 □, n=6 ◯, n=7 △

A.3 Crystal Formation in Mixtures of Hydrocarbon and Perfluoro Surfactants

Table A.3.1: Peak positions in neutron diffraction measurements

TDMAO-$C_5F_{11}CO_2H$	$q/(1/Å)$	TDMAO-$C_6F_{13}CO_2H$	$q/(1/Å)$	TDMAO-$C_7F_{15}CO_2H$	$q/(1/Å)$
	0.2115		0.1990		0.1906
	0.4276		0.4048		0.3842
	0.7285		0.7265		0.7205
	0.8178		0.8100		0.7941
	1.3157		1.3157		1.3192
	1.3349		1.3332		1.3401
	1.3782		1.1622		1.3627
	1.3936		1.2755		1.3936

TDMAOH$^+$Cl$^-$-$C_6F_{13}CO_2Li$	$q/(1/Å)$	TDMAOH$^+$Cl$^-$-LiPFOS	$q/(1/Å)$	TTABr-LiPFOS	$q/(1/Å)$
	0.1969		0.1571		0.1802
	0.4048		0.3510		0.3634
	0.7265		0.6158		0.7505
	0.8080		0.8884		1.0608
	1.3157		1.2963		1.2768
	1.3332		1.3488		1.3314
	1.3696				
	1.3987				

A.4 The System TDMAO (Tetradecyldimethylamine Oxide) - LiPFOS (Lithium Perfluorooctylsulfonate) - Dependence on the Composition

The cmcs in the system TDMAO-LiPFOS were determined according to section 10.1.7 and the interaction parameter β was determined with $8.7 k_B T$ according to section 9.2.

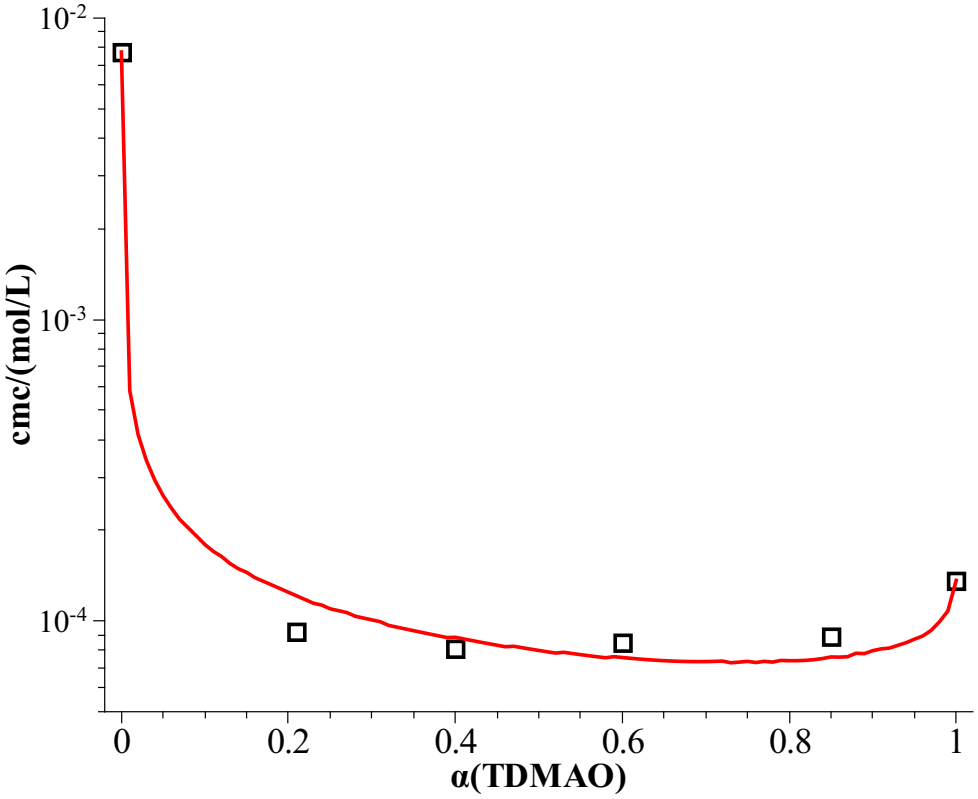

Figure A.4.1: Critical micelle concentration (cmc) determined by conductivity measurements; TDMAO- LiPFOS measurement - □, theory with $\beta = -8.7 k_B T$ - red line, 25°C

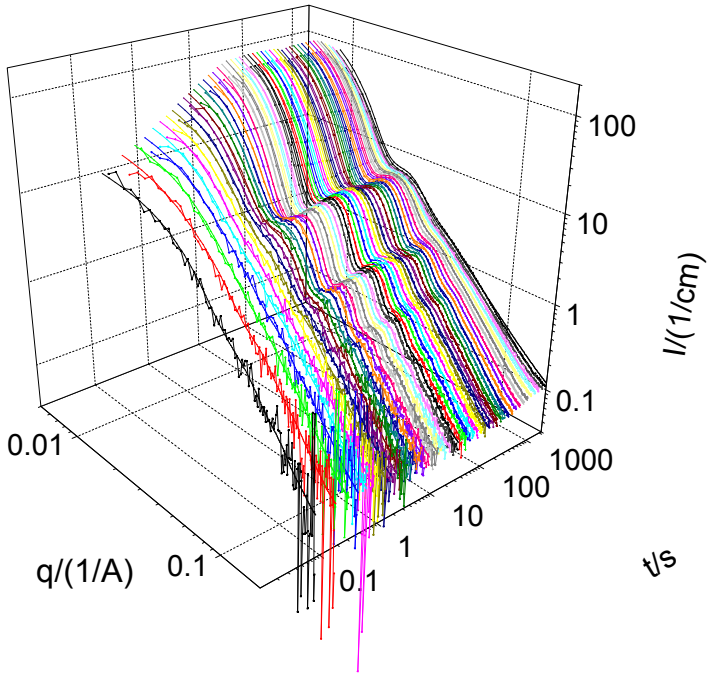

Figure A.4.2: Evolution of the aggregates in the system TDMAO-LiPFOS (5:5) at 50mM and 25°C, SANS measurements

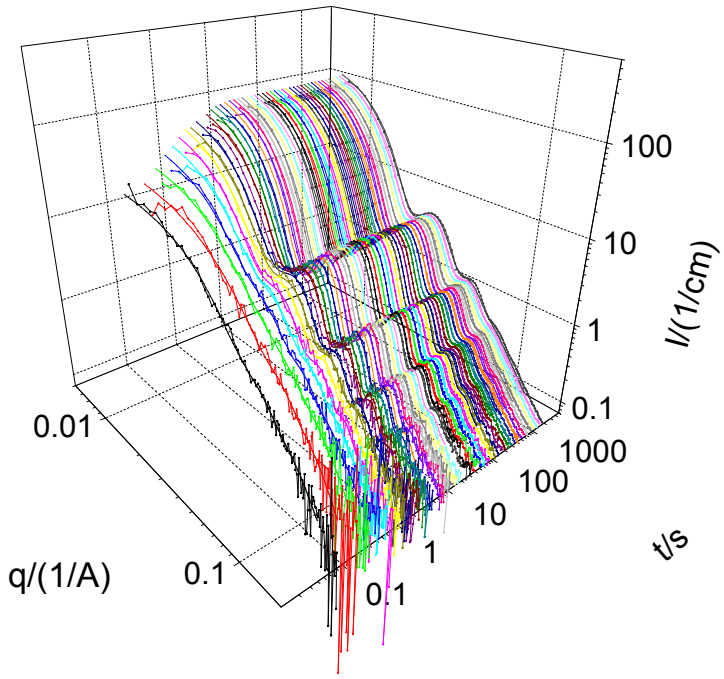

Figure A.4.3: Evolution of the aggregates in the system TDMAO-LiPFOS (55:45) at 50mM and 25°C, SANS measurements

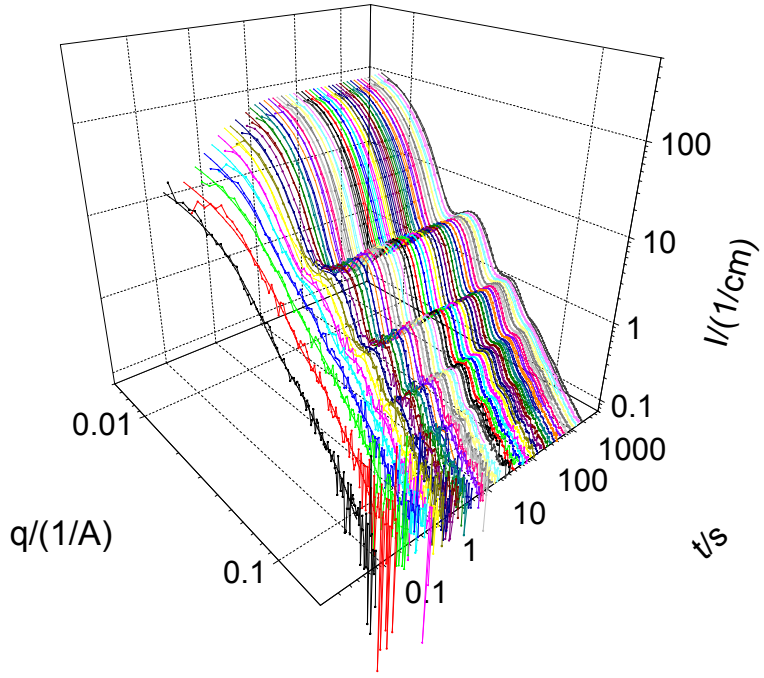

Figure A.4.4: Evolution of the aggregates in the system TDMAO-LiPFOS (6:4) at 50mM and 25°C, SANS measurements

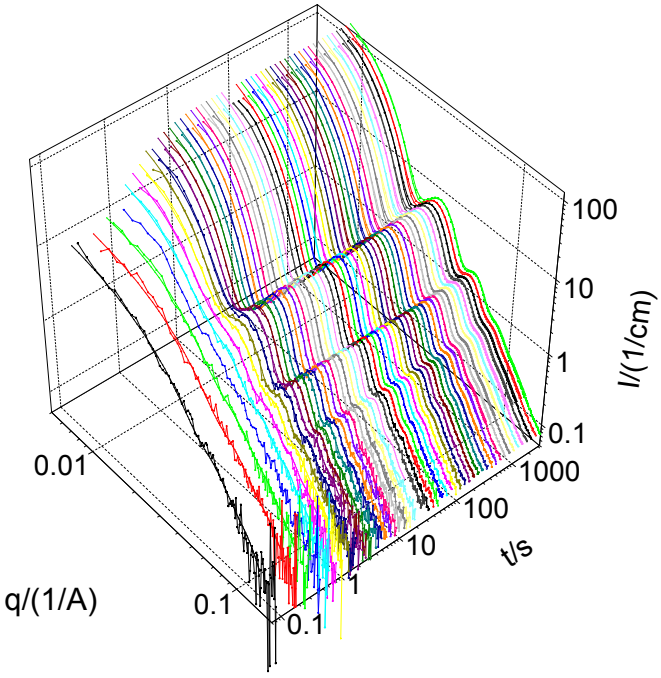

Figure A.4.5: Evolution of the aggregates in the system TDMAO-LiPFOS (65:35) at 50mM and 25°C, SANS measurements

A.5 Temperature Dependent Vesicle Formation in the System TDMAO-LiPFOS

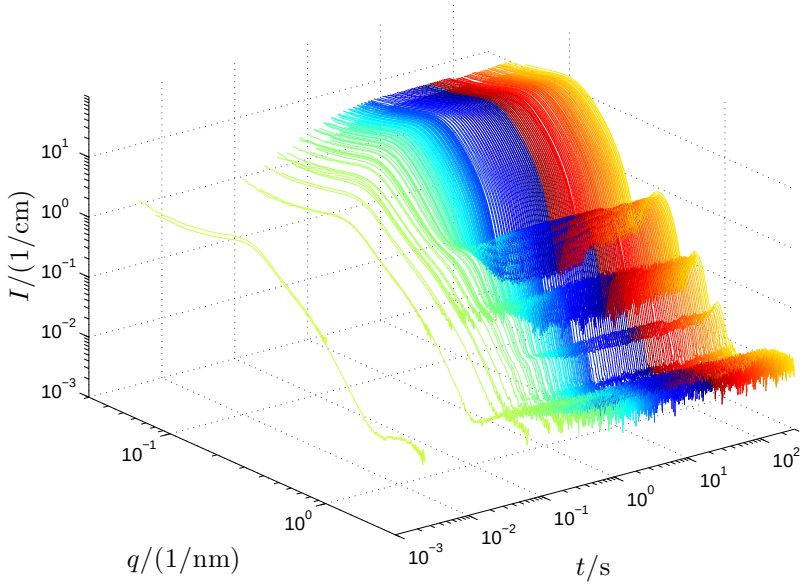

Figure A.5.1: Evolution of the aggregates in the system TDMAO-LiPFOS (55:45) at 50mM and 20°C, SAXS measurements

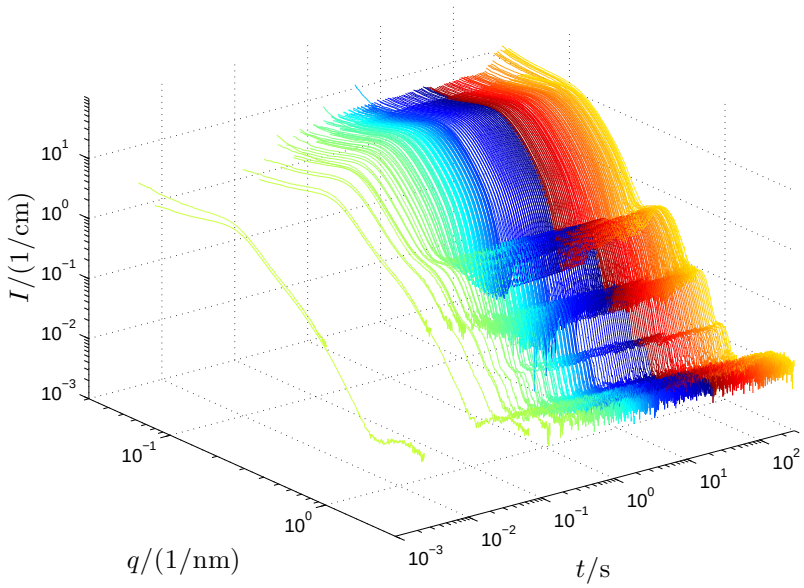

Figure A.5.2: Evolution of the aggregates in the system TDMAO-LiPFOS (55:45) at 50mM and 30°C, SAXS measurements

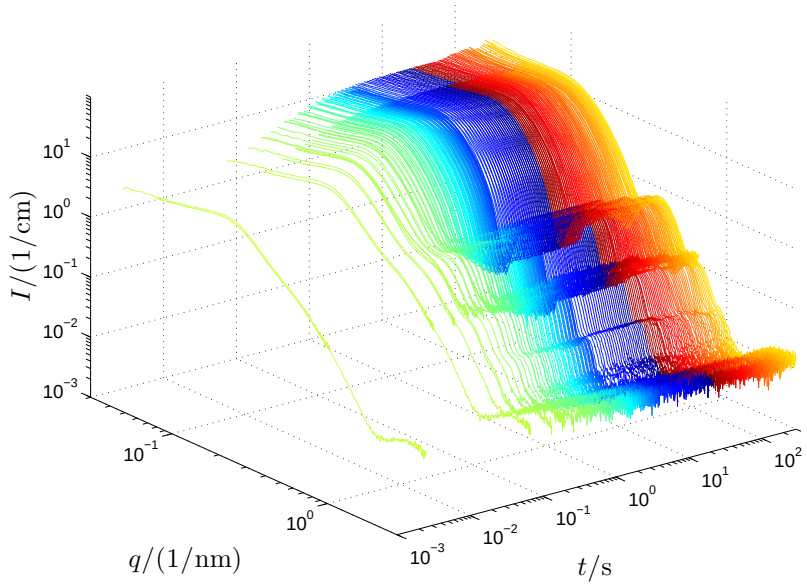

Figure A.5.3: Evolution of the aggregates in the system TDMAO-LiPFOS (55:45) at 50mM and 35°C, SAXS measurements

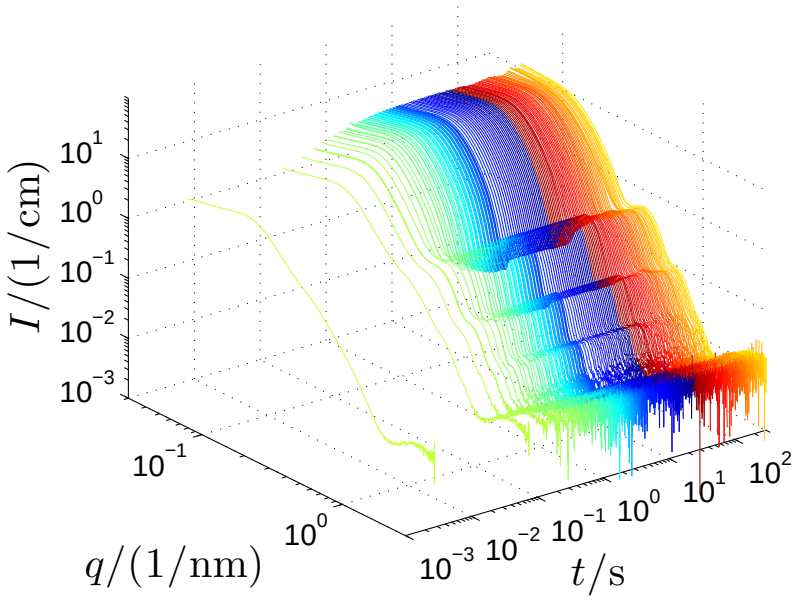

Figure A.5.4: Evolution of the aggregates in the system TDMAO-LiPFOS (55:45) at 50mM and 40°C, SAXS measurements

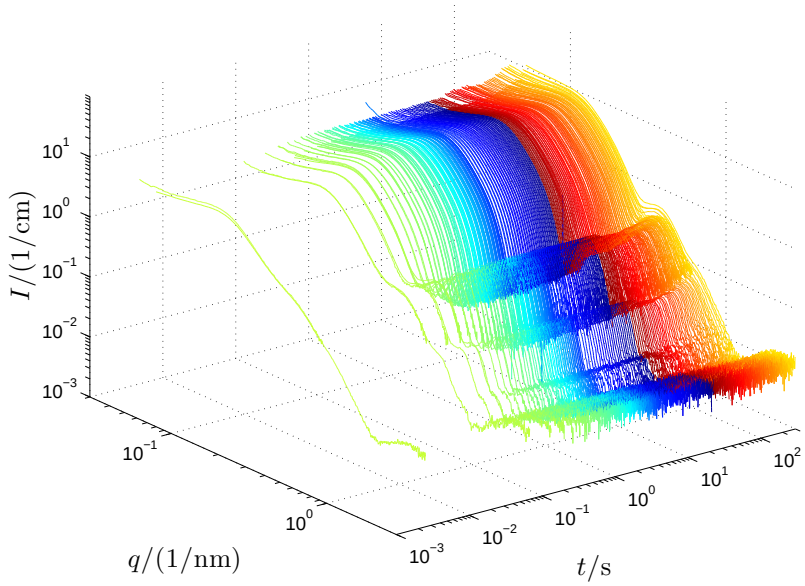

Figure A.5.5: Evolution of the aggregates in the system TDMAO-LiPFOS (55:45) at 50mM and 45°C, SAXS measurements

A.6 Influence of the Amphiphilic Polymer Pluronic L35 on the System TDMAO-LiPFOS

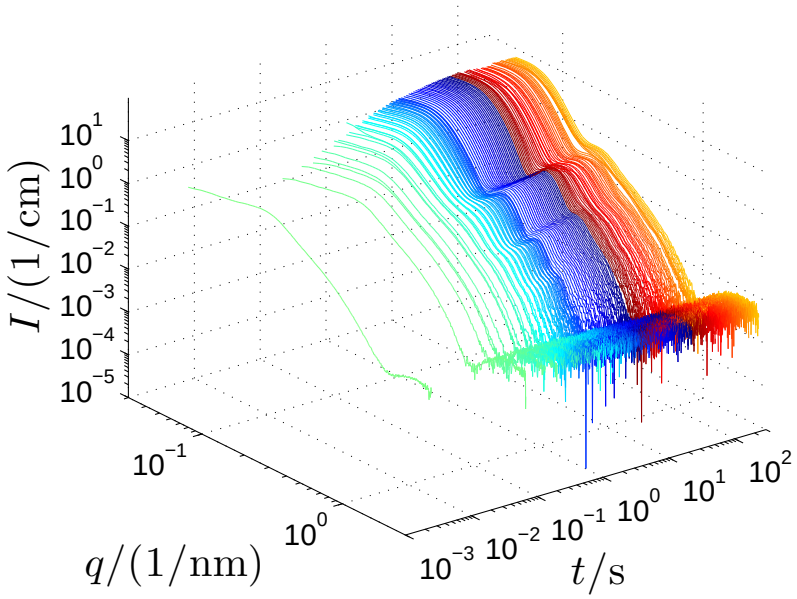

Figure A.6.1: Evolution of the aggregates in the system TDMAO-LiPFOS (55:45) + 0.05mol% Pluronic L35 (0.01375mM Pluronic L35) at 50mM and 25°C, SAXS measurements

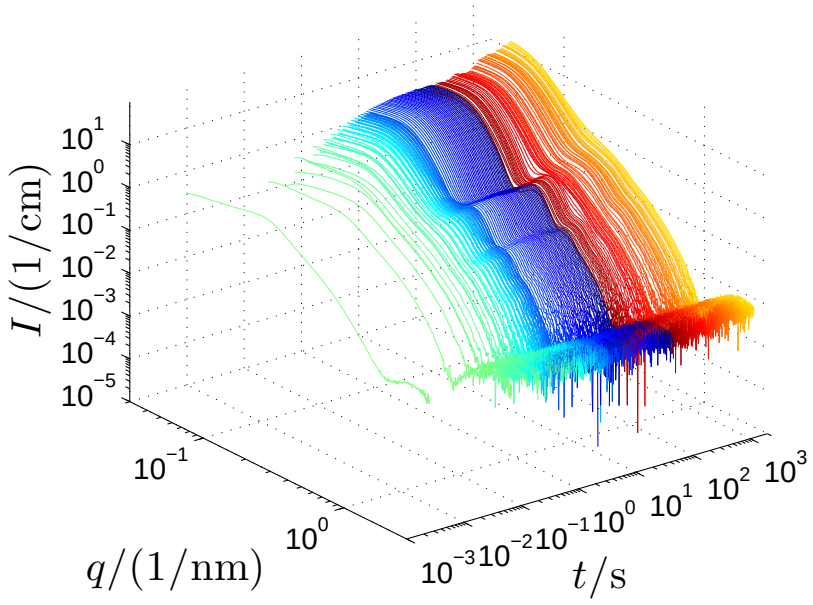

Figure A.6.2: Evolution of the aggregates in the system TDMAO-LiPFOS (55:45) + 0.1mol% Pluronic L35 (0.0275mM Pluronic L35) at 50mM and 25°C, SAXS measurements

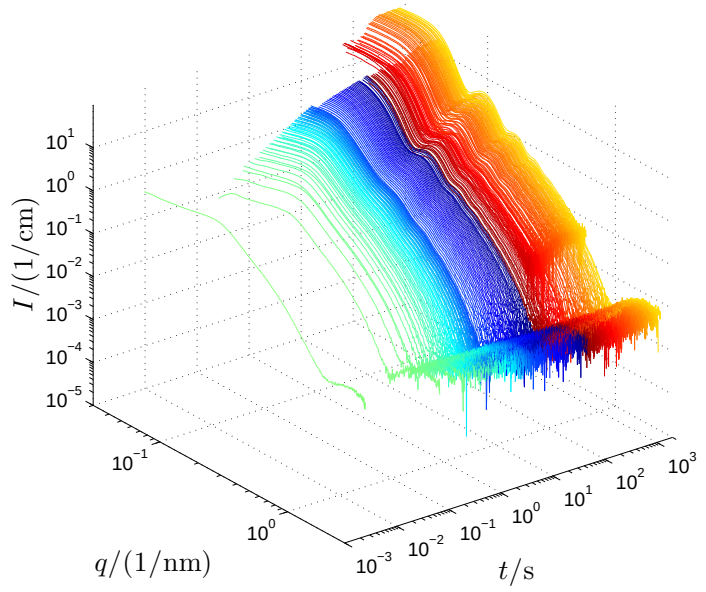

Figure A.6.3: Evolution of the aggregates in the system TDMAO-LiPFOS (55:45) + 0.5mol% Pluronic L35 (0.1375mM Pluronic L35) at 50mM and 25°C, SAXS measurements

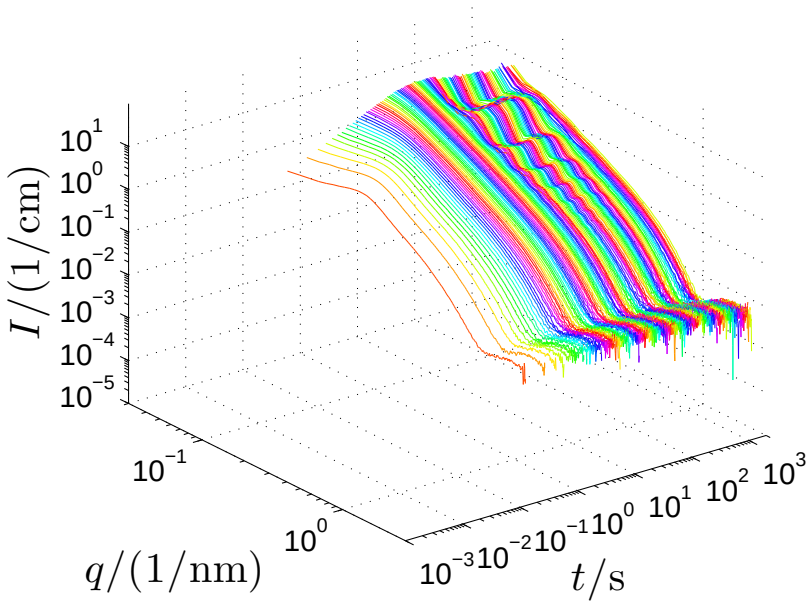

Figure A.6.4: Evolution of the aggregates in the system TDMAO-LiPFOS (55:45) + 2mol% Pluronic L35 (0.55mM Pluronic L35) at 50mM and 25°C, SAXS measurements

A.7 Influence of the Polymer Architecture

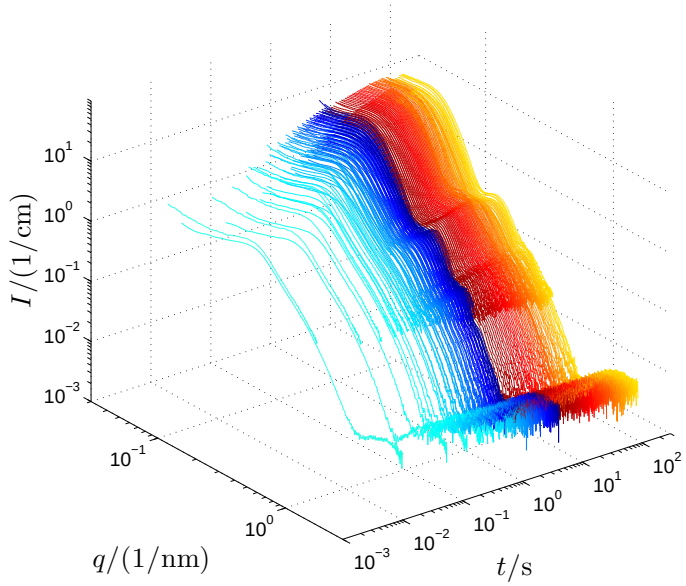

Figure A.7.1: Evolution of the aggregates in the system TDMAO-LiPFOS (55:45) + 0.05mol% Pluronic L35 (0.01375mM Pluronic F38) at 50mM and 25°C, SAXS measurements

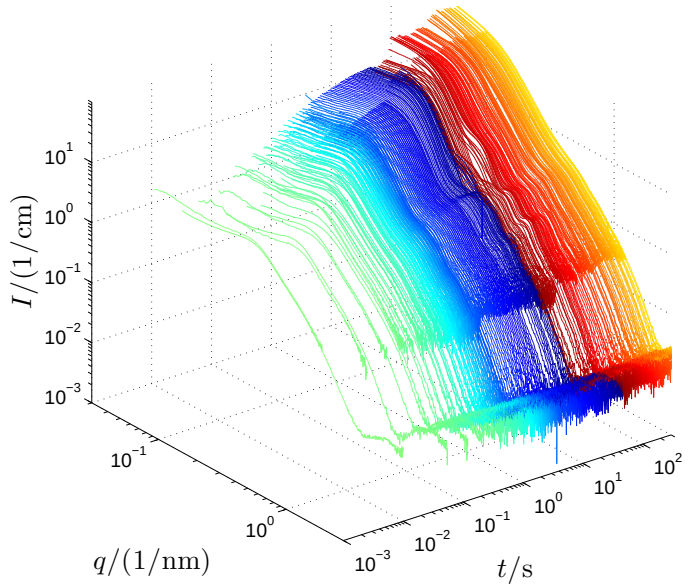

Figure A.7.2: Evolution of the aggregates in the system TDMAO-LiPFOS (55:45) + 0.1mol% Pluronic L35 (0.055mM Pluronic F38) at 50mM and 25°C, SAXS measurements

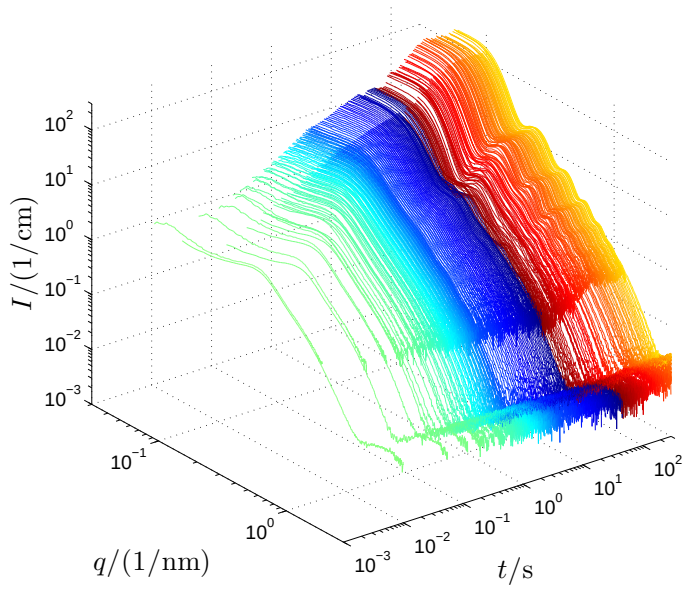

Figure A.7.3: Evolution of the aggregates in the system TDMAO-LiPFOS (55:45) + 0.5mol% Pluronic L35 (0.1375mM Pluronic F38) at 50mM and 25°C, SAXS measurements

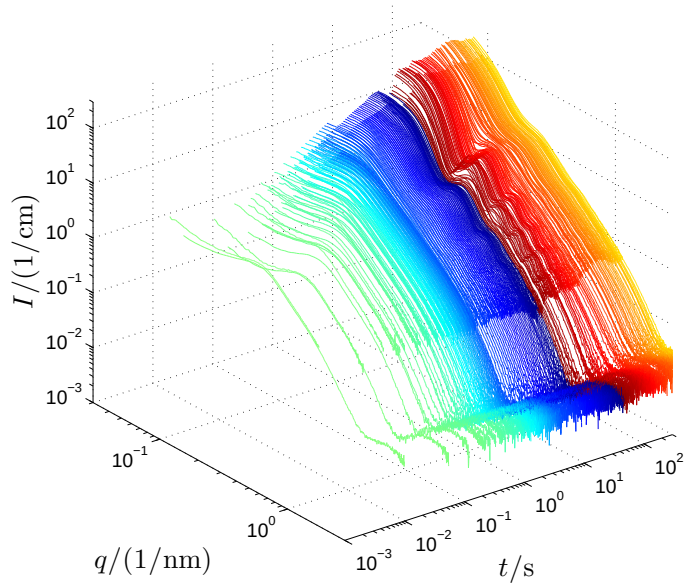

Figure A.7.4: Evolution of the aggregates in the system TDMAO-LiPFOS (55:45) + 1mol% Pluronic L35 (0.275mM Pluronic F38) at 50mM and 25°C, SAXS measurements